Emerging semiconductor nanostructure materials for single-photon avalanche diodes

by

Brad van Kasteren

A thesis

presented to the University of Waterloo

in fulfillment of the

thesis requirement for the degree of

Doctor of Philosophy

in

Electrical and Computer Engineering

Waterloo, Ontario, Canada, 2023

Examining Committee Membership

The following served on the Examining Committee for this thesis. The decision of the Examining Committee is by majority vote.

External Examiner: Joshua Bienfang
Adjunct Faculty, Institute for Physical Sciences and Technology,
University of Maryland

Supervisors: David Cory
Professor, Dept. of Chemistry,
University of Waterloo

Michael Reimer
Associate Professor, Dept. of Electrical & Computer Engineering,
University of Waterloo

Internal Member: Michal Bajcsy
Associate Professor, Dept. of Electrical & Computer Engineering,
University of Waterloo

Youngki Yoon
Associate Professor, Dept. of Electrical & Computer Engineering,
University of Waterloo

Internal-External Member: Thomas Jennewein
Associate Professor, Dept. of Physics and Astronomy,
University of Waterloo

Author's Declaration

This thesis consists of material all of which I authored or co-authored: see Statement of Contributions included in the thesis. This is a true copy of the thesis, including any required final revisions, as accepted by my examiners.

I understand that my thesis may be made electronically available to the public.

Statement of Contributions

I was the sole author for Chapter 1, Chapter 2, and Chapter 7 which were written under the supervision of Dr. Michael Reimer and Dr. David Cory and were not written for publication.

Study lead and writeup of Section 7.2 by Brad van Kasteren, with contributions of intellectual input from William F. Losin and Burak Tekcan, numerical modelling by William F. Losin, and material stack design by Burak Tekcan. Sections 7.3 - 7.6 were prepared by Brad van Kasteren with contributions of intellectual input from Michael Reimer, review by Dr. Jean-Philippe Bourgoin, and the noted implemented work by Burak Tekcan, William Losin, and Cole Fehr.

This thesis consists in part of four manuscripts written for publication. Exceptions to sole authorship of material are as follows:

Research Presented in Chapter 3:

Scientific publication manuscript (in full) and supplementary (in part) from Nature Nanotechnology. Sandra J. Gibson, Brad van Kasteren, Burak Tekcan, Yingchao Cui, Dick van Dam, Jos E. M. Haverkort, Erik P. A. M. Bakkers, and Michael E. Reimer. Tapered InP nanowire arrays for efficient broadband high-speed single-photon detection. Nature Nanotechnology January 2019. DOI: https://doi.org/10.1038/s41565-019-0393-2

Dr. Michael Reimer was the principal investigator of this research which was undertaken through support from the Canada First Research Excellence Fund and Industry Canada. Dr. Gibson, Burak Tekcan, Dr. Yingchao Cui, Dr. Dick van Dam, Dr. Jos E. M. Haverkort, and Dr. Erik P. A. M. Bakkers were co-authors on the publication relating to this work. Non-authored project contributors included R. Ronaldo, J. P. Bourgoin, and V. Zwiller who aided in the electronics set-up, assistance with the optics, and in useful discussions, respectively. Further contributors included S. Kölling and M. A. Verheijen who prepared the cross-sectional lamella by focused ion beam (FIB) and TEM analysis, respectively. Additionally, thanks was given to Dr. D. van Dam et al. (10.1021/acsnano.6b06874) for data used in Figure 3-2b–d.

The research contributions by Brad van Kasteren were conducted at the University of Waterloo under the supervision of Dr. Michael Reimer and Dr. David Cory. S.J.G. performed the photocurrent testing. S.J.G. drafted the manuscript and supplementary information with input from all authors. Manuscript

and supplementary additions addressing reviewer response concerns for publication were completed by S.J.G., B.v.K., B.T. and M.E.R. D.v.D. and B.v.K. performed the optical measurements and simulations. B.T. performed the temperature-dependent dark current measurements and device simulations of the depleted nanowire core. Y.C. fabricated the devices. M.E.R. supervised the work. All authors approved the final version of the manuscript.

Research Presented in Chapter 4:

Scientific publication manuscript from Scientific Reports, in part: Burak Tekcan, Brad van Kasteren, Sasan V. Grayli, Daozhi She, Man Chun Tam, Dayan Ban, Zbigniew Wasilewski, Adam W. Tsen, and Michael E. Reimer. Semiconductor nanowire metamaterial for broadband near-unity absorption. Scientific Reports. May 2022. DOI: https://doi.org/10.1038/s41598-022-13537-y

I was equal authors with Burak Tekcan and Sasan V. Grayli. The shared contributions of the manuscript which overlapped with the thesis work of co-author Burak Tekcan, who's focus was semiconductor device design and fabrication, is paraphrased in this thesis. The published article manuscript sections which were paraphrased include the Abstract, Introduction, Broadband Near-Unity Absorber — Tapered Nanowire Metamaterial, Results, and Conclusions.

Dr. Michael Reimer was the principal investigator of this research which was undertaken through support from Canada First Research Excellence Fund, NSERC, and Industry Canada. The research contributions from Brad van Kasteren were conducted at the University of Waterloo under the supervision of Dr. Michael Reimer and Dr. David Cory with funding from the Canada First Research Excellence Fund, NSERC, and Industry Canada. Burak Tekcan, Brad van Kasteren, and Sasan V. Grayli contributed equally to the work. Brad van Kasteren provided the initial design of the nanowire metamaterial through numerical calculation, performed data analysis, and reviewed and edited the manuscript. Burak Tekcan performed the sample preparation, nanofabrication, device characterization, and edited the manuscript. Sasan drafted the manuscript with Dr. Michael Reimer and assistance from all authors, performed data analysis, assisted with device characterization, and ran the optical simulations. Daozhi Shen assisted with device characterization and Man Chun Tam and Zbigniew Wasilewski provided the MBE grown InGaAs wafers. Dayan Ban and Adam Tsen provided scientific support and the FTIR experimental setup, respectively.

Research Presented in Chapters 5 and 6:

Chapter 5 and Chapter 6 consist of scientific article manuscripts (in full) which are being prepared for publication, tentatively titled Designing Perfect Absorbers Using Semiconductor Metasurfaces on High-Index Substrate for Photodetection and Mode-Matching Method for Efficient Coupling and Near-Unity Absorptance in a Single Tapered Semiconductor Nanowire Photodetector, respectively. Dr. Michael Reimer was the principal investigator of this research. The research contributions by Brad van Kasteren were conducted at the University of Waterloo under the supervision of Dr. Michael Reimer and Dr. David Cory. This research was undertaken thanks in part to funding from the Canada First Research Excellence Fund, Mitacs, and Innovation Science and Economic Development Canada.

The prospective article of Chapter 5 is currently co-authored by Brad van Kasteren, Dr. Sasan V. Grayli, William Losin, and Dr. Michael Reimer. The manuscript was drafted by Brad van Kasteren and Sasan V. Grayli with input from all authors. The study was designed by S.V.G. and B.v.K.. S.V.G. performed the numerical optical modelling and analysis with intellectual input from B.v.K.. B.v.K. and W.L. performed the numerical electrical modelling and analysis with intellectual input from S.V.G.. M.E.R. supervised the work.

The prospective article of Chapter 6 is currently co-authored by Brad van Kasteren, Dr. Sasan V. Grayli, Sathursan Kokilathasan, William Losin, and Dr. Michael Reimer. The manuscript was drafted by Brad van Kasteren with input from all authors. B.v.K., S.V.G, and M.E.R. designed the study. B.v.K. and S.K. performed the numerical optical modelling and analysis of the cylindrical waveguide with intellectual input from S.V.G.. S.V.G. performed the numerical optical modelling and analysis of the tapered nanowire with intellectual input from B.v.K.. B.v.k. and W.L. performed the numerical electrical modelling with intellectual input from S.V.G.. M.E.R. supervised the work.

Abstract

Detecting of light at the single photon level has a far-reaching impact that enables a broad range of applications. In sensing, advances in single-photon detection enable low light applications such as night-time operation, rapid satellite communication, and long-range three-dimensional imaging. In biomedical engineering, advancing single-photon detection technologies positively impacts patient care through important applications like singlet oxygen detection for dose monitoring in cancer treatment. In industry, impacts are made on state-of-the-art technologies like quantum communication which relies on the efficient detection of light at the fundamental limit. While the high impact of single-photon detection technologies is clear, the potential for improvement and challenges faced by prominent single-photon detection technologies remains. Superconducting single-photon detectors push the bounds of performance, but their high cost and lack of portability limits their prospect for far reaching applicability. Single-photon avalanche diodes (SPADs) are a promising alternative which can be made portable, absent of the need for cryogenic cooling, but they generally lack the performance of superconducting detectors. The materials in SPAD designs dictate operation, and conventional materials implemented being defined according to intrinsic material properties, limits SPAD performance. However, new classes of advanced materials are being realized which exhibit modified electromagnetic properties from the engineered arrangement of subwavelength structural units and low-dimensional properties. Such materials include metamaterials and low-dimensional materials, and they have been shown to enhance optoelectrical properties that are critical to avalanche photodiodes, like rapid photo response, enhanced absorption, and reduced dark current. In this work, the application of such advanced materials in SPADs is explored. Tapered nanowires and nanowire arrays are optimized for enhanced absorption and shown experimentally at room temperature to demonstrate high speed near-unity absorptance response at the single-photon level. In the metamaterial and nanowire devices, the gain and timing jitter are shown to be significantly improved over conventional bulk-based designs. Furthermore, the modelling of metamaterials in a SPAD device design and its operation with external single-photon detection circuitry is studied. The analysis is further shown to extend down to single nanowire devices which offers an elegant approach for integrated photonic circuits.

Acknowledgements

I express my sincere gratitude to my supervisors, Professor Michael Reimer and Professor David Cory, for offering me the opportunity and support to pursue my research interests. I extend this deepest gratitude to my former committee member and first university supervisor and mentor, Professor Safieddin Safavi-Naeini, who introduced me to and guided me in what became my academic journey. To my current committee, Professors Thomas Jennewein, Michal Bajcsy, and Youngki Yoon, I am deeply grateful for your council in achieving my academic milestones. Furthermore, I am greatly appreciative of Canada First Research Excellence Fund and the Faculty of Engineering for their generosity in offering the financial support without which this work would not have been made possible.

Many thanks to my academic colleagues, fellow members of Professor Michael Reimer's and Professor David Cory's academic research groups, Single Quantum Systems, and the RAC, IQC, and UW staff, faculty, and students who supplied resources and supported me with my studies. Special appreciation to Dr. Burak Tekcan, Dr. Sasan Vosoogh-Grayli, William Losin, Cole Fehr, Dr. Francois Sfigakis, Roberto Romero, Peter Sprenger, Alex Mitrovic, Sathursan Kokilathasan, Dr. Sandra Gibson, Christine Dietrich, and John Dietrich for their contributions to my academic work, preparations, and timely arrival.

Finally, a sincere thank you to my family and friends for all the personal support; being there to keep motivations high, ensuring my continued efforts, and helping to overcoming the many challenges of my studies.

Dedication

To my loving parents and family, caring friends and community, and my encouraging academic associates.

Table of Contents

List of Figures

List of Tables

List of Acronyms and Abbreviations

Abbreviation/Acronym	Definition
1D	One-Dimensional
2D	Two-Dimensional
3D	Three-Dimensional
AC	Alternating Current
APD	Avalanche Photodiode
AQC	Active Quenching Circuit
BCB	Benzocyclobutene
CMOS	Complementary Metal–Oxide–Semiconductor
DC	Direct Current
DCR	Dark Count Rate
DE	Detection Efficiency
DIP	Dual In-Line Package
ED	Electric Dipole
EDR	Electric Dipole Resonance
EH	TM Component Dominant Hybrid Mode
ELR	Electric Lattice Resonance
EM	Electromagnetic
EQ	Electric Quadrupole
EQE	External Quantum Efficiency
ESD	Electrostatic Discharge
FAQC	Fast Active Quenching Circuit

FDTD	Finite-Difference Time-Domain
FPGA	Field-Programmable Gate Array
FTIR	Fourier-Transform Infrared
FWHM	Full Width at Half Maximum
GRIN	Graded-Index
HBT	Heterojunction Bipolar Transistor
HE	TE Component Dominant Hybrid Mode
IQE	Internal Quantum Efficiency
IR	Infrared
ITO	Indium Tin Oxide
LCD	Liquid Crystal Display
LIDAR	Light Detection and Ranging
LRM	Leaky Resonant Mode
MBE	Molecular Beam Epitaxy
MD	Magnetic Dipole
MDR	Magnetic Dipole Resonance
MLR	Magnetic Lattice Resonance
MM	Multimode
MOVPE	Metal–Organic Vapour-Phase Epitaxy
MQ	Magnetic Quadrupole
MQC	Mixed Quenching Circuit
NIR	Near Infrared
NW	Nanowire

PCB	Printed Circuit Board
PMT	Photomultiplier Tube
PNR	Photon Number Resolution
PQC	Passive Quenching Circuit
QD	Quantum Dot
RA	Rayleigh Anomaly
RC	Resistive-Capacitive
RF	Radio Frequency
RIE	Reactive Ion Etching
SAGCM	Separate Absorption, Grading, Charge, and Multiplication
SAM	Separate Absorption and Multiplication
SEM	Scanning Electron Microscope
SM	Single Mode
SMA	SubMiniature Version A
SN-SPAD	Semiconductor Nanowire Single-Photon Avalanche Diode
SNSPD	Superconducting Nanowire Single-Photon Detector
SPAD	Single-Photon Avalanche Diode
SPD	Single-Photon Detector
SWIR	Short-Wave Infrared
TE	Transverse Electric
TEC	Thermoelectric Cooler
TM	Transverse Magnetic
UV	Ultraviolet

VA	Applied Voltage
VB	Breakdown Voltage
VE	Excess Voltage (Beyond VB)
VIS	Visible

Chapter 1
Introduction

1.1 A Brief History on Light

One of the earliest scientific perceptions of light dates back to the 5th century BC, when the Greek philosopher Empedocles concluded that light emanates as rays from the eye. It was not until 1000 AD that a contradicting theory that light emanates as rays from external sources was scientifically established. Later, in the 17th century, Descartes defined light as a form of pressure which travels from a source to a detector through space, from which Hooke and Huygens established the wave theory of light. The contradictory notion that light behaves like a particle was put forward by Gassendi at a similar point in time, but the wave description became the favourable of the two models due to the results of Young's double slit experiment, Fresnel's diffraction experiments, and the derivation of Maxwell's equations[1].

In 1897, J.J. Thompson discovered discrete negative charged particles moving through vacuum, an observation which required the wave model of electromagnetism be further reviewed. This result led to Planck's quantized description of light, which was embraced by Einstein in the description of the photoelectric effect. By 1913, Bohr contributed to the quantum model with quantized energy and angular momentum and de Broglie expanded on this even further in his hypothesis that the wave-like nature of light extends to particles of matter. A framework for quantum mechanics rapidly followed Dirac's quantum electromagnetic (EM) field description in 1927, whereby the primary contributors were Heisenberg, Born, Schrödinger, Pauli, and Dirac[1].

Shortly after, the atomic-cascade photon-pair source was developed in the 1950s. This source was used in what represented the first single-photon source in the 1970s and 1980s, confirming the quantum nature of light[1]. Complimenting the research surrounding the new quantized physical models of light in the 1970s, papers pertaining to single-photon detectors (SPDs) and sources soared from several papers per year to hundreds over the span of around 15 years. Similarly, techniques utilizing single-photon technologies like single-photon measurements, quantum cryptography, and quantum metrology jumped from tens of papers per year to hundreds[1,2]. To this day, single-photon-based technologies prove valuable in many active areas of interest including astronomy, sensing, biomedical engineering, and the growing field of quantum information science[3].

Detecting light in the single-photon regime enables observations over longer distances. This trait proves useful in low light applications such as night-time operation, identification and tracking of diffuse reflectors, communication of images from satellites at high speed, and acquiring three-dimensional (3D) images at long range with high resolution[3]. In biomedical engineering, advancing technologies for detecting light at the fundamental limit has a positive impact on important applications such as singlet oxygen detection for dose monitoring in cancer treatment[3]. Single-photon technologies also influence the tech sector, where state-of-the-art technologies like quantum communication and fault-tolerant analysis testing of complementary metal–oxide–semiconductor (CMOS) circuits depend on sensing individual photons, directly benefiting from the advances in SPDs[3]. Single-photon technology is also at the heart of advanced applications in quantum information processing, such as quantum cryptography, quantum computing, and the study of quantum phenomena[4].

It has become well known that light has intrinsic momentum in the form of linear and angular momentum, in addition to a characteristic energy[5]. These properties give the photon its ability to interact with matter and exchange both energy and momentum[6]. This level of understanding dates back to the years of Paul A. M. Dirac, where he presented quantized models to describe angular momentum of polarized light resulting from electric dipole (ED) radiation[7]. Similarly, atomic models of this era included the property of characteristic angular momentum and an understanding of which was demonstrated by researchers and experimentalists such as Rabi, Bloch, and Purcell in their work on nuclear magnetic resonance[8]. More recently, about 25 years ago, it was discovered that the angular momentum of light comes in two forms: spin and orbital angular momentum, furthering the potential for coupling photons with atomic spins. In 2006 a device capable of converting between the two types of angular moment was devised. This was just one example of modern works which illustrates the potential use of photons as a control and communication medium in both classical and quantum computing and networking, and the youth of the field with a bright future[5].

1.2 Single-Photon Detector Platforms

SPDs have demanding technological applications, and as such they have a wide variety of device designs attempting to achieve the high-performance need for these applications. Numerous SPD schemes exist to satisfy many important performance metrics demanded by the broad range of applications[1]. The metrics primarily considered in the design of SPDs include operation temperature, detection efficiency (DE), bandwidth, timing jitter, dark count rate (DCR), max count rate, photon

number resolution (PNR) capability, afterpulsing, and active area[1]. An ideal SPD has perfect performance in all of the critical metrics, including a 100% DE, PNR capability, arbitrarily accurate timing jitter, and high count rate without any drawbacks such as dark counts. A near-ideal level of these properties can be achieved in some of the performance metrics in various detector designs but the same is not true for a detector which operates at a near-ideal level in all of the performance metrics. All SPD designs tend to have their strengths and weaknesses and are selected based on the demands of the application and cost. Generally, SPDs fall under one of the three material systems: photomultipliers, semiconductors, and superconductors. Of the photomultiplier family, photomultiplier tubes (PMT) are of the most popular designs. Likewise, single-photon avalanche diodes (SPAD) and superconducting nanowire single-photon detectors (SNSPD) for the semiconductor and superconductor families are among the most used, respectively[1].

1.3 Photomultiplier Tubes

PMTs are SPDs that rely on the multiplication of an initial photoelectron generated at a photocathode after single photon absorption. The photoelectron is exposed to an electric field that accelerates it towards a cascade of dynodes. These subsequent dynodes are photoemissive electrode surfaces, which amplify the signal to many electrons through ejected secondary emission. This repeated process multiplies the electrons substantially for a measurable readout from collection at the PMT anode. The higher DE spectral range of these sensors is around 185 nm to 900 nm (peak of 30% at λ = 260 nm). PMTs can detect over a broader range at longer wavelengths from 300 nm to 1700 nm, but at significantly lower efficiency peak (peak of 1% at λ = 1200 nm)[1]. In general, however, PMT designs are limited in their DE (40% @ 500 nm), especially in the infrared (IR) (2% @ 1550nm), and they have good max count rates (10 x10^6 /s) and some PNR capability. PMTs can also operate at room (300K) and commercial thermoelectric cooler (TEC) (~200K+) temperatures with a large active area (millimeter scale), relatively low DCR (100 /s), and good timing resolution (0.3 ns)[1]. The notable shortcomings of PMTs are their tendency for lower detection efficiencies than competing technologies and the sizable footprint of bulky vacuum tubes. The reduced DE is especially true in the near-infrared (NIR) regime and longer wavelengths because a photon in this range is unable to provide an electron with sufficient energy to overcome the vacuum level barrier, which is the requirement for photoemission at the photocathode[1].

1.4 Superconducting Detectors

Superconducting SPDs include a variety of devices with different operating principles. Notable designs include superconducting transition edge sensor, SNSPDs, and superconducting tunnel junctions. Though each of these superconducting detectors operate according to different governing principles, prominent technologies rely on the generation and readout of an electronic response from an incident photon through the disruption of superconducting states or small temperature changes. Superconducting-based detectors have demonstrated higher performance than PMTs and semiconductor designs, including full PNR, low timing jitter (< 3 ps), high detection efficiencies (88% @ 694 nm), and even maintaining high detection efficiencies in the IR regime (95% @ 1556 nm)[1,9]. However, no one superconducting SPD has yet achieved high performance across all critical SPD metrics simultaneously as their high performance requires trade-offs between these metrics. Furthermore, superconducting SPDs depend on cryogenic operating temperatures (0.1K – 5K) for their high-performance operation.

1.5 Single-Photon Avalanche Diodes

The operation of SPADs is based on the positive feedback of a carrier multiplication process called an avalanche. When operating an avalanche photodiode (APD) (p-n junction) in reverse bias, it can enter a region of high gain. In this linear regime just before the avalanche breakdown a small change in the reverse bias causes a substantial current change. For single-photon detection, the diode is operated beyond breakdown between avalanche and quiescent states with external circuitry. During such operation, the circuitry prepares the SPAD in the quiescent state, absent a generated carrier for avalanche. When a carrier is generated, ideally upon photon arrival and absorption, a large avalanche current that can be sensed is triggered for photon counting. Following such a trigger event, the external circuitry resets the SPAD and prepares it in the quiescent state again for subsequent single-photon detection. SPAD designs tend to have a high DE (74% @ 600 nm), particularly in the visible (VIS), but drop off at longer wavelengths in the NIR and short-wave infrared (SWIR)(35% at 950 nm, 26% at 1550 nm)[1,10]. More critical SPAD metric performance analysis can be found in a recent review article[11]. These semiconductor-based devices also operate at room and commercial TEC temperatures, and they have demonstrated superior performance over PMTs in the other critical SPD metrics too. However, like superconducting-based SPDs, no one semiconductor detector achieves a high performance across all metrics simultaneously and high-performance operation in the SWIR regime remains a challenge[1].

While several notable points of comparison between the various SPD platforms have been introduced, more recent insights into the competing mainstream SPD technologies are abundant in literature. PMTs, SPADs, and superconducting SPDs remain among the most popular technologies, but recent articles present more current insights in depth. Such insights include advances in popular SPD technologies, their comparison of improved performance in critical SPD metrics, more extensive lists of SPD designs, and reviews with nuanced SPD operation and performance details[1,3,9,12–19].

1.5.1 The Applications, Impact, and Issues of Single-Photon Avalanche Diodes

Single-photon technologies have a widespread reach and single-photon detection technologies find applicability in single molecule fluorescence spectroscopy, CMOS defect analysis, laser remote sensing through light detection and ranging (LIDAR), singlet oxygen luminescence for dose monitor in cancer treatment. Single-photon detection technology is also important in quantum information science such as photon correlation measurements, single and entangled photon source characterization, quantum computing, and quantum cryptography[20]. While SPD technologies are numerous, each present their advantages and disadvantages. Modern SNSPDs are capable of meeting much of the performance needs in demanding applications, but they are extremely expensive, have a limited simultaneous spectral bandwidth and high efficiency, and their required operating temperatures have more demanding power requirements, which hinders their practical portability[1,3,11,14,16,21–23]. SNSPDs are capable of maximizing their efficiency from the UV through IR ($\lambda > 10$ μm) but doing so requires tuning the device cavity[24]. As a result, these detectors are unable to achieve the simultaneous high efficiency and broad bandwidth. Also, compact SNSPD operational solutions utilizing Gifford-McMahon, Stirling, Joule-Thomson, and hybrid two stage high frequency pulse tube and He Joule-Thomson cryocoolers are being explored. However, such compact cryogenic coolers currently lack the cooling power necessary for high-performance superconducting SPDs. In 2017-2018, superconducting SPD integration with miniaturized cryocooler solutions achieved 50% and 20% system detection efficiencies at wavelengths of 1550 nm and 1310 nm, respectively[23].

Commercial semiconductor devices such as silicon and InGaAs/InP SPADs are currently a favourable alternative SPD technology because they are capable of good performance in critical SPD performance metrics, and they can overcome superconducting device shortcomings. This popularity is also partly attributed to being a more practical option, as SPADs are less expensive and they can operate at or near room temperature, circumventing the issue of low temperature operation. Furthermore, SPADs

generally outperform the competing room-temperature and near room temperature single-photon detection technology (PMTs) in critical SPD metrics. As a result, SPADs demonstrate the potential to be a leading mainstream technology for single-photon detection applications. Commercial state-of-the-art SPADs based on silicon target markets in the areas of medicine, science, information security, industry, aerospace, and defense. The demand for detectors in these markets is increasing with the technological demands of LIDAR, photon correlation spectroscopy, astronomical observation, optical range finding, and adaptive optics, revealing the need for development of more advanced SPAD technologies.

Novel SPADs are likely to find applicability in the existing market, replace current technologies, and enable new research areas. APDs are currently a prominent commercial photodetector technology which attempts to satisfy commercial demands. This is advantageous for novel SPAD developments, as they can share similar industry standardized nanofabrication techniques and equipment. This compatibility will enable a faster adoption and commercial availability of a novel SPAD technology. The result of such novel SPAD developments can find the technology applied in new research areas like quantum LIDAR, remote sensing, dose monitoring for cancer therapy, quantum cryptography, CMOS testing, high speed optical communication of images and data streams from space, among other yet unforeseen applications[3]. In particular, the relatively low power demand from SPADs on TECs will prove invaluable in remote systems, mobile, or unmanned settings like satellites, airborne, and off-grid powered (solar or wind) platforms. In such applications, power is at a premium and the relatively low power requirements of SPAD technologies will increase the sustainability of such systems. Furthermore, SPADs can be in self-contained in lightweight, compact, low power modules, enabling new applications to emerge which are not possible with current sensing technologies. For instance, in remote sensing applications, the SPAD modules can enable the installation of new types of remote monitoring instruments with advanced capabilities for automated systems like robotics, planes, and satellites.

Current high-performance APDs and single-photon counting modules generally depend on silicon avalanche detectors or thin films. However, these SPAD designs have their shortcomings, including the tendency of having a narrow spectral bandwidth. Furthermore, silicon SPADs are attributed with poor performance in the SWIR. This poor performance is because of the insufficient energy of the light, relative to the silicon bandgap, to promote carriers for single-photon detection. Thicker films may be used to increase the absorption efficiency in silicon APDs in the VIS and NIR regions, but this is

achieved at the expense of temporal performance. As a result, current silicon SPADs are unable to offer broadband, fast, highly efficient single-photon detection operation throughout the VIS to SWIR spectrum with precise timing jitter, and thus lacking in comparison to SNSPDS[2,14]. Even with the incorporation of higher absorption efficiency materials in SPADs, such as InGaAs, issues with noise and low efficiency remain[1]. These limitations restrict the types of signals and environmental conditions that can be surveyed practically by the technology.

1.5.2 Separate Absorption-Multiplication Region

For SWIR applications, SPAD devices often include a lower bandgap material to absorb light at longer wavelengths. However, SPADs employing these materials are typically plagued with noise, so strategies to overcome this limitation are at the forefront of developments. Such strategies include separate absorption and multiplication regions and more complex material doping and layering. The engineered doping profile in such SPAD designs allow internal electric fields to be designed to acceptable limits within the low bandgap region and higher levels in the high bandgap region for reducing DCR while accommodating multiplication[25]. Additional charge and grading layers have also been added to further enhance the electric field control and energy band smoothening, respectively. The separate absorption and multiplication and the separate absorption, multiplication, grading, and charge layer structures are referred to as an SAM and SAGCM, respectively. TEC systems are also added to such SPAD designs to compensate for the increased DCR by lowering thermal energy and thus thermal excitation events[1].

1.6 Materials

SPADs are highly material dependent devices, even their basic operation has demanding requirements for absorptance and conduction. Beyond a suitable bandgap energy, there exists increasing demands for material quality and SPAD governing material properties, which directly impact many of the critical SPAD performance metrics. For instance, material impact ionization rates govern avalanche probability, breakdown voltage (VB), and p-n junction locations, and DCR is influenced by defects, trap densities, and energy band structures[26]. As such, material development is critical to the performance of SPADs.

Planar structures are the conventional structure for APDs and many device governing principles have been defined for such SPAD designs[25–28]. However, less conventional structures are presenting

themselves as potentially viable structures for incorporation into SPADs through attractive demonstrations of exotic optical response and photodetection performance. Novel SPD designs attempt to overcome performance weaknesses by exploiting quantum effects and exotic optical responses in next-generation materials, as demonstrated in quantum-dot-resonant tunnel diode devices and gated field effect transistors. Furthermore, low-dimensional materials have been used in novel technologies including phototransistors based on two-dimensional (2D) materials such as graphene, hybrid graphene quantum-dot systems, and single nanowire (NW) optoelectronics. The potential for high-performance optoelectronic applications using these novel materials in SPDs has been demonstrated, but these novel technologies have not reached the level of performance of commercial devices. Typically, these novel technologies may achieve high performance in one metric but lack in another, such as exhibiting high gain or fast operation[3]. While recent publications of emerging SPD technologies show that they are still unable to replace traditional Si and InGaAs/InP SPADs, current literature highlights the evolution and notable progress of the novel technologies[3,13]. Recent works also present significant advances in NW-based APDs, including the demonstrations in 2019 of simultaneously fast temporal response (rise time < 1 ns) and high gain ($> 10^5$) with precise timing jitter (< 20 ps) in a tapered InP NW-based APD and < 10 Hz DCR, 7.8 MHz count rate, and timing jitter < 38 ps in an InGaAs/GaAs NW-based APD[3,29]. Furthermore, optimistic analysis of NW material systems continue to be released, including recent analysis on the beneficial relationship between speed, efficiency, and number of NWs which was presented in 2022 with InGaAs/InP NW arrays[30].

Thus, a novel material-based solution to SPADs overcoming their current limitations shows promise, but further investigations are required. The developments of novel detectors will require a route with the potential to overcome the selectivity dependence and poor NIR and SWIR performance faced by current SPDs. Advanced materials such as metamaterials, metasurfaces, and low-dimensional materials are some examples of modern material classes that pose as attractive options to such sensing qualities. These novel materials are capable of extending performance beyond what is possible with conventional technologies, including enhanced absorptance[3,31–34]. Through the incorporation of advanced materials into SPAD design, the material qualities like near-unity broadband absorptance may be achieved and engineered for target wavelength regions.

1.7 Thesis Goal

A focus of this thesis is to explore metasurfaces, semiconductor NW metamaterials, and low-dimensional semiconductor nanostructures for use in overcoming the current limitations of SPADs through the incorporation of these novel materials. Such SPAD shortcomings in focus include the limited DE in the SWIR and their inability to achieve simultaneous high performance in all critical SPD metrics.

1.8 The Prospect of Advanced Materials

There has been remarkable progress in the research developments of SPAD design with conventional structures and materials[25–28,35–40]. The demands for material quality are well understood, tradeoffs between critical performance metrics have been examined, and insights into the compromises that must be made in these designs enable them to achieve high performance for select applications. However, such design compromises also limit the SPADs by impeding their ability to attain high performance in all metrics. As a result, the pursuit for a SPAD technology with overall high performance in all metrics and further reaching applicability remains. This pursuit fuels an increasing demand for higher SPAD material performance, the application of advanced nanostructured materials, and nano-optoelectronics. The field of research is young, but some novel material applications into quantum devices like SPADs have yielded prospective results[34,41]. Some nanomaterials of particular interest belong to the classes of metamaterials, metasufaces, and lowdimensional materials. These material systems use nanostructures, geometries, patterns, etc. to exhibit exotic optical responses unobserved in their bulk counterparts. These alternative materials offer abilities to modulate intrinsic-optical properties and an opportunity to enhance absorption and overcome the current limitations of conventional planar SPADs.

1.8.1 Metamaterials, Metasurfaces, and Lower Dimension Materials

Materials are conventionally defined according to their repeating atomic and molecular structures and have a long list of intrinsic properties: chemical, electrical, magnetic, mechanical, etc., each with their respective sub-categorizations. The term metamaterial is used to describe EM materials of a different class, and with differing properties from their conventional, natural material counterparts. Metamaterials are attributed with the same atomic and molecular compositions as their conventional material counterpart, but they exhibit modified EM properties. These modified properties result from artificially arranged or engineered unit structuring with a subwavelength inhomogeneity scale at the

light wavelength of interest. A metamaterial is composed of structural units called metaatoms in a lattice with subwavelength periodicity (lattice constant), and its material parameters are ascribed according to its macroscopic homogenized optical response and effective properties[42]. Like metamaterials, metasurfaces are materials composed of an artificial unit structure and they also exhibit exotic properties; however, their structuring is spatially limited to a 2D surface. Optical resonators are an example of engineered metasurfaces at subwavelength dimensions, which are used to spatially control properties of incident light such as phase, amplitude, polarization, and the resulting wavefront. The application of metasurfaces has shown that leveraging their unique behaviour allows for higher performance alternatives to conventional optical components at a reduced scale. Metasurfaces have been shown to achieve enhanced absorption and outperform conventional optical components, such as lenses and waveplates, at a fraction of the size, making them an attractive technology for consumer optics, electronics industries, and SPADs[34,43].

Another interesting class of materials which are finding their place in nano-optoelectronic devices are low-dimensional materials. Low-dimensional materials can demonstrate interesting physics for use in optoelectronic devices like high carrier mobility and enhanced absorption[31]. Two-dimensional materials including graphene and one-dimensional (1D) materials such as single semiconductor NWs are examples of low-dimensional materials, being structured at the subwavelength level. Low-dimensional materials differ from metamaterials as they are not defined according to artificially engineered periodic structuring, but they also show potential for high-performance photonic technologies, especially for SWIR technologies. The focus of using these novel materials in SWIR technologies is driven by the demand from influential applications like in telecom and integrated photonics[31].

Integrated photonic circuits are on-chip-based photonic systems that are designed to execute useful functions through photonic operations. For example, waveguides can be placed side-by-side closely on a chip for a set propagation length to create the tunable integrated photonic circuit analogue of bulk beam splitters known as directional couplers. These integrated photonic circuit elements leverage the evanescent coupling of waveguide modes to prepare waveguide output power equivalences to a beam splitter[44]. In the case of integrated quantum architectures, integrated photonic circuits have already demonstrated core quantum operations like quantum gates[45,46]. As such, integrated photonic technologies are showing their promise in replacing conventional optical systems, necessitating the study of options for the smallest footprint optoelectronic devices for integration.

Low-dimensional-material-based nano-optoelectronic devices have already demonstrated optoelectronic operation with remarkable performance, including picosecond response time[41]. Single semiconductor NWs (a low-dimensional material) have shown high-performance SWIR operation, have a small lateral footprint, and are thus a contender for enabling the production of high demand sensors. The single semiconductor NW platform shows prospect in minimizing pixel area size, simultaneously offering high performance capabilities of interest to quantum photonic technologies, and fulfilling the need for enhanced material properties to strengthen SPAD performance in critical metrics[47].

1.9 Published and Prospective Publication Developments in this Work

1.9.1 Tapered InP Nanowire Arrays for Efficient Broadband High-Speed Single-Photon Detection

SPDs are critical components in a wide variety of applications and the necessity for an overall high-performance SPAD in fields like astronomy, laser ranging, remote sensing, classical communications, quantum information, and biomedical imaging remains. This is especially true for the IR wavelengths and necessitates the inclusion of new technologies for SPAD advancement[12]. An overall higher performance SPAD demands improved detection efficiencies over a broader bandwidth (over the VIS, NIR and SWIR regimes) with high-speed operation and timing resolution to elevate SPADs in the competition against superconducting NWs[12]. This was a focus of the published article of Chapter 3, where we have developed a tapered InP NW p–n junction array that overcomes these drawbacks to achieve high-efficiency photodetection over a broad bandwidth (~500 nm), with the high speed and gain that enables single-photon detection, all while operating at room temperature. Owing to the uniquely designed size and shape of the NWs, near-unity DE over a broad wavelength range from the ultraviolet (UV) to NIR is possible. The operation at higher temperatures is advantageous for sensing applications requiring portability. For example, applications requiring remote sensing of low powered signals like nighttime operation of devices, communication of images from satellites, and acquiring 3D images at long range with high resolution. Such applications are enabled by photon detection at the fundamental limit (single photons), which provides capabilities for observation over larger distances. Furthermore, single-photon detection finds critical use in the medical field, like in singlet oxygen detection for cancer treatment dose monitoring, whereby a sensitive detector enables doses to be more accurately supplied and monitored in patients to better avoid over- or underdosing, both of which can

have a negative impact on a patient's health. These examples are only a subset of the vital applications that rely on the advancement of single-photon detection technologies, such as the NW p-n junction array, for enhanced capabilities.

1.9.2 Semiconductor Nanowire Metamaterial for Broadband Near-Unity Absorption

The publication on tapered InP NW arrays demonstrated the potential of the structured array for single-photon sensitivity and high-performance operation through its large gain and simultaneously fast speed. It also highlights the potential to be extended to other materials and target spectra, particularly for the SWIR through incorporation of the tapered NW array design into InGaAs, a smaller bandgap material. In the work "semiconductor nanowire metamaterial for near-unity absorption" we study the potential impact of incorporating the structured array with InGaAs. Numerical analysis is performed to present the physics of the structured array as a metamaterial in cylindrical and tapered arrays of different geometries. Then, the metamaterial is tuned for the broadband and enhanced (near-unity) absorption from VIS into the SWIR (400 nm - 1650 nm). The metamaterial is fabricated, characterized, and experimentally demonstrates its enhanced absorption and anti-reflection properties with close agreement to the modelled performance up to 1650 nm wavelength.

1.9.3 Designing Perfect Absorbers Using Semiconductor Metasurfaces on High-Index Substrate for Photodetection

Early opto-electronic fabrication study measurements of the InGaAs tapered NW arrays performed by Burak Tekcan showed undesirable noise and device response for SPAD operation. While circuit, operating temperature, and device level changes were being explored to alleviate these issues, alternate metasurface designs were simultaneously investigated. In this prospective publication a metasurface structure inspired by the semiconductor NW metamaterial was analyzed. The analysis of the metasurface begins with the physical study of high-performance disk-like resonator absorbers and the negative impact that arises from their inclusion on a high-index substrate, a feature of practical microfabricated electronic devices. A taller, multipole resonance structure is found to alleviate the negative effects of the high-index substrate while maintaining the high-performance resonator qualities like tunable, near-unity selective absorption. The high-performance metasurface found following the analysis is composed of shorter unit structures than the cylindrical NW array metamaterial and poses as a promising alternative for SPAD development.

1.9.4 Mode-Matching Method for Efficient Coupling and Near-Unity Absorptance in a Single Tapered Semiconductor Nanowire Photodetector

Modern optics laboratory system integration into optical circuits is being realized as a reliable technological advancement from the bulky tabletop alternatives for photonic quantum computing. This shift is in part due to integrated circuit designs being more stable and scalable. Integrated photonic circuit technologies also provide a means to manipulate single photons and produce quantum gate operations for quantum photonic circuits. Such operations would be useful for optoelectronic and photonic applications, such as optical communications and quantum gate operators[48,49]. However, recent demonstrations of integrated photonic circuits suffered from poor injection and extraction efficiencies (~60%)[49], and efforts are being made to address the challenge of producing on-demand single and entangled photon sources and detectors that integrate well with the optical circuits[31].

A tapered NW-based solution making use of a NW quantum dot (QD) source and NW detector, like those of the Reimer group, may prove valuable in addressing this integrated source and detector photonic circuit design challenge[3,50,51]. The Reimer group's NW devices have the unique property of being identical size and shape, a property which can be leveraged for mode matching the NW-based source and detector. Investigating the mode-matching condition via EM field emission and absorption is an essential step towards a NW-based transmission network. In this prospective publication on a single-NW mode-matching method, we implement modal theory and mode-matching techniques to further illustrate the potential of the single NW platform for nano-optoelectronic applications. The study includes analysis of the modal properties of a cylindrical NW to find a limit of light-matter interaction with the structure and define the smallest footprint of the NW receiver. The cylindrical NW is then implemented as a waveguide base to a tapered NW structure, where the designed tapered profile is shown via finite-difference time-domain (FDTD) modelling to exhibit efficient coupling. The mode-matched single tapered NW is then implemented with an absorbing medium and further optimized to present the high-performance capabilities of the approach; near-unity absorptance at the target wavelength. The capabilities of the method are then further examined for nano-optoelectronic systems. This examination includes the numerical study of the single tapered NW near-unity absorber as a sensor through the incorporation of a radial p-n junction. This investigation further reveals the potential of tapered NWs for alleviating efficiency issues of optoelectronic devices and quantum (and classical) integrated photonic circuits.

1.10 References

1. *Single-photon generation and detection: experimental methods in the physical sciences*. (Elsevier/AP, Academic Press is an imprint of Elsevier, 2013).
2. Dello Russo, S. *et al.* Advances in Mid-Infrared Single-Photon Detection. *Photonics* **9**, 470 (2022).
3. Gibson, S. J. *et al.* Tapered InP nanowire arrays for efficient broadband high-speed single-photon detection. *Nature Nanotechnology* **14**, 473–479 (2019).
4. Itzler, M. A. *et al.* Advances in InGaAsP-based avalanche diode single photon detectors. *Journal of Modern Optics* **58**, 174–200 (2011).
5. Marrucci, L., Manzo, C. & Paparo, D. Optical Spin-to-Orbital Angular Momentum Conversion in Inhomogeneous Anisotropic Media. *Phys. Rev. Lett.* **96**, 163905 (2006).
6. Fischer, U. C. *et al.* On the Coupling of Photon Spin to Electron Orbital Angular Momentum.
7. Fischer, U. C. On Photon Spin and the Electrodynamic Origin of the Charge of the Electron.
8. Rabi, I. I., Zacharias, J. R., Millman, S. & Kusch, P. A New Method of Measuring Nuclear Magnetic Moment. *Phys. Rev.* **53**, 318–318 (1938).
9. Korzh, B. *et al.* Demonstration of sub-3 ps temporal resolution with a superconducting nanowire single-photon detector. *Nat. Photonics* **14**, 250–255 (2020).
10. Signorelli, F. *et al.* Low-Noise InGaAs/InP Single-Photon Avalanche Diodes for Fiber-Based and Free-Space Applications. *IEEE J. Select. Topics Quantum Electron.* **28**, 1–10 (2022).
11. Ceccarelli, F. *et al.* Recent Advances and Future Perspectives of Single-Photon Avalanche Diodes for Quantum Photonics Applications. *Adv Quantum Tech* **4**, 2000102 (2021).
12. Hadfield, R. H. Single-photon detectors for optical quantum information applications. *Nature Photon* **3**, 696–705 (2009).
13. Wang, H. *et al.* Emerging Single-Photon Detectors Based on Low-Dimensional Materials. *Small* **18**, 2103963 (2022).
14. Liu, C., Ye, H.-F. & Shi, Y.-L. Advances in near-infrared avalanche diode single-photon detectors. *Chip* **1**, 100005 (2022).
15. Lita, A. E., Reddy, D. V., Verma, V. B., Mirin, R. P. & Nam, S. W. Development of Superconducting Single-Photon and Photon-Number Resolving Detectors for Quantum Applications. *J. Lightwave Technol.* **40**, 7578–7597 (2022).
16. Hofbauer, M., Schneider-Hornstein, K. & Zimmermann, H. *Single-photon Detection for Data Communication and Quantum Systems*. (IOP Publishing, 2021). doi:10.1088/978-0-7503-2584-4.

17. Fang, Y.-Q. *et al.* InGaAs/InP single-photon detectors with 60% detection efficiency at 1550 nm. *Review of Scientific Instruments* **91**, 083102 (2020).
18. Sanzaro, M. *et al.* Single-Photon Avalanche Diodes in a 0.16 μm BCD Technology With Sharp Timing Response and Red-Enhanced Sensitivity. *IEEE J. Select. Topics Quantum Electron.* **24**, 1–9 (2018).
19. Shin, S. *et al.* Advances in the Large Area Picosecond Photo-Detector (LAPPD): 8" x 8" MCP-PMT with Capacitively Coupled Readout. (2022) doi:10.48550/ARXIV.2212.03208.
20. Chunnilall, C. J., Degiovanni, I. P., Kück, S., Müller, I. & Sinclair, A. G. Metrology of single-photon sources and detectors: a review. *Opt. Eng* **53**, 081910 (2014).
21. Zhang, J., Itzler, M. A., Zbinden, H. & Pan, J.-W. Advances in InGaAs/InP single-photon detector systems for quantum communication. *Light Sci Appl* **4**, e286–e286 (2015).
22. Calabretta, M. M. *et al.* Portable light detectors for bioluminescence biosensing applications: A comprehensive review from the analytical chemist's perspective. *Analytica Chimica Acta* **1200**, 339583 (2022).
23. Bhargav, A. M., Rakshit, R. K., Das, S. & Singh, M. Metrology Perspective of Single-Photon Detectors: Review on Global Calibration Methods. *Adv Quantum Tech* **4**, 2100008 (2021).
24. Verma, V. B. *et al.* Single-photon detection in the mid-infrared up to 10 μm wavelength using tungsten silicide superconducting nanowire detectors. *APL Photonics* **6**, 056101 (2021).
25. Cao, S. *et al.* Theoretical Analysis of InGaAs/InAlAs Single-Photon Avalanche Photodiodes. *Nanoscale Research Letters* **14**, 3 (2019).
26. Donnelly, J. P. *et al.* Design Considerations for 1.06-um InGaAsP–InP Geiger-Mode Avalanche Photodiodes. *IEEE J. Quantum Electron.* **42**, 797–809 (2006).
27. Acerbi, F., Anti, M., Tosi, A. & Zappa, F. Design Criteria for InGaAs/InP Single-Photon Avalanche Diode. *IEEE Photonics J.* **5**, 6800209–6800209 (2013).
28. Liu, M. *et al.* High-Performance InGaAs/InP Single-Photon Avalanche Photodiode. *IEEE J. Select. Topics Quantum Electron.* **13**, 887–894 (2007).
29. Farrell, A. C. *et al.* InGaAs–GaAs Nanowire Avalanche Photodiodes Toward Single-Photon Detection in Free-Running Mode. *Nano Lett.* **19**, 582–590 (2019).
30. Bianconi, S. *et al.* Strategy for Addressing the Low Quantum Efficiency of Nanowire Photodetectors. *ACS Photonics* **9**, 2280–2286 (2022).

31. Eng, P. C., Song, S. & Ping, B. State-of-the-art photodetectors for optoelectronic integration at telecommunication wavelength. *Nanophotonics* **4**, 277–302 (2015).
32. Tekcan, B. *et al.* Semiconductor nanowire metamaterial for broadband near-unity absorption. *Sci Rep* **12**, 9663 (2022).
33. Zhang, D. *et al.* All-optical modulation of quantum states by nonlinear metasurface. *Light Sci Appl* **11**, 58 (2022).
34. Chen, L. *et al.* Research on the Metasurface for Single-Photon Avalanche Photodiode. *Front. Phys.* **8**, 585871 (2020).
35. Wen, J. *et al.* Origin of large dark current increase in InGaAs/InP avalanche photodiode. *Journal of Applied Physics* **123**, 161530 (2018).
36. Karve, G. *et al.* Geiger mode operation of an In0.53Ga0.47As-In0.52Al0.48As avalanche photodiode. *IEEE J. Quantum Electron.* **39**, 1281–1286 (2003).
37. Aull, B. F. *et al.* Geiger-Mode Avalanche Photodiodes for Three-Dimensional Imaging. **13**, (2002).
38. Dautet, H. *et al.* Photon counting techniques with silicon avalanche photodiodes.
39. Kim, O. K., Forrest, S. R., Bonner, W. A. & Smith, R. G. A high gain $In_{0.53}Ga_{0.47}As$/InP avalanche photodiode with no tunneling leakage current. *Appl. Phys. Lett.* **39**, 402–404 (1981).
40. Susa, N., Nakagome, H., Mikami, O., Ando, H. & Kanbe, H. New InGaAs/InP avalanche photodiode structure for the 1-1.6 um wavelength region. *IEEE J. Quantum Electron.* **16**, 864–870 (1980).
41. Li, Z. *et al.* Review on III-V Semiconductor Single Nanowire-Based Room Temperature Infrared Photodetectors. *Materials* **13**, 1400 (2020).
42. Cai, W. & Shalaev, V. *Optical Metamaterials*. (Springer New York, 2010). doi:10.1007/978-1-4419-1151-3.
43. Zhang, S. *et al.* Metasurfaces for biomedical applications: imaging and sensing from a nanophotonics perspective. *Nanophotonics* **10**, 259–293 (2021).
44. Crespi, A. *et al.* Integrated photonic quantum gates for polarization qubits. *Nat Commun* **2**, 566 (2011).
45. Knill, E., Laflamme, R. & Milburn, G. J. A scheme for efficient quantum computation with linear optics. *Nature* **409**, 46–52 (2001).
46. Wang, J., Sciarrino, F., Laing, A. & Thompson, M. G. Integrated photonic quantum technologies. *Nat. Photonics* **14**, 273–284 (2020).

47. LaPierre, R. R., Robson, M., Azizur-Rahman, K. M. & Kuyanov, P. A review of III–V nanowire infrared photodetectors and sensors. *J. Phys. D: Appl. Phys.* **50**, 123001 (2017).
48. Stopmski, S. *et al.* Application specific photonic integrated circuits for telecommunications. in *2013 Conference on Lasers & Electro-Optics Europe & International Quantum Electronics Conference CLEO EUROPE/IQEC* 1–1 (IEEE, 2013). doi:10.1109/CLEOE-IQEC.2013.6801254.
49. Matthews, J. C. F., Politi, A., Stefanov, A. & O'Brien, J. L. Manipulation of multiphoton entanglement in waveguide quantum circuits. *Nature Photon* **3**, 346–350 (2009).
50. Reimer, M. E. *et al.* Bright single-photon sources in bottom-up tailored nanowires. *Nat Commun* **3**, 737 (2012).
51. Dalacu, D., Poole, P. J. & Williams, R. L. Nanowire-based sources of non-classical light. *Nanotechnology* **30**, 232001 (2019).

Chapter 2
Background

In this section, a range of background topics relevant to the core manuscripts of Chapters 3 - 6 are covered with some depth to offer insight into key words, phrases, and content. The content of Sections 2.1, 2.2, and 2.3 was prepared with the textbook "Single-Photon Generation and Detection" by Migdall et al. as a guide; it provides further detailed background on these topics[1].

2.1 Single-Photon Avalanche Diode Development

The research problems faced in SPAD development are interdisciplinary, so it is convenient to define the technological constraints according to a sub-categorized hierarchy of four foundational technologies, as follows: (i) materials, (ii) device design, (iii) signal processing (circuitry), and (iv) higher level multiplexing. In this hierarchy the constraints on one technology result from the limitations of those in lower levels[2].

Chapters 3 to 6 are referred to as the primary works of this thesis, which include published (Chapters 3 and 4) and prospective publication studies (Chapters 5 and 6) and primarily involve technological developments related to (i) – (iii). Further SPAD developments outside of these primary works are included in Chapter 7 and they relate to (ii) and (iii). The aim of Chapter 7 is to highlight the ongoing developments and future opportunities for the NW p-n junction array SPADs. These developments are omitted from the primary work chapters as further efforts remain for their prospective publication. As such, relevant background regarding Chapters 3 to 6 is included in subsequent sections of this chapter, while additional relevant SPAD development background is reserved to Chapter 7 future opportunities. Higher level multiplexing (iv) refers to the use of additional systems to convert between a single consolidated signal and multiple separated signals for measurement enhancements. For example, an optical system consisting of a series of connected beamsplitters along one path may be incorporated with SPADs at the branching paths to decompose a single consolidated signal into multiple signals for added PNR capabilities[1]. While (iv) technologies are beneficial to SPAD development, they are outside of the scope of this thesis and their further discussion is not included in subsequent chapters.

2.2 Single-Photon Detector Performance Metrics

The performance of SPDs is determined according to a wide range of metrics, and the primary metrics of SPDs are covered here. These metrics are reviewed with SPADs as the focus and some of the intricate tradeoffs that pose as challenges to SPAD design are introduced.

2.2.1 Detection Efficiency

The DE (η_{DE}) of an SPD is defined as the total detection event probability, i.e., the probability that an incident photon is successfully converted into a detectable electrical signal. In the case of SPADs, the DE is dictated by the product of absorption efficiency (η_{absorb}) of incident photons, the fraction of absorbed photons generating an output signal (η_{QE}^{i}), and efficiency of registering the output on readout electronics ($\eta_{threshold}$). The absorption efficiency is determined by the probability of absorbing a photon in the SPAD active region. The absorption efficiency is affected by material qualities such as bandgap and can be improved through effective metamaterial qualities that enhance absorption. The parameter η_{QE}^{i} is referred to as the internal quantum efficiency (IQE). In the single-photon operation of SPADs, the probability that an incident photon is successfully converted into a detectable signal increases with the SPAD's ability to multiply the generated electron hole pair. It is through the SPAD multiplication process that low-power incident light can generate the larger currents that can be sensed. As such, the DE in SPADs can be improved through the proper design around a material's carrier creation efficiency by photon absorption and enhancing carrier multiplication.

Compared to η_{absorb} and η_{QE}^{i}, which are governed at the device and material level, $\eta_{threshold}$ is determined by external electronics systems. The threshold efficiency denotes the ability of external counting and timing electronics to read and register a signal output from the SPAD. While a near-unity threshold efficiency can often be achieved with adequate electronics, circuit design decisions that reduce this efficiency may be employed. For instance, dark count (SPD noise) signals may differ enough from photon trigger events to be negated through tighter threshold tolerances, trading threshold efficiency for reduced noise. A concept diagram is included in Figure 2-1, which illustrates the different efficiencies and how they relate to an incident photon from free space into a SPAD measurement apparatus[1].

In SPAD semiconductor design, DE is one of the critical metrics to maximize; however, it has tradeoffs during operation with other critical metrics. For instance, the applied voltage (VA) across the SPAD

can be increased and the operating temperature can be decreased during SPAD operation to improve the DE. However, increasing VA and decreasing the operating temperature raises DCR and exacerbates afterpulsing probability, respectively, which negatively impacts the overall SPAD performance[3].

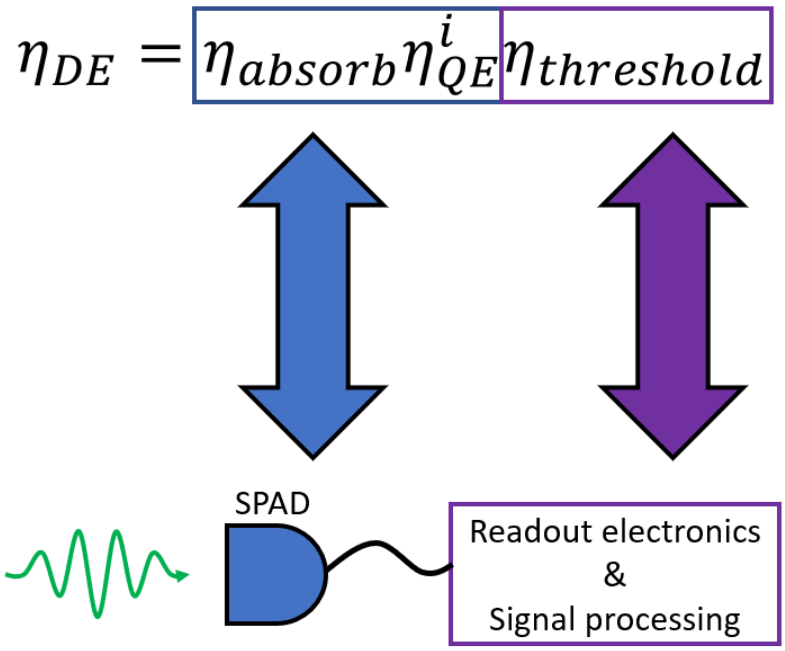

Figure 2-1: Detection efficiency diagram. Total detection efficiency in terms of the detector (absorption and internal) and external electronics (threshold) efficiencies. Figure 2-1 adapted from ref. 1, Elsevier Inc.

2.2.2 Spectral Bandwidth

The spectral bandwidth of an SPD is defined by the wavelength operating range where it is sensitive to light. A SPAD that is designed to be broadband has a large spectral bandwidth and is capable of photon absorption over a large range of wavelengths. In selective SPAD designs, the device is attributed with a narrow spectral bandwidth and may be used for application specific target photon absorption over a limited range of wavelengths.

2.2.3 Photon Number Resolving

PNR denotes a detector's ability to effectively distinguish between and count the number of incident photons. Generally, a detector is considered to have no-, some-, or full PNR capability. Detectors

without PNR capabilities can be considered as a click or no click detector. This means the detector's operation does not provide any information to distinguish the number of incoming photons. If one or more photons arrive then the detector may produce a signal, and if no photons arrive (or dark count events occur) then no signal is generated. Full PNR capabilities of an SPD indicates that the number of photons incident on the detector can be distinguished and counted. In comparison, detectors with some PNR can distinguish the number of incident photons to some extent but without clearly defined or quantized signals under certain operating conditions. Conventional SPADs do not inherently have PNR capabilities, but some PNR capabilities can be obtained through the collective operation of SPADs incorporated into an array of pixels[1].

2.2.4 Crosstalk

A natural evolution for individual SPADs is their incorporation into a SPAD array, which enables imaging in addition to some PNR capabilities. An aim in SPAD arrays is to achieve high throughput and miniaturization while maintaining high SPAD performance like DE. In such SPAD systems, crosstalk becomes an important metric. Crosstalk corresponds to the production of signals of multiple array elements and causing an inaccurate evaluation of the optical signal. The two contributing mechanisms include optical and electrical crosstalk. Optical crosstalk occurs when the carriers in a p-n junction operated in the avalanche regime recombine by radiative recombination and release a photon. The emitted photon may then be subsequently absorbed by and trigger an avalanche in a neighbouring array detector element. The probability of the photon emission event is very low, on average 1 photon per 10^5 carriers crossing the p-n junction. In the case of electrical crosstalk, it occurs when carriers in a quasi-neutral region diffuse laterally to neighbouring detector regions and trigger an avalanche process[1].

2.2.5 Rise Time, Fall Time, Timing Latency, and Timing Jitter

The photo response output from SPDs has characteristic electrical readout pulses that can be temporally characterized according to rise and fall times, as well as timing latency and jitter. In SPADs, these timings include the time the signal takes for the photo generated current to be amplified and quenched. The time it takes for the signal to go from its minimum (10%) to its maximum (90%) value is referred to as the rise time, and conversely fall time from a maximum to a minimum. These timings are critical for detectors as the play an important role in determining the maximum rate of operation.

The timing latency refers to the difference in time between photon incidence and the electrical output signal passing a defined threshold. There are numerous causes of the slight difference between photon arrival time and output measurement[4]. For example, the timing difference in signal acquisition may differ when a photon is absorbed at different locations in the detector active region. Photons that are absorbed closer to the multiplication region may produce a measurable signal faster than photons absorbed further from the multiplication region. This difference in signal acquisition speed may occur because the carrier generated closer to the multiplication region is subjected to a shorter transport pathway before amplification and is thus amplified for readout faster. Similarly, the carriers generated at different positions in the active region are likely to experience local excess voltage (VE) i.e., reverse bias above breakdown non-uniformities. These varying local VE will impact the amplification process, can cause temporal difference in the signal acquisition, and thus result in time latency between photon arrival readout events.

When superimposing the output signals of various detection events, through an oscilloscope trigger, a pulse waveform with a defined width can be measured. The thickness of the triggered waveform illustrates the differences in timing latency and can be used to measure the timing latency variance between pulses. The variance in the timing latency is referred to as the timing jitter. This measurement is illustrated in Figure 2-2a, where the left most waveforms are detected earlier than the rightmost waveforms[5]. The pulse timings can be binned and placed into a histogram as shown in Figure 2-2b to illustrate the timing jitter[5]. The full width at half maximum (FWHM) of the binned histogram acts as a characteristic measure of the timing jitter. In SPADs the timing jitter has been shown to decrease with increased VE[6]. This reduced timing jitter in planar SPADs at higher VE occurs because the carriers are exposed to higher electric fields, which enhance avalanche lateral diffusion mechanism efficiencies[1].

2.2.6 Count Rate, Dead Time, Reset Time, and Recovery

The count rate of an SPD denotes the speed at which single-photon events can be measured. In SPADs, the count rate is maximized by reducing the recovery time. The dead time of a detector denotes the period from the start of a detection event to the beginning of a detector's required reset. That is; it acts as a measure of time when the DE is zero and the device is unable to produce an output signal response for another incoming photon. The reset time of a detector denotes the length of time taken to restore it to its original state (full DE) from the end of the dead time (zero DE).

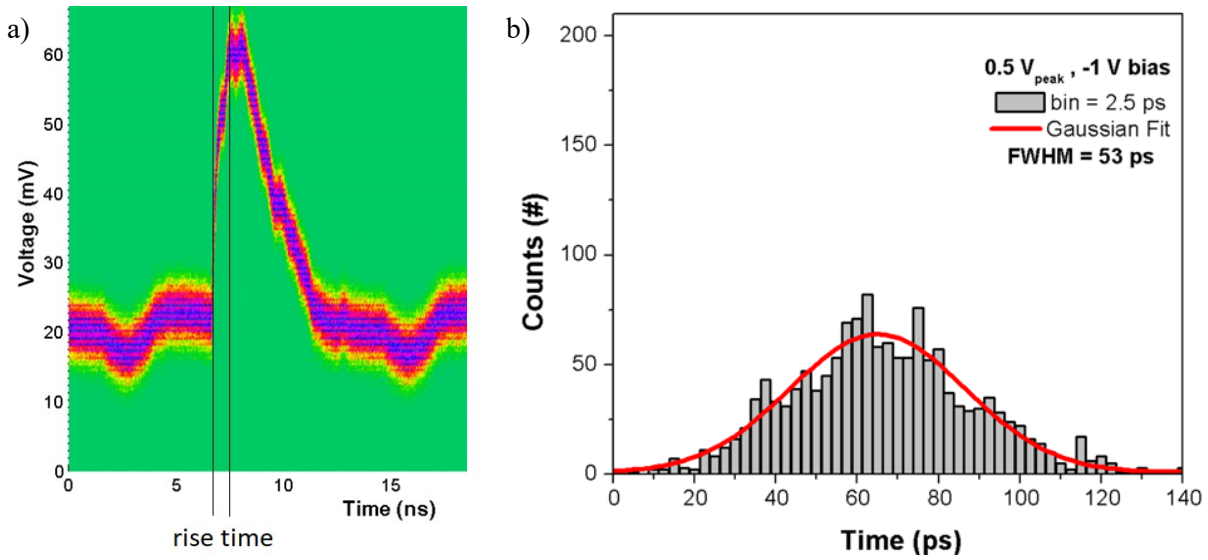

Figure 2-2: Single-photon semiconductor nanowire avalanche diode signal response. a) Temporal overlap of triggered InP nanowire avalanche photodetector signal output events from a pulsed laser noting the rise time and illustrating the fall time and timing jitter. **b)** Histogram produced from the binned cross section data of the signal output timings. The cross section is taken from the data in **a)**, at 50% peak height, and the full width at half maximum of the corresponding histogram is used as a measure of the timing jitter. Figure 2-2a and Figure 2-2b adapted from ref. 5, Nature Publishing Group.

The combined duration of deadtime and reset time is called the recovery time of the detector. That is; the recovery time of the detector corresponds to the temporal period from the beginning of a detection event to a point when the detector is re-armed and ready for another detection event. A concept diagram illustrating the DE dependence on these temporal metrics during operation is included in Figure 2-3[1].

2.2.7 Dark Count Rate and Background Count Rate

DCR is an SPD metric that denotes the number of false positive trigger events registered (pulses) by a detector per second while in complete darkness (no light illumination). Ideally, the DCR would be zero, since a perfect detector is triggered only by incoming light, but the DCR is a non-ideality that must be minimized in SPDs. The total DCR of a SPAD refers to the internal noise source, which depends on many carrier production contributors, including thermal and electric field assisted (generation and tunnelling) production. These thermal and electric field assisted noise contributors scale with temperature and voltage (electric field), respectively[3,7].

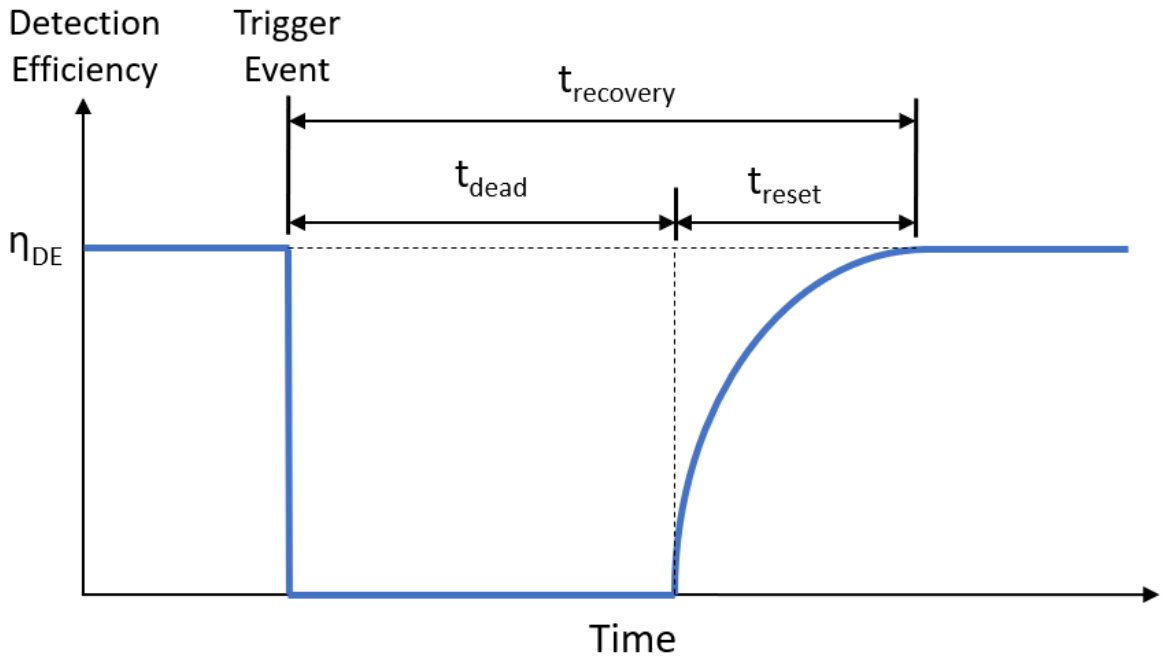

Figure 2-3: Illustration of the detection efficiency dependence on single-photon detector operation with annotations indicating the deadtime, reset, and recovery periods with respect to the photon arrival trigger event. Figure 2-3 adapted from ref. 1, Elsevier Inc.

Prominent mechanisms include trap-assisted tunneling, band-to-band tunnelling, and thermal generation; however, the dominant DCR contributor varies significantly with device design and operation[3,8]. The DCR in III-V SPADs can be particularly troublesome, partly due to the current III-V SPAD material quality and prominence of traps[3,9,10]. The SPAD operating temperature can be reduced to decrease DCR but only to a level where the field-dependent contributors (unaffected by temperature) become dominant, limiting the DCR reduction achievable through operating temperature[3]. Conveniently, this limit is typically within the range achievable by TECs. Predominant DCR contributors may be associated with traps that remain challenging to address since suppressing their presence predominantly relies on improving the material and microfabrication quality. As such, the activation energies of traps offer insight into their origin and can aid in identifying predominant DCR mechanisms[6,8,9].

Beyond advances in the materials and microfabrication, device design measures are employed to alleviate the prominence of DCR contributors unaffected by operating temperature, including the

engineering of absorption and multiplication region thicknesses, active area size, and material stack composition[3]. Also, as previously noted when operating a SPAD for higher DE by increasing the VA (and to an extent temperature[3]), it also causes an increase in unwanted DCR, resulting in a trade-off between the two. This increase in DCR at higher VE can be attributed to the increased prominence of electric field dependent contributors including a higher probability of trap-assisted tunnelling and band-to-band tunnelling. The higher reverse bias also increases the avalanche probability and thus the likelihood that dark carriers trigger a false detection event[1]. The trade-offs between critical metrics, such as DE and DCR, in planar SPADs has been well studied. A concept diagram illustrating some of these critical device metric codependences discussed in this section is included in Figure 2-4[3,6,10,11]. Furthermore, during SPD operation it may not be possible to completely isolate the detector from receiving background photons. That is, stray photons beyond the intended signal may reach the device and cause false trigger events at a rate denoted as the background count rate. While the background count rate is not intrinsic to detectors, some designs are particularly susceptible to it[1].

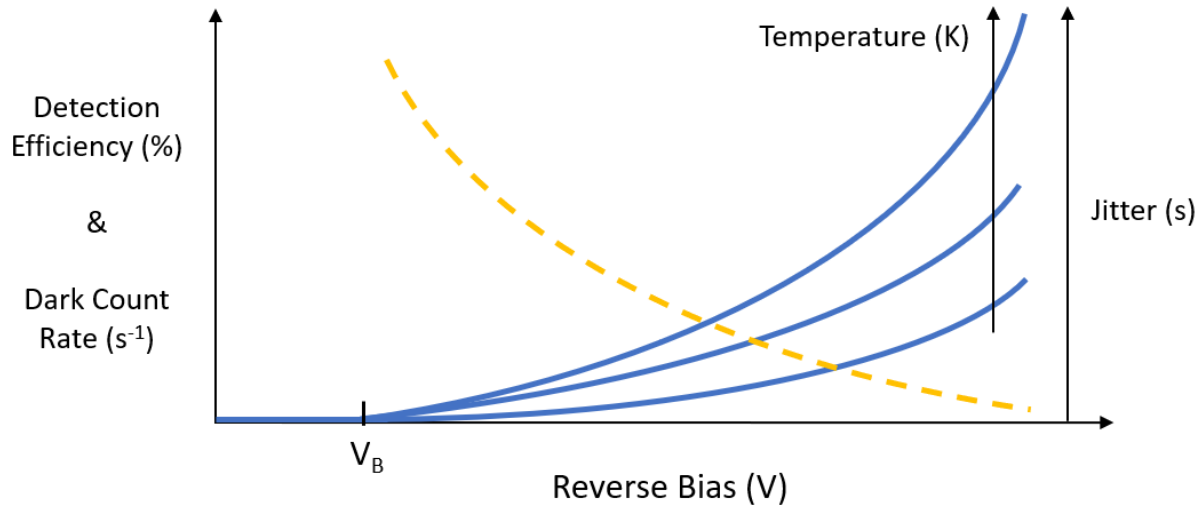

Figure 2-4: Trends of single-photon avalanche diode critical device metric trade-offs. The left *y*-axis indicates the competing detection efficiency and dark count rate, which show opposite trends with increasing temperature and reverse bias (blue solid lines). The right *y*-axis indicates the timing jitter, which decreases with increasing reverse bias (yellow dashed line). The breakdown voltage is denoted by V_B, indicating the Geiger-mode regime where the critical single-photon avalanche diode device metrics apply.

2.2.8 Afterpulse Probability

Minority carrier traps may hold on to carriers after an avalanche occurs and release after the device is reset, triggering another avalanche absent the arrival of a photon. The probability that such an event occurs after an avalanche is called the afterpulse probability. These afterpulse events have statistical properties with a trap lifetime, which depends partly on the energy level of the trap. The stochastic nature of the afterpulse events allows for some distinguishability between them and photogenerated avalanche pulses, as they are correlated in time with the original avalanche pulse. Similar to other critical SPAD metrics, design considerations can be implemented to reduce afterpulsing. In the case of afterpulsing probability, it becomes more problematic with decreasing temperature and VE since the trapped carriers take longer to be released. External circuitry methods, like a hold-off process, can help to reduce the impact of afterpulsing. This method involves holding the SPAD in a quenched state for a period of time after an avalanche, until the afterpulse probability is known to be sufficiently low, allowing trapped charges to release without an opportunity to avalanche[1]. A trend diagram illustrating some of the critical device metric codependences with afterpulsing is presented in Figure 2-5.

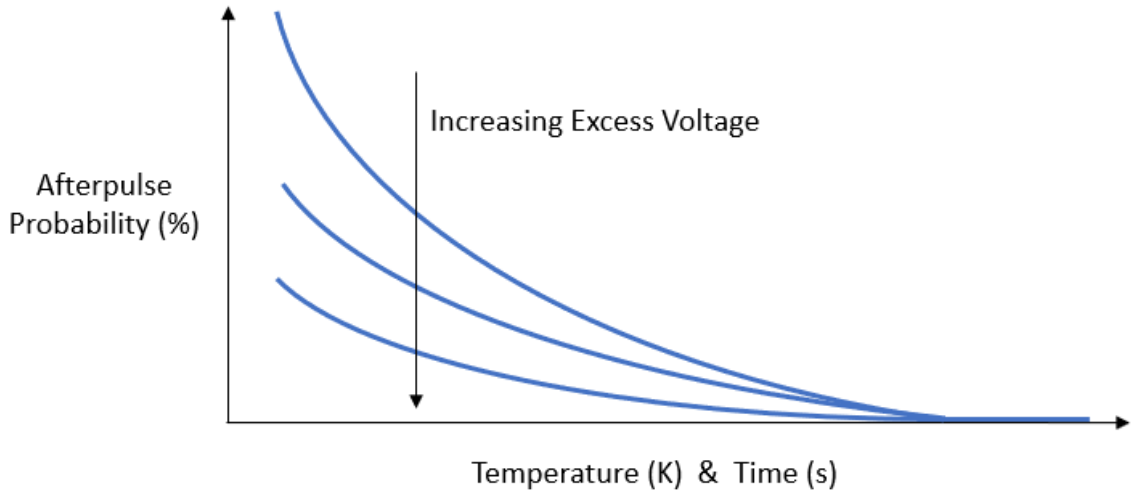

Figure 2-5: Single-photon avalanche diode afterpulse probability trend. The afterpulse probability decreases with increasing temperature, time, and excess voltage. Time in the *x*-axis indicates the period following an avalanche event.

2.2.9 Active Area

The detector active area refers to the region of the device that is sensitive to incident photons. An image of a set of fabricated SPAD devices prepared by Dr. Reimer's research group is included in Figure 2-6 (left). Figure 2-6 (right) illustrates a magnified device, indicating the active area and top metal contact (circular electrode and wire-bond pad) for electrical connection to the SPAD. A larger active area in the range of 100 µm x 100 µm in a device can be advantageous for applications since it is simpler for incident light to couple to the SPAD as compared to smaller active area devices of 10 µm x 10 µm[1]. However, a large active area can be detrimental to device performance since critical metrics increase with active area size, such as DCR[12]. Thus, SPAD designs must be considerate of the active area size since it cannot be trivially increased.

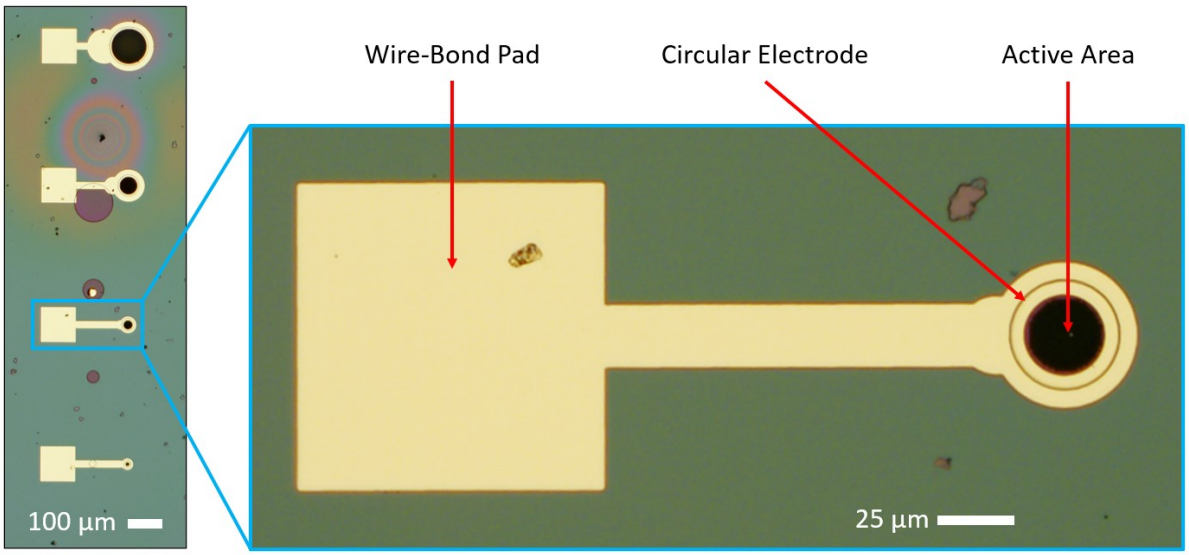

Figure 2-6: Fabricated InGaAs/InAlAs single-photon avalanche diode devices prepared by Dr. Reimer's research group. The left image shows a range of sample devices with different active area sizes. The blue rectangle illustrates the position of the magnified device image on the right. The magnified image indicates the active area of the device along with other device features (wire-bond pad and circular electrode), which are required for electrical contact to the sample. Scale bars are included for reference in their respective image.

2.2.10 Operating Temperature

The operating temperature of SPDs is also a critical property. Some detectors must be cooled to cryogenic temperatures to function, making them inappropriate for some applications. SPADs can operate over a broad range of temperatures, with varying degrees of performance as observed through the temperature dependence of several critical device metrics. One of the desirable advantages of SPADs for broad applicability; however, is their ability to operate in room temperature and near room temperature environments, within the limits of TECs[1].

2.3 Single-Photon Avalanche Diode Geiger-Mode Operation

In the single-photon detection operation of SPADs, the device is prepared with a reverse bias in excess of the VB, where the diode gain is considered to be undefined. Prior to receiving a photon, the device is in an *off* state and produces no current, as there is a large electric field in the depletion region, but no free carriers present to avalanche. After receiving a photon, a carrier is generated in a region with an electric field, which rapidly accelerates it for impact ionization. The impact ionization process multiplies the carriers to produce a self-sustainable avalanche. The avalanche current grows exponentially to a level that is proportional to VE, limited by the space-charge effect. At this point of the operation, the SPAD is in an *on* state, and the sustained avalanche must be quenched by external circuitry. Ideally, a photon will trigger the *on* state, but unwanted dark carrier generation triggers the same response. Quenching is performed by dropping the voltage to (or below) ~VB, suppressing the avalanche and resetting the detector back to an *off* state. The detector dead time arises from this *off* period between avalanche onset and voltage reset. Furthermore, the duration of the quiescent state is given by the difference of the SPAD recovery time and trigger onset. The operation of the detector in this way is referred to as Geiger-mode operation because the operation is analogous with gas counters of ionizing radiation. A concept diagram of the SPAD operation process is included in Figure 2-7[1].

2.4 The Current State of Single-Photon Avalanche Diodes

SPADs are a popular alternative to PMT and superconducting SPDs as they are compact, low power dissipating, low cost, and reliable designs capable of achieving good timing jitter and DE performance at or near room temperature operation. SPAD materials are fundamental to this performance and range in options, such as silicon and III-V, which have different benefits and shortcomings[1].

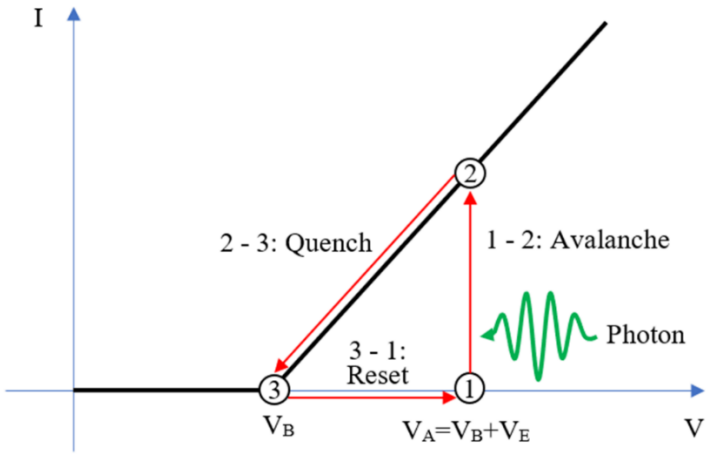

Figure 2-7: Diagram of typical single-photon avalanche diode (SPAD) operating current-voltage (I-V) relationship across the diode. The SPAD operation is defined by three events; avalanche, quench, and reset. The device is prepared in a quiescent state (1) ready for photon detection at the applied voltage (VA) equal to the sum of the breakdown voltage (VB) and excess voltage (VE), VA = VB + VE. Photon absorption triggers the SPAD, taking it from the quiescent state (1) to a triggered state (2) with the onset of a large measurable current generated from an avalanche. During the quenching process (2 – 3) the avalanche current is suppressed, and the voltage drops to VB, bringing the device to a quenched state (3). The reset process (3 – 1) takes the SPAD back to a quiescent state for subsequent photon detection. The quenching and reset processes are performed by SPAD circuitry and electronics[1]. Figure 2-7 adapted from ref. 1, Elsevier Inc.

Silicon is a popular material choice, having inherent advantages like low cost and the potential for added fabrication complexity because of the maturity of silicon-based technology. Among SPADs, silicon is capable of higher-end performance in critical metrics like DCR but a significant limitation of the material is its inhibited DE at longer wavelengths. The low DCR of silicon can be partly attributed to material growth quality and its relatively large bandgap as compared to alternative SPAD intrinsic materials. The use of silicon in SPADs aids in reducing thermal and field assisted carrier production like trap-assisted thermal generation, and thus DCR[1]. However, the larger bandgap of silicon also inhibits photogeneration in the SWIR regime because of the insufficient energy of longer wavelength photons, thus hindering absorption and SPAD DE. As such, IR DE is a focus for SPAD designs, so unique structures like resonators and thicker absorption regions are being employed to enhance absorption efficiencies, but the need for higher DE devices in this range remains. Popular alternatives

to Si fall within the group of III-V semiconductor materials, which provide absorption capabilities in a broad range of wavelengths, making them highly attractive options.

SPADs based on III-V materials are capable of improved absorption efficiency in the SWIR region, but they must often overcome the challenges of higher DCR. For instance, InGaAs is a popular SPAD absorber material targeting the SWIR region, which also suffers from elevated DCR due to its smaller bandgap. This smaller bandgap enables SWIR absorption, but it also exacerbates contributors to the dark carrier production. As such, a focus of III-V material-based SPADs is to improve DCR through material quality, device design, cooling, and external circuitry. Silicon SPADs have a material quality advantage being developed on a more mature platform but promising performance results are still found in III-V SPAD device designs incorporating a separate absorption and multiplication (SAM) structure. For example, these devices can be composed of a dedicated InGaAs absorbing layer for the target wavelength and a separate InP multiplication layer for a high avalanche probability with lower DCR. The engineering of the SAM structure circumvents field dependent noise (DCR) contributors of the absorbing material by tuning for a low field in the absorbing layer. This is one of the design decisions implemented to accommodate for and benefit from the use of both a low bandgap and high bandgap material in a single device.

The SAM design includes some field in the absorbing region to transport the generated carriers into the high field multiplication region, but the electric field is reduced to a level that inhibits tunnelling[10]. To facilitate the necessary avalanche breakdown for SPAD operation, the SAM design designates the high field multiplication region to a higher bandgap material, which is less susceptible to field dependent noise contributors. As such, the drawbacks of increased DCR from incorporating InGaAs into the SPAD are minimized, while leveraging its longer wavelength absorption qualities for higher DE deeper into the SWIR regime. More recent SPAD stacks include a charge and grading layer also and they are referred to as separate absorption, grading, charge, and multiplication (SAGCM) heterostructures. The charge layer is placed between the InP and InGaAs layers to better tailor the electric field profile for critical SPAD qualities such as high avalanche and sufficiently low tunneling probabilities. Depending on the charge layer material, hole trapping effects may occur due to a valence band offset between InGaAs and InP. As such, a grading layer is included to add an intermediate step in the energy levels to ease the valance band energy transition. Lower operating temperatures are also adopted in III-V SPADs to reduce DCR. InGaAs/InP SPADs at operating temperatures within the operating range of TECs (-70°C) have been shown to achieve comparable performance metrics (DE, timing jitter, and

DCR) to the higher performance room-temperature-operated Si SPADs with similar active area size and hold-off times. This comparison highlights the required operating conditions of III-V material-based SPADs to achieve a high performance similar to silicon-based SPADs. Though opportunities for improvement to III-V material-based SPADs remain, the prospect of the technology is clear[1].

2.5 Emerging Materials for Single-Photon Avalanche Photodiodes

A high demand for improved materials remains for III-V SPAD development, and while improvements are conventionally sought through the material growth process, leveraging the effective properties of metamaterials is another emerging trend for advancing optoelectronic devices[15,16]. In particular, the DE of SPADs relies heavily on maximizing the absorption efficiency, and the design capabilities of metamaterials enables a degree of freedom for targeting narrow and broadband wavelengths for near-unity absorption[17].

In the following section, background is introduced for prospective metamaterial designs based on cylindrical and disk-shaped dielectric resonators and low-dimensional materials for targeted enhanced absorption. Such materials have undergone notable study[18], demonstrate desirable models for enhanced absorption performance for photodetection technologies[5,19], and present a similar geometry to the InP p-n junction NW array photodetector of Chapter 3. The overlap between these novel materials and the NW array photodetector prompted the published study "semiconductor nanowire metamaterial for broadband near-unity absorption" of Chapter 4. This overlap also motivated the prospective publication studies on the near-unity absorbing metasurface on a high-index substrate and mode-matching method for efficient single tapered NW absorbers for photodetection applications of Chapters 5 and 6, respectively.

2.5.1 Cylindrical-Based Nano-Structured Dielectric Resonators

The repeating unit structure in the InP p-n junction NW array of Chapter 3 is tapered but has a cylindrical geometry. To understand the semiconductor NW p-n junction array properties and the effects of periodicity, it was studied from a metamaterial perspective. This study included the analysis of high index dielectric resonators of similar geometries in a low index medium. The resonator geometries of interest include nano- disks, pillars, wires, and cones. Background is provided for the behaviours of the different geometries in environments relevant to photodetector-based applications (isolated, on a dielectric, and in an array) along with methods for maximizing their absorptance.

2.5.2 Single Cylindrical Structure Resonances

The modal properties of a NW waveguide can be defined according to the conventional description of a cylindrical fiber with a step-index profile[20–22]. The modes supported in these cylindrical structures include the transverse electric (TE_{0m}), transverse magnetic (TM_{0m}), TE component dominant hybrid (HE_{vm}), and TM component dominant hybrid (EH_{vm}) modes. The eigenvalue Eqs. (2-1), (2-2), and (2-3) apply to the hybrid, TE_{0m}, and TM_{0m} modes, respectively. Here, m is the root of the eigenvalue equation, where $m = 1$ corresponds to the modal solution with the smallest U (largest β) for a given v.

$$\left\{\frac{J_v'(U)}{UJ_v(U)} + \frac{K_v'(W)}{WK_v(W)}\right\}\left\{\frac{J_v'(U)}{UJ_v(U)} + \frac{n_{cl}^2}{n_{co}^2}\frac{K_v'(W)}{WK_v(W)}\right\} = \left(\frac{v\beta}{kn_{co}}\right)^2\left(\frac{V}{UW}\right)^4 \tag{2-1}$$

$$\frac{J_1(U)}{UJ_0(U)} + \frac{K_1(W)}{WK_0(W)} = 0 \tag{2-2}$$

$$\frac{n_{co}^2 J_1(U)}{UJ_0(U)} + \frac{n_{cl}^2 K_1(W)}{WK_0(W)} = 0 \tag{2-3}$$

Where J_v is the Bessel function of the first kind, K_v is the modified Bessel function of the second kind, v is the order, n_{cl} is the cladding index, n_{co} is the core index, and k is the free space-wave number ($k = 2\pi/\lambda$). β is the propagation constant, which follows Eq. (2-4) and satisfies the inequality in Eq. (2-5) for bound modes.

$$\beta = \frac{1}{\rho}\left\{\frac{V^2}{2\Delta} - U^2\right\}^{1/2} \tag{2-4}$$

$$kn_{cl} < \beta \leq kn_{co} \tag{2-5}$$

Where ρ is the core radius and Δ is the profile height parameter defined in Eq. (2-6). The core parameter (U), cladding parameter (W), and waveguide parameter (V) are defined according to Eqs. (2-7), (2-8), and (2-9), respectively. The range of the single-mode regime follows $0 < V < 2.405$, where the fundamental HE_{11} mode (absent a cutoff) has the smallest U for all V. Some interesting parameter relationships are highlighted in these expressions, including between the fiber radius and the wavelength of light (λ) with higher order modes. It can be observed in Eq. (2-9), that the single mode (SM) regime and lower order modes rely on a smaller ratio of radius to wavelength, and higher order modes can be supported by decreasing the wavelength or increasing the fiber radius.

$$\Delta = \frac{n_{co}^2 - n_{cl}^2}{2n_{co}^2} \tag{2-6}$$

$$U = \rho(k^2 n_{co}^2 - \beta^2)^{1/2} \tag{2-7}$$

$$W = \rho\left(\beta^2 - k^2 n_{cl}^2\right)^{1/2} \tag{2-8}$$

$$V = k\rho\left(n_{co}^2 - n_{cl}^2\right)^{1/2} \tag{2-9}$$

The electric (e) and magnetic (h) field components in the core (co) and cladding (cl) of the step-index fiber HE_{vm} and EH_{vm} modes follow Eqs. (2-10) – (2-21).

$$e_{r,co} = -\frac{a_1 J_{v-1}(UR) + a_2 J_{v+1}(UR)}{J_v(U)} f_v(\phi) \tag{2-10}$$

$$e_{\phi,co} = -\frac{a_1 J_{v-1}(UR) - a_2 J_{v+1}(UR)}{J_v(U)} g_v(\phi) \tag{2-11}$$

$$e_{z,co} = -\frac{iU J_v(UR)}{\rho\beta J_v(U)} f_v(\phi) \tag{2-12}$$

$$h_{r,co} = \left(\frac{\varepsilon_0}{\mu_0}\right)^{1/2} \frac{k n_{co}^2 a_3 J_{v-1}(UR) - a_4 J_{v+1}(UR)}{\beta J_v(U)} g_v(\phi) \tag{2-13}$$

$$h_{\phi,co} = -\left(\frac{\varepsilon_0}{\mu_0}\right)^{1/2} \frac{k n_{co}^2 a_3 J_{v-1}(UR) + a_4 J_{v+1}(UR)}{\beta J_v(U)} f_v(\phi) \tag{2-14}$$

$$h_{z,co} = -i\left(\frac{\varepsilon_0}{\mu_0}\right)^{1/2} \frac{U F_2 J_v(UR)}{k\rho J_v(U)} g_v(\phi) \tag{2-15}$$

$$e_{r,cl} = -\frac{U a_1 K_{v-1}(WR) - a_2 K_{v+1}(WR)}{W K_v(W)} f_v(\phi) \tag{2-16}$$

$$e_{\phi,cl} = -\frac{U a_1 K_{v-1}(WR) + a_2 K_{v+1}(WR)}{W K_v(W)} g_v(\phi) \tag{2-17}$$

$$e_{z,cl} = -\frac{iU K_v(WR)}{\rho\beta K_v(W)} f_v(\phi) \tag{2-18}$$

$$h_{r,cl} = \left(\frac{\varepsilon_0}{\mu_0}\right)^{1/2} \frac{k n_{co}^2 U a_5 K_{v-1}(WR) + a_6 K_{v+1}(WR)}{\beta W K_v(W)} g_v(\phi) \tag{2-19}$$

$$h_{\phi,cl} = -\left(\frac{\varepsilon_0}{\mu_0}\right)^{1/2} \frac{k n_{co}^2 U a_5 K_{v-1}(WR) - a_6 K_{v+1}(WR)}{\beta W K_v(W)} f_v(\phi) \tag{2-20}$$

$$h_{z,cl} = -i\left(\frac{\varepsilon_0}{\mu_0}\right)^{1/2} \frac{U F_2 K_v(WR)}{k\rho K_v(W)} g_v(\phi) \tag{2-21}$$

Where the coordinate origin is in the center of the fiber, r is the distance from the origin, and ϕ is the polar coordinate in the plane normal to the fiber axis (z-axis). Additionally, the normalized radius is

given by $R = r/\rho$, ε_0 is the free-space dielectric constant, and μ_0 is the free-space permeability. The expressions for $f_v(\phi)$ (even and odd modes), $g_v(\phi)$ (even and odd modes), F_2, and a_1 to a_6 are defined according to Eqs. (2-22) – (2-32).

$$f_{v,even}(\phi) = \cos(v\phi) \tag{2-22}$$

$$f_{v,odd}(\phi) = \sin(v\phi) \tag{2-23}$$

$$g_{v,odd}(\phi) = -\sin(v\phi) \tag{2-24}$$

$$g_{v,odd}(\phi) = \cos(v\phi) \tag{2-25}$$

$$F_2 = \left(\frac{V}{UW}\right)^2 \frac{v}{b_1+b_2} \tag{2-26}$$

$$a_1 = \frac{F_2-1}{2} \tag{2-27}$$

$$a_2 = \frac{F_2+1}{2} \tag{2-28}$$

$$a_3 = \frac{F_1-1}{2} \tag{2-29}$$

$$a_4 = \frac{F_1+1}{2} \tag{2-30}$$

$$a_5 = \frac{F_1-1+2\Delta}{2} \tag{2-31}$$

$$a_6 = \frac{F_1+1-2\Delta}{2} \tag{2-32}$$

Where b_1, b_2, and F_1 are defined by Eqs. (2-33), (2-34), and (2-35), respectively.

$$b_1 = \frac{1}{2U}\left\{\frac{J_{v-1}(U)}{J_v(U)} - \frac{J_{v+1}(U)}{J_v(U)}\right\} \tag{2-33}$$

$$b_2 = -\frac{1}{2W}\left\{\frac{K_{v-1}(W)}{K_v(W)} + \frac{K_{v+1}(W)}{K_v(W)}\right\} \tag{2-34}$$

$$F_1 = \left(\frac{UW}{V}\right)^2 \frac{b_1+(1-2\Delta)b_2}{v} \tag{2-35}$$

The electric and magnetic field components in the core and cladding of the step-index fiber TE modes follow Eqs. (2-36) – (2-41).

$$e_{\phi,co} = -\frac{J_1(UR)}{J_1(U)} \tag{2-36}$$

$$h_{r,co} = \left(\frac{\varepsilon_0}{\mu_0}\right)^{1/2} \frac{\beta J_1(UR)}{k J_1(U)} \tag{2-37}$$

$$h_{z,co} = i\left(\frac{\varepsilon_0}{\mu_0}\right)^{1/2} \frac{U J_0(UR)}{k\rho J_1(U)} \tag{2-38}$$

$$e_{\phi,cl} = -\frac{K_1(WR)}{K_1(W)} \tag{2-39}$$

$$h_{r,cl} = \left(\frac{\varepsilon_0}{\mu_0}\right)^{1/2} \frac{\beta K_1(WR)}{k K_1(W)} \tag{2-40}$$

$$h_{z,cl} = -i\left(\frac{\varepsilon_0}{\mu_0}\right)^{1/2} \frac{W K_0(WR)}{k\rho K_1(W)} \tag{2-41}$$

Where $e_r = e_z = h_\phi = 0$. The electric and magnetic field components in the core and cladding of the step-index fiber TM modes follow Eqs. (2-42) – (2-47).

$$e_{r,co} = \frac{J_1(UR)}{J_1(U)} \tag{2-42}$$

$$e_{z,co} = \frac{iU J_0(UR)}{\rho\beta J_1(U)} \tag{2-43}$$

$$h_{\phi,co} = \left(\frac{\varepsilon_0}{\mu_0}\right)^{1/2} \frac{k n_{co}^2 J_1(UR)}{\beta J_1(U)} \tag{2-44}$$

$$e_{r,cl} = \frac{n_{co}^2 K_1(WR)}{n_{cl}^2 K_1(WR)} \tag{2-45}$$

$$e_{z,cl} = -\frac{i n_{co}^2 W K_0(WR)}{n_{cl}^2 \rho\beta K_1(W)} \tag{2-46}$$

$$h_{\phi,cl} = \left(\frac{\varepsilon_0}{\mu_0}\right)^{1/2} \frac{k n_{co}^2 K_1(WR)}{\beta K_1(W)} \tag{2-47}$$

Where $e_\phi = h_r = h_z = 0$.

These supported modes are present in waveguiding NWs and can be leveraged for mode matching and enhanced absorption in single cylindrical particles and arrays of long tapered NWs[17]. The modal vector field profiles of several lower order modes in a cross section of a step-index fiber are included in Figure 2-8a to Figure 2-8c. In cylindrical resonators of a reduced height, the applied model remains of the same form but the opposing circular faces constrain the resonant response and require modified boundary conditions[23]. Furthermore, the modal resonances at the reduced size become approximately

dipole in nature, which enables approximations to be applied such as the discrete dipole approximation used in metasurface design models[24].

The structural unit in nano-disk resonators is a cylindrical particle that takes on the form of a small puck. When considering the lowest order modes of the nano-disk, light interaction with the single (isolated) dielectric particle (in air) can be described through the interacting EM field with the isolated particle's supported electric and magnetic resonant modes[18]. The diagrams in Figure 2-8d and Figure 2-8e illustrate the magnetic dipole (MD) mode and ED mode generated inside of these dielectric cylindrical structures when driven by an in plane EM field at normal incidence[18]. In Figure 2-8d, the MD moment is oscillating in and out of the page, while the ED oscillates side to side. For the MD mode, the driving field (red) couples to the displacement current loop (orange) inside of the dielectric structure to induce the MD (blue), as observed in Figure 2-8d. Comparatively, the ED mode is coupled to the driving field through the collective polarization of the dielectric material, as shown in Figure 2-8e[18].

Modifying the height of cylindrical particle alters the incident field's ability to drive the supported modes. For instance, shorter particles will cause a retardation for the excitation of the MD mode. Also, the particle's ability to scatter is lower when it is shorter because of a lower polarizability caused by the reduced volume. The height and the resonant mode wavelength scale together, causing a red shift of both ED and MD when the height of the structure is increased[18]. A similar effect is obtained through increasing the particle diameter, d, where the resonant wavelength of the dipole modes are approximated by the condition $\lambda/n \sim d$, where n is the refractive index of the dielectric[18]. Depending on the intrinsic material properties, the red shift for the ED may be faster than the MD, this allows for the manipulation of the particle geometry for the tuned spectral overlap or separation of these modes. This tuning modifies the interaction with incident light for enhanced qualities, such as improved selectivity and higher absorption at a targeted wavelength when the modes are made to overlap[25]. Further increasing the diameter above the approximate condition for the dipole mode resonant wavelength causes the structure to support higher-order Mie resonance (transverse) modes, including a magnetic quadrupole (MQ) and electric quadrupole (EQ), as shown in Figure 2-8d and Figure2-8e[18,26]. Similarly, increasing the height of the particle causes it to support additional Fabry-Pérot cavity (longitudinal) multipole resonances, called magnetic and electric multipole modes[26]. The magnetic (electric) multipole modes can be decomposed into multiple dipoles modes MD_1 (ED_1) and MD_2 (ED_2), as shown in Figure 2-8d and Figure2-8e. As the length of the cylindrical structure continues to increase it takes

on fiber-like guided/leaky modal properties, which follow the conventional cylindrical step index waveguide modal description[20,21,27].

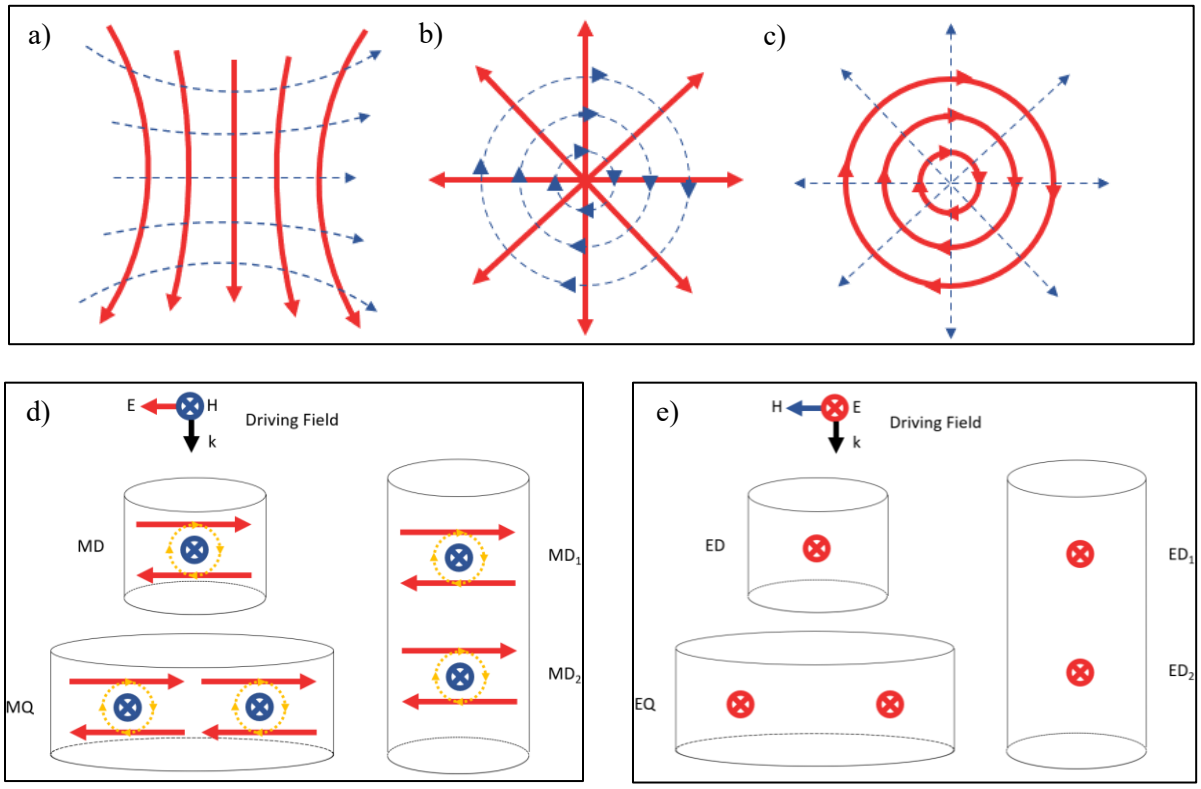

Figure 2-8: Cylindrical resonator mode diagrams with the corresponding driving fields denoted above the structure outlines. The vector direction of the **a)** HE_{11}, **b)** TM_{01}, and **c)** TE_{01} electric (red solid lines) and magnetic (blue dashed lines) field vectors in a step-index fiber cross section. **d)** The magnetic resonance modes with the driving field (red, side-to-side), displacement current loop (orange, dashed), and magnetic dipole (MD) (blue, normal to the page). The small structure supporting the MD is illustrated in the top left. The larger diameter structure supporting the magnetic quadrupole (MQ) is illustrated in the bottom left. The rightmost (longer) structure outline in the panel illustrates the magnetic multipole decomposed into MD_1 and MD_2. **e)** The electric resonance modes coupled to the driving field through the collective polarization of the dielectric material. The (red) electric dipole is oscillating normal to the page, and the structure outline arrangement matches that of **d)**. The electric dipole (ED), electric quadrupole (EQ) and decomposed electric multipole (ED_1 and ED_2) are denoted accordingly. Figure 2-8a, Figure 2-8b, and Figure 2-8c adapted from ref. 20, Chapman and Hall. Figure 2-8d and Figure 2-8e adapted from ref. 18, Optica.

When a dielectric substrate of approximately matching refractive index is added under the resonator, it has a notable impact on the resonances. For example, the presence of a dielectric substrate allows the current loop to extend into it. This effect causes a spectral broadening of the resonances and reduction of the particle's selectivity. At small heights, the extension of the current loop also diminishes the retardation of the MD that was previously achieved when the particle was surrounded by air.

2.5.3 Cylindrical Particle Resonator Array

When the individual cylindrical structures are placed into an array, each of them forms a metaatom comparable to a unit cell. These metaatoms can be collectively constructed into a metasurface with optical characteristics attributed from the individual particles[16]. The operation of many metasurfaces can be understood through the Huygen's principle in optics, which describes the characteristic wavefront in the far field by the interference of many point sources. The 2D array of particles making up a metasurface can be considered as the individual point sources in the Huygen's principle description through which the farfield wavefront is defined[28–30]. The placement of the particles into the array can cause lattice dependent effects such as electric lattice resonance (ELR) and magnetic lattice resonance (MLR)[25]. The ELR and MLR arise from dipole interactions of adjacent particles. These lattice resonances often appear at wavelengths below the Raleigh anomaly, i.e. the in-plane diffractive optical mode in periodic systems with $\lambda \approx np$ (here assuming a normal angle of incidence), and they are impacted by the array spacing orthogonal to their respective lateral mode moments[15,25]. Here, n is the refractive index and p is the array periodicity.

For small particles with dimensions comparable to the wavelength of light of interest, the scattering phenomena is governed by Mie scattering[26]. Under strict conditions, the electric and magnetic dipole resonances (MDRs) can be made to overlap at the same wavelength. In the case that the Mie magnetic and electric coefficient are of the same magnitude (and phase), then backscattering will be suppressed, and forward scattering is promoted. This condition leads to the interference mode named after Milton Kerker who predicted this effect in 1983[31]. The Kerker condition for the back- and forward scattering cases of a spherical particle are described by Eqs. (2-48) and (2-49), respectively. The enhanced forward case occurs when the Mie electric coefficient, a_m, and Mie magnetic coefficient, b_m, are equal to one another, and implementing the condition with a particle composed of a dissipative medium it can enable enhanced absorption[32–34]:

$$Q_{backward\ scattering} = \frac{1}{a^2k^2}\left|\sum_{m=1}^{\infty}(2m+1)\,(-1)^m(a_m - b_m)\right|^2 \tag{2-48}$$

$$Q_{forward\ scattering} = \frac{1}{a^2k^2}|\sum_{m=1}^{\infty}(2m+1)\,(a_m + b_m)|^2 \quad (2\text{-}49)$$

Where a is radius of the particle, k is the wavenumber of the medium surrounding the particle, and m indexes the order (where m = 1 is the dipole term, m = 2 is the quadrupole term, etc.). The Kerker condition has been experimentally demonstrated for disk-shaped particles by controlling the aspect ratio, $A = d/h$, where d is the disk diameter and h is the disk height[24]. Furthermore, satisfying the Kerker condition in an array can result from the overlap of the ELR and MLR by tuning the metasurface periodicity, leading to Kerker interference[35].

For cylindrical metaatoms that are relatively long, their diameter can be reduced into a NW structure to operate in the SM regime. That is, the cylindrical NW structure can support the propagation of the HE_{11} guided mode of a target wavelength resonantly, which are leaky by nature. Hence, these modes are referred to as leaky resonant modes (LRMs), and they are similar to the guided modes in optical fibers. The leaky nature of LRMs in nanoscale structures leads to scattering of the travelling light inside of the fiber-like particles. Thus, placing these cylindrical structures into an array can enable the construction of a metamaterial where the neighbouring fiber-like particles can recollect the LRM scattered light of another particle. Such metamaterials are also governed by particle diameter and periodicity, where the periodicity affects the recollection of the LRM scattered light[17,36]. When the cylindrical particles are tapered into truncated cones, it produces a cylindrical geometry with a range of diameters, broadening the range of supported resonant wavelengths[5,36]. Leveraging the tuned collective resonances of these particle geometries in an array is what enables a tapered dissipative semiconductor NW array metamaterial to achieve near-unity broadband absorptance.

2.5.4 Low-Dimensional Materials

Nanotechnologies are being developed with single 1D NW structures, similar to the single cylindrical resonator particle used in metamaterials, for the development of high-performance optoelectronics[37]. When used as a single unit, the 1D cylindrical structure may be referred to as a low-dimensional material. And where metasurfaces are composed of repeating units like the cylindrical particle, atomically thin materials like graphene and molybdenum ditelluride (with intrinsic properties) form the 2D class of low-dimensional materials. These advanced materials have drawn attention because recent developments have shown that the small volumes of their operating scale can be leveraged to achieve high performance in important optoelectronic metrics such as low dark currents, short response times, and large bandwidths[38].

2.6 Numerical Optical Modelling by Finite Difference Time Domain Method

The Lumerical FDTD simulation tool was implemented for optical modelling. The FDTD method uses the discretization of time and space and Maxwell's equations, of the form presented in Eqs. (2-50) and (2-51), to compute electric and magnetic fields for analysis[39].

$$\nabla \times \mathbf{E} = -\frac{\mu_o \partial \mathbf{H}}{\partial t} \tag{2-50}$$

$$\nabla \times \mathbf{H} = \sigma \mathbf{E} + \frac{\partial (\epsilon \mathbf{E})}{\partial t} \tag{2-51}$$

In Eqs. (2-50) and (2-51), **E** is the electric field, **H** is the magnetic field, μ_0 is the magnetic permeability, σ is the conductance, and ε is the electric permittivity. These formulae can be used to describe complex systems. However, consider the modified expression of Eq. (2-50) included in Eq. (2-52) for simplicity, where it is assumed that there is only variation in the *x*-dimensional space and a *z*-component to the electric field. The time and space components of the governing equations are discretized for computation, taking on a form similar to that of Eq. (2-53).

$$\frac{\partial E_z}{\partial x} = \frac{\mu_o \partial H_y}{\partial t} \tag{2-52}$$

$$\frac{E_{n+1}^m - E_n^m}{\Delta x} = \mu_o \frac{H_{n+1/2}^{m+1/2} - H_{n+1/2}^{m-1/2}}{\Delta t} \tag{2-53}$$

Here, *m* represents the time coordinate and *n* represents the space coordinate. Similarly, using this coordinate system, the electric permittivity and magnetic permeability can be made spatially dependent. Defining the simulation process in such a way makes it convenient to define the material used at any point in space and visualize a propagating waveform in time and space. The ability to define the material at any point allows for the creation of objects, and the ability to define and animate the electric and magnetic fields makes it intuitive to understand whether or not a user implemented numerical model setup was properly executed.

A temporal update scheme for computation can be defined by rearranging the discretized governing formula into an equation with the field to be found (subsequent in time) in terms of the previous field in time plus the space derivative. For example, Eq. (2-54) provides the temporal update scheme obtained from rearranging the governing Eq. (2-53). It is the computation of these temporal update schemes that provides the solutions for the propagating electric and magnetic fields. The complete

spatial field can be chronologically assembled to create an animation of the propagating waveform. This is a particular advantage of the FDTD method, which enables insightful optical response analysis.

$$H_{n+1/2}^{m+1/2} = H_{n+1/2}^{m-1/2} + \frac{E_{n+1}^{m} - E_{n}^{m}}{\Delta x} \frac{\Delta t}{\mu_o} \tag{2-54}$$

Simplified expressions were presented to illustrate the FDTD operation, but Lumerical implements the FDTD method for modelling complex systems and streamlines the process through a user interface. This streamlined process allowed for the rapid definition and modelling of the enhanced absorption capabilities of the metamaterials and low-dimensional material structures in this thesis. The FDTD method has been well studied and excellent resources are available for a more in-depth description, including in the Ansys Optics knowledge base for FDTD (https://optics.ansys.com/hc/en-us).

2.7 References

1. *Single-photon generation and detection: experimental methods in the physical sciences*. (Elsevier/AP, Academic Press is an imprint of Elsevier, 2013).
2. Itzler, M. A. *et al.* Advances in InGaAsP-based avalanche diode single photon detectors. *J. Mod. Opt.* **58**, 174–200 (2011).
3. Acerbi, F., Anti, M., Tosi, A. & Zappa, F. Design Criteria for InGaAs/InP Single-Photon Avalanche Diode. *IEEE Photonics J.* **5**, 6800209–6800209 (2013).
4. Aull, B. F. *et al.* Geiger-Mode Avalanche Photodiodes for Three-Dimensional Imaging. **13**, (2002).
5. Gibson, S. J. *et al.* Tapered InP nanowire arrays for efficient broadband high-speed single-photon detection. *Nat. Nanotechnol.* **14**, 473–479 (2019).
6. Liu, M. *et al.* High-Performance InGaAs/InP Single-Photon Avalanche Photodiode. *IEEE J. Sel. Top. Quantum Electron.* **13**, 887–894 (2007).
7. Xu, Y., Xiang, P. & Xie, X. Comprehensive understanding of dark count mechanisms of single-photon avalanche diodes fabricated in deep sub-micron CMOS technologies. *Solid-State Electron.* **129**, 168–174 (2017).
8. Wen, J. *et al.* Origin of large dark current increase in InGaAs/InP avalanche photodiode. *J. Appl. Phys.* **123**, 161530 (2018).
9. Meng, X. *et al.* InGaAs/InAlAs single photon avalanche diode for 1550 nm photons. *R. Soc. Open Sci.* **3**, 150584 (2016).

10. Cao, S. *et al.* Theoretical Analysis of InGaAs/InAlAs Single-Photon Avalanche Photodiodes. *Nanoscale Res. Lett.* **14**, 3 (2019).
11. Donnelly, J. P. *et al.* Design Considerations for 1.06-um InGaAsP–InP Geiger-Mode Avalanche Photodiodes. *IEEE J. Quantum Electron.* **42**, 797–809 (2006).
12. Sanzaro, M. *et al.* InGaAs/InP single-photon detector with low noise, low timing jitter and high count rate. in (eds. Razeghi, M., Tournié, E. & Brown, G. J.) 93701T (2015). doi:10.1117/12.2079778.
13. Hadfield, R. H. Single-photon detectors for optical quantum information applications. *Nat. Photonics* **3**, 696–705 (2009).
14. Liu, C., Ye, H.-F. & Shi, Y.-L. Advances in near-infrared avalanche diode single-photon detectors. *Chip* **1**, 100005 (2022).
15. Mitrofanov, O. *et al.* Perfectly absorbing dielectric metasurfaces for photodetection. *APL Photonics* **5**, 101304 (2020).
16. Kamali, S. M., Arbabi, E., Arbabi, A. & Faraon, A. A review of dielectric optical metasurfaces for wavefront control. *Nanophotonics* **7**, 1041–1068 (2018).
17. Tekcan, B. *et al.* Semiconductor nanowire metamaterial for broadband near-unity absorption. *Sci. Rep.* **12**, 9663 (2022).
18. van de Groep, J. & Polman, A. Designing dielectric resonators on substrates: Combining magnetic and electric resonances. *Opt. Express* **21**, 26285 (2013).
19. Yao, Y. *et al.* Recent progresses on metamaterials for optical absorption and sensing: a review. *J. Phys. Appl. Phys.* **54**, 113002 (2021).
20. Snyder, A. W. & Love, J. D. *Optical waveguide theory*. (Chapman and Hall, 1983).
21. Tong, L. *et al.* Subwavelength-diameter silica wires for low-loss optical wave guiding. *Nature* **426**, 816–819 (2003).
22. Tong, L., Lou, J. & Mazur, E. Single-mode guiding properties of subwavelength-diameter silica and silicon wire waveguides. *Opt. Express* **12**, 1025 (2004).
23. Ming, X., Liu, X., Sun, L. & Padilla, W. J. Degenerate critical coupling in all-dielectric metasurface absorbers. *Opt. Express* **25**, 24658–24669 (2017).
24. Staude, I. *et al.* Tailoring Directional Scattering through Magnetic and Electric Resonances in Subwavelength Silicon Nanodisks. *ACS Nano* **7**, 7824–7832 (2013).

25. Babicheva, V. E. & Moloney, J. V. Lattice effect influence on the electric and magnetic dipole resonance overlap in a disk array. *Nanophotonics* **7**, 1663–1668 (2018).
26. Yang, Y. *et al.* Multimode directionality in all-dielectric metasurfaces. *Phys. Rev. B* **95**, 165426 (2017).
27. Ma, Y., Guo, X., Wu, X., Dai, L. & Tong, L. Semiconductor nanowire lasers. *Adv. Opt. Photonics* **5**, 216 (2013).
28. Chen, M., Kim, M., Wong, A. M. H. & Eleftheriades, G. V. Huygens' metasurfaces from microwaves to optics: a review. *Nanophotonics* **7**, 1207–1231 (2018).
29. Decker, M. *et al.* High-Efficiency Dielectric Huygens' Surfaces. *Adv. Opt. Mater.* **3**, 813–820 (2015).
30. Ollanik, A. J., Smith, J. A., Belue, M. J. & Escarra, M. D. High-Efficiency All-Dielectric Huygens Metasurfaces from the Ultraviolet to the Infrared. *ACS Photonics* **5**, 1351–1358 (2018).
31. Kerker, M., Wang, D.-S. & Giles, C. L. Electromagnetic scattering by magnetic spheres. *J. Opt. Soc. Am.* **73**, 765 (1983).
32. Rahimzadegan, A., Alaee, R., Rockstuhl, C. & Boyd, R. W. Minimalist Mie coefficient model. *Opt. Express* **28**, 16511 (2020).
33. Tzarouchis, D. & Sihvola, A. Light Scattering by a Dielectric Sphere: Perspectives on the Mie Resonances. *Appl. Sci.* **8**, 184 (2018).
34. Liu, W. & Kivshar, Y. S. Generalized Kerker effects in nanophotonics and meta-optics. *Opt. Express* **26**, 13085 (2018).
35. Babicheva, V. E. & Evlyukhin, A. B. Resonant Lattice Kerker Effect in Metasurfaces With Electric and Magnetic Optical Responses. *Laser Photonics Rev.* **11**, 1700132 (2017).
36. Fountaine, K. T., Kendall, C. G. & Atwater, H. A. Near-unity broadband absorption designs for semiconducting nanowire arrays via localized radial mode excitation. *Opt. Express* **22**, A930–A940 (2014).
37. Krogstrup, P. *et al.* Single-nanowire solar cells beyond the Shockley–Queisser limit. *Nat. Photonics* **7**, 306–310 (2013).
38. Li, Z. *et al.* Review on III-V Semiconductor Single Nanowire-Based Room Temperature Infrared Photodetectors. *Materials* **13**, 1400 (2020).
39. Kane Yee. Numerical solution of initial boundary value problems involving maxwell's equations in isotropic media. *IEEE Trans. Antennas Propag.* **14**, 302–307 (1966).

Chapter 3

Tapered InP Nanowire Arrays for Efficient Broadband High-Speed Single-Photon Detection[1]

3.1 Preface

SPAD advancement is reliant on implementing emerging high-performance materials. However, a better understanding of the optoelectronic properties of metamaterials and low-dimensional materials is required before the technologies are ready for added external circuitry for Geiger-mode single-photon detection operation. The previous section introduced some of the foundational background for the optical and electromagnetic behaviours of metamaterials and low-dimensional materials as well as the performance qualities required of SPADs. Device design in SPADs has reached a certain maturity, but primarily in planar structures, and the design rules for integrating metamaterials and low-dimensional materials have not had a chance to reach the same degree of understanding. Furthermore, the unique phenomena exhibited in these advanced materials often extends to their optoelectrical qualities, adding to the complexity of the problem. As such, revealing the design and high-performance optoelectronic operation of a tapered semiconductor NW p-n junction array, in the following published study, advances the necessary understanding for practical integration of advanced materials into SPADs.

3.2 Manuscript

*Sandra J. Gibson[1], Brad van Kasteren[1], Burak Tekcan[1], Yingchao Cui[2], Dick van Dam[2], Jos E. M. Haverkort[2], Erik P. A. M. Bakkers[2] and Michael E. Reimer[1]**

[1]Institute for Quantum Computing and Department of Electrical & Computer Engineering, University of Waterloo, Ontario, Canada. [2]Department of Applied Physics, Eindhoven University of Technology, Eindhoven, The Netherlands. *e-mail: michael.reimer@uwaterloo.ca

---

[1] This is an Accepted Manuscript of an article published by Nature Publishing Group in Nature Nanotechnology on 04 March 2019, available online: https://www.nature.com/articles/s41565-019-0393-2. Sandra J. Gibson, Brad van Kasteren, Burak Tekcan, Yingchao Cui, Dick van Dam, Jos E. M. Haverkort, Erik P. A. M. Bakkers and Michael E. Reimer, "Tapered InP nanowire arrays for efficient broadband high-speed single-photon detection"

3.2.1 Summary

Superconducting nanowire single-photon detectors with peak efficiencies above 90% and unrivalled timing jitter (< 30 ps) have emerged as a potent technology for quantum information and sensing applications. However, their high cost and cryogenic operation limit their widespread applicability. Here, we present an approach using tapered InP nanowire p–n junction arrays for high-efficiency, broadband and high-speed photodetection without the need for cryogenic cooling. The truncated conical nanowire shape enables a broadband, linear photoresponse in the ultraviolet to near-infrared range (~500 nm bandwidth) with external quantum efficiencies exceeding 85%. The devices exhibit a high gain beyond 10^5, such that a single photon per pulse can be distinguished from the dark noise, while simultaneously showing a fast pulse rise time (< 1 ns) and excellent timing jitter (< 20 ps). Such detectors open up new possibilities for applications in remote sensing, dose monitoring for cancer treatment, three-dimensional imaging and quantum communication.

3.2.2 Introduction

Detection of light at the single-photon level is advantageous for a wide range of applications in astronomy, sensing and biomedical engineering, as well as being a key driver of the rapidly developing field of quantum information science[1–3]. Many photon-starved situations benefit from high-sensitivity detectors as well, for example in remote sensing of low-power signals such as night-time operation, identification and tracking of diffuse reflectors, communication of images from satellites at high speed, and acquiring 3D images at long range with high resolution[3–5]. Indeed, the ability to detect light at the fundamental limit (that is, single photons) enables observations over longer distances. Other possible applications in the longer term include singlet oxygen detection for dose monitoring in cancer treatment[6,7], quantum communication[2] and fault-tolerant analysis testing of CMOS circuits[8,9].

State-of-the-art SNSPDs[6,10] have emerged to meet most of the demands of these applications but have limited portability due to their operating temperature. Other commercial devices such as silicon and InGaAs/InP SPADs overcome this issue of low temperature operation; however, they have limited efficiencies of only 65% at 650 nm and 10% at 1550 nm for high-speed operation, and the timing resolution is an order of magnitude worse than that of superconducting NWs[2]. Alternative designs have surfaced that incorporate quantum effects and next-generation materials such as quantum-dot-resonant tunnel diode devices[11] or gated field-effect transistors[12], phototransistors based on 2D materials such as graphene[13,14], as well as hybrid graphene quantum-dot systems[15]. However, thus far, they have not

reached the level of performance of commercial devices, as they exhibit either high gain or fast operation, but not both. See Supplementary Table 3-1 for a comparison of these single-photon technologies.

We have developed a tapered NW p–n junction array that overcomes all of these drawbacks to achieve high-efficiency photodetection over a broad bandwidth (~500 nm), with the high speed and gain that enables single-photon detection, all while operating at room temperature. Owing to the unique size and shape of the NWs, near-unity DE over a broad wavelength range from the UV to NIR is possible. Operation at higher temperatures is advantageous for sensing applications requiring portability, for example for use in the medical field or launching detectors on nanosatellites, where weight and space is at a premium[16–18].

3.2.3 Tapered Nanowire P-N Junction Array Design

A scanning electron microscope (SEM) image of an uncontacted NW detector array is shown in Figure 3-1a, while a micrograph of a contacted NW array in cross-section is presented in Figure 3-1b. There are three important features of this NW detector design that are required to achieve near-unity broadband photodetection efficiency. The first is the NW tapering (the NW has a conical structure with tip smaller than the base), which minimizes reflections of incoming light as a result of the adiabatic increase in the effective refractive index from vacuum ($n = 1$) at the NW tip towards bulk InP ($n = 3.4$) as the light propagates down the structure. Second, by gradually increasing the NW diameter towards the base, there is a continuum of available diameters from the top to bottom for the resonant coupling of guided modes over a broad wavelength range. Finally, the NW periodicity is optimized to maximize the absorption efficiency. The NW spacing should be far enough apart to ensure that resonant waveguide modes are present, but close enough that light cannot pass through the NW array. This parameter requires optimization because if the NWs are too close, reflections would increase due to an increase in the effective refractive index towards the bulk value, causing the high-efficiency broadband absorption to vanish.

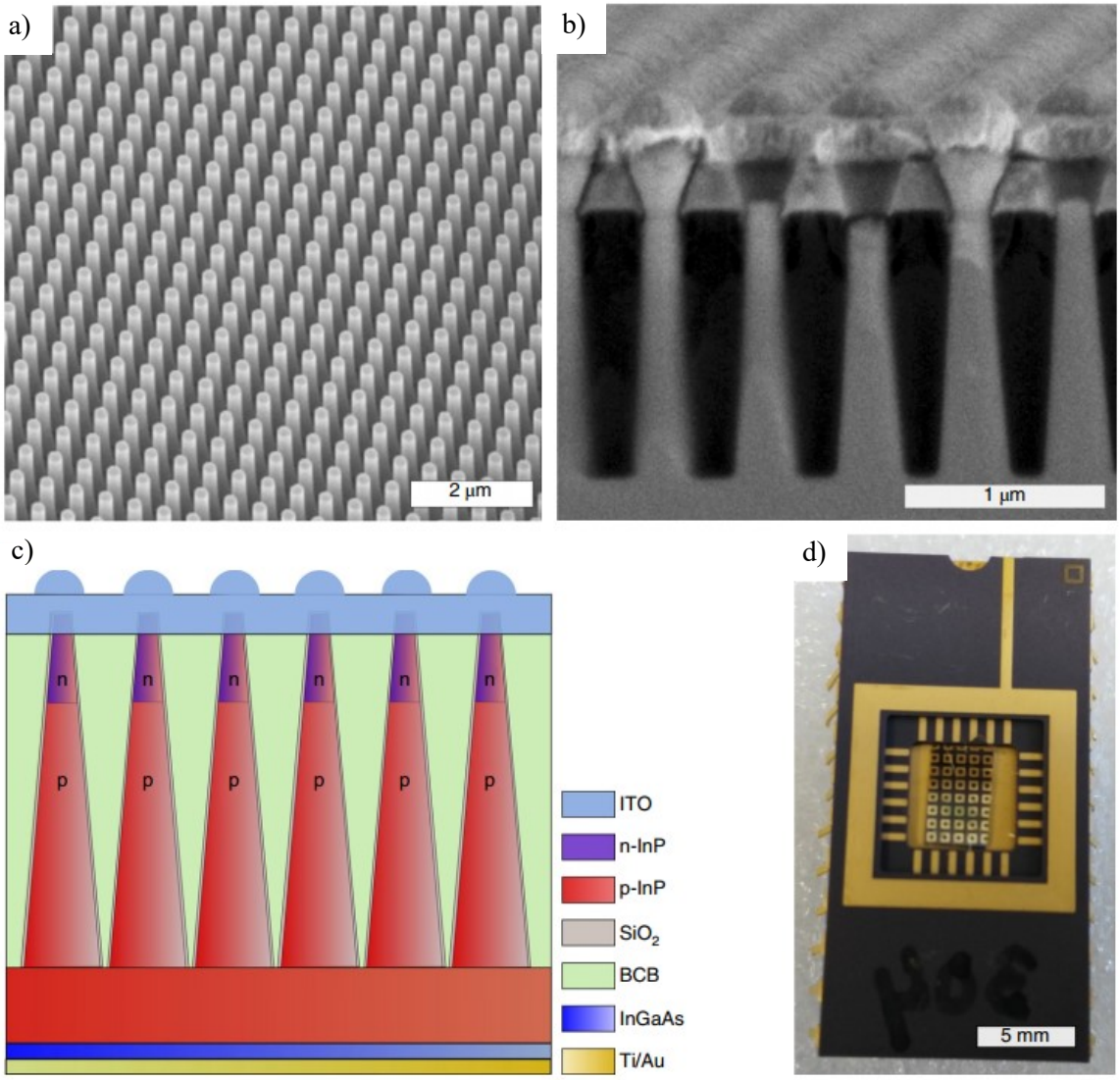

Figure 3-1: Tapered nanowire (NW) array device design. a) Scanning electron microscope image of the InP NW array after etching, imaged at a tilt angle of 30° from the substrate normal. **b)** Cross-sectional view of the completed device, showing the NW tapering, the planarizing benzocyclobutene layer (black region between the NWs) and the deposited indium tin oxide top contact layer. **c)** Schematic view of the full device structure from **b)** also illustrating the bottom contacting layers. **d)** Photograph of the device mounted and wire bonded to a standard ceramic chip carrier. There are approximately 35 devices (5 × 7) on this chip with individual gold contacts surrounding the NW array with an active device area of 300 × 300 µm^2. Figure 3-1b adapted from ref. 52, American Chemical Society.

Our InP tapered NW p–n junction detector devices were fabricated using a top-down dry-etching approach, which yields a uniform, ordered array of conical NWs, as shown in Figure 3-1a. High-quality planar p–n junction layers were first grown by metal–organic vapour-phase epitaxy (MOVPE), followed by nanoimprint lithography and reactive ion etching (RIE). The shape of the top-down etched NWs can be tuned by adjusting the dry-etching parameters, such as the etchant flux, the ratio between the CH 4 and H2 fluxes, the substrate temperature, and the radiofrequency power. The optimized etching conditions resulted in a sloped sidewall profile, producing truncated conical NWs that are 1.6 μm long and are spaced with a 513 nm periodicity, with a top diameter of 150±10 nm and bottom diameter of 350±20 nm. Less than 20% volume fraction, as compared to the original planar film structure, is occupied by the NWs. A cross-section of the resulting tapered NW array with a top contact is shown in Figure 3-1b. The black region visible between the NWs is a layer of benzocyclobutene (BCB), which is used to planarize the sample before contacting the NWs with indium tin oxide (ITO). This ITO layer is 300 nm thick and serves as the transparent top contact. Owing to the deposition conditions, the ITO layer naturally takes on a microstructure whereby it increasingly accumulates around the NW tip. In addition, Figure 3-1b shows how the space above the BCB is also filled with ITO, creating a continuous and conformal layer of ITO without spaces, yielding improved contact resistance. The complete device structure from Figure 3-1b is depicted schematically in Figure 3-1c, while a picture of the completed detector package is shown in Figure 3-1d. Each black square corresponds to an independent 300 μm × 300 μm active device area which is surrounded by a 200-μm-wide gold perimeter, serving as a ring contact used for wire bonding.

3.2.4 Measured Performance

3.2.4.1 Broadband Photodetection

The dark visual appearance of the NW array (black square in Figure 3-1d) indicates that the majority of light incident on the array is captured by the material. Indeed, vertically oriented NW arrays can be patterned and specifically arranged to act as near-perfect absorbers[19–23]. In a ray optics picture, light should pass between the NWs; however, experimental and theoretical studies have shown that, given the correct choice of NW ensemble parameters (such as length, diameter, and periodicity), near-unity absorption efficiency can be achieved. Moreover, arrays can be engineered such that the absorption is also insensitive to wavelength, incident angle and polarization[22–24]. For instance, the measured absorption spectra from 450 nm to 925 nm of a tapered NW array with NW height of 1.6 μm, radii

from 30 nm (top) to 100 nm (base), and periodicity of 450 nm demonstrated an angle insensitivity by only showing < 10% change in the absorption from an angle of incidence ranging from 0° to 30°[23]. The device dimensions can also be chosen such that the absorptance is highly wavelength selective. This wavelength selectivity is because the NWs act as nanoscale dielectric waveguides. Light couples resonantly to guided modes of the NW depending on its diameter. Thus, by varying the NW diameter towards the base, multiple wavelengths can be absorbed, with longer wavelengths being absorbed further down the NW, as shown in Figure 3-2a. This design results in near-unity absorption efficiency over a broad wavelength range, as well as locating the peak absorption position close to the embedded p–n junction (see Supplementary Figure 1 of the published article of this chapter for a device design schematic).

The broadband high-efficiency absorption of the NW array is displayed in Figure 3-2b, where using the fabricated device parameters including contacts in a FDTD model predicts an average of 85% absorption in the wavelength range from 450 nm to 900 nm. For comparison, without contacts, an average of 95% absorption over the entire wavelength range is predicted (Figure 3-7). Only 6% reflectance was measured from the uncontacted array (Figure 3-2c), which confirms that reflected losses have also been minimized due to the tapered NW geometry. The device also exhibits excellent measured external quantum efficiency (EQE) i.e., ratio of charge carriers collected to the number of incident photons. This excellent EQE is shown in Figure 3-2d, with a peak efficiency of 87% at 860 nm and greater than 70% throughout the entire wavelength range. These combined attributes of broad spectral coverage and high photoconversion efficiency also make these NW arrays an ideal platform for high-performance multispectral photodetectors.

3.2.4.2 Distinguishing Single Photons

We investigated the photocurrent response of the NW APD and multiplication factor at room temperature and the possibility of distinguishing a single photon per pulse from the dark noise. The results of this study are summarized in Figure 3-3. Figure 3-3a presents the current–voltage characteristics of the device for varying incident optical power. The dark current is relatively low and is 25 pA at −1.0 V reverse bias. The low dark current indicates the excellent quality of the array material, etched surface and contacts.

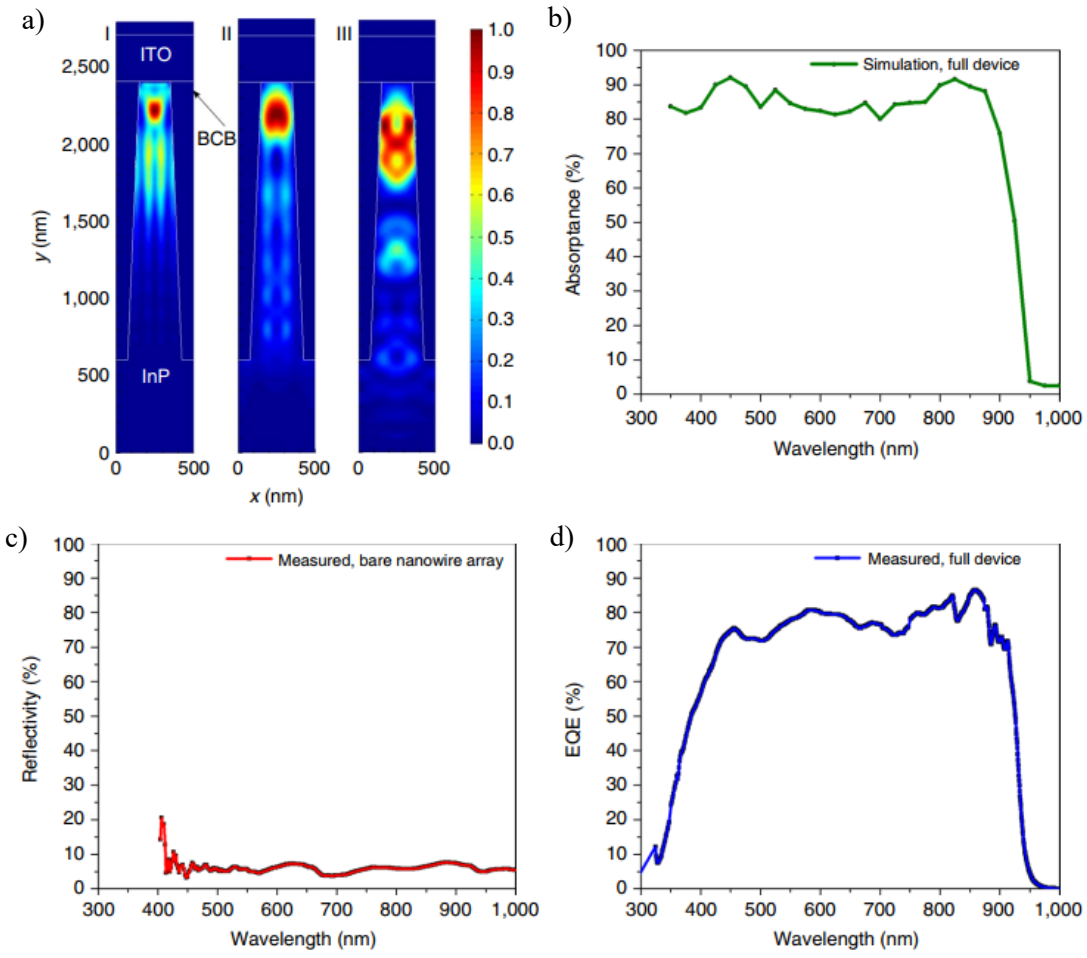

Figure 3-2: Near-unity absorption. a) Finite-difference time-domain numerically modelled absorptance located along a contacted nanowire (NW) for (I) 500 nm, (II) 700 nm and (III) 890 nm wavelength excitation, showing the position of peak absorptance close to the p–n junction location, 200 nm from the NW tip. Red, maximum absorption (normalized to 1). Blue, minimum absorption. b**)** Numerically modelled absorptance of the completed NW ensemble device. The patterned InP NW array with conical shape exhibits high absorptance over a broad spectral range from 400 to 900 nm (peak efficiency of 87%, ~85% average from 450 to 900 nm). c**)** Reflection losses in an uncontacted NW array, averaging less than 6% over the entire wavelength range. d**)** Measured external quantum efficiency of the full device at 0 V shows a similar qualitative behaviour to the absorptance, maintaining a value higher than 70%. Short wavelengths are absorbed in the indium tin oxide contact layer, while wavelengths longer than the InP bandgap are transmitted. Figure 3-2b and Figure 3-2d adapted from ref. 52, American Chemical Society.

In avalanche photodetectors the shot noise from the dark current is a critical parameter, as it can be the limiting factor for the device detectivity, which represents the smallest signal strength that can be successfully resolved. Considering a primary contributor to the dark current is from thermally generated carriers, it can be significantly reduced by TECs. Additionally, the total dark current is proportional to the active device area, which can be significantly reduced in future work by decreasing the detector size by two orders of magnitude, as our current device size is relatively large (300×300 μm^2). Other strategies frequently employed in conventional thin-film InGaAs/InP APDs to reduce the dark current and afterpulsing effects can also be employed in future device designs, such as pulse or sinusoidal gating[1,25,26], fast active quenching[27,28] or negative feedback structures[29,30].

With increasing reverse bias in Figure 3-3a the current rises slowly until approximately −9.5 V where an abrupt threshold is reached and the current rapidly grows. The magnitude of the breakdown voltage (VB ≈ −13 V, Supplementary Figure 6 of the published article of this chapter) signifies an avalanche breakdown mechanism in accordance with theory[31], whereby VB > $6E_g/q$. Here, E_g is the semiconductor bandgap and q is the electron charge. This process occurs when the electric field in the junction reaches a critical magnitude such that photogenerated free carriers that are swept into the depletion region gain sufficient energy to cause impact ionization of bound carriers, effectively multiplying the current. Depending on the magnitude of the electric field and the impact ionization rates of the material, each carrier can undergo many subsequent ionization events, resulting in a self-sustaining avalanche. In InP, the ionization rates of electrons (α) and holes (β) approach similar values at electric field intensities approaching the breakdown. The ionization rates are related through the ionization rate ratio, $k = \beta/\alpha$. We note that the avalanche breakdown mechanism was observed in eight out of twelve of the devices studied. The other types of reverse bias characteristic that were measured are summarized in Supplementary Figure 6a of the published article of this chapter. The characteristic shift of the VB towards higher reverse bias with increasing temperature confirms that the breakdown behaviour observed originates from the avalanche mechanism (Supplementary Figure 6b of the published article of this chapter).

The photocurrent response of the device in the photoconductive region, where there is no gain in Figure 3-3b, exhibits a highly linear dependence in the average photocurrent as a function of excitation power at a wavelength of 700 nm. From the linear response exhibited by this device in Figure 3-3b an IQE of ~73% was extracted. Next, attenuating the incident optical power down to a single photon per pulse, the photocurrent remains easily distinguishable from the dark noise, as observed in Figure 3-3c. The

photocurrent also remains linear in this low-power regime, as shown in Figure 3-3d, where the power density and photocurrent are presented as the number of photons and electrons per pulse.

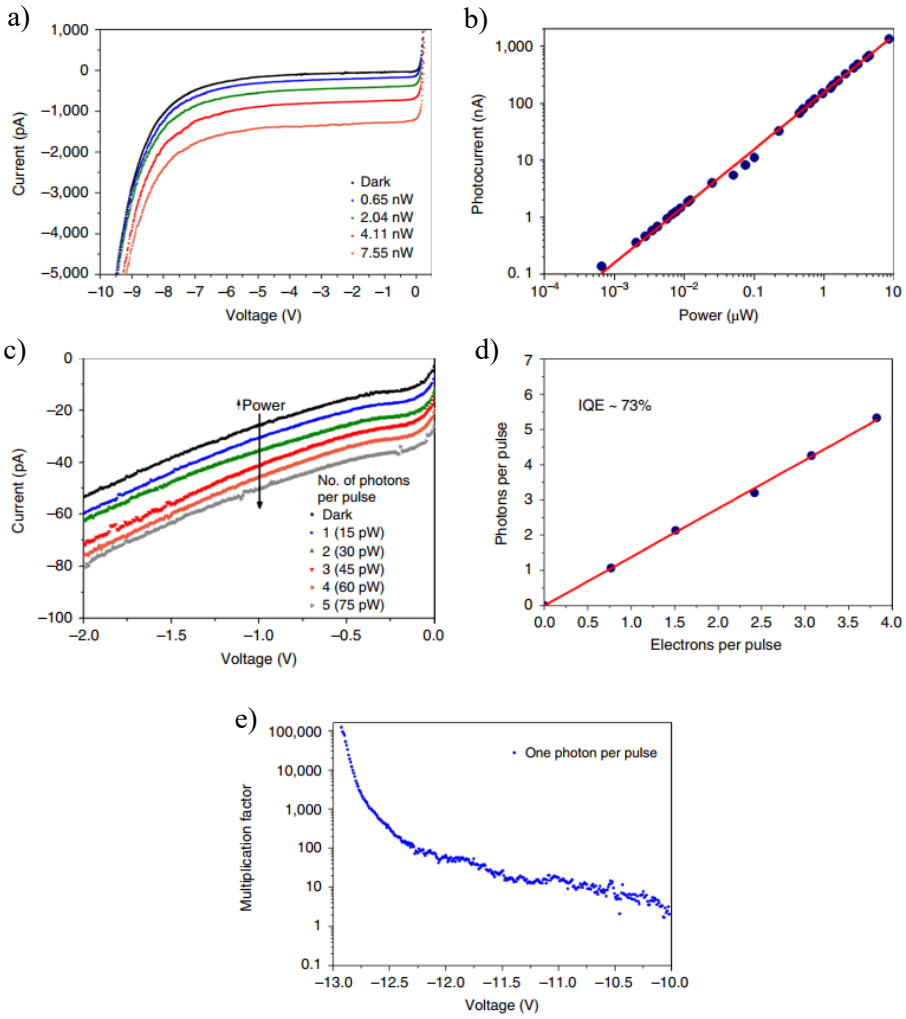

Figure 3-3: Photocurrent response and avalanche photodetection. a) Photocurrent response measured at 300 K in reverse bias under continuous-wave excitation at 700 nm for varying excitation power showing the avalanche threshold voltages. **b)** The sub-avalanche photocurrent response, measured at −1.0 V bias, is highly linear over a large dynamic range from microwatts down to picowatts. **c)** By attenuating a 40 MHz pulsed laser excitation (3 ps pulse width) at 690 nm down to a single photon per pulse, the average photocurrent signal can be distinguished from the dark current. **d)** Sub-avalanche photocurrent response measured under pulsed excitation at 690 nm and −1.0 V reverse bias in the single-photon regime. For this device, an internal quantum efficiency of 73% was

achieved at room temperature, corresponding to more than 0.7 electrons per pulse under an illumination of a single photon per pulse. **e)** Calculated multiplication gain in the avalanche regime at ambient room temperature under illumination of one photon per excitation pulse.

Despite carrying out measurements at room temperature, more than 0.7 electrons per pulse are created in response to illumination of a single photon per pulse. This result illustrates that even at room temperature the device demonstrates the high sensitivity required for single-photon-level detection.

3.2.4.3 High-Gain Avalanche Photodetection

The multiplication gain in the avalanche region can be estimated using Eq. (3-1).

$$M = \frac{I_{ph}(V) - I_{dark}(V)}{I_{ph(0)} - I_{dark(0)}} \tag{3-1}$$

where $I_{ph}(V)$ and $I_{dark}(V)$ are the measured excited and dark currents, and $I_{ph(0)}$ and $I_{dark(0)}$ are the average measured excited and dark currents in the low-bias region with unity gain (that is, $M = 1$). The multiplication factor was calculated for an excitation of one photon per pulse and the result is given in Figure 3-3e. A linear region exists from −10 V to −12 V where the gain rises steadily from a factor of 5 to 100. Approaching the breakdown threshold, the gain rapidly increases, reaching a large current gain of greater than 10^5 at −12.75 V. This high multiplication factor for a vertically oriented InP photodiode array is consistent with the high gain reported in previously horizontally contacted single InP NW devices[32,33].

The high multiplication gains reported here arise due to a low dark current, which reduces further with repeated measurement sweeps (Supplementary Figure 7 of the published article of this chapter). We identified through device numerical modelling that the low dark current is a result of the depletion region extending the entire length of the NWs because of their surface states (Supplementary Figure 13 of the published article of this chapter). The numerical model for depletion by surface states of a p-InP NW was based on solving Poisson's equation in cylindrical coordinates. From the numerical modelling, the critical NW diameter for NW depletion was found to be 344 nm. This result was reaffirmed through energy band analysis by the absence of a quasi-neutral region in the modelled NW that had a diameter less than the critical diameter. The fabricated NWs have a top diameter of 150 nm and bottom diameter of 350 nm; thus, the modelling is in agreement with the prediction that the NW core is fully depleted. This explanation is corroborated by recent work where deliberate electrostatic depletion of a single InP NW photodetector using ferroelectric-enhanced side gates significantly reduced the dark current and

improved the photoconductive gain[32]. Control over this process could prove highly advantageous for future device performance and stability.

3.2.4.4 Temporal Response

A high-speed photodetector is an important metric for SPADs as the rise and fall time determines the minimum intrinsic contribution to the total dead time. This is the amount of time required for the detector to return to a state where it is ready to register the arrival of another photon. In previous work on NW-based APDs, the high multiplication gain was not accompanied by a fast photocurrent response[34]. Instead, single InP NW APDs with high gain of 10^4 to 10^5 exhibited a poor temporal response on the order of several to tens of milliseconds[32,33]. This poor temporal response was attributed to a high overall resistive-capacitive (RC) time constant i.e., the charge (discharge) time of a capacitor through a resistor from a no-charge (full-charge) state to 63.2% (36.8%) of the applied direct current (DC) (initial voltage) value. The high RC time constant was a result of the high series device resistance and large parasitic capacitances in the electrical contacting. In contrast, high-bandwidth InP NW bipolar junction transistors[35] demonstrated a fast photocurrent response with a FWHM of 300 ps but revealed a significantly lower gain factor of ~40.

NWs have also demonstrated persistent photoconductivity[34,36] in many materials including InP. This arises from the delayed relaxation of the photoexcited carriers due to charge trapping effects such that the device exhibits a long effective recombination time. In SPADs, longer trap relaxation times are known to exacerbate afterpulsing as they extend the time after avalanche when a carrier may be released and cause false trigger events with statistical significance. However, we do not attribute our high multiplication gain to a persistent photoconductivity effect, as in several other reports[34,37,38], because we have also simultaneously measured a rapid temporal response. A comparison of the gain versus temporal response for NW-based devices, including our device, is presented in Figure 3-8.

The temporal photoresponse of our NW APD array is presented in Figure 3-4. The 50 Ω input on an oscilloscope with 500 MHz bandwidth was used to measure the photocurrent as a voltage pulse with no external amplification. In Figure 3-4a, the photocurrent response is shown at an applied reverse bias of −10 V under pulsed excitation. An apparent ringing in the output signal is observed, which may be solved in future work by maintaining radiofrequency impedance-matching standards throughout the circuit. A modified Gaussian fit of the pulse, shown in Figure 3-4b, yields a 10−90% rise time of 0.6 ns and a FWHM of 1.2 ns.

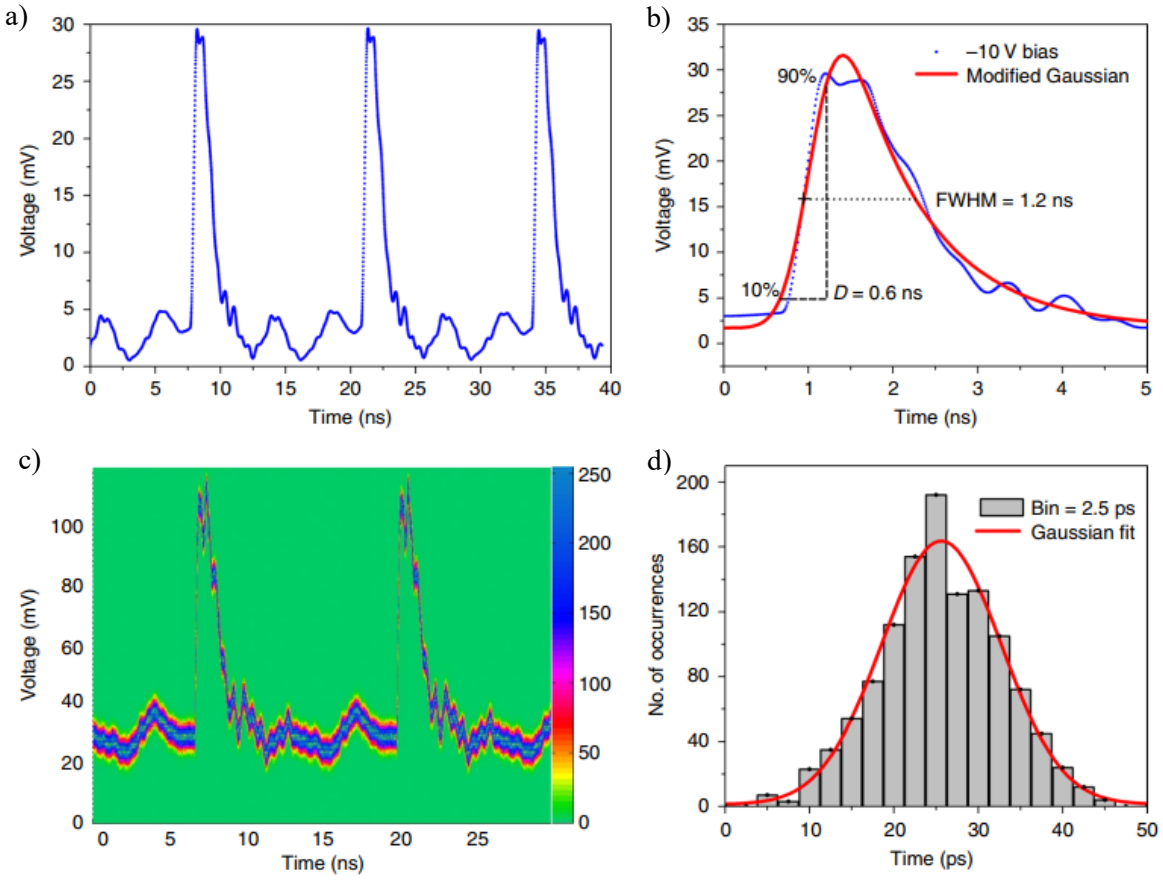

Figure 3-4: Temporal response. a) Output voltage pulse measured at a reverse bias of −10 V under pulsed excitation at 76 MHz repetition rate with 870 nm wavelength and power of 100 µW. **b)** On fitting the pulses using an exponentially modified Gaussian function, rise times of less than 0.6 ns and full width at half maximum (FWHM) of less than 1.2 ns were obtained. **c)** A persistence plot of the photocurrent pulse waveform under 76 MHz excitation at a power of 100 µW for a reverse bias of −10 V. The colour bar indicates the number of waveform occurrences. **d)** The FWHM of the Gaussian fit to the histogram, taken at 50% of the pulse rising edge from **c)** was used to estimate a timing jitter of 17 ps.

This measured response time (τ_{meas}) is a slight overestimation of the intrinsic device temporal response (τ_{device}) because the response of the oscilloscope (τ_{scope}), the bias-tee ($\tau_{bias\text{-}T}$), and the laser pulse width (τ_{laser}) all contribute to the total measured response time as in Eq. (3-2).

$$\tau_{meas} = \sqrt{\tau_{device}^2 + \tau_{scope}^2 + \tau_{bias-T}^2 + \tau_{laser}^2} \tag{3-2}$$

The temporal response also improves with increasing reverse bias as expected and is illustrated in Supplementary Figure 9 of the published article of this chapter. This improvement is due to the increasing electric field and decreasing junction capacitance, which reduces the RC time constant of the device.

This rapid recovery time makes this NW array an excellent candidate for high-speed avalanche photodetection, a requirement for both optical communication and single-photon-counting applications. A low overall contribution from the contact resistance, estimated to be on the order of several ohms[39], plays a major role in this fast recovery time. In addition, the p–n junction is placed close to the top of the NW where the highest optical absorption takes place (Figure 3-2a). This junction placement significantly reduces the average transit time of the carriers in the low field drift region, further contributing to the observed fast response time. It has also been shown that shrinking the volume of the avalanche region using microstructures can improve the temporal response and dramatically reduce the excess noise[40–42]. The reduced excess noise is due to a smaller effective ionization rate ratio, k_{eff}, of the microstructure as compared to the bulk material. The excess noise in an APD results from the inherently stochastic multiplication process of the secondary carriers that are generated and decreases with reduced variance in the spatial ionization probability[43]. Microstructures can be engineered with small avalanche regions and sharp electric field gradients to leverage the dead-space effect, whereby a generated carrier must travel some distance in an accelerating field before it has sufficient energy to multiply due to impact ionization. Such microstructure engineering can lower k_{eff} by reducing the variance in a carrier's ionization path length. NW APDs utilize this mechanism to achieve a lower k_{eff} and thus excess noise. It was found in other work that the measurement of k_{eff} in NWs was significantly smaller than the k of bulk material[44,45]. Furthermore, by employing a high-speed transmission line electrode design to contact the array, we expect this temporal response can be further improved. For example, a high-speed linear photodetector was fabricated from crossed InP NWs contacted using an integrated coplanar waveguide signal line, where a pulse FWHM of 14 ps was obtained[46].

We highlight here that the speed of the detector is not the only important metric for the temporal performance of the device. Another important consideration is the timing jitter, which represents the uncertainty in the arrival time of a detection event due to fluctuations in the output pulse. In a Geiger-mode photon counter this is generally discriminated using a fast voltage comparator, which signals when the leading edge of the avalanche current has passed a suitable threshold. The time from photon absorption to discrimination is not fixed due to spatial variation of the electric field and the finite transit

time of the carriers within the device volume. A random equivalent-time sampling oscilloscope was used to acquire a persistence trace of the output pulse under the same excitation conditions. The persistence mode superimposes many multiple subsequent waveforms on the same view, with more frequent data emphasized with deeper saturation or hotter colours, as shown in Figure 3-4c. This mode allows pulse noise and an upper bound on the intrinsic timing jitter of the photodiode to be visualized and estimated. A plot of the population histogram of the persistence data taken at 50% of the pulse rising edge was used to evaluate the inherent pulse jitter. A Gaussian fit to the histogram in Figure 3-4d yielded a FWHM value of 17 ps. The jitter in the output pulse also decreases with increasing reverse bias as expected and is shown in Supplementary Figure 10 of the published article of this chapter. The inherent timing jitter of the APD is expected to depend strongly on the electric field, as high electric fields decrease the avalanche build-up time and the time uncertainty. This jitter is exceptionally low compared to the total device jitter measured in InGaAs/InP APDs, which have more than 100 ps FWHM[1,26,47]. We note that this quoted timing jitter in the literature typically contains a contribution from the jitter of the quenching electronics as well. Therefore, our NW array detectors are well suited for use in high-performance applications where the precise photon arrival time is crucial, such as in quantum information science or time-of-flight surveillance measurements.

3.2.5 Conclusions

We have demonstrated a tapered NW avalanche photodetector with a combined near-unity multispectral absorption, high multiplication gain, fast time response and high timing resolution. This method can straightforwardly accommodate material and array engineering to optimize device performance and extend operation to the IR and beyond (as illustrated for an InGaAs NW array in Figure 3-7). For example, SAM structures based on InGaAs/InP[1,48,49] or InGaAs/Si could be fabricated. In the latter case, we envision that III–V NWs (InGaAs) on silicon could benefit from the best of both materials. In this design, near-unity absorption in the IR can be achieved from the InGaAs NW region and the multiplication can occur in silicon with low noise. Another method to investigate to further improve the excess noise and the time response comprises superlattice APD structures[50]. Furthermore, distributed Bragg reflector structures[51] could also be used to filter unwanted wavelengths. Finally, the tapered NW avalanche photodetectors presented in our work show potential as fast linear avalanche photodetectors or Geiger-mode single-photon-counting modules with the addition of TECs.

3.2.6 Methods

The III–V material stack, including p–n junction layers, was grown on a Zn-doped (100) InP wafer by MOVPE. The NW array was then defined using a combined nanoimprint lithography and RIE technique. Particular effort was committed to developing additional process steps to ensure excellent sidewall smoothness and surface quality (Supplementary Figure 2 and Figure 12 of the published article of this chapter). See Supplementary 1 in the published article of this chapter for further details on the fabrication process. The reflectivity of the bare NW array was measured using an integrating sphere. The device was then planarized using a BCB layer and contacted using 300 nm ITO. The completed device was epoxied to a standard ceramic chip carrier and the active areas were wire-bonded to the carrier pins. The absorptance of the completed device structure was numerically modelled using the FDTD method with Lumerical optical software. Further details on the numerical modelling and optimization process are provided in Section 3.3.2.

The absorbed photon number was estimated as in Eq. (3-3).

$$\frac{P}{\frac{hc}{\lambda}} \times A \times \frac{1}{f} \tag{3-3}$$

where P is the excitation power, A is the (numerically modelled) absorptance, f is the laser repetition rate and λ is the wavelength. The incident optical power was attenuated to the single photon per pulse level using a combination of stacked neutral density filters and a continuous variable filter wheel to achieve an effective power of 15, 30, 45, 60 and 75 pW focused on the device. The power density was monitored using a 90:10 fiber-optic beamsplitter installed in the optical path after the filter wheel, and the power ratio between the two paths was first calibrated at higher incident power levels.

The chip carrier was mounted on a printed circuit board (PCB) adapter with 50 Ω SubMiniature version A (SMA) connectors. The assembly was then mounted onto an *xyz* optical stage, and a lens with a focal length of 50 mm was used to focus the laser spot on the active area of the device. The stage was then finely adjusted to give the maximum photocurrent at 0 V. A Keithley 6485 picoammeter was used to perform the dark current and photocurrent measurements.

Current–voltage (I-V) relationship measurements were taken in single sweeps, sequentially from low to high power, without repeated sweeps in between. This was done in an effort to minimize dark current shifts due to either light exposure or multiple sweeps to yield the best comparison (Supplementary Figure 8 of the published article of this chapter). The sweep direction was always from positive to

negative voltage (0.75 V to −13.0 V). The reading rate of the instrument was set to one power line cycle or 16.6 ms with a measurement delay of 10 ms. For temporal measurements with pulsed excitation, a radiofrequency bias-T (MiniCircuits ZX85-126-5+) was used to apply the DC reverse bias to the photodiode and extract the photocurrent pulse, which was measured using SMA cables connected to the 50 Ω input of a LeCroy WaveExpert 100H random equivalent time sampling oscilloscope.

Photocurrent measurements were performed using a Picoquant PDL800D pulse laser driver with a LDH-P-690 head operated at 690 nm and 40 MHz or a Coherent Mira 900 Ti:sapphire 3-ps pulsed laser operated at 870 nm and 76 MHz, as specified in the main text. The laser power was calibrated using a 90:10 fiber beamsplitter with neutral density filters on the signal arm and a power meter monitoring the 90% arm.

3.3 Supplementary Information for "Tapered InP Nanowire Arrays for Broadband High-efficiency and High-Speed Photodetection"[1]

Sandra J. Gibson, Brad van Kasteren, Burak Tekcan, Yingchao Cui, Dick van Dam, Jos E.M. Haverkort, Erik P.A.M Bakkers and Michael E. Reimer

3.3.1 Preface

The supplementary of the published article of this chapter is included, in part, below. Further details on the numerical modelling and device comparison are provided. This additional information illustrates the impact of tapering of the NW arrays on the absorption profile, with comparison to the selectivity of cylindrical NW arrays. Details on the numerical modelling tuning process, and potential high absorption performance capability of InGaAs NW arrays is also included. Lastly, the high-performance of the NW p-n junction array for prospective SPAD technology is illustrated through a gain-temporal response performance comparison with other semiconducting NW (graphically) and other state-of-the-art single-photon detection (tabulated) technologies.

---

[1] This is the Supplementary Information, in part, of an Accepted Manuscript of an article published by Nature Publishing Group in Nature Nanotechnology on 04 March 2019, available online: https://www.nature.com/articles/s41565-019-0393-2. Sandra J. Gibson, Brad van Kasteren, Burak Tekcan, Yingchao Cui, Dick van Dam, Jos E. M. Haverkort, Erik P. A. M. Bakkers and Michael E. Reimer, "Tapered InP nanowire arrays for efficient broadband high-speed single-photon detection"

3.3.2 Optimization of Nanowire Array for Broadband Absorption

We optimized the NW geometry using FDTD numerical modelling in Lumerical in order to maximize the absorption efficiency over a broad wavelength range. For an uncontacted, tapered NW array, the absorption efficiency with optimized parameters can be made near-unity over the entire wavelength range from the UV to the bandgap of the semiconductor (Figure 3-5). This optimization was performed using periodic boundary conditions for an array of InP NWs. As shown in Figure 3-5, a tapered NW array exhibits a near-unity, flat absorption curve, outperforming both a planar InP film of the same nominal thickness and optimized cylindrical NW array. The cylindrical NW array exhibits a peak in the absorption curve due to limited resonant guided modes, which is not desirable for a broadband detector.

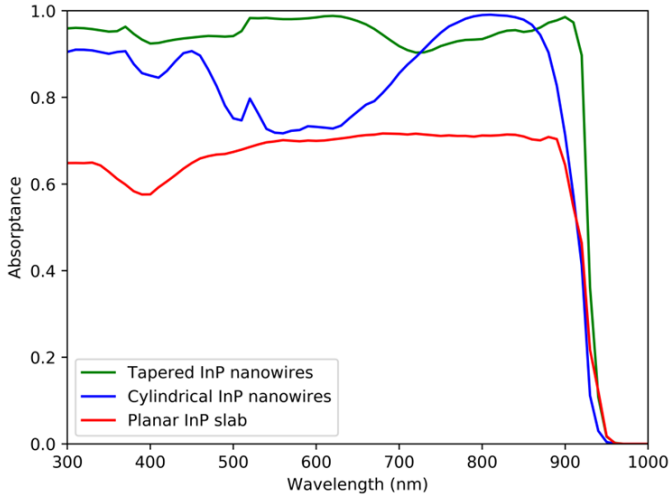

Figure 3-5: Comparison of nanowire (NW) detector geometries to planar slab. Comparison of finite-difference time-domain numerically modelled absorptance of a planar InP slab, optimized cylindrical NW array with radius 90 nm and 510 nm periodicity, and tapered NW array modelled after the physical device in our work, with top radius 75 nm, bottom radius 175 nm, and periodicity of 513 nm. The thickness of the planar slab and NW length were both 1.8 μm in this comparison. The NW arrays are free-floating, ensuring that only absorption within the NWs was considered.

In order to determine the optimized parameters for the tapered NW array, the top NW radius and periodicity (pitch) were varied and absorptance modelled under an illumination of 800 nm. The results are given in Figure 3-6a for an uncontacted array and in Figure 3-6b for the ITO contacted array planarized with BCB. The maximum absorption obtained is ~99.8% for the uncontacted array and

~95% for the contacted array. Through this optimization process the ideal tapered NW dimensions were found at 475 nm periodicity and 81 nm top radii. These optimized NW dimensions are similar to the experimentally investigated ones (513 nm periodicity, 75 nm top radius). The small difference in dimensions shows minimal effect in the modelled absorption efficiency (< 1%). The modelled structures also included a 500 nm substrate to better resemble the experimental device, and a NW height of 1.8 μm. This NW height was selected as it provided a suitable (near max) volume for absorption while still providing good speed and multiplication gain. A 4.78° full tapering angle was used as it provided the necessary modes for broadband absorption while maintaining a sufficiently low effective refractive index for near-unity absorption. Additionally, the tapering focuses the field distribution near the NW tip to enhance the electrical attributes, such as timing resolution. The source wavelength was selected to be 800 nm, as it is near the limit set by the bandgap of InP.

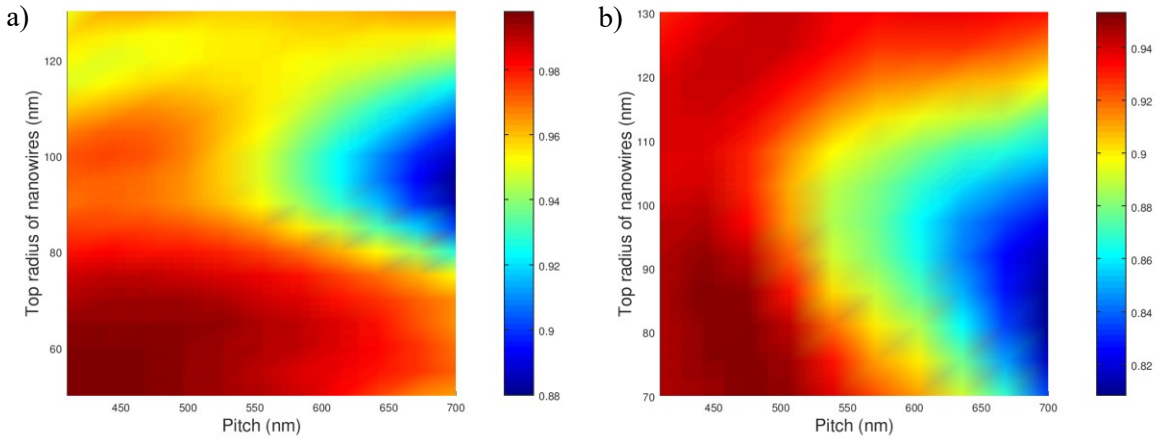

Figure 3-6: Absorptance optimization of the tapered nanowire (NW) geometry. a) Absorptance optimization plot obtained from sweeping critical device parameters of an uncontacted tapered NW array at an incident wavelength of 800 nm. The critical device parameters swept included the NW periodicity (pitch) and radius, while keeping the NW tapering constant at 6 degrees. The maximum absorptance obtained approaches unity (99.8%) as indicated by the absorptance colour bar and was realized for a 410 nm periodicity and 50 nm top radius. **b)** Absorptance optimization plot for an indium tin oxide (ITO) contacted tapered NW array with an incident wavelength of 800 nm, including the benzocyclobutene (BCB) layer around the NWs. A maximum absorptance near 95% was realized at a periodicity of 475 nm and top radius of 81 nm after including these BCB and ITO layers.

Selecting this wavelength meant the resulting optimized structure can provide a resonant mode for all wavelengths up to the bandgap, thereby enhancing the broadband absorption capabilities of the NW array.

As shown in Figure 3-7, simply changing the NW material from InP to InGaAs extends the range of high efficiency absorption from the NIR to IR. Additional details of the FDTD numerical modelling are included in the supplementary information of the published article of this chapter.

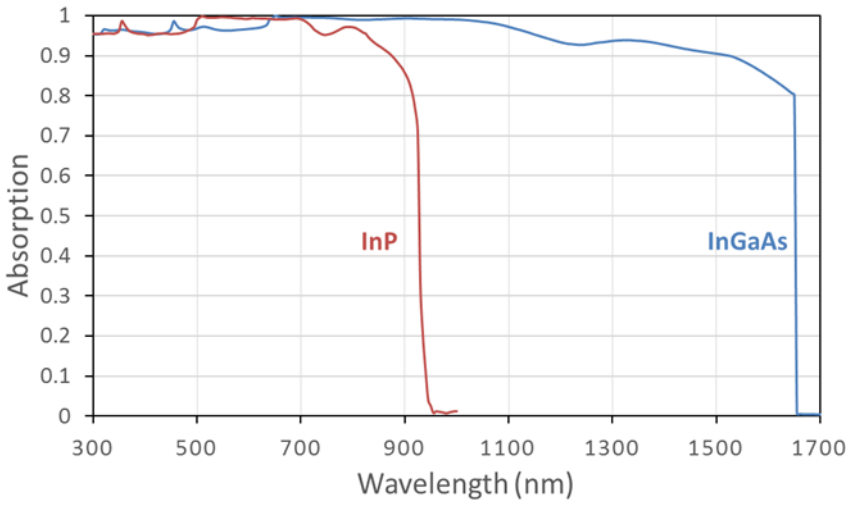

Figure 3-7: Broadband near-unity absorption. Modelled absorption spectra of optimized, uncontacted InP and InGaAs tapered nanowire (NW) arrays illustrating the extension of near-unity absorption deeper into the infrared regime. The InP NWs had a 100 nm top radius, 175 nm bottom radius, 1.8 μm height, and 500 nm periodicity. The InGaAs NWs had a 115 nm top radius, 300 nm bottom radius, 1.6 μm height, and 640 nm periodicity. Both structures also include a 500 nm substrate of their own respective materials (InP and InGaAs) to model experimental devices.

3.3.3 Gain Versus Temporal Response for Nanowire-Based Devices

Here we highlight that previous work on semiconductor NWs, as summarized in Figure 3-8, had either high gain combined with low speed or high speed combined with low gain, but not both. The lack of realizing both simultaneously make previous work on NWs not suitable for single-photon detection. In contrast, our device exhibits both high gain and high speed simultaneously for the first time. Moreover, the timing jitter that we demonstrate rivals state-of-the-art superconducting NW detectors[8,9] without the need for cryogenic cooling. Finally, we conclude that the high efficiency broadband absorption

combined with the high speed and high gain that we demonstrate has never been realized. These combined attributes make this a promising technology for advancement in single-photon detection applications.

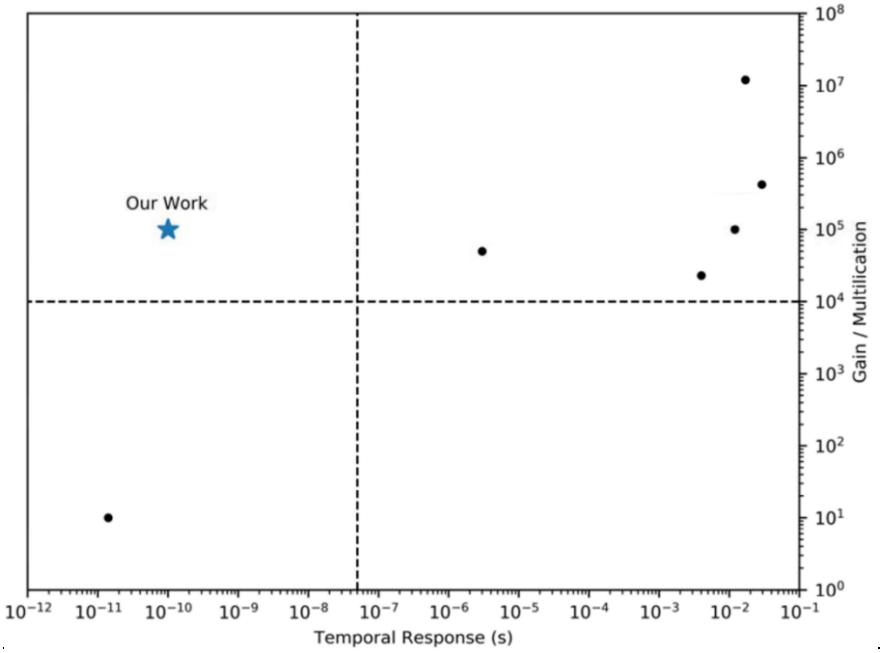

Figure 3-8: Comparison of gain and speed for semiconducting nanowire-based technologies. The gain and speed for our detector (star) is compared against other semiconducting nanowire-based technologies (dots). The vertical dashed line indicates a temporal response of 50 ns while the horizontal dashed line indicates a gain of 10^4. To be suitable for single-photon detection applications the device needs to operate in the upper left quadrant. Our work satisfies both requirements, indicating promise for single-photon detection applications. In addition to these device parameters, we have demonstrated high efficiency, broadband absorption, the combination of which has no competing single-photon technology (including commercially) to date. These attributes were simultaneously achieved with an excellent timing jitter rivalling state-of-the-art superconducting nanowire detectors without the need of cryogenic cooling. Figure 3-8 adapted from the published article supplementary of Chapter 3.

3.3.4 Comparison of State-of-the-Art Single-Photon Technologies

The comparison in Table 3-1 of state-of-the-art single-photon technologies exemplifies the unprecedented performance of our device, having a peak efficiency and timing jitter comparable to commercial superconducting NW devices, but with a superior bandwidth and room temperature

operation. With the next iteration of InGaAs NW devices that we are developing, the bandwidth is expected to surpass the current generation, exceeding 1200 nm (see Figure 3-7).

Table 3-1: Table comparing state-of-the-art single-photon technologies. Table 3-1 adapted from the published article supplementary of Chapter 3.

Device Type	Performance Metrics			Drawback
	Peak Efficiency	Timing Jitter (ps)	Bandwidth (nm)	
Tapered Nanowire Array (Our Work)*	87% @ 860 nm	< 20	~ 500	None
Superconducting Nanowire	93% @ 1570 nm	< 150	~ 100	Cryogenic requirements and limited bandwidth
Superconducting Nanowire	85% @ 1310 nm	< 20	~ 300	Cryogenic requirements and limited bandwidth
Silicon avalanche photodiodes (APDs)	65% @ 650 nm	350	~ 200	Limited efficiency, timing jitter, and limited bandwidth
InGaAs/InP APDs	24% @ 1300 nm	400	~ 250	Limited efficiency, timing jitter, and limited bandwidth
Quantum-dot-resonant tunnel diode	12% @ 550 nm	1.5×10^5	~ 200	Cryogenic requirements, low efficiency, and limited bandwidth
Quantum dot gated field effect transistor	2% @ 805 nm	N/A	N/A	Cryogenic requirements and low efficiency

*The timing jitter was measured with a power exceeding one photon per pulse, as described in Figure 3-4.

3.4 References

1. Zhang, J., Itzler, M. A., Zbinden, H. & Pan, J.-W. Advances in InGaAs/InP single-photon detector systems for quantum communication. *Light Sci. Appl.* **4**, e286 (2015).
2. Hadfield, R. H. Single-photon detectors for optical quantum information applications. *Nat. Photon.* **3**, 696–705 (2009).
3. Chunnilall, C. J. et al. Metrology of single-photon sources and detectors: a review. *Opt. Eng.* **53**, 81910 (2014).
4. Natarajan, C. M., Tanner, M. G. & Hadfield, R. H. Superconducting nanowire single-photon detectors: physics and applications. *Supercond. Sci. Technol.* **25**, 63001 (2012).
5. Shin, D. et al. Photon-efficient imaging with a single-photon camera. *Nat. Commun.* **7**, 12046 (2016).
6. Marsili, F. et al. Detecting Single Infrared Photons with 93% System Efficiency. *Nat. Photon.* **7**, 210-204 (2013).
7. Altena, R., Perik, P. J., van Veldhuisen, D. J., de Vries, E. G. & Gietema, J. A. Cardiovascular toxicity caused by cancer treatment: strategies for early detection. *Lancet Oncol.* **10**, 391–399 (2009).
8. El-Desouki, M. M., Palubiak, D., Deen, M. J., Fang, Q. & Marinov, O. A novel, high-dynamic-range, high-speed, and high-sensitivity CMOS imager using time-domain single-photon counting and avalanche photodiodes. *IEEE Sens. J.* **11**, 1078–1083 (2011).
9. Tsang, J. C., Kash, J. A. & Vallett, D. P. Picosecond imaging circuit analysis. *IBM J. Res. Dev.* **44**, 583–603 (2000).
10. *Single Quantum Eos. SNSPD Closed-Cycle System* (Single Quantum, 2018); http://singlequantum.com/wp-content/uploads/2018/08/Single-Quantum-Eos.pdf
11. Li, H. W. et al. Quantum dot resonant tunneling diode single photon detector with aluminum oxide aperture defined tunneling area. *Appl. Phys. Lett.* **93**, 153503 (2008).
12. Rowe, M. A. et al. Single-photon detection using a quantum dot optically gated field-effect transistor with high internal quantum efficiency. *Appl. Phys. Lett.* **89**, 253505 (2006).
13. Xia, F., Mueller, T., Lin, Y. M., Valdes-Garcia, A. & Avouris, P. Ultrafast graphene photodetector. *Nat. Nanotechnol.* **4**, 839–843 (2009).
14. Koppens, F. H. L. et al. Photodetectors based on graphene, other two-dimensional materials and hybrid systems. *Nat. Nanotechnol.* **9**, 780–793 (2014)

15. Konstantatos, G. et al. Hybrid graphene quantum dot phototransistors with ultrahigh gain. *Nat. Nanotechnol.* **7**, 363–368 (2012).
16. Vallone, G. et al. Experimental Satellite Quantum Communications. *Phys. Rev. Lett.* **115**, 040502 (2015).
17. Bedington, R. et al. Nanosatellite experiments to enable future space-based QKD missions. *EPJ Quantum Technol.* **3**, 12 (2016).
18. Oi, D. K. L. et al. Nanosatellites for quantum science and technology. *Contemp. Phys.* **58**, 25–52 (2017).
19. Hu, L. & Chen, G. Analysis of optical absorption in silicon nanowire Arrays for photovoltaic applications. *Nano Lett.* **7**, 3249–3252 (2007).
20. Anttu, N. et al. Absorption of light in InP nanowire arrays. *Nano Res.* **7**, 816–823 (2014).
21. Wallentin, J. et al. InP nanowire array solar cells achieving 13.8% efficiency by exceeding the ray optics limit. *Science* **339**, 1057–1060 (2013).
22. Fountaine, K. T., Kendall, C. G. & Atwater, H. A. Near-unity broadband absorption designs for semiconducting nanowire arrays via localized radial mode excitation. *Opt. Express* **22**, A930-A940 (2014).
23. Fountaine, K. T., Cheng, W. H., Bukowsky, C. R. & Atwater, H. A. Near-Unity Unselective Absorption in Sparse InP Nanowire Arrays. *ACS Photon.* **3**, 1826–1832 (2016).
24. Azizur-Rahman, K. M. & LaPierre, R. R. Wavelength-selective absorptance in GaAs, InP and InAs nanowire arrays. *Nanotechnology* **26**, 295202 (2015).
25. Namekata, N., Adachi, S. & Inoue, S. Ultra-low-noise sinusoidally gated avalanche photodiode for high-speed single-photon detection at telecommunication wavelengths. *IEEE Photon. Technol. Lett.* **22**, 529–531 (2010).
26. Liang, Y. et al. Low-Timing-Jitter Single-Photon Detection Using 1-GHz Sinusoidally Gated InGaAs / InP Avalanche Photodiode. *IEEE Photon. Technol. Lett.* **23**, 887–889 (2011).
27. Acerbi, F., Frera, A. Della, Tosi, A. & Zappa, F. Fast active quenching circuit for reducing avalanche charge and afterpulsing in InGaAs/InP single-photon avalanche diode. *IEEE J. Quantum Electron.* **49**, 563–569 (2013).
28. Liu, J. et al. Fast Active-Quenching Circuit for Free-Running InGaAs(P)/InP Single-Photon Avalanche Diodes. *IEEE J. Quantum Electron.* **52**, 4000306 (2016).

29. M. A. Itzler, X. Jiang, B. Nyman, K. S. InP-based Negative Feedback Avalanche Diodes. *Proc. SPIE* **7222**, 72221K (2009).
30. Lunghi, T. et al. Free-running single-photon detection based on a negative feedback InGaAs APD. *J. Mod. Opt.* **59**, 1481-1488 (2012).
31. Sze, S., Simon, M. & Kwok, K. N. *Physics of Semiconductor Devices.* (Wiley, New York, 2006).
32. Zheng, D. et al. When Nanowires Meet Ultrahigh Ferroelectric Field-High-Performance Full-Depleted Nanowire Photodetectors. *Nano Lett.* **16**, 2548–2555 (2016).
33. Bulgarini, G. et al. Avalanche amplification of a single exciton in a semiconductor nanowire. *Nat. Photon.* **6**, 455–458 (2012).
34. Shen, L., Pun, E. Y. B. & Ho, J. C. Recent developments in III–V semiconducting nanowires for high-performance photodetectors. *Mater. Chem. Front.* **1**, 630-645 (2017).
35. Ko, W. S. et al. Ultrahigh Responsivity-Bandwidth Product in a Compact InP Nanopillar Phototransistor Directly Grown on Silicon. *Sci. Rep.* **6**, 33368 (2016).
36. VJ, L. et al. A Perspective on Nanowire Photodetectors: Current Status, Future Challenges, and Opportunities. *IEEE J. Sel. Top. Quantum Electron.* **17**, 1002–1032 (2011).
37. Xu, Q. & Dan, Y. Uncovering the density of nanowire surface trap states hidden in the transient photoconductance. *Nanoscale* **8**, 15934–15938 (2016).
38. Zhang, A., Kim, H., Cheng, J. & Lo, Y.-H. Ultrahigh responsivity visible and infrared detection using silicon nanowire phototransistors. *Nano Lett.* **10**, 2117–2120 (2010).
39. Cui, Y. *High-efficiency Nanowire Solar Cells.* PhD thesis, Eindhoven Univ. Technology (2015).
40. Assefa, S., Xia, F. & Vlasov, Y. A. Reinventing germanium avalanche photodetector for nanophotonic on-chip optical interconnects. *Nature* **464**, 80–84 (2010).
41. Saleh, B. E. A., Hayat, M. M. & Teich, M. C. Effect of Dead Space on the Excess Noise Factor and Time Response of Avalanche Photodiodes. *IEEE Trans. Electron Devices* **37**, 1976–1984 (1990).
42. Saleh, M. A. et al. Impact-ionization and noise characteristics of thin III-V avalanche photodiodes. *IEEE Trans. Electron Devices* **48**, 2722–2731 (2001).
43. Huang, J., Banerjee, K., Ghosh, S. & Hayat, M. M. Dual-Carrier High-Gain Low-Noise Superlattice Avalanche Photodiodes. *IEEE Trans. Electron Devices* **60**, 2296–2301 (2013).

44. Senanayake, P. et al. Thin 3D multiplication regions in plasmonically enhanced nanopillar avalanche detectors. *Nano Lett.* **12**, 6448–6452 (2012).
45. Farrell, A. C. et al. Plasmonic field confinement for separate absorption-multiplication in InGaAs nanopillar avalanche photodiodes. *Sci. Rep.* **5**, 17580 (2015).
46. Logeeswaran, V. J. et al. A 14-ps full width at half maximum high-speed photoconductor fabricated with intersecting InP nanowires on an amorphous surface. *Appl. Phys. A* ***91***, 1–5 (2008).
47. Tosi, A., Calandri, N., Sanzaro, M. & Acerbi, F. Low-noise, low jitter, high detection efficiency InGaAs/InP Single-Photon Avalanche Diode. *IEEE J. Sel. Top. Quantum Electron.* **20**, 1 (2014).
48. Namekata, N., Adachi, S. & Inoue, S. 1.5 GHz single-photon detection at telecommunication wavelengths using sinusoidally gated InGaAs/InP avalanche photodiode. *Opt. Express* **17**, 6275–6282 (2009).
49. Ma, C. L. F., Deen, M. J. & Tarof, L. E. Multiplication in Separate Absorption, Grading, Charge, and Multiplication InP-InGaAs Avalanche Photodiodes. *IEEE J. Quantum Electron.* **31**, 2078–2088 (1995).
50. Brennan, K. Theory of the Doped Quantum Well Superlattice APD: A New Solid-State Photomultiplier. *IEEE J. Quantum Electron.* **22**, 1999–2016 (1986).
51. Yue, A.-W., Wang, R.-F., Xiong, B. & Shi, J. Fabrication of a 10 Gb/s InGaAs/InP Avalanche Photodiode with an AlGaInAs/InP Distributed Bragg Reflector. *Chin. Phys. Lett.* **30**, 038501 (2013).
52. van Dam, D. et al. High-efficiency nanowire solar cells with omnidirectionally enhanced absorption due to self-aligned indium-tin-oxide Mie scatterers. *ACS Nano* **10**, 11414–11419 (2016).

Chapter 4
Semiconductor Nanowire Metamaterial for Broadband Near-Unity Absorption[1]

4.1 Preface

While the tapered NW array metamaterial has demonstrated high performance in a broadband near-unity room temperature operated InP photodetector, its broad applicability relies on the demonstration of its performance in alternate materials for targeting variable spectral regions with a range of bandwidths. While operation in the VIS range is beneficial for a range of applications, the far-reaching implementation of the NW metamaterial requires it to perform further into the IR. Chapter 3 highlighted the importance of extending operation to the IR and demonstrated the potential via numerical modelling. The following chapter includes the published study which demonstrates the extended target enhanced absorption spectrum of the semiconductor NW array deeper into the IR regime. Numerical modelling is used to tailor and study the optical response of the modified tapered (cylindrical) metamaterial, finding an unprecedented broadband (selective) near-unity absorption extended further into the IR through the use of InGaAs as the intrinsic NW metaatom material. The success of the tapered-NW metamaterial numerical analysis was further reinforced through its quantitative agreement with the measured high-performance absorption efficiency of a fabricated and experimentally characterized metamaterial.

[1] This is an Accepted Manuscript of an article published by Nature Publishing Group in Scientific Reports 11 June 2022, available online: https://www.nature.com/articles/s41598-022-13537-y. Burak Tekcan, Brad van Kasteren, Sasan V. Grayli, Daozhi Shen, Man Chun Tam, Dayan Ban, Zbigniew Wasilewski, Adam W. Tsen, and Michael E. Reimer, “Semiconductor nanowire metamaterial for broadband near-unity absorption”

4.2 Manuscript

*†Burak Tekcan[1,2], †Brad van Kasteren[1,2], †Sasan V. Grayli[1,2], Daozhi Shen[1,4,5], Man Chun Tam[2,3], Dayan Ban[2,3], Zbigniew Wasilewski[2,3], Adam W. Tsen[1,3,4,6], Michael E. Reimer[1,2,6]**

[1]Institute for Quantum Computing, University of Waterloo, Ontario, Canada. [2]Department of Electrical & Computer Engineering, University of Waterloo, Ontario, Canada. [3]Waterloo Institute for Nanotechnology, University of Waterloo, Ontario, Canada. [4]Department of Chemistry, University of Waterloo, Ontario, Canada. [5]Centre for Advanced Materials Joining, University of Waterloo, Ontario, Canada, [6]Department of Physics and Astronomy, University of Waterloo, Ontario, Canada.

†These authors contributed equally to this work.

4.2.1 Summary

A portable semiconductor near-unity absorber enables the transformation of a wide range of applications including sensing, health, imaging, and quantum information. However, conventional detectors currently rely on bulk semiconductor absorbers and have well under unity efficiencies. Here, we demonstrate near-unity efficiency with a prospective metamaterial absorber composed of a novel InGaAs tapered nanowire array. Through numerical modelling, the material is tuned in geometry and periodicity for 97% (average) absorptance and fabricated with a measured 93% (average) absorptance over an unprecedented 900 nm to 1500 nm wavelength range at room temperature. Numerical analysis of the metamaterial finds that the mechanism for enhanced absorption of normally incident light is the result of coupling into leaky resonant waveguide and transverse modes and reabsorption of scattered light by adjacent nanowires. The work can find broad applicability through its broadband near-unity absorption in the IR and near room temperature operation and has potential to enable a new generation of quantum detectors.

4.2.2 Introduction

Optical metamaterials are demonstrating interesting qualities and offer promise for the inherent advantages they exhibit over their bulk counterpart including the enhanced absorption gained through the engineered arrangement and the collective response of their metaatoms[1–7]. The properties of propagating photons, such as polarization and refraction, have also been shown to be controlled through interaction with metamaterials for a range of technologies[1–10]. Dielectric and semiconductor metamaterials were used to demonstrate light manipulation with lower losses than previous

technologies[1,2,11–14]. As such, the freedom to control the magnetic and electric field response through inherently dielectric materials enables the realization of highly absorbing or transmissive metamaterials with unique qualities that are highly desired in sensing and imaging applications[3,5,8,9,11,15–19]. Near-unity absorbing semiconductor metamaterials have been previously demonstrated through the spectral overlap of electric- and magnetic-field modes of Mie resonators and NWs. However, the near-unity absorption efficiency achieved was limited to a narrow bandwidth (~tens of nanometers)[9,20,21].

In this work, we overcome this narrow bandwidth limitation in a novel (InGaAs) semiconductor metamaterial composed of an array of tapered NW metaatoms. The NW geometry and array periodicity are engineered to produce a near-unity absorber over an unprecedented wavelength range, from 400 nm to 1650 nm, with an average calculated absorptance of 92% (97% from 900 nm to 1500 nm). The material was fabricated and then characterized at room temperature for IR performance by Fourier-transform infrared (FTIR) spectroscopy. Broadband near-unity absorption (wavelength of 900 nm to 1500 nm) was measured in the metamaterial with an average absorption efficiency of 93%. The bulk InGaAs of similar thickness was also measured to illustrate the enhanced absorptance from the metamaterial. The near-unity absorber achieves high performance demands without a need for cryogenic cooling for broad applicability with prospective impacts reaching quantum technologies in imaging, sensing, communication, and computing to biomedical applications such as dose monitoring for cancer treatment and imaging of the eye to identify potentially blinding diseases.

4.2.3 Mechanisms for Enhanced Absorption in Nanowire Metamaterials

To design a broadband, near-unity absorber, we first investigate the role of periodicity on the absorption profile in cylindrical NWs. Although high absorption in cylindrical NWs has been previously investigated[22–24], the role of periodicity on achieving near-unity absorption has been largely unexplored until now. Figure 4-1a shows a schematic view of a cylindrical NW metamaterial, depicting how LRMs are being excited in the NW array. There are two main avenues for absorption in cylindrical NW metamaterials when it is illuminated from the top. First, light can be directly absorbed in the NW through coupling to leaky hybrid electric and magnetic modes (HE_{11} and EH_{11})[20,22,23]. Second, light can be indirectly absorbed by scattering from one NW to another one through excitation of TE and TM modes, thus, leading to further absorption. In this latter case, the leaky guided modes migrate towards the NW sidewall as they travel downwards. At the interface of the NW sidewall and the surrounding dielectric medium, the leaky modes decouple from the NW and subsequently emit into free space. This

emitted light then interacts with neighbouring NWs within the array by coupling to both TE and TM modes. The strong interaction of the electric field between neighboring NWs for metaatoms with diameter of 200 nm, periodicity of 833 nm and height of 1400 nm is illustrated in Figure 4-1b. The resulting spatial absorption profile from these mechanisms in the NW metaatoms is shown in Figure 4-1c.

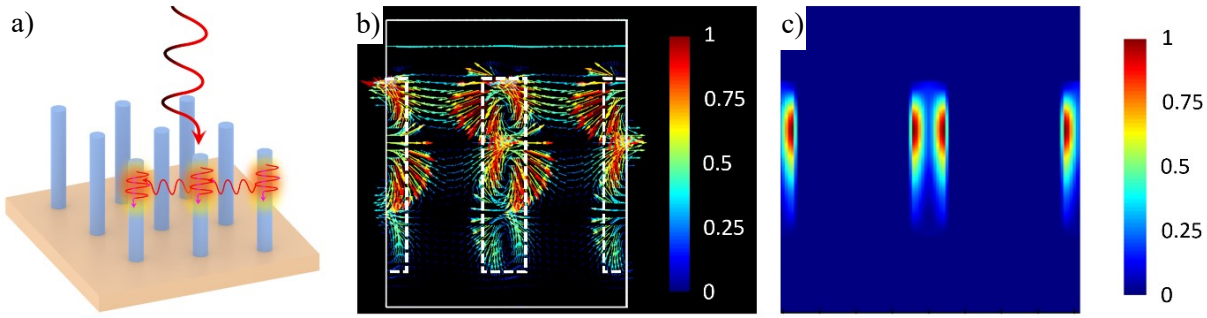

Figure 4-1: Mechanisms for enhanced absorption. a) Schematic view of the collective interaction of a cylindrical nanowire (NW) metamaterial depicting the direct and indirect coupling to leaky guided and transverse modes. The leaky nature of the guided modes in the NWs leads to free-space scattering of the electric field, which is then recoupled into the neighbouring NW metaatoms via excitation of transverse electric and transverse magnetic modes. **b)** Numerically modelled electric field response of a NW array with periodicity of 833 nm, NW diameter of 200 nm and height of 1400 nm. The interaction of the electric field between neighbouring NWs is depicted by the vectors and their color indicates the field strength. **c)** Localized absorption profile (indicated by the color) of the NW metamaterial at λ = 1020 nm with the same dimensions as **b)**. In the **b)** and **c)** color bars, red represents the maximum magnitude (normalized to 1) and blue is the minimum.

The eigenvalue equation, which satisfies Maxwell's equation for cylindrical boundary conditions, describes the angle dependence of the excited modes in the NWs[25]. This eigenvalue equation supports the mechanisms of enhanced absorption in NW metamaterials as described previously and illustrated in Figure 4-1. For all incident angles that are not perpendicular to the NW axis, light will couple into HE and EH leaky guided modes. However, when the incident angle of light is perpendicular, purely TE or TM LRMs are excited, where the latter are the transverse modes that are excited in the neighboring NWs following decoupling of the leaky guided modes.

4.2.4 Narrowband Near-Unity Absorber — Cylindrical Nanowire Metamaterials

We further study the cylindrical NW case by analyzing the numerically modelled absorptance of a single InGaAs metaatom as a function of its radius (Figure 4-2a). For NW radii smaller than 175 nm, the absorption profile is narrowband as the NW supports a single resonant leaky guided mode only. As the cylindrical NW radius increases in this single-mode regime (< 175 nm), the supported resonant leaky modes shift to longer wavelengths. This observation is consistent with what has been previously reported[23]. However, increasing the radius further results in multiple leaky modes to be supported. In this regime of large NW radius, multiple leaky modes overlap, the spectral selectivity vanishes, and the absorption profile broadens as a result. We note that for a larger NW radius (> 660nm), the absorption profile is very similar to the bulk response of the same material. Although the spectral sensitivity in larger NW radii vanishes, the peak absorption efficiency of a single NW still remains far from unity.

In order to reach near-unity absorption efficiency we place the single NW in an array and optimize the periodicity. The role of the array periodicity on the absorption efficiency of a NW metamaterial has not yet been fully explored until now. Our analysis shows that the absorption efficiency of the cylindrical semiconductor NW metamaterial is directly linked to the array periodicity. The results of our analysis are summarized in Figure 4-2b and Figure 4-2c. Figure 4-2b shows the calculated absorptance for varying NW periodicity and incident wavelength, while Figure 4-2c takes 2D slices of this 3D plot from Figure 4-2b. Here, we find the maximum absorptance with the narrowest bandwidth occurs at the NW diameter to periodicity ratio of 0.24. Remarkably, by maintaining this ratio for varying periodicity, near-unity absorption efficiency (> 99%) can be selectively achieved in the wavelength range from approximately 1000 nm to 1400 nm (see Figure 4-2c). Furthermore, minimal roll-off in the absorption efficiency as the incident wavelength approaches the InGaAs bandgap is observed (~96% at 1500 nm and ~80% at 1650 nm).

To better understand the underlying mechanisms contributing to near-unity absorption in the NW metamaterial, we focus our attention on NWs with dimensions: 200 nm diameter and 1400 nm height. A NW height of 1400 nm was selected since this was close to the smallest height where broadband near-unity absorptance was achieved (see Supplementary Note 4 of the published article of this chapter). The calculated absorption efficiency with these NW dimensions as a function of periodicity is presented in Figure 4-2d. Near-unity absorption (> 99%) occurs for a range of periodicities between 676 nm to 885 nm.

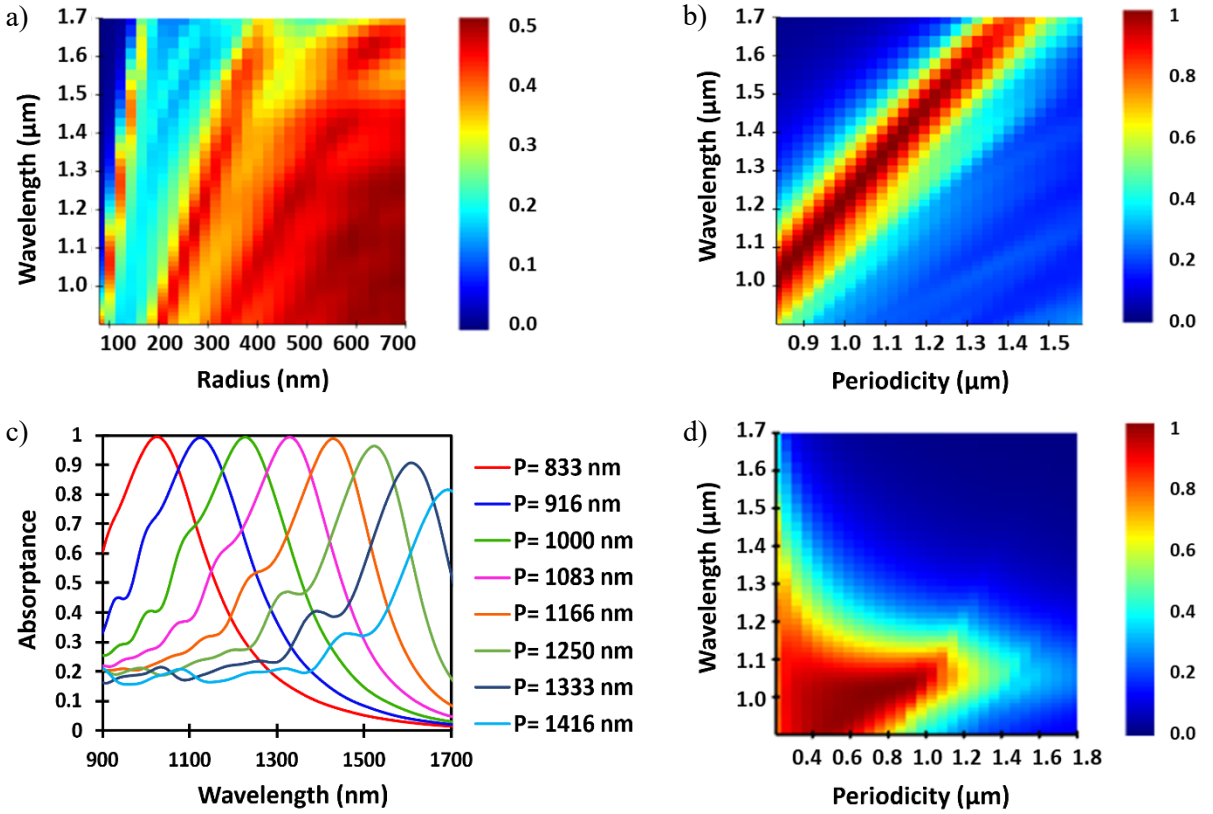

Figure 4-2: Finite-difference time-domain numerically modelled narrowband absorption efficiency from cylindrical InGaAs nanowires (NWs). a) Absorption efficiency (color bar) of a single cylindrical NW as a function of wavelength and radius. **b)** Shifting narrowband near-unity absorption efficiency (color bar) response of the NW metamaterial as a function of periodicity with a fixed diameter to periodicity ratio of 0.24. **c)** Two-dimensional slices of the absorption efficiency from **b)** showing tunability of the resonant response for near-unity absorption. **d)** Absorption efficiency (color bar) of a constant 200 nm diameter cylindrical NW metamaterial as a function of array periodicity. The NW height used in the numerical model for **a)** to **d)** is 1400 nm.

In this range of NW periodicities, the process of indirect absorption attributed to the decoupling of leaky resonant guided modes and excitation of TE or TM modes in neighbouring NWs is enhanced. This enhancement maximizes the overall absorption efficiency and highlights its dependence on the NW periodicity. Interestingly, this process of near-unity absorption only occurs when the NW spacing is optimized. When deviating from this optimized spacing the spectral sensitivity vanishes and the absorption efficiency drops. A smaller NW periodicity leads to a broadened absorption spectrum with

a lower maximum. In contrast, the absorption spectrum remains narrow for a larger NW periodicity, but the maximum gradually drops as the interaction between neighbouring NWs diminishes.

4.2.5 Broadband Near-Unity Absorber — Tapered Nanowire Metamaterial

Cylindrical NWs in metamaterials produce near-unity absorption capabilities with a narrow bandwidth. While this selectivity benefits some applications, others require a broadened sensitivity. To achieve a broadband response tapering was introduced into the numerically modelled NW unit structures to provide a continuum of diameters (and leaky guided modes) that enables coupling to a broad range of wavelengths[22,26–29]. InGaAs was the intrinsic material of the NWs, offering an inherent bandgap for IR absorption. A strategy employing numerical methods similar to Section 3.3.2 was performed to define the InGaAs metamaterial geometry. The method employed here had several differences; however, such as first modelling the single NW resonator before incorporation into an array.

First, the NW parameters were set to that of the single leaky guided mode cylindrical structure with peak absorption efficiency at the InGaAs absorption limit of $\lambda \sim 1650$ nm (radius = 170 nm, height = 1400 nm). Next, the bottom radius was modelled over a range from 170 nm to 450 nm, producing the surface absorption efficiency results in Figure 4-3a. Cross sections at four bottom radii (170 nm, 270 nm, 385 nm, and 441 nm) were plotted in 3b with corresponding particle geometry diagrams at the bottom radius limits. The optimal metaatom (bottom radius = 440 nm) was then repeated in a 2D square lattice where the periodicity was numerically modelled over a range 900 nm – 1800 nm (Figure 4-3c). Reduced absorption was found when the periodicity increased beyond 900 nm from the same weakening recollection effects found from neighbouring cylindrical NWs, demonstrating the inhibiting effect of a detuned periodicity on the absorption capabilities of the metamaterial. The ideal value for enhanced broadband (λ = 400 nm – 1650 nm) absorption efficiency in the metamaterial was found at a periodicity = 900 nm (Figure 4-3d). The calculated average absorption efficiency of this wavelength range was 92%. The prominent peak in Figure 4-3d at λ = 909 nm is attributed to a resonant lattice mode from the 900 nm periodic array. Other peaks in this broadband absorption efficiency are attributed to operating in the multimode (MM) regime and being suspended in air, as they are suppressed when modelled in the presence of the substrate (Figure 4-4c). Additional details on the NW metamaterial optimization process are presented in Supplementary 1-5 of the published article of this chapter.

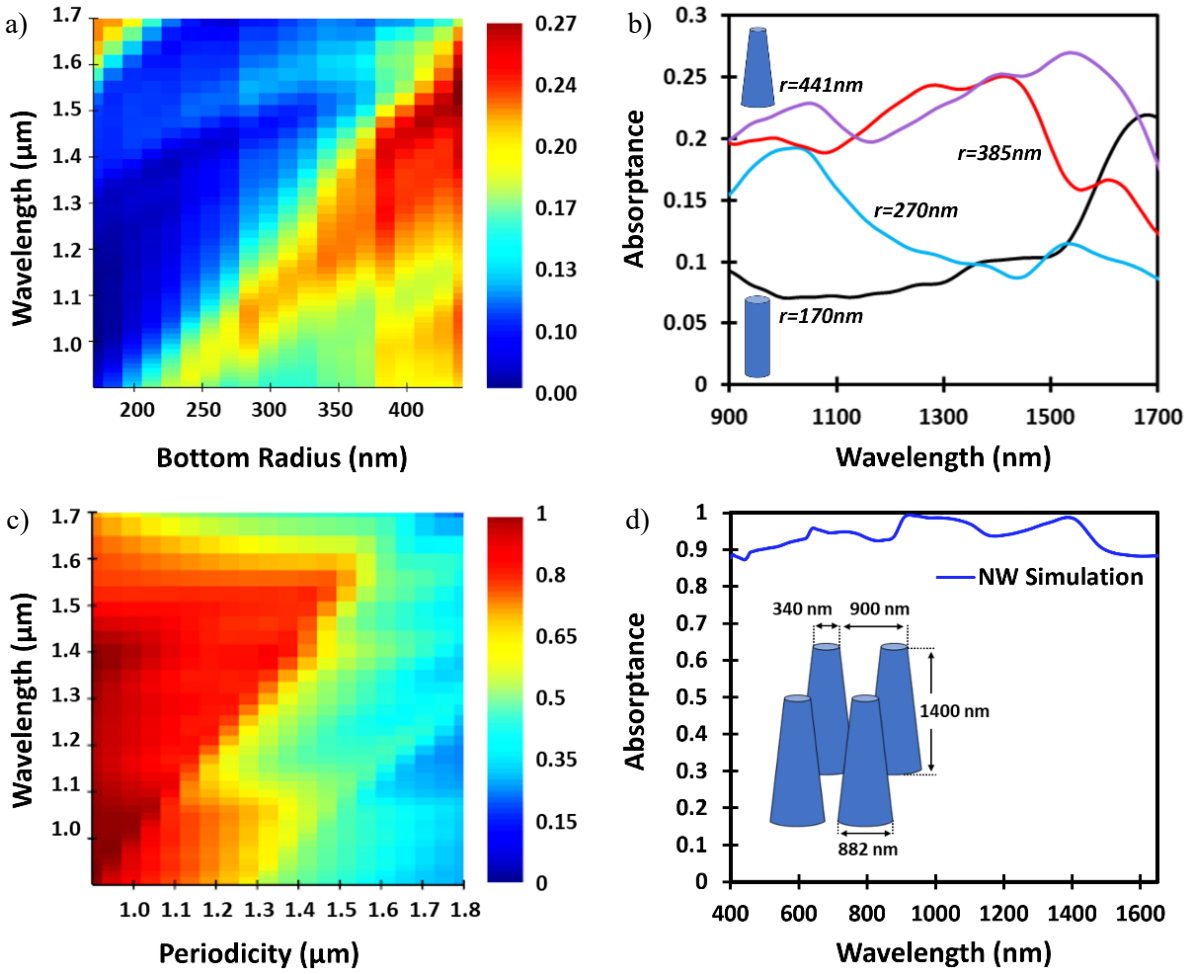

Figure 4-3: Finite-difference time-domain numerically modelled broadband absorption efficiency from tapered InGaAs nanowires (NWs). a) Numerically modelled single tapered NW absorption efficiency (colour bar) spectra as a function of bottom NW radius (top radius of 170 nm and height of 1400 nm). **b)** Absorption efficiency as a function of wavelength cross sections from **a)** at NW bottom radii of 170 nm, 270 nm, 385 nm, and 441 nm with NW geometry diagram insets for 170 nm and 441 nm bottom radius. **c)** Metamaterial absorption efficiency (colour bar) spectra as a function of array periodicity with metaatoms of height 1400 nm, top radius 170 nm, and bottom radius 441 nm. **d)** Near-unity broadband absorption efficiency (colour bar) spectra cross section from **c)** at the periodicity of 900 nm. The inset includes a diagram with dimensions of the metamaterial with an array periodicity of 900 nm and a metaatom tapered NW geometry of 441 nm bottom radius, 170 nm top radius, and a height of 1400 nm.

4.2.6 Results

The fabrication and measuring of the InGaAs NW metamaterial absorber was work of primary focus by fellow Dr. Reimer group member, Burak Tekcan.

The modelled metamaterial was fabricated in a 100 μm x 100 μm InGaAs tapered NW array area with the tuned dimensions found through numerical modelling through top-down microfabrication on a 2250 nm thick InGaAs film. Details of the fabrication process are included in Supplementary 5 and 6 of the published article of this chapter. The fabricated NW metamaterial (modelled metamaterial) had approximately a top radius of 175 nm (170 nm), bottom radius of 440 nm (441 nm), height of 1300 nm (1400 nm), and a periodicity of 900 nm (900 nm). An optical and SEM image of the metamaterial were taken and presented in Figure 4-4a and its inset, respectively. The high absorptance of the metamaterial is easily observed by the contrast between the film (InGaAs film) and the dark area of the tapered NW array, and the SEM image shows the high quality metaatom structures. FTIR spectroscopy was performed to measure the absorption efficiency through reflectance, transmittance, and absorptance characterization over the wavelength range of 900 nm to 1650 nm. Details of the characterization processes and a demonstration of the metamaterial's reproducibility are included in the published article and Supplementary 7 – 10 of the published article of this chapter. The numerical and measured reflectance (absorptance) are included in Figure 4-4b (Figure 4-4c), showing their quantitative agreement and the measured broadband near-unity absorptance of 93% average over the wavelength range of 900 nm to 1500 nm. Note that the numerical modelling for Figure 4-4b and Figure 4-4c was updated with the fabricated metamaterial dimensions and included a substrate (details in Supplementary 3 and 4 of the published article of this chapter). The measured reflectance remained below 4% (average of 3%) throughout the characterized wavelength range. The absorptance spectra of the modelled and measured InGaAs films on an InP substrate are included in Figure 4-4d for the comparison of the planar absorber at relevant thicknesses to the metamaterial absorptance spectra and illustration of the enhanced absorption qualities gained from the tapered NW array. The film was numerically modelled at thicknesses of 1000 nm, 1300 nm, and 2250 nm. The measured film was 2250 nm thick and finds quantitative agreement with its modelled counterpart.

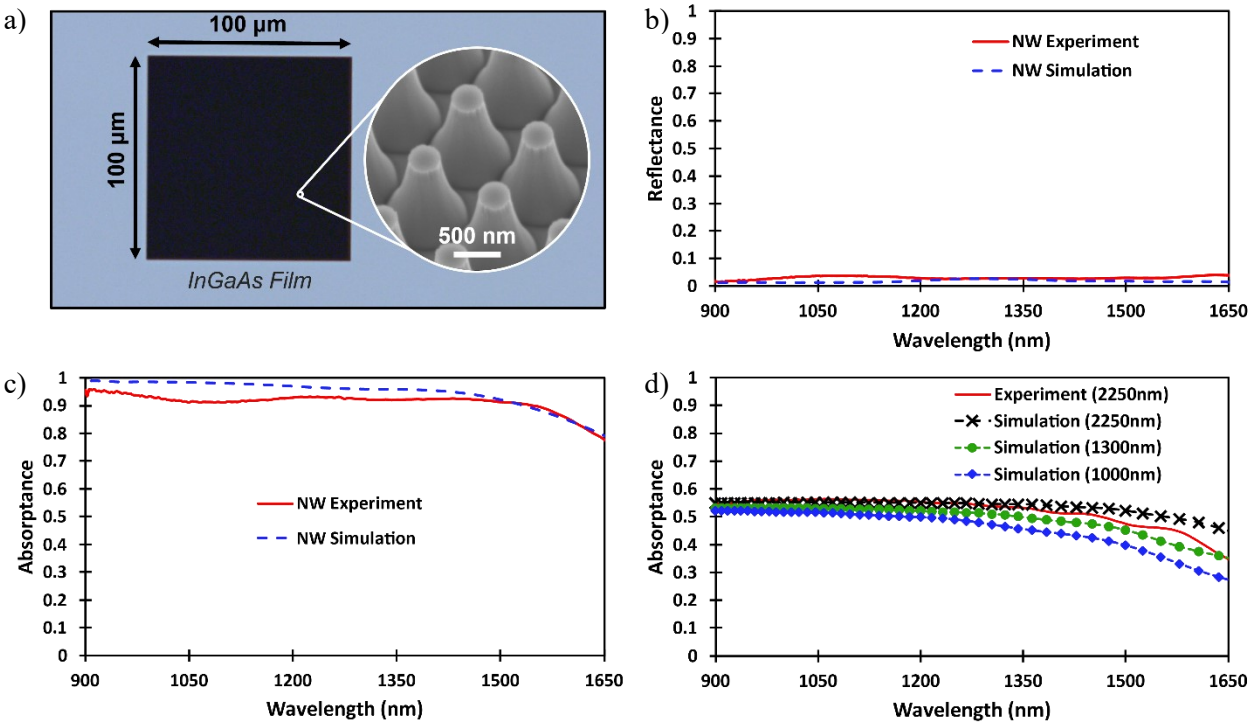

Figure 4-4: Near-unity nanowire (NW) metamaterial absorption. a) Optical image of the fabricated InGaAs tapered NW metamaterial (black square) on an InGaAs film (blue-grey) with a scanning electron micrograph inset of the tapered InGaAs NWs. **b)** Experimentally measured (modelled) NW metamaterial reflectance spectra with metaatom dimensions of 175 nm (170 nm) top radius, 440 nm (441 nm) bottom radius, and 1300 nm (1400 nm) height, and metamaterial array periodicity of 900 nm (900 nm). **c)** Experimentally measured (modelled) near-unity broadband metamaterial absorptance spectra with dimensions matching that of **b)** and an average absorptance of 93% (97%) from 900 nm to 1500 nm. **d)** Experimentally measured (modelled) absorptance spectra of the planar InGaAs film on an InP substrate with a film thickness of 2250 nm (1000 nm, 1300 nm, and 2250 nm).

4.2.7 Conclusion

The design and mechanisms for NW metamaterials with enhanced absorption qualities tuned for the IR were studied. The two identified mechanisms contributing to near-unity absorption in the NW metamaterials included the free-space coupling of normally incident light into the NW leaky guided modes and reabsorption through the transverse modes by neighbouring NWs. Furthermore, the high impact of periodicity on the enhanced absorption properties of the metamaterial was shown, along with an optimization process for achieving narrow and broadband near-unity absorption qualities in the

cylindrical and tapered NW metamaterials, respectively. Additionally, the fabricated near-unity broadband absorber found by numerical modelling and analysis was measured over a wavelength range of 900 nm to 1500 nm to experimentally demonstrate the broadband enhanced absorption (93% average efficiency) capabilities of the NW metamaterial. Though demonstrated here with InGaAs, the enhanced NW metamaterial absorber can also be prepared and tailored for other spectral regions of interest by applying appropriately selected semiconductor materials. Incorporating the broadband near-unity absorption efficiency metamaterial absorber into photodetection technologies will facilitate the delivery of next generation advancements for a further reaching impact on applications from biomedical to quantum information.

4.2.8 References

1. Jahani, S. & Jacob, Z. All-dielectric metamaterials. *Nature Nanotech* **11**, 23–36 (2016).
2. Kamali, S. M., Arbabi, E., Arbabi, A. & Faraon, A. A review of dielectric optical metasurfaces for wavefront control. *Nanophotonics* **7**, 1041–1068 (2018).
3. Staude, I. *et al.* Tailoring Directional Scattering through Magnetic and Electric Resonances in Subwavelength Silicon Nanodisks. *ACS Nano* **7**, 7824–7832 (2013).
4. Yao, Y. *et al.* Recent progresses on metamaterials for optical absorption and sensing: a review. *J. Phys. D: Appl. Phys.* **54**, 113002 (2021).
5. Jung, J., Park, H., Park, J., Chang, T. & Shin, J. Broadband metamaterials and metasurfaces: a review from the perspectives of materials and devices. *Nanophotonics* **9**, 3165–3196 (2020).
6. Paul, D. D. Optical Metamaterials: Fundamentals and Applications. *Physics Today* **63**, 57–58 (2010).
7. Soukoulis, C. M. & Wegener, M. Past achievements and future challenges in the development of three-dimensional photonic metamaterials. *Nature Photon* **5**, 523–530 (2011).
8. Ming, X., Liu, X., Sun, L. & Padilla, W. J. Degenerate critical coupling in all-dielectric metasurface absorbers. *Opt. Express, OE* **25**, 24658–24669 (2017).
9. Mitrofanov, O. *et al.* Perfectly absorbing dielectric metasurfaces for photodetection. *APL Photonics* **5**, 101304 (2020).
10. Yu, N. *et al.* Light Propagation with Phase Discontinuities: Generalized Laws of Reflection and Refraction. *Science* **334**, 333–337 (2011).

11. Decker, M. *et al.* High-Efficiency Dielectric Huygens' Surfaces. *Advanced Optical Materials* **3**, 813–820 (2015).
12. Groep, J. van de & Polman, A. Designing dielectric resonators on substrates: Combining magnetic and electric resonances. *Opt. Express, OE* **21**, 26285–26302 (2013).
13. Zhao, Q., Zhou, J., Zhang, F. & Lippens, D. Mie resonance-based dielectric metamaterials. *Materials Today* **12**, 60–69 (2009).
14. Chong, K. E. *et al.* Efficient Polarization-Insensitive Complex Wavefront Control Using Huygens' Metasurfaces Based on Dielectric Resonant Meta-atoms. *ACS Photonics* **3**, 514–519 (2016).
15. Fan, K., Suen, J. Y., Liu, X. & Padilla, W. J. All-dielectric metasurface absorbers for uncooled terahertz imaging. *Optica, OPTICA* **4**, 601–604 (2017).
16. He, Y. *et al.* Infrared perfect absorber based on nanowire metamaterial cavities. *Opt. Lett., OL* **38**, 1179–1181 (2013).
17. Cole, M. A., Powell, D. A. & Shadrivov, I. V. Strong terahertz absorption in all-dielectric Huygens' metasurfaces. *Nanotechnology* **27**, 424003 (2016).
18. Liu, X., Fan, K., Shadrivov, I. V. & Padilla, W. J. Experimental realization of a terahertz all-dielectric metasurface absorber. *Opt. Express, OE* **25**, 191–201 (2017).
19. Wang, Z. Y. *et al.* Broadband optical absorption by tunable Mie resonances in silicon nanocone arrays. *Sci Rep* **5**, 7810 (2015).
20. Cao, L. *et al.* Engineering light absorption in semiconductor nanowire devices. *Nature Mater* **8**, 643–647 (2009).
21. Yang, C.-Y. *et al.* Nonradiating Silicon Nanoantenna Metasurfaces as Narrowband Absorbers. *ACS Photonics* **5**, 2596–2601 (2018).
22. Fountaine, K. T., Kendall, C. G. & Atwater, H. A. Near-unity broadband absorption designs for semiconducting nanowire arrays via localized radial mode excitation. *Opt. Express, OE* **22**, A930–A940 (2014).
23. Wang, B. & Leu, P. W. Tunable and selective resonant absorption in vertical nanowires. *Opt. Lett., OL* **37**, 3756–3758 (2012).
24. Abujetas, D. R., Paniagua-Domínguez, R. & Sánchez-Gil, J. A. Unraveling the Janus Role of Mie Resonances and Leaky/Guided Modes in Semiconductor Nanowire Absorption for Enhanced Light Harvesting. *ACS Photonics* **2**, 921–929 (2015).
25. Snyder, A. W. *Optical Waveguide Theory*. (Springer US, 1983). doi:10.1007/978-1-4613-2813-1.

26. Gibson, S. J. *et al.* Tapered InP nanowire arrays for efficient broadband high-speed single-photon detection. *Nature Nanotechnology* **14**, 473–479 (2019).
27. Wang, B. & Leu, P. W. Enhanced absorption in silicon nanocone arrays for photovoltaics. *Nanotechnology* **23**, 194003 (2012).
28. Fountaine, K. T., Cheng, W.-H., Bukowsky, C. R. & Atwater, H. A. Near-Unity Unselective Absorption in Sparse InP Nanowire Arrays. *ACS Photonics* **3**, 1826–1832 (2016).
29. Diedenhofen, S. L., Janssen, O. T. A., Grzela, G., Bakkers, E. P. A. M. & Gómez Rivas, J. Strong Geometrical Dependence of the Absorption of Light in Arrays of Semiconductor Nanowires. *ACS Nano* **5**, 2316–2323 (2011).

Chapter 5
Designing Perfect Absorbers Using Semiconductor Metasurfaces on High-Index Substrate for Photodetection

5.1 Preface

The InGaAs tapered NW p-n junction array was able to demonstrate its enhanced absorption capabilities further into the IR, but non-idealities were encountered in its SPAD operation which required further investigation. While device and operating level changes were being studied, alternate platforms for the enhanced absorber were explored. The following section details a prospective study for publication on an alternate absorber design, a modified cylindrical particle metasurface. The research employed numerical methods to reveal the enhanced optical and electrical performance of an SAGCM cylindrical metasurface on a substrate for a near-unity absorber and photodetector application. A method to design the tunable near-unity absorber on a substrate was developed through numerical analysis of the particle and array resonances and the modelled optoelectronic response found an enhanced performance over its planar counterpart.

5.2 Manuscript

Brad van Kasteren[1,2], Sasan V. Grayli[1,2], William Losin[1,2], and Michael E. Reimer[1,2,3]

[1]Institute for Quantum Computing, University of Waterloo, Ontario, Canada. [2]Department of Electrical & Computer Engineering, University of Waterloo, Ontario, Canada. [3]Department of Physics and Astronomy, University of Waterloo, Ontario, Canada.

5.2.1 Introduction

Optical metasurfaces, comprised of dielectric resonators, have gained attention in recent years due to the ability to manipulate both magnetic and electric field of the incident through coupling to the modes in the metasurface[1–5]. Controlling the magnetic and the electric field of the photons has enabled exciting opportunities for designing a new class of nanophotonic devices that can impact different areas of science and technologies ranging from biomedical imaging to quantum communications[6–11]. The remarkable functionalities of all-dielectric metasurfaces in controlling of the light-matter interaction at nanoscale have led to creation of flat optics, near-zero index waveguides and directional scatterers[2–4,12]. Enhanced absorption has also been demonstrated with all semiconductor metasurfaces, which is a

desired attribute for improving the efficiency of solar cells as well as realizing low-light sensitive detectors[8,13–19]. A known shortcoming of current commercial APDs is DE in the wavelength band from 900 nm – 1000 nm, known as the valley of death, a region of particular importance for optical coherence tomography which can benefit from the improved selectivity gained from the incorporation of metasurfaces absorbers[20–24]. It has already been demonstrated that the implementation of a metasurface comprised of an array of NWs improves on the detector timing resolution over their bulk counterparts, a critical performance attribute for time of flight measurement that impacts a broad range of technologies[17,25].

One of the promising meta-optic approaches to realize a perfect absorber is by utilizing the Huygen's metasurfaces that are constructed from semiconductor resonators[2,3,8,13,19,26–28]. The disk-shaped resonators are among the commonly implemented geometrical designs that are used in the dielectric metasurface absorbers[13,14,19]. The interaction of light with the disk-shaped resonators will excite the EH and HE modes. By controlling the dimension of the disk-shaped resonators, these hybrid modes can support the out-of-plane electric- and magnetic- dipoles resonantly. The magnetic and electric dipole resonances of such resonators can further be overlapped at the same wavelength by modifying the diameter and the height of the disks[13,14,19,29]. The overlapping of the resonant excitation of the electric- and magnetic-dipoles in the semiconductor resonators will lead to generation of Kerker condition (Kerker interference),[30,31] in which the backscattering is suppressed. By embedding these semiconductor metasurface absorbers in low-index materials (e.g., silicon dioxide), the light that is coupled into the resonators will remain confined inside the structures, leading to a localized generation of charge-carriers for optoelectronic operation. In addition to the dimension of the resonators that can control the magnetic and electric dipole resonances, there are dipole modes that can be accessed through the interaction of two adjacent structures. When two resonators are close enough, the magnetic and electric dipoles can be excited with incident light. In a periodic lattice system, these dipoles can be coherently excited and are referred to as lattice resonances. The lattice resonances can often be observed at wavelengths close to the Rayleigh anomaly (RA) which is due to the in-plane diffraction of the incident light in the periodic surfaces. The lattice resonances can be shifted by changing the periodicity along different axes, thereby providing an opportunity for tuning the magnetic and electric dipole lattice resonances to the desired wavelengths. The lattice dipole resonances are particularly interesting when the magnetic and electric dipole resonances in the resonators cannot be overlapped. This interest is because the Kerker interference has been also demonstrated through the overlap of the magnetic and

electric lattice resonances created with semiconductor metasurfaces[19,32,33]. Up to now, the experimental and theoretical demonstration of the Huygen's metasurface absorbers have been discussed through the design of resonators that are embedded in low-index materials. In order to leverage the potential efficiency gains from metasurfaces in detector-based applications, strategies for charge collection also need to be implemented. Two strategies to achieve this include the lateral connection of the resonators for the collection of charges through in-plane electrodes or the vertical collection of charges through the substrate and a transparent electrode[8,17,19]. Here, we provide theoretical evidence for a near-unity metasurface absorber that is fabricated on a high-index substrate. The design is compatible with fabrication processes that are relied on for high quality semiconductors, grown through techniques such as molecular beam epitaxy (MBE) or MOCVD. This perfect absorber design takes advantage of lattice resonances as well as magnetic and electric multipolar resonances to achieve absorption at near-unity efficiency.

5.2.2 Narrowband Perfect Absorber

5.2.2.1 Low-Index Environment

We begin by demonstrating that the enhanced absorption can be achieved when magnetic and electric lattice resonances are coupled with the magnetic and electric dipole resonances, supported by each resonator, for the same wavelength. First, we design a periodic array of nano-disk resonators (suspended in air) for the absorption peak of λ = 1000 nm. We consider InGaAs, which is a III-V semiconductor with a small bandgap. We obtained the initial geometry of the nano-disk by using Eqs. (5-1) and (5-2), which can predict the radius (r) and the height (h) of the resonators:[13]

$$r \approx 0.61 \frac{\lambda_0}{\sqrt{(n^2-1)}} \tag{5-1}$$

$$h \approx \frac{\lambda_0}{2n} \tag{5-2}$$

Where λ_0 and n are the resonant wavelength and material refractive index, respectively. We use the values obtained from Eqs. (5-1) and (5-2) as the starting point and further modify the radius and the height of the nano-disk to realize a metasurface absorber for the target wavelength of 1000 nm. We use FDTD to model and design the near-unity metasurface absorber. In our modelling, we used a broadband plane-wave source that injects light from above the metasurface at 0° incident angle with the polarization of the injected beam along the x-direction. Figure 5-1a and Figure 5-1b illustrate the

absorptance of the metasurface with a periodicity of 650 nm, along both *x* and *y* directions, as a function of changes in radius and height, respectively. The white dashed lines are indicating the position of electric dipole resonances (EDRs) and MDRs. The radius (Figure 5-1a) and the height (Figure 5-1b), at which both magnetic and electric dipole resonances are in perfect overlap are highlighted with a dashed circle. In Figure 5-1a and Figure 5-1b the overlap between the magnetic and electric dipole resonances occurs when the radius and the height of the resonator are 194 nm and 160 nm, respectively. The presence of the MQ resonances can also be observed at shorter wavelengths and larger radii and heights. Next, we investigate the impact of the lattice resonances on the absorption efficiency of the designed metasurface. In Figure 5-1c, the dependence of absorptance on the separation of the resonators (periodicity) is shown. When using the optimized radius and height from Figure 5-1a and Figure 5-1b, the highest absorption efficiency is observed at 765 nm periodicity. For simplicity, we incorporate a square lattice i.e., a 2D array with matching *x* and *y* periodicity. While a square lattice works here, a modified target wavelength can be achieved by tuning the offset periodicities along the *x*- and *y*-direction to overlap the magnetic and electric dipole lattice resonances to the same wavelength. More complex periodic systems can be used to obtain enhanced absorption at the same target wavelength, but this process is outside of the scope of this thesis. Since we found that the magnetic and electric dipole resonances can be overlapped in nano-disk resonators, as shown in Figure 5-1a and Figure 5-1b, the periodicities can be varied symmetrically to match with the same resonant wavelength supported by the nano-disks. At 765 nm periodicity, the magnetic and electric dipole lattice resonances are both tuned to the same magnetic and electric dipole resonant wavelength that is supported by the nano-disk resonator. The coupling of the lattice resonances with the resonator's dipole resonances has produced enhanced absorption in the designed metasurface. We show in Figure 5-1d that the lattice resonances can be the dominant mode in the metasurface absorbers, as the peak absorption shifts with changes in the periodicity, which highlights the importance of the lattice resonant modes in designing a perfect metasurface absorber. The insets in Figure 5-1d depict the top-view of the MLR and the ELR field profiles for resonators with 194 nm radius, 160 nm height at 765 nm periodicity, which has the highest absorption efficiency for the $\lambda \approx 1000$ nm. We found that the enhanced absorption that results from the coupling of the resonator's dipole resonances with the lattice resonances can be preserved for selected wavelengths by maintaining the ratio of 0.51 between the resonator's diameter and the periodicity ($d/p \approx 0.51$) and a ratio of 0.41 between the height and diameter ($h/d \approx 0.41$). It can be observed in the Figure 5-1d insets that the MLR occurs along the direction of the polarization of the incident beam, as

opposed to the ELRs that are generated orthogonal to the incident light polarization. Based on this generalization, the MLRs can be controlled by modifying the separation of the resonators along the polarization of the incident light (here along *x*-axis) and the ELRs can be shifted by changing the periodicity of the metasurface orthogonal to the polarization of the injected beam. Furthermore, we can see in Figure 5-1e and Figure 5-1f that the reflectance and transmittance have been minimized for the target wavelength, indicating that the majority of the light at $\lambda \approx 1000$ nm has been confined in the metasurface.

5.2.2.2 Effect of a High-Index Substrate

Realizing a narrowband near-unity metasurface absorber, based on the described approach, requires the resonators to be embedded in a low-index medium. From the fabrication point of view, such metasurfaces can be constructed by using the available physical vapor deposition techniques for depositing the semiconductors as has been shown by various groups[8,19,28]. Therefore, the high quality III-V semiconductor films (e.g., InGaAs), that are grown through techniques such as MBE and MOCVD, cannot be easily used in the realization of these metasurface absorbers. Mainly this is because these semiconductors often require high-index substrate templates, indium-phosphide (InP) for example, for growth. In Figure 5-2, we show the selectivity loss effect in the absorption efficiency spectrum of the nano-disks that are designed for peak narrowband absorptance of $\lambda \approx 960$ nm from adding a high-index substrate. Figure 5-2a illustrates the absorption profile of the resonator that is embedded in low-index medium (here is air). Figure 5-2b shows the effect of a high-index substrate on absorption profile of the resonator, where it can be observed that the absorption profile has been extended into the substrate. Figure 5-2c and Figure 5-2e, show the normalized magnetic and electric field intensity in a resonator suspended in air (low-index environment). The location of the vector field maxima in Figure 5-2c and Figure 5-2e indicate that the modes are fully confined within the resonator. Figure 5-2d and Figure 5-2f illustrate the normalized magnetic and electric field intensities, respectively, for a resonator with the same geometry shown in Figure 5-2c and Figure 5-2e but on a high-index substrate. The high-index substrate, in this case, becomes an extension to the resonator and therefore the magnetic and electric field confinement disappears, as shown in the vector fields in Figure 5-2d and Figure 5-2f. The presence of the high-index substrate will lead to broadening of the absorption profile, and the selectivity that was observed earlier for the same resonator embedded in low-index medium vanishes (Figure 5-2g).

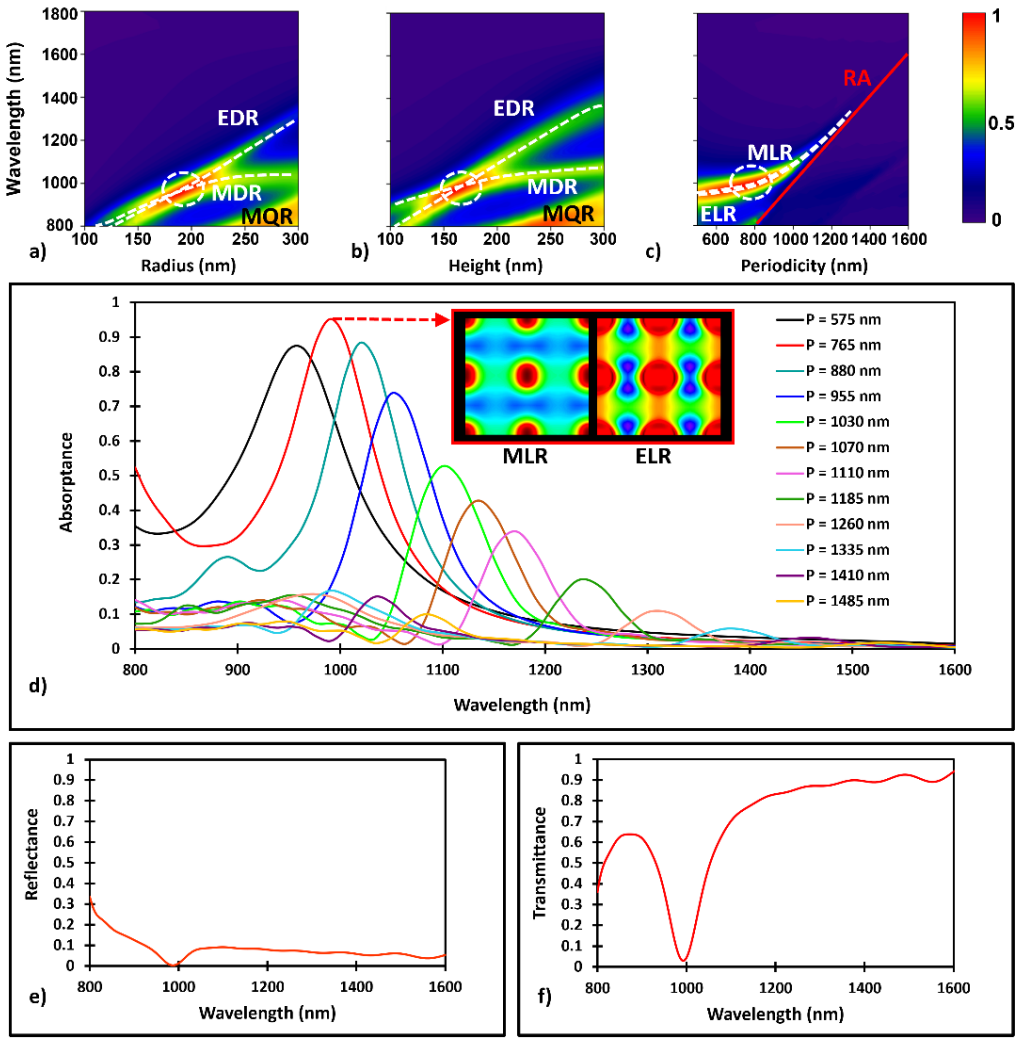

Figure 5-1: Optical properties of a metasurface perfect absorber made of InGaAs resonators suspended in air with *x*-polarized incident light. a) Shows the absorptance as a function of the resonator's radius with a fixed height of 143 nm and periodicity of 650 nm. It can be observed that the absorption efficiency maximizes when the magnetic dipole resonance (MDR) and electric dipole resonance (EDR) overlap at $\lambda \approx 1000$ nm when the radius is 194 nm. This is the wavelength at which the Kerker interference has occurred, and the backscattering has been suppressed. The low-index (here is air) environment surrounding the resonators will promote maximum confinement of the resonant fields inside of the resonators. **b)** The effect of resonator height on the absorption efficiency of the metasurface with the optimum radius from **a)** (194 nm) and periodicity of 650 nm. When the height of the resonator is 160 nm, the overlap of the MDR and EDR leads to Kerker interference and subsequently

the backscattering is minimized. **c)** Shows the effect of periodicity of the metasurface on its absorption efficiency at the optimized radius (194 nm) and height (160 nm) from **a)** and **b)**. The magnetic lattice resonance (MLR) and electric lattice resonance (ELR), which are resulting from the dipole interaction of the adjacent resonators, overlap at 765 nm periodicity (close to the RA indicated by the solid red line). The resonant wavelength of the MLR and ELR corresponding to this periodicity is the same as the MDR and EDR that are supported by the individual resonators in the metasurface. The dashed-line circles in **a)-c)** are highlighting the region at which the maximum absorptance is occurring. The color bar shows the normalized absorption efficiency of the metasurface. **d)** Illustrates the dominance of the lattice resonances for a metasurface that comprises of resonators with 194 nm radius and 160 nm height. Although the resonator is designed to support MDR and EDR at $\lambda \approx 1000$, the effect of lattice resonances appears to dominate the absorption characteristics of the metasurface. The highest absorptance occurs when the lattice resonances are overlapping with the MDR and EDR at $\lambda \approx 1000$. The inset (in red box) shows the magnetic- (left) and electric- (right) field profile of the metasurface for 765 nm periodicity. **e)**, **f)** Illustrate the reflectance and the transmittance, respectively, of the metasurface that comprises of resonators with 194 nm radius, 160 nm height and periodicity of 765 nm (along both *x*- and *y*-axis).

5.2.2.3 Perfect Absorber on a High-Index Substrate

In Figure 5-2, we showed that the fundamental dipole modes in the resonators are not supported by the nano-disk resonator once it was placed on a high-index substrate. Therefore, we focus our attention on the multipolar modes that are generated by larger size structures. It has been shown that in larger resonant structures the magnetic and electric resonances are available in multipolar modes[34,35]. The decomposition of the excited multipolar modes into dipole modes was also shown to be dominated by the ED moment when employing the resonator on a high-index substrate[34,35]. We aim to design a metasurface with a high-index substrate in which the decomposed electric and magnetic dipole modes are overlapped at the same resonant wavelength. To achieve this goal, we modify the dimension of the resonators, i.e., height and diameter, to find a partially overlapping wavelength region for the magnetic and electric dipole resonances. Next, the periodicity will be used to couple the lattice resonances to the magnetic and electric dipoles resonant modes of the resonator. It has also been shown that Mie-Fabry-Pérot resonators with a height $\approx \lambda$ and a circular cross-section[35] have the ability to support multipolar resonant modes[34,35].

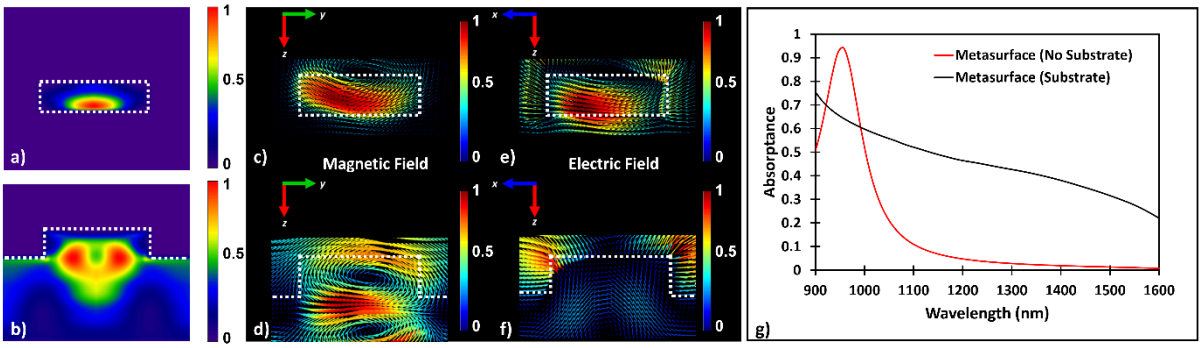

Figure 5-2: Impact of high-index substrate on the absorption profile of an InGaAs metasurface absorber. a) shows the absorption of profile of a resonator that is suspended in air at the peak absorption wavelength of $\lambda \approx 960$ nm. **b)** illustrates the absorption profile of the resonator in **a)** when it is placed on an InGaAs substrate. Comparing **a)** and **b)** shows how the presence of a high-index substrate has led to modification of the absorption profile. Evidently, **b)** shows that the substrate has become an extension to the resonator and thus the absorbed field is not fully confined in the nanostructure as it appears in **a)**. **c)** and **d)** show the magnetic field vector lines for the InGaAs resonator in air and on an InGaAs substrate, respectively. The introduction of the high-index substrate in **d)**, will allow the magnetic field to be extended beyond the resonator, where the magnetic field maxima appear to be in the substrate. **e)** and **f)** are illustrating the electric field vector lines of the InGaAs resonator in air and on an InGaAs substrate, respectively. The resonator in **e)** shows that the electric field is fully confined in the absence of a high-index substrate. When the resonator is placed on an InGaAs substrate in **f)**, the field confinement vanishes, and the electric field will be extended into the substrate. **g)** compares the absorptance of an InGaAs metasurface with (black) and without (red) the presence of a high-index substrate. It is evident that the presence of the high-index substrate has led to disappearance of the near-unity peak absorptance and the broadening of the absorption profile. The color bars in **a)-f)** are normalized to the highest field intensity.

Thus, in our design we place a nanostructure inspired by a Mie-Fabry-Pérot InGaAs resonator geometry on an InGaAs film supported by an infinitely long InP substrate. The thickness of the InGaAs film and the resonator were modified simultaneously during the numerical analysis to ensure a total combined thickness of the InGaAs resonator and InGaAs film was maintained at 1500 nm. It is known that the MD in the HE modes can exist for all wavelength for a given resonator size due to the absence of a cut-off frequency[36]. Therefore, the cut-off for the target wavelength can be determined by the EDR through choosing a diameter that supports the desired wavelength[13,14,29]. In our initial analysis the resonator

height is chosen to be equal to the wavelength of interest. We begin by selecting a single 930 nm tall InGaAs resonator on a 570 nm InGaAs film supported by an InP substrate. To identify the resonator with highest absorption efficiency at 930 nm, we analyzed a range of resonator radii with fixed height of 930 nm. The highest absorption efficiency was observed in a resonator with radius of 230 nm for $\lambda \approx 930$ nm. This structure was then placed in a periodic array to construct a metasurface absorber. The periodicity of the metasurface was set to 902 nm to maintain the 0.51 ratio between the resonator diameter and the periodicity. To improve the absorption efficiency of the metasurface, the radius and the height of the resonator in a periodic system are further optimized by varying these parameters as a function absorptance. Figure 5-3a and Figure 5-3b illustrate the dependence of the absorptance of the metasurface absorber on the resonator radius and height, respectively. For the fixed periodicity of 902 nm, the evolution of the radii in Figure 5-3a shows the absorptance of the metasurface for different magnetic and electric modes. The black dashed line in Figure 5-3a, for the smaller resonator radii, highlights the LRM regime, where the absorption is governed by two different mechanisms. Namely, direct absorption by the resonator and indirectly through the recollection of the scattered field from leaky mode by neighbouring nanostructures[37]. We identified two general electric and magnetic dipole modes that resulted from the decomposition of the magnetic and electric multipolar resonances, denoted as MD_1, ED_1, MD_2 and ED_2. It can be observed in Figure 5-3a that the overlap of the MD_2 and ED_2 combined with the coupling to lattice resonances, in the vicinity of the RA, occurs at a wavelength of 915 nm where the absorption efficiency is the highest. In Figure 5-3b, the height of resonator with a fixed radius at the optimized value (230 nm) and periodicity of 902 nm was studied to identify the shortest resonator with the highest absorption efficiency. The analysis revealed that the absorptance is maximized when the resonator height is 958 nm. Figure 5-3c, illustrates the effect of lattice resonances on the metasurface absorption efficiency. With a periodicity of 902 nm the coupling of the lattice resonances with the partially overlapping magnetic and electric multipole resonances of the resonator is made, yielding a metasurface with absorptance of 98% at the target wavelength. In Figure 5-3d, the magnetic (left) and electric (right) field vectors are shown for the metasurface at the peak absorption wavelength of 915 nm. The current loops generated from the decomposed magnetic and electric dipole moments also illustrate their spatial overlap in the resonator. The presence of the magnetic and electric lattice resonances is also noticeable on the outside of the resonator, as outlined by the dashed white line. Analysis of the multipolar modes of a single resonator compared with the same structure in a periodic array (Figure 5-3d) affirmed the perturbation of the excited fields in the nanostructure when

coupled with the lattice resonances. As it appears in Figure 5-3c, the presence of the lattice resonances is essential in achieving near-unity absorption efficiency in the described metasurface. Note also that the overlap of magnetic and electric fields in the resonator leads to the Kerker interference enabled through the assistance of the magnetic and electric lattice resonances. The absorption profile of the resonator at the wavelength of 915 nm is presented in Figure 5-3e. It can be observed from the absorption profile that the maximum absorption occurs in a small region inside of the resonator. We attribute this absorption characteristic of the resonator to the coupling of the lattice resonant modes to the magnetic and electric multipolar modes. In Figure 5-3f, the reflectance (R), transmittance (T) and absorptance (A) of the metasurface with the optimized geometry are shown. The figure shows the suppression of backscattering ($R < 0.3\%$) at the 915 nm target wavelength characteristic of Kerker interference. The transmittance has also been minimized through maximizing the material absorption. A peak absorptance of 98% is achieved at the target wavelength (λ = 915 nm) with a peak FWHM of approximately 50 nm.

We found that the dimension of the resonators and the periodicity (p) of a metasurface absorber on a high-index substrate can be predicted for different wavelengths by adhering to the relationships of Eqs. (5-3) – (5-5):

$$h \approx \lambda_0 \tag{5-3}$$

$$r \approx \frac{\lambda_0}{n} \tag{5-4}$$

$$\frac{2r}{p} \approx 0.51 \tag{5-5}$$

5.2.3 Avalanche Photodiode with a Metasurface Absorber on a High Index Substrate

The breadth and demanding nature of photodetector applications make it a natural focus for metasurface incorporation, namely as a perfect absorber for enhanced targeted narrowband detection[8,19]. To explore some of the potential performance improvements through the application of the perfect absorbers, the optoelectronic response of the InGaAs metasurface near-unity absorber on a high-index substrate was numerically modelled in an APD. For comparison, the performance of the InGaAs metasurface near-unity absorber was also modelled against a traditional planar APD counterpart. Both modelled devices were composed of an InGaAs/InAlAs SAGCM layer APD material structure that was inspired from literature[38].

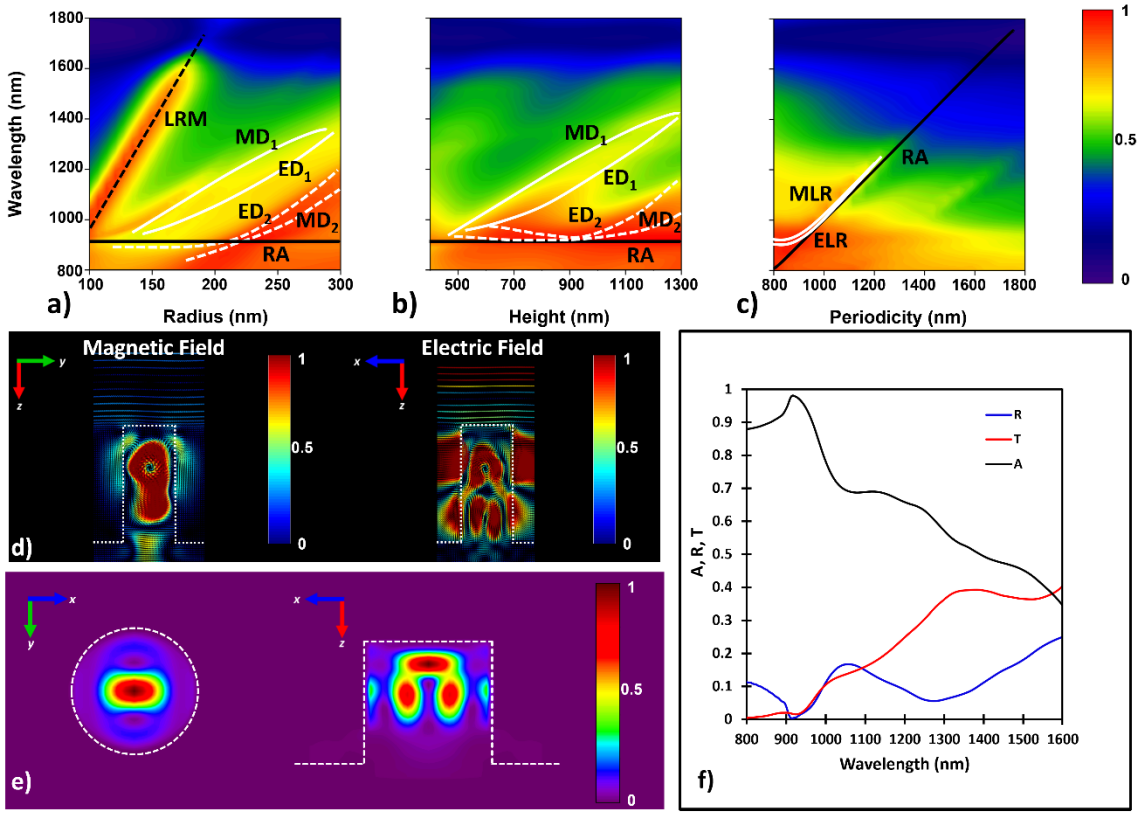

Figure 5-3: Optical property of a near-unity metasurface perfect absorber, tuned for peak absorptance at λ = 930 nm, on a high-index substrate. a) illustrates the absorptance of an InGaAs resonator (height = 930 nm and periodicity = 902 nm) on an InGaAs substrate, as the function of changes in the radius of the nano-disk. The decomposition of multipolar magnetic and electric resonances has led to appearance of magnetic and electric dipoles that are indicated by MD_1, MD_2 and ED_1, ED_2. It can be observed that the MD_2 and ED_2 overlap at a radius of 230 nm, which coincides with the presence of the Rayleigh anomaly (RA) indicated by the solid black line. The leaky resonant mode (LRM) regime is indicated by the black dashed line for smaller nano-disk radii where the high absorption efficiency is linked to scattering of the leaky modes from the individual nano-disks and recollection of this scattered field by the neighbouring nanostructures. **b)** shows the effect of height on the absorption efficiency of an InGaAs resonator on a high-index substrate. For the resonator with a height of 958 nm, radius of 230 nm, and periodicity of 902 nm, the overlap of the MD_2 and ED_2, which resulted from the decomposition of multipolar modes supported by the nano-disk, coincides with the

presence of the RA. **c)** demonstrates the impact of periodicity on the absorption efficiency of a metasurface comprised of InGaAs resonators with radius of 230 nm and height of 958 nm. The absorption efficiency for target wavelength of $\lambda = 930$ nm is maximized when the resonator's magnetic and electric dipoles are coupled with the lattice resonances which occurs at the periodicity of 902 nm. **d)** shows the magnetic field vector lines (left) and electric field vector lines (right) of the resonator with radius of 230 nm, height of 958 nm and periodicity of 902 nm on an InGaAs substrate at $\lambda = 915$ nm. The magnetic and electric field maxima occur at a region of the resonator which allows for the spatial overlap of the magnetic and electric fields. The presence of the magnetic and electric lattice resonances, marked as MLR and ELR respectively, can be observed. **e)** Illustrates the top-view cross-section (left) and side-view cross-section (right) absorption profile of the resonator in **d)**. The absorption maxima appear to be highly confined inside the resonator where the region with the maximum absorption (dark red) is 50 nm in diameter. **f)** Shows the reflectance (blue), transmittance (red) and absorptance (black) of an InGaAs metasurface absorber with radius of 230 nm, height of 958 nm, and periodicity of 902 nm on an InGaAs substrate. The peak absorptance is at $\lambda \approx 915$ nm with 98% absorption efficiency. The suppressed reflectance and transmittance for the same wavelength as the absorptance represents the Kerker interference. The color bar in **a)-e)** are normalized to the maximum field intensities shown in their respected panels.

The metasurface was employed as the APD active region with a targeted resonant absorption wavelength of 915 nm, achieved through InGaAs resonators with 958 nm height (situated on a 542 nm InGaAs film), 230 nm radius, and 902 nm periodicity. Conveniently, incorporating the metasurface as the active region of an SAGCM APD is attainable with conventional micro/nanofabrication techniques, namely through a top-down etch of its planar counterpart. The modelled metasurface APD performance and its prospect operation are illustrated in Figure 5-4a, which includes the dark and illuminated current density-voltage (J-V) curves with the calculated gain. The photocurrent density results were obtained under a source illumination of 0.136 W/cm^2 at the targeted resonant wavelength of the metasurface ($\lambda = 915$ nm). The resultant J-V reflects the profiles reported for an SAGCM layer APD material structure in reference[38], capturing the characteristic step at punch-through and the hard-knee of the avalanche breakdown at approximate reverse biases of 25 V and 53 V, respectively. Furthermore, a notable gain of 500 is found following punch-through at -25 V, approaching 7000 in the breakdown region (-53 V).

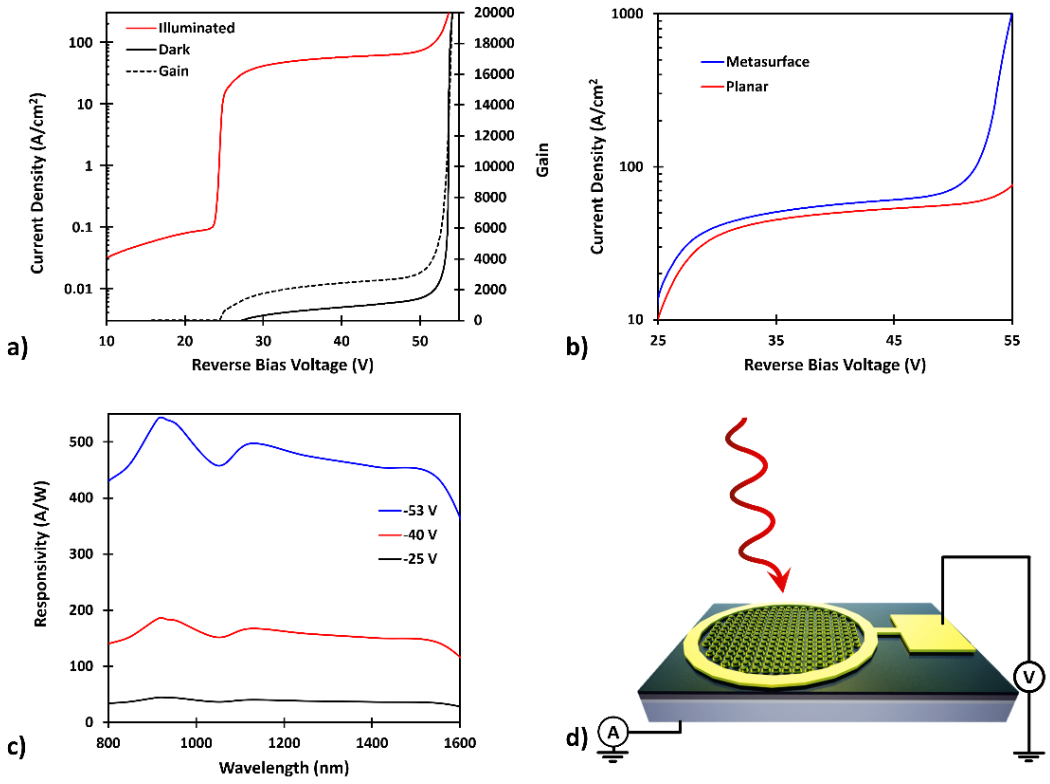

Figure 5-4: The modelled electrical response of an avalanche photodiode with an integrated metasurface perfect absorber active region on a high-index substrate. a) Characteristic APD dark (solid black line) and illuminated (solid red line) current density-voltage (J-V) relationship at the peak absorptance wavelength (915 nm) of the metasurface perfect absorber and illumination of 0.136 W/cm^2, and high gain (dashed black line) enhanced by the metasurface resonance. The characteristic step of punch-through and hard-knee of avalanche breakdown appear at approximate reverse biases of 25 V and 53 V, respectively. **b)** Separate absorption, grading, charge, and multiplication (SAGCM) device photodetection performance comparison between the metasurface (blue) and planar (red) avalanche photodiodes (APDs) with the metasurface APD leading its planar counterpart over the whole punch-through voltage range. **c)** Metasurface APD spectral responsivity over a broad spectral range with increasing resonance peak distinguishability in the operating regions of interest: punch through at -25 V (black) and -40 V (red) and avalanche breakdown at -53 V (blue). An enhanced responsivity attributed to the resonant wavelength response of the resonator is observed, mirroring the resonator absorptance characteristics, including the recurrence of a peak in the responsivity at the resonant wavelength, $\lambda = 915$ nm. **d)** A top illuminated metasurface APD concept design. The metasurface active

region is contained within the gold circular electrode. Such a device could be constructed with conventional top-down fabrication methods on a III-V semiconductor planar material stack like that of the modelled InGaAs/InAlAs SAGCM APD.

An enhanced gain in the metasurface APD was found to be attributed to the metasurface optical response. This improved performance was reflected in the illuminated J-Vs of the modelled devices, as shown in Figure 5-4b, which presents the metasurface APD exceeding the planar counterpart throughout the punch-through region. The current density was derived from the current flowing through the model region which contained several nanostructures. After compensating for the non-conductive regions around the 230 nm radius nanostructures, the dark (illuminated) currents per NW were found to be 17 pA (112 nA) and 167 pA (1.35 μA) in the punch-through (-25 V) and avalanche breakdown (-53 V) regions, respectively. A higher performance through the enhanced metasurface absorption was also revealed in the modelled spectral responsivity, illustrated in Figure 5-4c. The generated responsivity expressed similar characteristic features to the metasurface absorptance spectra, including a common peak at the resonant wavelength of 915 nm owing to the metasurface spectral selectivity. The spectral responsivity was produced at three increasing reverse bias voltages to demonstrate the prospective operation and increased peak distinguishability within the punch-through (-25 V and -40 V) and avalanche-breakdown (-53 V) regions. When operated near breakdown, the enhanced performance from the metasurface in the APD provides over 80 A/W higher responsivity at resonance than that at the adjacent minimum, λ = 1047 nm. A concept of a top-illuminated metasurface APD design is illustrated in Figure 5-4d. This concept device makes use of the modelled SAGCM material stack and metasurface absorber, and though absent in the modelled devices, BCB and ITO were included as transparent planarization and contact layers, respectively. The dome-like microstructures present in the concept design are known constructs that form in the transparent ITO top contacts of similar NW devices[17,39]. The gold contact ring present around the perimeter of the active region was included as a platform for wire-bond electrical contacting.

5.2.4 Conclusion

We further demonstrated the unique nature of metasurfaces and their applicability for optoelectronic devices, offering a resonator type structure that retains its unique metasurface qualities despite the presence of a high index substrate. Through the modelling and analysis of our metasurface design we established a method to controllably achieve a near unity peak absorption at a targeted wavelength.

Furthermore, the method demonstrates a capability to enhance the optical response and selectivity in practical optoelectronic device designs. With applications continuing to demand smaller and higher performance optoelectronics, it becomes necessary to develop novel device designs that exceed the limitations of the currently available technologies with practical solution. Given this demand and the feasibility of our metasurface fabrication, a natural avenue for further development includes its direct integration in APDs for application specific enhanced performance. For instance, the high targeted efficiency achieved in our modelled metasurface, and device was achieved over the range of 900 nm to 1000 nm, a region of importance for optical coherence tomography where currently available commercial APDs have lower efficiency. As a result, the experimental demonstration of the metasurface APD in this range could immediately exhibit its prospect for advancing ophthalmology and cardiology disease screening and diagnostics quality, improving the standard of health care.

5.2.5 References

1. Schuller, J. A., Zia, R., Taubner, T. & Brongersma, M. L. Dielectric Metamaterials Based on Electric and Magnetic Resonances of Silicon Carbide Particles. *Phys. Rev. Lett.* **99**, 107401 (2007).
2. Staude, I. *et al.* Tailoring Directional Scattering through Magnetic and Electric Resonances in Subwavelength Silicon Nanodisks. *ACS Nano* **7**, 7824–7832 (2013).
3. Pfeiffer, C. & Grbic, A. Metamaterial Huygens' Surfaces: Tailoring Wave Fronts with Reflectionless Sheets. *Phys. Rev. Lett.* **110**, 197401 (2013).
4. Kamali, S. M., Arbabi, E., Arbabi, A. & Faraon, A. A review of dielectric optical metasurfaces for wavefront control. *Nanophotonics* **7**, 1041–1068 (2018).
5. Jahani, S. & Jacob, Z. All-dielectric metamaterials. *Nature Nanotech* **11**, 23–36 (2016).
6. Zhang, S. *et al.* Metasurfaces for biomedical applications: imaging and sensing from a nanophotonics perspective. *Nanophotonics* **10**, 259–293 (2021).
7. Zheng, C. *et al.* All-Dielectric Metasurface for Manipulating the Superpositions of Orbital Angular Momentum via Spin-Decoupling. *Advanced Optical Materials* **9**, 2002007 (2021).
8. Mitrofanov, O. *et al.* Perfectly absorbing dielectric metasurfaces for photodetection. *APL Photonics* **5**, 101304 (2020).
9. Bao, Y. *et al.* On-demand spin-state manipulation of single-photon emission from quantum dot integrated with metasurface. *Science Advances* **6**, eaba8761 (2020).

10. Georgi, P. *et al.* Metasurface interferometry toward quantum sensors. *Light Sci Appl* **8**, 70 (2019).
11. Yavas, O., Svedendahl, M. & Quidant, R. Unravelling the Role of Electric and Magnetic Dipoles in Biosensing with Si Nanoresonators. *ACS Nano* **13**, 4582–4588 (2019).
12. Dong, T. *et al.* Ultra-low-loss on-chip zero-index materials. *Light Sci Appl* **10**, 10 (2021).
13. Fan, K., Suen, J. Y., Liu, X. & Padilla, W. J. All-dielectric metasurface absorbers for uncooled terahertz imaging. *Optica, OPTICA* **4**, 601–604 (2017).
14. Liu, X., Fan, K., Shadrivov, I. V. & Padilla, W. J. Experimental realization of a terahertz all-dielectric metasurface absorber. *Opt. Express, OE* **25**, 191–201 (2017).
15. Ming, X., Liu, X., Sun, L. & Padilla, W. J. Degenerate critical coupling in all-dielectric metasurface absorbers. *Opt. Express, OE* **25**, 24658–24669 (2017).
16. Liao, Y.-L. & Zhao, Y. Ultra-narrowband dielectric metamaterial absorber with ultra-sparse nanowire grids for sensing applications. *Sci Rep* **10**, 1480 (2020).
17. Gibson, S. J. *et al.* Tapered InP nanowire arrays for efficient broadband high-speed single-photon detection. *Nature Nanotechnology* **14**, 473–479 (2019).
18. Wang, B. & Leu, P. W. Enhanced absorption in silicon nanocone arrays for photovoltaics. *Nanotechnology* **23**, 194003 (2012).
19. Zhou, Z.-X. *et al.* Germanium Metasurfaces with Lattice Kerker Effect in Near-Infrared Photodetectors. *ACS Nano* **16**, 5994–6001 (2022).
20. Smith, A. M., Mancini, M. C. & Nie, S. Second window for in vivo imaging. *Nature Nanotech* **4**, 710–711 (2009).
21. Weissleder, R. A clearer vision for in vivo imaging. *Nat Biotechnol* **19**, 316–317 (2001).
22. Owens, E. A., Lee, S., Choi, J., Henary, M. & Choi, H. S. NIR fluorescent small molecules for intraoperative imaging. *WIREs Nanomedicine and Nanobiotechnology* **7**, 828–838 (2015).
23. Sajedi, S., Sabet, H. & Choi, H. S. Intraoperative biophotonic imaging systems for image-guided interventions. *Nanophotonics* **8**, 99–116 (2019).
24. Hong, G., Antaris, A. L. & Dai, H. Near-infrared fluorophores for biomedical imaging. *Nat Biomed Eng* **1**, 1–22 (2017).
25. Incoronato, A., Locatelli, M. & Zappa, F. Statistical Modelling of SPADs for Time-of-Flight LiDAR. *Sensors* **21**, 4481 (2021).
26. Decker, M. *et al.* High-Efficiency Dielectric Huygens' Surfaces. *Advanced Optical Materials* **3**, 813–820 (2015).

27. He, Y. *et al.* Infrared perfect absorber based on nanowire metamaterial cavities. *Opt. Lett.* **38**, 1179–1181 (2013).
28. Hale, L. L. *et al.* Perfect absorption in GaAs metasurfaces near the bandgap edge. *Opt. Express* **28**, 35284–35296 (2020).
29. Groep, J. van de & Polman, A. Designing dielectric resonators on substrates: Combining magnetic and electric resonances. *Opt. Express* **21**, 26285–26302 (2013).
30. Kerker, M., Wang, D.-S. & Giles, C. L. Electromagnetic scattering by magnetic spheres. *J. Opt. Soc. Am.* **73**, 765 (1983).
31. Liu, W. & Kivshar, Y. S. Generalized Kerker effects in nanophotonics and meta-optics. *Opt. Express, OE* **26**, 13085–13105 (2018).
32. Babicheva, V. E. & Evlyukhin, A. B. Resonant Lattice Kerker Effect in Metasurfaces With Electric and Magnetic Optical Responses. *Laser & Photonics Reviews* **11**, 1700132 (2017).
33. Babicheva, V. E. & Moloney, J. V. Lattice effect influence on the electric and magnetic dipole resonance overlap in a disk array. *Nanophotonics* **7**, 1663–1668 (2018).
34. Butakov, N. A. & Schuller, J. A. Designing Multipolar Resonances in Dielectric Metamaterials. *Sci Rep* **6**, 38487 (2016).
35. Yang, Y. *et al.* Multimode directionality in all-dielectric metasurfaces. *Phys. Rev. B* **95**, 165426 (2017).
36. Snitzer, E. Cylindrical Dielectric Waveguide Modes. *J. Opt. Soc. Am.* **51**, 491–498 (1961).
37. Tekcan, B. *et al.* Semiconductor nanowire metamaterial for broadband near-unity absorption. *Sci Rep* **12**, 9663 (2022).
38. Cao, S. *et al.* Theoretical Analysis of InGaAs/InAlAs Single-Photon Avalanche Photodiodes. *Nanoscale Research Letters* **14**, 3 (2019).
39. van Dam, D. *et al.* High-Efficiency Nanowire Solar Cells with Omnidirectionally Enhanced Absorption Due to Self-Aligned Indium–Tin–Oxide Mie Scatterers. *ACS Nano* **10**, 11414–11419 (2016).

Chapter 6
Mode-Matching Method for Efficient Coupling and Near-Unity Absorptance in a Single Tapered Semiconductor Nanowire Photodetector

6.1 Preface

The measurement of optoelectronic devices that integrate low-dimensions materials have demonstrated the prospect of the 1D single NW platform in appealing integrated applications and the potential for high-performance optoelectronic devices at the nanoscale. The low-dimensional technologies are able to leverage the substantially reduced structural volume to improve critical performance metrics. Such a dependence was presented in Chapter 3, where a reduced dark current was attributed to the fully depleted NW core. The application of single NWs, however, often has limited absorption efficiency owing to their small footprint. The prospective publication results in Chapter 6 explore a method aimed at improving the absorption efficiency in low-dimensional devices by utilizing a tapered NW structure. This work implements numerical modelling to present a mode-matching method which enables tunable near-unity absorptance in a single NW absorber. The results illustrate the potential of the tapered NW structure in low-dimensional materials, photodetection, and advancing respective technologies already shown applicable to the 1D single NW platform.

6.2 Manuscript

Brad van Kasteren[1,2], Sasan V. Grayli[1,2], Sathursan Kokilathasan[1,2], William Losin[1,2], and Michael E. Reimer[1,2,3]

[1]Institute for Quantum Computing, University of Waterloo, Ontario, Canada. [2]Department of Electrical & Computer Engineering, University of Waterloo, Ontario, Canada. [3]Department of Physics and Astronomy, University of Waterloo, Ontario, Canada.

6.2.1 Summary

Modern electronics continue the trend into the nanoscale to harness new physics and unlock operating efficiencies unachievable with current methods. As such, high-performance miniaturized optoelectronics are in high demand for emerging areas such as integrated nanophotonic and quantum

technologies. Efforts are being made to design highly efficient devices with a small footprint to address this demand. However, the single-photon detector technologies capable of the necessary efficiencies often lack practical qualities like low energy consumption and room temperature operation. Near room temperature operating semiconductor nanowires offer a promising platform for addressing the high-performance demands at a nanoscale while remaining practical but require improvements to operating efficiencies. In this study, we offer a method for maximizing coupling and absorption efficiencies for high-performance nanoscale optoelectronic devices, demonstrated here in a modelled single semiconductor nanowire photodetector with near-unity absorptance. Through mode-matching techniques and adiabatic coupling, we confine a focused linearly polarized Gaussian beam incident normal to the surface. The mode-matching technique demonstrates a wavelength tunable method that achieves near-unity absorption (> 99%) in a single tapered InP nanowire at a limit of light-matter interaction. The methods of this work can be applied in the design of nano-optoelectronic devices to maximize absorption efficiency with the smallest footprint of modern fabrication techniques. Applying this mode-matching method can enable a range of nano-optoelectronic technologies with a far-reaching impact on influential applications including biomedical imaging, sensing, integrated photonics, quantum memories, quantum communication, and quantum photonics.

6.2.2 Introduction

With recent advances in nanophotonic systems, promising alternatives to bulky tabletop equipment in optoelectronics are being developed at the nanoscale through promising platforms with conventional fabrication methods, such as integrated optical circuits and quantum technologies[1–5]. As nanophotonic technology has matured, it has demonstrated promise for scalability and a means to manipulate light with a high degree of stability for broad integration, including at the single-photon level[4,6,7]. These qualities are highly sought after for quantum information technologies, and they have already been found to be capable of performing quantum gate operations for optical quantum communications, interconnects, and processors[4,8]. Furthermore, nanophotonic solutions are continuing to find innovative ways to develop semiconductor nano-optoelectronic devices while targeting the extensive silicon platform like CMOS electronics[9–14]. These miniaturized technologies can also find practical use in classical optoelectronic and photonic applications, given the high performance of the basic elements like beam splitters, waveplates, and phase shifters[4,6,7]. As such, nano-optoelectronic devices offer an opportunity for practical use in low-cost, high-performance photonic systems in a small footprint. These necessary qualities are critical for industrialization and enabling their practical incorporation into

commercial technologies[13]. Nano-optoelectronics are demonstrating potential for far-reaching, impactful systems ranging from biomedical imaging to computation and energy to emerging quantum technologies[2,5,15–19]. There is a high demand for enhancing absorption and coupling efficiencies in these technologies, which is especially true in photodetector technologies where absorption efficiency is critical to the total detector efficiency performance[12,17,20].

Though the demand for solutions are high and current nanophotonic device efforts show promise, recent developments have not yet fully realized a practical high-performance platform. For instance, Superconducting devices like superconducting NW detectors have demonstrated exceptional photodetection capabilities, but their operating temperatures rely on bulky cryogenic systems which are expensive to operate and have limited portability[21]. Alternative room temperature and thermoelectrically cooled low-dimensional technologies[18], employing 1D and 2D platforms like semiconductor NWs and graphene, overcome this issue and show promise as high-performance nanoscale optoelectronic platforms[2,12,17,20,22–24], but these technologies have yet to fully achieve the performance of superconducting device efficiencies. However, single NWs remain of particular interest, with semiconductor NWs having desirable optical and electrical qualities such as low dark current through NW core depletion and inherently tunable selectivity, that have already demonstrated promise in a variety of nanoscale optoelectronics including APDs, photoconductors, phototransistors, photoconductive switches, and heterojunction photodetectors[1,12,16,17]. A popular approach for single NW applications includes operating the NW devices with the NW in a horizontal configuration[12,17,20,25,26]. This includes laying the NW on its side and coupling to TE/TM modes with light orthogonal to the NW axis[27]. This method lacks the conditions necessary to draw in and confine the large spot size of light into the NW, thereby hindering absorptance and thus DE. Furthermore, the laterally placed NW is not fit for general use in optoelectronic because it forces a polarization requirement on the incident source signal. The alternative vertical (standing) NW configuration involves illuminating parallel to the NW axis, coupling to the HE/EH modes, and is capable of larger absorption cross sections and polarization independence through its radial symmetry. Single standing NWs are of particular interest for near room temperature nano-optoelectronics because of their potential in achieving a low lateral limit of size, critical to the pixel size of sensors and miniaturization of optoelectronics[12]. Though findings for the NW optoelectronic platform have shown promise, the devices tend to lack the efficiencies achieved in superconducting devices necessary for high-performance nano-optoelectronics. High coupling and absorption efficiencies are critical in high-

performance optoelectronics and remain a core challenge to the single NW platform because of its substantially reduced footprint[20].

In this work, we present a mode-matching method that can be applied to nanophotonic devices for enhanced coupling, near-unity absorption, and improved optoelectrical response. We focus on the single NW platform, modelled through a single tapered semiconductor (InP) NW with near-unity absorption, for achieving the smallest footprint high-performance nano-optoelectronic devices. Through mode-matching conditions, from a Gaussian source to the fundamental circular waveguide mode (HE_{11}), a process is detailed using numerical modelling to realize a tunable, selective, standing single tapered semiconductor NW coupler, near-unity absorber, and sensor. Inspiration for the tapered semiconductor near-unity absorber geometry was drawn from NW QD on-demand sources, improving the NW-based nanophotonic platform for enhanced emission and collection efficiencies. The NW sources have demonstrated potential for achieving the demanding qualities of integrated quantum photonic circuits; integration capable, bright, efficient, on-demand single entangled photon generation[28–31]. As is the case in optical fibers, the waveguide-like nature of NWs enables them to benefit from tapering for enhanced efficiencies[29,32,33]. Here, leveraging the adiabatic transition in effective refractive index is found to suppress the reflection of incident light and enables its confinement into the HE_{11} NW waveguide mode. Also, mode matching to the NW detector is made with an incident Gaussian source. Such Gaussian emission can be achieved in nanophotonic devices by graded-index (GRIN) material lenses for the practical application of this mode-matching method to improve on currently limited efficiencies, including those of QD imbedded NW devices for the IR[12,15,34–36]. The wave guiding properties of the HE_{11} mode and the NW cross section have been previously explored, but to our knowledge the process of coupling by adiabatic mode matching for the NW platform, shown here to produce near-unity absorptance at a reduced scale through a tapered semiconductor NW, has yet to be realized[33,37–42]. The modal analysis of a lossless NW structure is studied and then implemented in a lossy tapered NW to achieve the efficient coupling, suppressed reflection, and mode confinement necessary for maximum absorptance in the nanostructure. The application of this process can enable a single standing NW to act as an efficient coupler or a near-unity absorber to compliment a range of NW-based nano-optoelectronic applications. The electrical attributes of the near-unity tapered NW absorber was modelled in a radial p-n junction diode to demonstrate its potential performance as a prospective NW optoelectronic device through the application of the mode-matching method. We present a concept application of the standing single semiconductor tapered NW

diodes in a sensor array where the pixel density of the sensor array is maximized through the nanoscale-sized lateral footprint of the single NW platform. The NW designs are also made to be considerate of practical fabrication by conventional microfabrication processes. These qualities, as well as its mirroring structural geometry to its already fabricated and measured single NW source counterpart, make it an excellent candidate for use in integrated photonic circuits, quantum technologies, and nanophotonic systems where the single NW platform can be implemented for the receiver, emitter, and couplers towards achieving near-ideal operating efficiency performance of classical or quantum nano-optoelectronics.

6.2.3 Nanowire Modal Analysis and Properties of Interest

NWs have been shown to possess waveguide-like properties with supported modes similarly modelled to those of conventional circular fiber waveguide[33,38,43]. The equations used to model circular step index fibers are well studied and offer a convenient method for analyzing the field modes and finding the smallest radius of the fiber-like nanostructure that will still interact with incident light. Targeting the smallest possible radius in this way implies that the focus for device operation should be limited to the SM regime. The SM regime is also made the focus for the detector operations because it has the added benefit of wavelength selectivity, a quality that is inhibited when extending into MM operation. This design decision allows for a simple approximate upper limit to be set for the NW radius, namely the characteristic first circular fiber mode (HE_{11}) cut-off before MM operation. The HE_{11} mode is always available, absent a lower cut-off, but the effective refractive index and degree of power confinement in the fiber rapidly decreases with the radius at subwavelength-diameters[38,43]. To operate as a photodetector, the NW waveguide must still interact with, confine, and absorb to capture the incident light detection. Thus, a lower limit is not as easily defined. To find a suitable lower limit for the NW radius, the bounds for these limits must be quantified. Because of the relative nature of the diameter and wavelength for fiber waveguides, it is convenient to consider mode regions with respect to the fiber parameter (V), represented in Eq. (6-1)[43]:

$$V = \frac{2\pi\rho}{\lambda}\left(n_{co}^2 - n_{cl}^2\right)^{1/2} \tag{6-1}$$

Where ρ is the NW radius, λ is the wavelength, and n_{co} and n_{cl} are the refractive index of the NW and cladding respectively. We first consider cylindrical semiconductor (InP) NWs (in air), though the method can extend to a variety material options, and attempt to find the radial limits for the smallest possible NW absorber. Conventional step index modal equations[43] were used to numerically model the

NW in air, using $n_{co} = 3.4$ and $n_{cl} = 1$. The propagation constant, β, is derived from these standard formulas and can be related to the effective refractive index of the different modes through the relationships $\beta = 2\pi n_{eff}/\lambda c$. Where n_{eff} is the effective refractive index and c is the speed of light in vacuum[41]. V was swept from 0 to 7 and the n_{eff} modal dependence for a range of the lower order NW waveguide modes are found, as illustrated in Figure 6-1a.

The change in effective refractive index for the HE_{11} mode illustrates when the light begins to interact with the waveguide, and plotting against V produces a more general form for analysis due to the use of a radius to wavelength ratio. The upper bound dimension for the smallest detector follows the results from literature, indicated by the SM cut-off before the MM regime in a step-index profile circular fiber ($V < \sim 2.405$)[43]. For the lower bound, we designate a limit for light-matter interaction by the region where the n_{eff} for the HE_{11} mode deviates from n_{cl}. For the InP NW in air this occurs at $V \approx 1.66$. As V increases beyond this value the HE_{11} n_{eff} rapidly increases, indicating more substantial interaction between the incident light of this wavelength with the waveguide. According to these limits, we define the critical regions for the smallest detector waveguide design. Namely, the non-interacting SM (1), interacting SM (2), and MM (3) regions with cut-offs at $V \approx 1.66$ and $V \approx 2.405$. With the regions defined according to V, it is convenient for engineering the NW absorber to represent the n_{eff} of the HE_{11} mode in terms of radii and wavelength, as shown in the contour plot of Figure 6-1b. The wavelength range and wavelength dependent index, $n(\lambda)$, are selected according to the absorbing region of the NW absorber material (InP). Then the radius is swept through the regions of interest and the radius-wavelength positions are mapped to their respective n_{eff} from their corresponding value of V. A white dashed line indicates the cut-off between regions (1) and (2) where $n_{eff} \approx n_{cl}$, identifying the radius-wavelength combination where light begins to interact with the waveguide. The blue dashed line indicates the SM cut-off between regions (2) and (3), trending along $n_{eff} \approx 2$.

Numerical methods, employing FDTD, were used to model the modal properties at the critical cut-off positions indicated by the white markers in Figure 6-1b. A mode source is used to inject a guided mode into a (lossless) InP NW waveguide surrounded by air at $\lambda = 460$ nm. This numerical model is used to gather the electric (**E**) and magnetic (**H**) vector field patterns and magnitude distributions inside of the structure. The left panel, Figure 6-1c, illustrates the HE_{11} mode with the expected vector field profile in the waveguide at the SM cut-off position ($\rho = 45$ nm)[43–45]. The waveguide cross section normal to the NW axis (xy-plane) of $|\mathbf{E}|$ and $|\mathbf{H}|$ are plotted in the top left of the panel and bottom left of the panel, respectively. In the right column of the panel, a cross section of $|\mathbf{E}|$ parallel to the NW axis is included

(*yz*-plane), showing the characteristic repeating current loops of the guided mode. The field distributions indicate that a notable confinement of the HE_{11} mode is found for both the electric and magnetic field throughout the waveguide at the SM cut-off, a necessary quality for the NW absorber. Comparably, the right panel, Figure 6-1d, illustrates the matching but subtle HE_{11} field patterns from a weak interaction with the structure at the $n_{eff} \approx n_{cl}$ cut-off position (ρ = 30 nm). In the right panel, the corresponding cross sections positions are |**E**| in the *yz*-plane (left), |**E**| in the *xy*-plane (top right), and |**H**| in the *xy*-plane (bottom right). Note that the colour bar for Figure 6-1c and Figure 6-1d indicates the normalized field magnitude, where all |**E**| are normalized to the largest electric field vector magnitude ($|\mathbf{E}_{max}|$) of the set of electric field figures and all |**H**| are normalized to the largest magnetic field vector magnitude ($|\mathbf{H}_{max}|$) of the magnetic field figures.

6.2.4 Mode Matching to a Single Nanowire Waveguide (Lossless)

Coupling from free space to the confined HE_{11} mode of the cylindrical NW waveguide base is performed through mode matching, leveraging the tapered NW tip that faces the incident light. The tapering exposes the incident field to an adiabatically increasing effective refractive index from the $n_{eff} \approx n_{cl}$ region to n_{eff} at the SM cut-off. The tapered NW detector is inspired by standing tapered NW QD sources. The tapered nanostructures of these sources demonstrated a practical means for efficient coupling of an embedded QD's emission to the Gaussian mode and presents a template for deriving the mode-matching conditions for the NW detector[28–31,46]. The dimensions for the tapered NW waveguide can be defined according to the regions (1), (2), and (3), and the numerical modelling (FDTD) of the tapered NW QD source is performed with a dipole emitter (imitating the QD) to inform the mode-matching source parameters for the detector. We select a target wavelength of λ = 480 nm, and the NW receiver radius is estimated to be ρ = 45 nm. The modelled NW includes a gold nanoparticle with a top radius of ρ = 25 nm. This particle is included to accurately model a fabricated nanostructure like the NW sources, which are grown using a catalyst particle. Note also that the gold particle is smaller than the region (1) cut-off radius (~35 nm) at the target wavelength from Figure 6-1b[29,31]. The tapering (full) angle is set to 1°, based on the ideal tapering in NW QD sources for outcoupling single photons from inside the NW adiabatically to the outside with maximum efficiency[29]. The emission properties of the modelled NW QD source of these dimensions follows literature, producing an approximately Gaussian far field[47]. As such, a focused (*y*-polarized) Gaussian beam is implemented for the mode-matching method to couple to the tapered NW receiver.

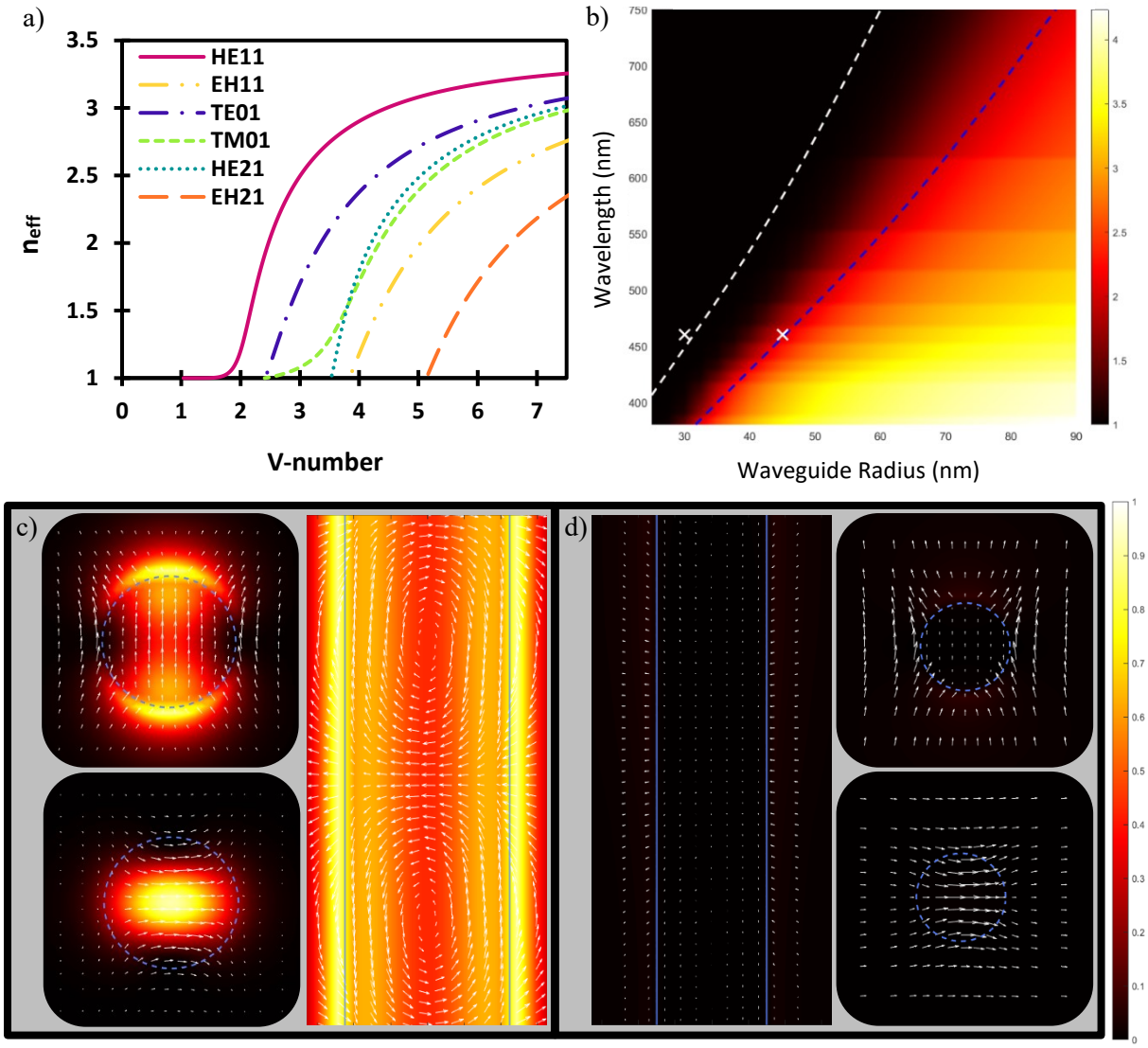

Figure 6-1: Cylindrical InP nanowire waveguide modal analysis. a) The n_{eff} dependence on the fiber parameter (V) of a step-index cylindrical waveguide ($n_{co} = 3.4$ and $n_{cl} = 1$) indicating the cut-offs of the first six supported modes (HE_{11}, TE_{01}, TM_{01}, HE_{21}, EH_{11}, and EH_{21}), as well as the non-interacting region before the single mode cut-off ($V \approx 2.405$) of the HE_{11} mode, where $n_{eff} \approx 0$. **b)** HE_{11} n_{eff} (colour bar) surface plot dependence on the step-index cylindrical waveguide radius and light wavelength. The white dashed line (left) indicates the $n_{eff} \approx n_{cl}$ and the blue dashed line (right) indicates the HE_{11} single mode cut-off. The crosses indicate the wavelength and radius positions used in panel **c)** and **d)**. **c)** Modelled HE_{11} mode of a (lossless) InP ($n_{co} = 3.4$) NW waveguide surrounded by air ($n_{cl} = 1$) at the SM cut-off position ($\rho = 45$ nm, $\lambda = 460$ nm). The *xy*-plane cross section of the electric (**E**) and magnetic

(**H**) vector field patterns and magnitude distributions inside of the structure in the top left and bottom left of the panel, respectively. The *yz*-plane cross section of the electric (**E**) vector field pattern and magnitude distribution on the right of the panel. **d)** Matching but subtle HE_{11} field patterns to **c)** from a weakly interacting NW structure at the $n_{eff} \approx n_{cl}$ cut-off position (ρ = 30 nm) with |**E**| in the *yz*-plane (panel left), |**E**| in the *xy*-plane (panel top right), and |**H**| in the *xy*-plane (panel bottom right). The colour bar indicates the normalized field magnitude, where all |**E**| are normalized to the $|\mathbf{E}_{max}|$ of the set of electric field figures and all |**H**| are normalized to the $|\mathbf{H}_{max}|$ of the magnetic field figures.

Furthermore, a Gaussian beam profile is a convenient choice for the practical application of the mode-matching method as compatible nanophotonic technologies that are necessary for efficiently mode matching to a single tapered NW receiver have already been demonstrated[34,35]. The light is injected parallel to the NW axis where the HE (target) and EH modes are accepted and the TE and TM modes are prohibited by the circular waveguide[43]. The numerical modelling of the NW source also offered initial estimates for remaining mode-matching parameters like convergence angle, beam waist position, source position, and waist radius qualities. These parameters were subsequently optimized by numerical sweeps around the initial guesses to arrive at the mode-matched NW waveguide of Figure 6-2a, which illustrates a *yz*-plane cross section of |**E**| normalized to its $|\mathbf{E}_{max}|$. The focused Gaussian beam shows minimally interacting light at the tip of the NW and the subsequent adiabatic coupling into the NW waveguide. The overlaid blue lines show |**E**| (*y*-axis) in 1D space (along the *x*-axis) in the regions between the cut-offs, ρ = 25 nm, ρ = 30 nm, and ρ = 45 nm (normalized to $|\mathbf{E}_{max}|$ at ρ = 45 nm), highlighting the transition from free space to the confined HE_{11}. The *xy*-plane cross sections of |**E**| (colour bar normalized to $|\mathbf{E}_{max}|$ at ρ = 45 nm) in the NW waveguide are also taken at ρ = 25 nm, ρ = 30 nm, and ρ = 45 nm and illustrated in Figure 6-2b, Figure 6-2c, and Figure 6-2d, respectively. The blue dashed circles outline the NW waveguide, highlighting the gradual confinement and change of the HE_{11} mode from their equivalent radius cylindrical fiber counterparts in Figure 6-1 with increasing n_{eff}. The NW waveguide is also inherently wavelength selective because of its mode-matching conditions. For instance, when illuminated under mode-matched conditions, at λ = 480 nm, the light is clearly well coupled and confined, as observed in the vector field (**E**) of Figure 6-2f. However, when changing to a longer or shorter wavelength, the coupling of the incident field is inhibited. The poor coupling of the cases lacking mode-matching conditions are illustrated for the longer (λ = 900 nm) and shorter (λ = 400 nm) wavelength in Figure 6-2e and Figure 6-2g, respectively. In the event of using a smaller wavelength (λ = 400 nm), the waveguide will be in the MM regime and thus lack the necessary quality of a resonant

guided mode and maximum coupling. For increasing wavelengths, the n_{eff} of the NW decreases, inhibiting the waveguide's ability to confine the light. Note that the colour bar of Figure 6-2e, Figure 6-2f, and Figure 6-2g indicates $|\mathbf{E}|$ which are normalized to $|\mathbf{E}_{max}|$ of Figure 6-2f.

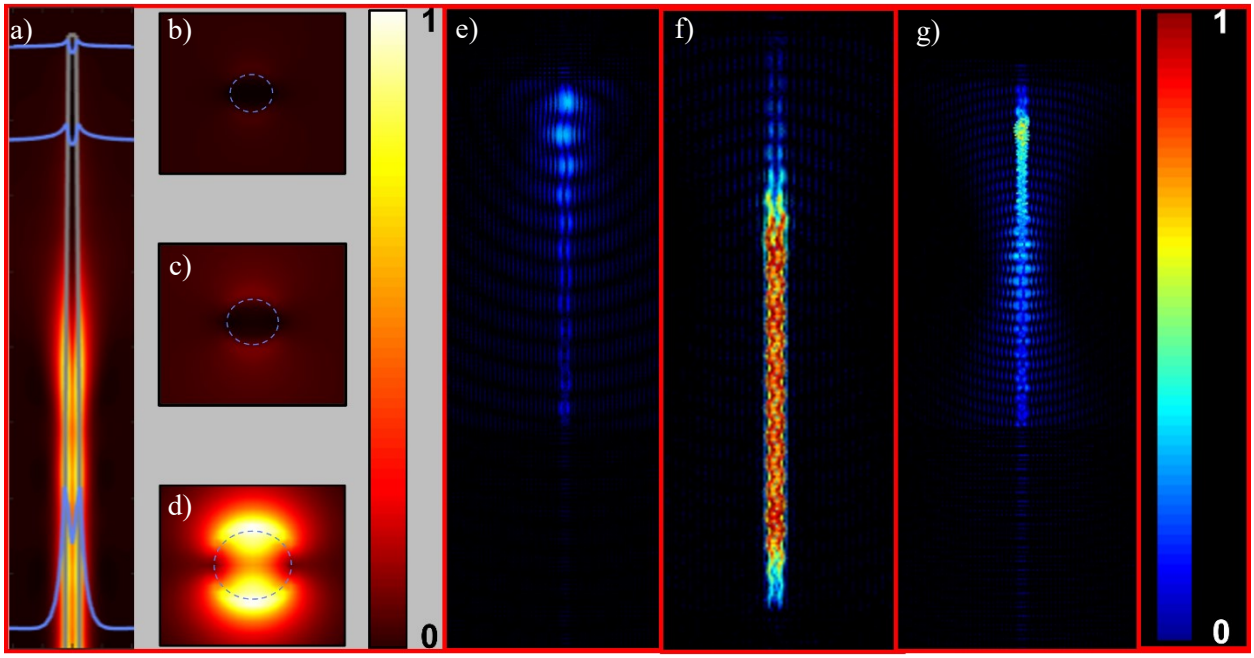

Figure 6-2: Mode-matched coupling to a lossless single tapered InP nanowire (NW). a) A *yz*-plane cross section of $|\mathbf{E}|$ normalized to its $|\mathbf{E}_{max}|$ resulting from a focused mode-matched Gaussian beam (λ = 480 nm) and adiabatic coupling into the tapered InP NW waveguide. The overlayed blue lines show $|\mathbf{E}|$ (*y*-axis) in 1D space (along the *x*-axis) in the regions between the cut-offs at radii ρ = 25 nm, ρ = 30 nm, and ρ = 45 nm (normalized to $|\mathbf{E}_{max}|$ at ρ = 45 nm). The *xy*-plane cross sections of $|\mathbf{E}|$ in the NW waveguide (normalized to $|\mathbf{E}_{max}|$ at ρ = 45 nm) taken at **b)** ρ = 25 nm, **c)** ρ = 30 nm, and **d)** ρ = 45 nm. The colour bar for **a)-d)** indicates the normalized field value. **e)** Electric vector field profile on the same NW structure as **a)** at λ = 900 nm, **f)** λ = 480 nm, and **g)** λ = 400 nm with the **e)-g)** colour bar normalized to $|\mathbf{E}_{max}|$ of Figure 6-2f.

6.2.5 Single Nanowire Near-Unity Absorber

A NW numerical model matching the lossless case is prepared, except with a modified InP material to include its wavelength dependent extinction coefficient. Introducing loss to the NW produces a significant attenuation of the light with propagation down the waveguide, leading to a modified

response and conditions for maximum absorptance[48]. In the model, a broadband Gaussian source is mode matched to the NW waveguide with a radius of $\rho \approx 45$ nm for identifying a modified target wavelength. Maintaining the other derived conditions, an updated resonant wavelength is found for this radius at $\lambda \approx 510$ nm. A wavelength sweep was also repeated for larger NW waveguide of radius $\rho \approx 55$ nm and $\rho \approx 65$ nm. Increasing the waveguide radius extends the NW absorber into longer target wavelength with a red shifted selectivity at $\lambda \approx 610$ nm and $\lambda \approx 710$ nm for $\rho \approx 55$ nm and $\rho \approx 65$ nm, respectively. The trend also demonstrates the inherent tunability of the NW absorber achieved with the changing of waveguide radius. Because of this change in target wavelength, the beam waist position needed to be adjusted to obtain the mode-matching condition. The absorptance spectra of at the three modelled radii following the updated mode-matching conditions are included in Figure 6-3a, illustrating the near-unity selective behaviour of the single standing mode-matched tapered-NW absorber. Figure 6-1b is adapted with cyan markers and presented as an inset in Figure 6-3a to illustrate how the modified waveguide dimensions of the tapered NW absorber relate to the n_{eff} cut-offs. The absorptance (A) spectra of the mode-matched tapered NW absorber ($\rho \approx 55$ nm) with its corresponding transmittance (T) and reflectance (R) can be observed in Figure 6-3b. The added inset to Figure 6-3b presents the $|\mathbf{E}|$ cross section in the yz-plane of the NW absorber, which emphasizes the rapid absorption of the incident field ($\lambda = 615$ nm) in the tapered NW tip before reaching the waveguide region resulting from mode matching. Additionally, the A, R, and T spectra illustrate the inherent anti-reflective nature of the tapered NW at the target wavelength and that scattering is the predominant cause of absorption loss of the NW absorber. The scattering cross section was studied at unoptimized mode-matching parameters (focal point position, convergence angle, and wavelength) to reveal scattering characteristics of the NW. The detuning spanned a range around the mode-matched values and reveals an inverse relationship between absorptance and scattering cross section, illustrating that when the mode-matched conditions are met the scattering cross section is minimized for maximum absorptance, as shown in Figure 6-3c, Figure 6-3d, Figure 6-3e, and Figure 6-3f. The change in focal point position requirement for mode matching to the NW absorber, with the red-shifted target wavelength, can also be observed in the detuning trends of Figure 6-3c and Figure 6-3e. That is, the focal point position of the Gaussian beam is required to be positioned deeper into the NW waveguide for increasing wavelengths. As for the convergence angle response (Figure 6-3d and Figure 6-3f), the target wavelength is found to tend to lower values with an increasing convergence angle, illustrating some

potential for tuning the maximally absorbed wavelength of the NW absorber through the selected convergence angle of the source.

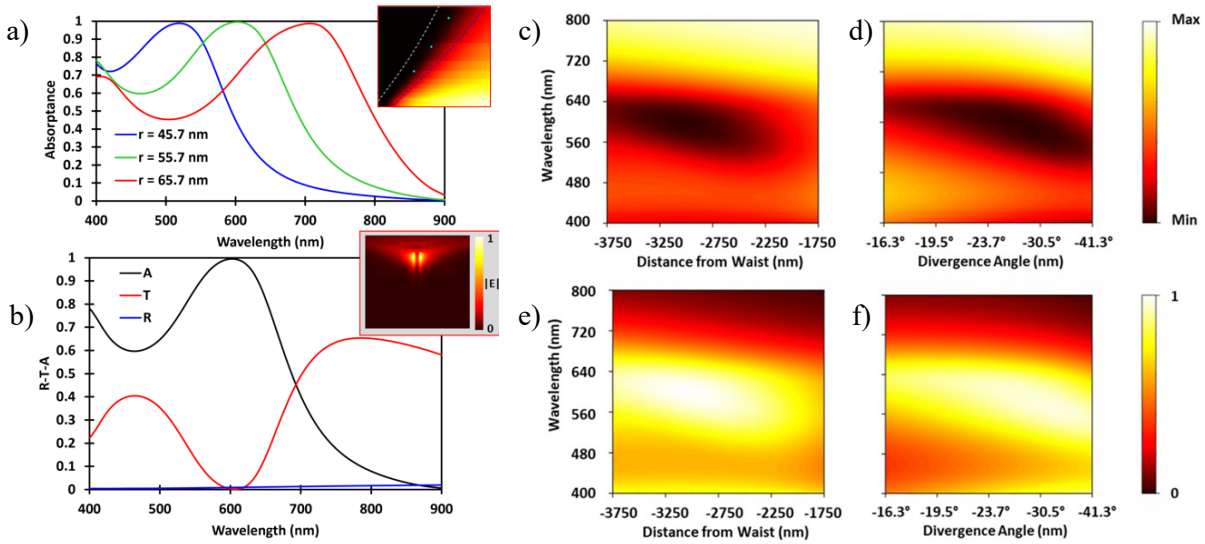

Figure 6-3: Mode-matched coupling to a near-unity (99.7%) single tapered InP nanowire (NW) absorber. a) Absorptance spectra of three modelled radii (ρ = 45.7 nm, ρ = 55.7 nm, and ρ = 65.7 nm) in mode-matched single tapered InP NW absorbers. The inset includes an adapted Figure 6-1b with cyan markers identifying the modified waveguide dimensions as they relate to the neff cut-off regions. **b)** The absorptance (A), transmittance (T), and reflectance (R) spectra of the mode-matched tapered NW absorber ($\rho \approx 55$ nm) with an inset of the $|\mathbf{E}|$ profile in the yz-plane cross section of the NW absorber at λ = 615 nm. Scattering cross section (colour bar) dependence on the wavelength with the detuning of the mode-matching condition parameters of **c)** focal point position and **d)** convergence angle. Absorptance (colour bar) dependence on the wavelength with the detuning of the mode-matching condition parameters of **e)** focal point position and **f)** convergence angle.

6.2.6 Single Nanowire Photodetector

The electrical characteristics of semiconductor NWs have presented desirable qualities that make them an appealing optoelectronic platform, having already been demonstrated in applications such as photoconductors, photovoltaic, phototransistors, and photoconductive switches[1,12,17]. NW optoelectronic developments have applied axial and radial p-n junctions for photodetection[17]. NW photovoltaic devices with axial junctions have been presented with higher efficiencies than their radial counterparts, but radial junctions remain an attractive format because of their performance in other

desirable properties like reduced bulk recombination and fast response times. As such, NW radial p-n junctions would benefit from the higher efficiencies enabled by the mode-matching method[12,49]. The NW near-unity absorber poses as a prospective means to improve DE in nano-optoelectronics. To study the potential performance impact of the NW near-unity absorber, we model several critical optoelectrical characteristics of the NW absorber integrated with a radial p-n junction in the software: Ansys Charge. We model the optoelectrical attributes of an InP core-shell radial p-n junction integrating the single tapered NW near-unity absorber (ρ = 45 nm) under the mode-matched conditions for enhanced absorption in a prospective design targeting applications that demand high speed and sensitivity. The modelled NW diode includes a 21 nm radius $1x10^{18}$ cm^{-3} n-doped core and a 24 nm thick $1x10^{18}$ cm^{-3} p-doped shell with contacts at the NW tip and base. A concept diagram of the modelled radial junction tapered NW sensor is included in Figure 6-4a. The device geometry is designed to be considerate of conventional fabrication techniques of high quality tapered NWs with a high built-in junction potential[30,50,51]. The resulting unbiased electric field, Re(**E**), profile under $5x10^{-13}$ W illumination is predominantly orthogonal to the NW axis and spans the length of the NW core, as observed in Figure 6-4b. From the optical absorption modelling, the *yz*-plane cross-section of the generation rate profile in the single tapered NW near unity absorber is produced with respect to a source power of 1 W at λ = 514 nm in Figure 6-4c. It is clear to see the result of the enhanced absorption response in the carrier generation rate. For instance, the generated carriers are at a minimum at the top and bottom of the tapered NW where the light does not interact or reach in the absorber, respectively. Also, the carrier generation is concentrated primarily along the sidewalls in the bottom half of the taper from the rapid absorption of the incident light upon interaction with the absorber. The regions with significant generated carriers overlap with the built-in field produced by the radial junction, immediately subjecting the carriers to a field for their rapid transport and collection, necessary qualities for the high-speed response of the near-unity absorber. An artistic concept was prepared for a prospective nano-sensor including a 2x2 array of selective near-unity absorber radial p-n junction of different radii and mode matched for different target wavelengths in Figure 6-4d. The prospective sensor is illustrated receiving a multiwavelength source split into 4 fibers for signal decomposition by the wavelength selective mode-matched sensors. The concept nano-sensor includes BCB planarization and isolated ITO top contact layers, photonic wire-bond coupling fibers, and circular gold top electrodes around the single tapered semiconductor NW photodetectors. Though some promise is clear, further device operation modelling such as illumination dependent I-V and temporal response is required to

better understand the potential of this NW absorber radial p-n junction application as a low-dimensional material opto-electronic device.

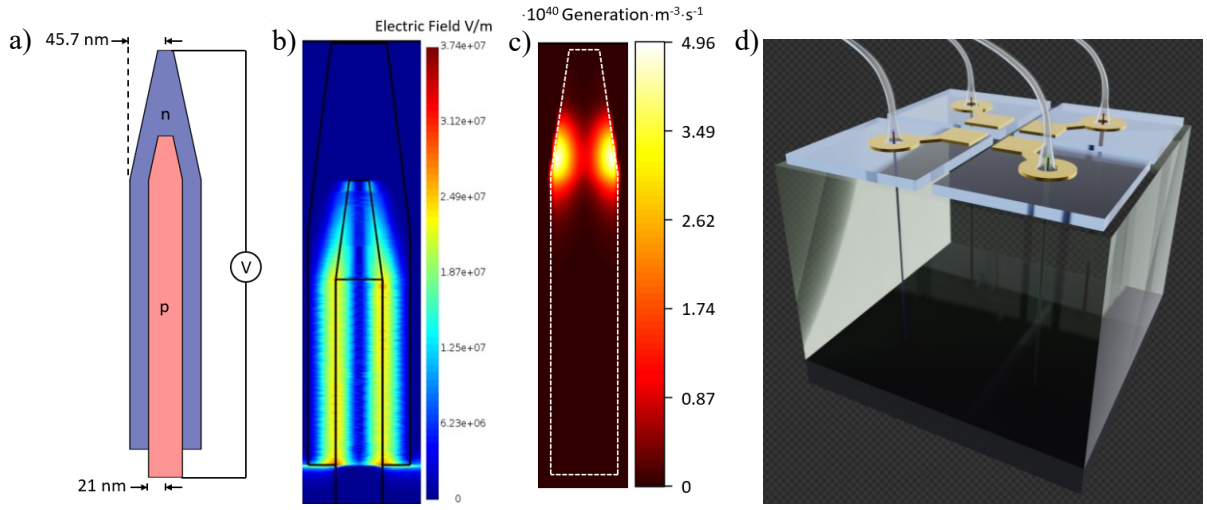

Figure 6-4: Prospective implementation of the near-unity single tapered InP nanowire (NW) perfect absorbed into a radial p-n junction nano-optoelectronic device. a) Concept design of the semiconductor radial junction single NW p-n junction. The design includes a 21 nm radius $1x10^{18}$ cm^{-3} p-doped core and a 24 nm thick $1x10^{18}$ cm^{-3} n-doped shell (ρ = 45 nm) and contacted from the isolated base and NW tip. **b)** Modelled built in electric field (colour bar), Re(**E**), of the tapered single InP NW structure produced from the defined radial p-n junction at 0 V bias and $5x10^{-13}$ W illumination. **c)** Modelled generation rate (colour bar) profile resulting from the near-unity absorptance of the NW absorber with respect to a source power of 1 W at λ = 514 nm. **d)** Artistic impression of a concept nano-optoelectronic device incorporating the near-unity absorbers as photodetectors. The concept device also includes a BCB planarization layer, isolated ITO top contacts, gold top electrodes for wire-bonding, and photonic wire-bonds applied to the selective single NW photodetectors.

6.2.7 Conclusions

We have presented a mode-matching method for maximizing coupling and absorption efficiencies for high-performance nanoscale optoelectronic devices. We leverage the adiabatic nature of tapered coupling to present the potential of the mode-matching method in nano-optoelectronics, demonstrated through the numerical modelling of a single semiconductor tapered NW near-unity (> 99%) absorber and core-shell NW photodetector. With the push for nanoscale optoelectronics, demands are high for efficient and practical room temperature technologies. Single semiconductor tapered NWs offer a

compelling platform to satisfy this demand but important performance qualities, including limited efficiencies, prevent their widespread application. The mode-matching method aids in counteracting this limitation by enhancing efficiencies, complimenting the already advantageous qualities of the NW platform, such as the capability for polarization independence and selective wavelength tunability for targeted confinement. As such, the methods of this work expand the capabilities of the single NW platform for nano-optoelectronic devices for their application in practical high-performance nano-optoelectronic technologies with the smallest achievable footprint. The mode-matching method here minimized the footprint for a wavelength selective approach with InP; however, similar techniques can be applied to study mode matching in different bandwidths with other materials and in the MM regime for broader bandwidth devices. Further work could also include the numerical study of mode-matched single tapered NWs in a quantum network for enhanced efficiencies through the mode-matching techniques with QD imbedded NW devices for telecommunication. Similarly, mode matching can be explored in specific nanophotonic systems, such as in the selective NW detectors of the concept device, which requires the impact of the transparent planarization and top contact layers to be accounted for prior to fabrication. The realization of efficiency improvements by the mode-matching method can also be investigated in the application of GRIN material lenses with single tapered NW nano-optoelectronic devices. These examples highlight the potential of the mode-matching method in our work, which shows promise for a far-reaching impact on technologies from biomedical imaging to integrated photonics in classical and quantum applications through its potential to improve the performance in an already extensive class of nano-optoelectronics.

6.2.8 References

1. Li, Y., Qian, F., Xiang, J. & Lieber, C. M. Nanowire electronic and optoelectronic devices. *Materials Today* **9**, 18–27 (2006).
2. Knill, E., Laflamme, R. & Milburn, G. J. A scheme for efficient quantum computation with linear optics. *Nature* **409**, 46–52 (2001).
3. Politi, A., Matthews, J. C. F. & O'Brien, J. L. Shor's Quantum Factoring Algorithm on a Photonic Chip. *Science* **325**, 1221–1221 (2009).
4. Wang, J., Sciarrino, F., Laing, A. & Thompson, M. G. Integrated photonic quantum technologies. *Nat. Photonics* **14**, 273–284 (2020).

5. Eng, P. C., Song, S. & Ping, B. State-of-the-art photodetectors for optoelectronic integration at telecommunication wavelength. *Nanophotonics* **4**, 277–302 (2015).
6. Matthews, J. C. F., Politi, A., Stefanov, A. & O'Brien, J. L. Manipulation of multiphoton entanglement in waveguide quantum circuits. *Nature Photon* **3**, 346–350 (2009).
7. Aspuru-Guzik, A. & Walther, P. Photonic quantum simulators. *Nature Phys* **8**, 285–291 (2012).
8. Nielsen, M. A., Chuang, I. & Grover, L. K. *Quantum Computation and Quantum Information*. *American Journal of Physics* **70**, 558–559 (2002).
9. Logeeswaran, V. J. *et al.* A 14-ps full width at half maximum high-speed photoconductor fabricated with intersecting InP nanowires on an amorphous surface. *Appl. Phys. A* **91**, 1–5 (2008).
10. Chiba, K., Yoshida, A., Tomioka, K. & Motohisa, J. Vertical InGaAs Nanowire Array Photodiodes on Si. *ACS Photonics* **6**, 260–264 (2019).
11. Brenneis, A. *et al.* Photocurrents in a Single InAs Nanowire/Silicon Heterojunction. *ACS Nano* **9**, 9849–9858 (2015).
12. LaPierre, R. R., Robson, M., Azizur-Rahman, K. M. & Kuyanov, P. A review of III–V nanowire infrared photodetectors and sensors. *J. Phys. D: Appl. Phys.* **50**, 123001 (2017).
13. Vj, L. *et al.* A Perspective on Nanowire Photodetectors: Current Status, Future Challenges, and Opportunities. *IEEE J. Select. Topics Quantum Electron.* **17**, 1002–1032 (2011).
14. Otuonye, U., Kim, H. W. & Lu, W. D. Ge nanowire photodetector with high photoconductive gain epitaxially integrated on Si substrate. *Appl. Phys. Lett.* **110**, 173104 (2017).
15. van Kouwen, M. P. *et al.* Single quantum dot nanowire photodetectors. *Appl. Phys. Lett.* **97**, 113108 (2010).
16. Gibson, S. J. *et al.* Tapered InP nanowire arrays for efficient broadband high-speed single-photon detection. *Nat. Nanotechnol.* **14**, 473–479 (2019).
17. Li, Z. *et al.* Review on III-V Semiconductor Single Nanowire-Based Room Temperature Infrared Photodetectors. *Materials* **13**, 1400 (2020).
18. Hadfield, R. H. Single-photon detectors for optical quantum information applications. *Nature Photon* **3**, 696–705 (2009).
19. Zhan, Y. *et al.* Enhanced photoabsorption in front-tapered single-nanowire solar cells. *Opt. Lett.* **39**, 5756 (2014).
20. Sun, J., Han, M., Gu, Y., Yang, Z. & Zeng, H. Recent Advances in Group III-V Nanowire Infrared Detectors. *Advanced Optical Materials* **6**, 1800256 (2018).

21. Marsili, F. *et al.* Detecting single infrared photons with 93% system efficiency. *Nature Photon* **7**, 210–214 (2013).
22. Koppens, F. H. L. *et al.* Photodetectors based on graphene, other two-dimensional materials and hybrid systems. *Nature Nanotech* **9**, 780–793 (2014).
23. Konstantatos, G. *et al.* Hybrid graphene–quantum dot phototransistors with ultrahigh gain. *Nature Nanotech* **7**, 363–368 (2012).
24. Xia, F., Mueller, T., Lin, Y., Valdes-Garcia, A. & Avouris, P. Ultrafast graphene photodetector. *Nature Nanotech* **4**, 839–843 (2009).
25. Mauthe, S. *et al.* High-speed III-V nanowire photodetector monolithically integrated on Si. *Nat Commun* **11**, 4565 (2020).
26. Bulgarini, G. *et al.* Avalanche amplification of a single exciton in a semiconductor nanowire. *Nature Photon* **6**, 455–458 (2012).
27. Cao, L. *et al.* Engineering light absorption in semiconductor nanowire devices. *Nature Mater* **8**, 643–647 (2009).
28. Claudon, J. *et al.* A highly efficient single-photon source based on a quantum dot in a photonic nanowire. *Nature Photon* **4**, 174–177 (2010).
29. Reimer, M. E. *et al.* Bright single-photon sources in bottom-up tailored nanowires. *Nat Commun* **3**, 737 (2012).
30. Dalacu, D., Poole, P. J. & Williams, R. L. Nanowire-based sources of non-classical light. *Nanotechnology* **30**, 232001 (2019).
31. Haffouz, S. *et al.* Bright Single InAsP Quantum Dots at Telecom Wavelengths in Position-Controlled InP Nanowires: The Role of the Photonic Waveguide. *Nano Lett.* **18**, 3047–3052 (2018).
32. Ma, Y., Guo, X., Wu, X., Dai, L. & Tong, L. Semiconductor nanowire lasers. *Adv. Opt. Photon.* **5**, 216 (2013).
33. Tong, L. *et al.* Subwavelength-diameter silica wires for low-loss optical wave guiding. *Nature* **426**, 816–819 (2003).
34. Maruf, R. A. *et al.* High Efficiency Fiber-Coupled Single-Photon Source Based on Quantum Dot Embedded in a Semiconductor Nanowire. in *Conference on Lasers and Electro-Optics* JW2A.14 (Optica Publishing Group, 2020). doi:10.1364/CLEO_AT.2020.JW2A.14.

35. Luque-González, J. M. *et al.* An Ultracompact GRIN-Lens-Based Spot Size Converter using Subwavelength Grating Metamaterials. *Laser & Photonics Reviews* **13**, 1900172 (2019).
36. Kuyanov, P. & LaPierre, R. R. Photoluminescence and photocurrent from InP nanowires with InAsP quantum dots grown on Si by molecular beam epitaxy. *Nanotechnology* **26**, 315202 (2015).
37. Anttu, N. Absorption of light in a single vertical nanowire and a nanowire array. *Nanotechnology* **30**, 104004 (2019).
38. Tong, L., Lou, J. & Mazur, E. Single-mode guiding properties of subwavelength-diameter silica and silicon wire waveguides. *Opt. Express* **12**, 1025 (2004).
39. Krogstrup, P. *et al.* Single-nanowire solar cells beyond the Shockley–Queisser limit. *Nature Photon* **7**, 306–310 (2013).
40. Le Kien, F., Busch, T., Truong, V. G. & Nic Chormaic, S. Higher-order modes of vacuum-clad ultrathin optical fibers. *Phys. Rev. A* **96**, 023835 (2017).
41. Wiedemann, U. *et al.* Measurement of submicrometre diameters of tapered optical fibres using harmonic generation. *Opt. Express* **18**, 7693 (2010).
42. Mokkapati, S., Saxena, D., Tan, H. H. & Jagadish, C. Optical design of nanowire absorbers for wavelength selective photodetectors. *Sci Rep* **5**, 15339 (2015).
43. Snyder, A. W. & Love, J. D. *Optical waveguide theory*. (Chapman and Hall, 1983).
44. Kumar, R. *et al.* Interaction of laser-cooled ^{87} Rb atoms with higher order modes of an optical nanofibre. *New J. Phys.* **17**, 013026 (2015).
45. Wang, X. *et al.* High Gain Submicrometer Optical Amplifier at Near-Infrared Communication Band. *Phys. Rev. Lett.* **115**, 027403 (2015).
46. Bleuse, J. *et al.* Inhibition, Enhancement, and Control of Spontaneous Emission in Photonic Nanowires. *Phys. Rev. Lett.* **106**, 103601 (2011).
47. Bulgarini, G. *et al.* Nanowire Waveguides Launching Single Photons in a Gaussian Mode for Ideal Fiber Coupling. *Nano Lett.* **14**, 4102–4106 (2014).
48. Dagytė, V. & Anttu, N. Modal analysis of resonant and non-resonant optical response in semiconductor nanowire arrays. *Nanotechnology* **30**, 025710 (2019).
49. Gallo, E. M. *et al.* Picosecond response times in GaAs/AlGaAs core/shell nanowire-based photodetectors. *Appl. Phys. Lett.* **98**, 241113 (2011).
50. Haggren, T. *et al.* Lithography-free shell-substrate isolation for core–shell GaAs nanowires. *Nanotechnology* **27**, 275603 (2016).

51. Chia, A. C. E. & LaPierre, R. R. Electrostatic model of radial pn junction nanowires. *Journal of Applied Physics* **114**, 074317 (2013).

Chapter 7
Future Opportunities

7.1 Preface

While the NW metamaterial has demonstrated an unprecedented broadband near-unity enhanced absorption using InGaAs, the challenge of integrating the advanced materials for SPAD operation remains. As previously noted, SPAD development can be subcategorized into four primary technologies of focus: (i) materials, (ii) device design, (iii) signal processing (circuitry), and (iv) higher level multiplexing[1]. The primary works detailed the design and behaviour of advanced materials. In the following sections, the work progress and relevant background on the signal processing (circuitry) and some of the device design considerations are presented, along with proposals for future work opportunities. As the signal processing had not yet been successfully implemented in the metamaterial SPAD development process, higher level multiplexing had not yet been pursued.

7.2 InGaAs/InAlAs Nanowire Metaatom Single-Photon Avalanche Diode Design

To operate as a SPAD, the NW metamaterial was doped with a p-n junction during fabrication for photodetection capabilities. The tapered NW p-n junction arrays of the first primary work were fabricated with n-doped NW tips and p-dope NW base (and substrate), details of which are included in the supplementary information of the published article of Chapter 3. Early SPAD operation measurements with these devices were unsuccessful, as discerning a single trigger event was not achieved even under lower temperature operation (approx. -50°C). The experimental work, results, and analysis of the InP metamaterial SPAD i.e., the semiconductor nanowire single-photon avalanche diode (SN-SPAD), measurements are included in Section 7.5. The InGaAs metamaterial was developed to extend operation deeper into the IR, but they were also fabricated with a similarly designed p-n junction array to perform similar optoelectronic response measurements. However, the InGaAs devices operated from room temperature down to 100K did not produce the characteristic I-Vs for SPAD operation, though some success was found in optoelectronic responsivity measurements performed on the samples by Burak Tekcan. These results and design details are considered in the work of his thesis. As the IR spectral region remained the target for the SN-SPAD, an SAGCM design was incorporated into the structure. InGaAs remained the absorber and InAlAs was the multiplication region material. The active area of the SAGCM samples were also reduced to ~25 μm in radius to decrease the DCR, down from

the 300 µm x 300 µm of the InP metamaterial and 100 µm x 100 µm of the InGaAs metamaterial SN-SPADs. Some success was found in the I-V characteristics of the device samples; however, high dark currents inhibited their potential for SPAD operation even at reduced temperature operation. To better understand the device design qualities and operation for SPAD applications, the metaatoms of the SAGCM metamaterial devices developed by Burak Tekcan were numerically modelled with critical bulk device design concepts from literature. The following study is meant to provide insight for the operating behaviour of the tapered NW p-n junction array behaviour compared to planar SPAD operating qualities.

7.2.1 Introduction

SPAD design requires a comprehensive understanding of a wide range of trade-offs, as critical performance metrics often compete with one another, requiring unique design considerations and parameters to be leveraged for state-of-the-art performance. Concepts from literature are applied in electrical numerical modelling via Ansys Lumerical CHARGE of a NW array based InGaAs/InAlAs SAGCM design for possible fabrication into a high-performance SPAD. For detailed information on the simulation tool, see Ansys optics knowledge base for Charge (https://optics.ansys.com/hc/en-us) which has resources describing the simulation tool's methods and examples. Bulk SAGCM structures have been well studied, but the impact of incorporating the SAGCM stack into a NW array has not been rigorously investigated[2–4]. This report presents analysis of several conventional SPAD design parameters on a tailored SAGCM structure in a single NW device. The material stack implemented in the numerical analysis was prepared by fellow Dr. Reimer group member, Burak Tekcan, for SN-SPAD fabrication with an active area defined by an array of many of the individual NWs modelled here. Three of the major design factors discussed here appeared to be critical in the performance of SPADs from literature, including the electric field profile, energy band structure, and I-Vs. These factors were analyzed alongside another factor of interest, the carrier density, available in the electrical modelling software to better understand the feasibility of a NW array based InGaAs/InAlAs SAGCM SPAD.

7.2.2 Nanowire Material Stack

The modelled material stack, Figure 7-1a, is an SAGCM structure with qualities similar to those presented in literature[3]. The material stack was imported into Lumerical electrical modelling software, where a tapered NW structure of the form shown in Figure 7-1b was generated. Optical models of InGaAs tapered NW arrays found high absorptance performance with a top diameter, taper angle,

height, and periodicity of 350 nm, 11°, 1400 nm, and 900 nm, respectively[5]. These parameters were used to define the structure in the Lumerical models, which included a NW top diameter and taper angle of 350 nm and 15°, respectively. The height and periodicity modelled in this study differed from the optical models, however. In this study, a range of NW heights (etch depths) is swept with one modelled region width (*x*-axis). The heights (*z*-axis) ranged from 0 nm to 2100 nm to determine the effect of etching through different SAGCM layers. Also, the modelled region width is set to 2 µm to accommodate the largest NW bottom radius at the maximum 2100 nm height instead of matching the smaller periodicity optimized for absorptance. Of the studied heights, the most insightful results are found for the 1300 nm NW, so the 1300 nm height Lumerical models are in focus for all subsequent discussions. Though the 1300 nm height results offered the most useful data for analysis, it is not necessarily the best height for performance. The numerical models have many parameters that capture different physics, and all of the modelling performed can benefit from more analysis to improve confidence in the data. However, some interesting insights are still realized from the analysis of the 1300 nm height NW numerical modelling.

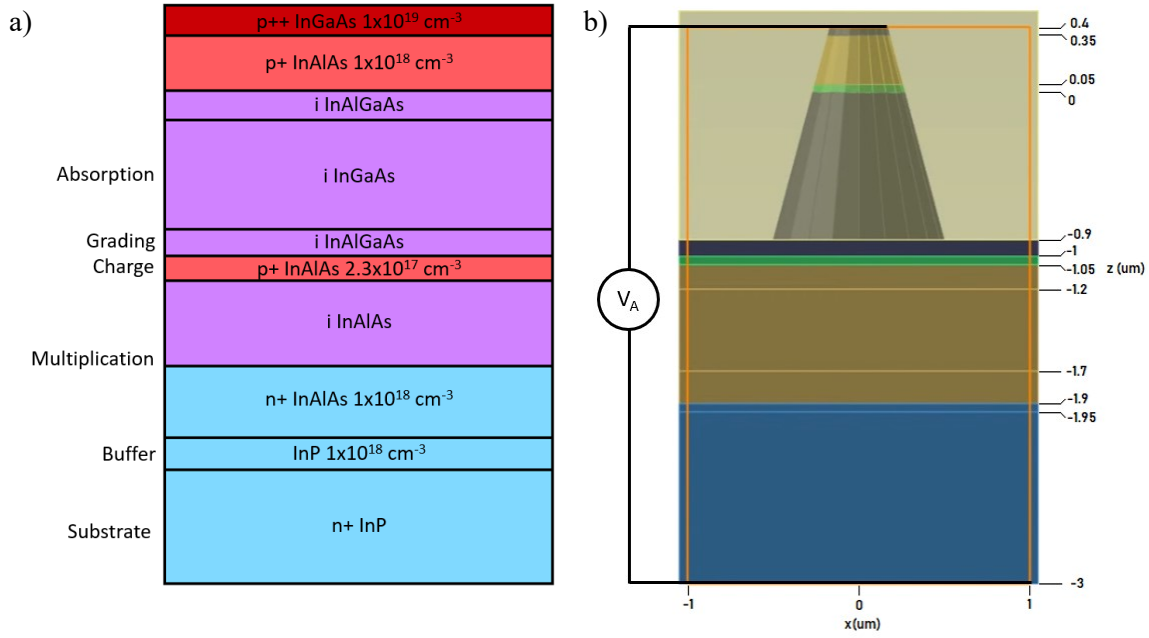

Figure 7-1: Modelled InGaAs/InAlAs single-photon avalanche diode structures with separate absorption, grading, charge, and multiplication layers. a) The InGaAs/InAlAs material stack on an InP substrate cross-section with denoted device layers, materials, and doping concentrations **b)** 1300 nm tapered nanowire single-photon avalanche diode Lumerical model with denoted layer thicknesses.

7.2.3 Electric Field Profile

Examples from literature offered desirable electric field profiles for an InGaAs/InAlAs SAGCM SPAD[2]. A cross section of the NW SPAD electric field along the *z*-axis results from the Lumerical modelling is included in Figure 7-2. The numerically modelled electric field profile shows common qualities with the expected results from literature, including the high multiplication region (from z = -1.2 μm to z = -1.7 μm) field and low absorption region (z = 0 μm to z = -1 μm) field. This field profile transports the generated carriers from light absorption in the low-field absorption layer to the high-field region for multiplication, while limiting unwanted dark current contributions from the low-bandgap absorber layer. For clarity, the dashed violet line is included to indicate the end of the absorption layer. Though common attributes are found with the example field from literature, the modelled NW SPAD does not yet appear to have reached a desirable avalanche breakdown. That is, the produced electric field profile at the highest achievable modelled bias does not yet extend across the whole multiplication and absorption region of the device.

The *z*-component field plotted in Figure 7-2 illustrates the dynamics of the field profile with increasing reverse bias. As reverse bias increases the fields generally increase and the negative field regions from the charge layer and contact/cladding invert. From this, it is apparent that the field in the multiplication region will continue to increase. This continued increase may be problematic as the peak field in this region is already near the tunneling threshold electric field of 680 kV/cm despite not yet appearing to be operating in the targeted breakdown mode[2]. Furthermore, the field in the InGaAs layer is near zero, a quality that limits DE in SPADs because of the generated carrier's reduced chance of reaching the multiplication layer before recombination. This low field in the absorption region suggests that the etch depth must be further optimized for this material stack. Alternative solutions, such as modifying the doping concentrations, can also be implemented in the numerical modelling to achieve a higher field in the absorption region for this NW geometry. However, incorporating such doping modifications to the SN-SPAD currently in development would require the growth of another planar material stack.

Non-uniformities in the active area breakdown are also known to be a problematic quality[6]. For instance, in the work titled "New InGaAs/InP Avalanche Photodiode Structure for the 1-1.6 μm Wavelength Region" by N. Susa et al. the mesa structure was etched with a "positive beveled surface at the n-InP layer" to prevent edge breakdown[7]. In SPADs, non-uniformities in the field may alter critical performance metrics like DE and temporal response based on the photon absorption location[8]. Surface electric field plots over the tapered NW structure were thus studied to identify potentially

problematic non-uniformities arising from the structure's geometry from factors like edge and corner effects, which may cause breakdown variation. The 2D electric fields for the 1300 nm etched NW at 0 V and -37 V are included in Figure 7-3a and Figure 7-3b. Both electric field profiles do not show any significant field enhancement of concern at the corners or edges. While the numerical modelled electric field demonstrates minimal variation at the NW base, imperfections during the development process of NWs including inhomogeneities in the doping profile and microfabrication processes, such as faster etch rates (deeper etch depth) at the active area device perimeter, are suspected to be potential causes breakdown of non-uniformities in the device active region. More extensive numerical models incorporating etch depth and doping variation may offer insight into breakdown variation between neighbouring NWs within the same active area. Furthermore, the breakdown variations across the SN-SPAD active area may also be characterized experimentally through emission intensity measurements to study the prominence of modelled behaviours[8].

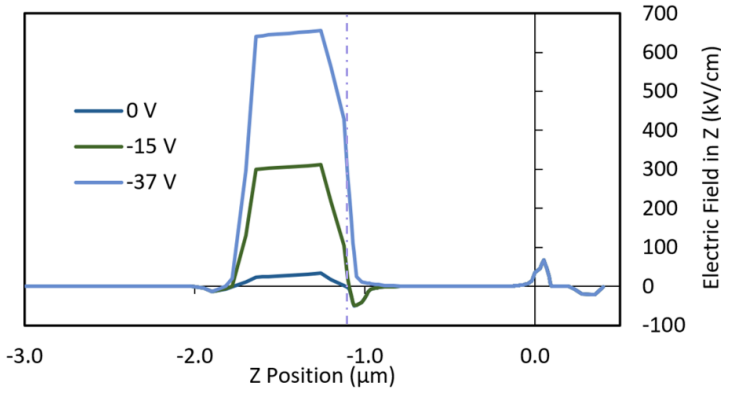

Figure 7-2: Modelled InGaAs/InAlAs nanowire single-photon avalanche diode electric field profiles at x = 0 µm and bias voltages of 0 V, -15 V, and -37 V.

7.2.4 Band Diagram

Another critical feature often studied for SPAD design is the energy band structure. In the article "InGaAs/InAlAs single-photon avalanche diode for 1550 nm photons" by X. Meng et al. a band diagram for a comparable device was presented[4]. Figure 7-4a illustrates the Lumerical modelled NW energy band diagram at 0 V with generally matching trends to the literature example. Though general observations can be made from the literature example, analysis of key details like the impact of the grading layers on the energy bands remains difficult. In the Lumerical NW models, however, the impact

of the grading layer is easily observed. The large energy barriers that would have otherwise been present without the grading layers are found to be split into multiple smaller energy barriers. The larger energy barrier can be observed in Figure 7-4b, where the numerical modelling was run with the InAlGaAs layers removed and substituted for intrinsic InGaAs. Also, in addition to the valance and conduction band structure, the Lumerical NW models presented includes the intrinsic (Ei), electron (Efn), and hole (Efp) fermi energies. The relative energy levels remain relatively constant even after the band bending that occurs from reverse biasing to the model's limit (-37 V). The band structure at -37 V bias is included in Figure 7-4c and Figure 7-4d with reduced *z*-axis limits to distinguish the otherwise obscured energy levels of the full band diagram of Figure 7-4e. In this SPAD design, electrons are the carrier selected to undergo multiplication. Figure 7-4c emphasizes the importance of the grading layer in improving the electron transport to the multiplication layer and substrate. That is, the discrete and reduced energy barriers in the conduction band resulting from the grading layer are clearly visible at the InAlGaAs grading and InGaAs absorbing layer heterojunction (violet dashed line at -1 μm).

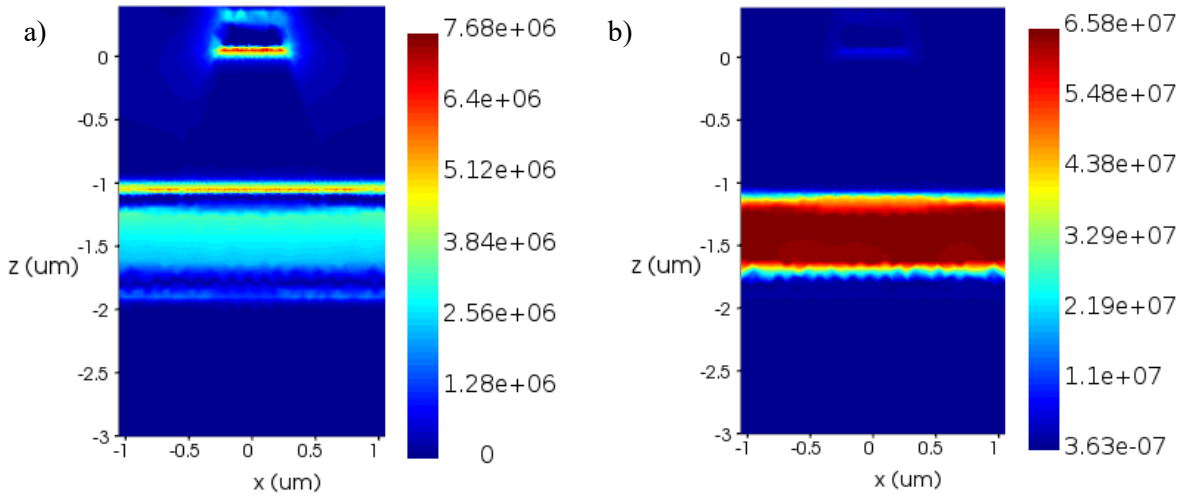

Figure 7-3: Modelled InGaAs/InAlAs nanowire single-photon avalanche diode *xz*-plane cross-section electric field profiles. Electric field profile at reverse biases of **a)** 0 V and **b)** -37 V. The colour bar indicates the electric field intensity in V/m.

7.2.5 Charge Distribution

Another interesting design factor included in the Lumerical modelling software, which was studied included the carrier density profile, where some interesting trends were observed. Similar to the electric field profile analysis, the carrier density profiles are presented in both line and surface diagrams in

Figure 7-5 and Figure 7-6, respectively. Figure 7-5a illustrates the dynamics of the electron density with increasing reverse bias. As the reverse bias increases, the electrons appear to saturate in the multiplication region and accumulate at the grading-absorption layer heterointerface. In contrast, the dynamics of the hole density with increasing reverse bias shown in Figure 7-5b appear to demonstrate saturation in layers up to the absorption layer, and the gradual depletion of the absorption layer. Combined, these figures illustrate that the structure is not fully depleted. A fully depleted structure is suspected to have a profile like the electron and hole densities in the multiplication region at 0 V, that is, a stair-like profile through the whole stack; not limited to discrete regions. The observed trends suggest that such a profile may form across the device at higher reverse biases, but the modelled voltage did not reach the values to confirm this response in the carrier densities.

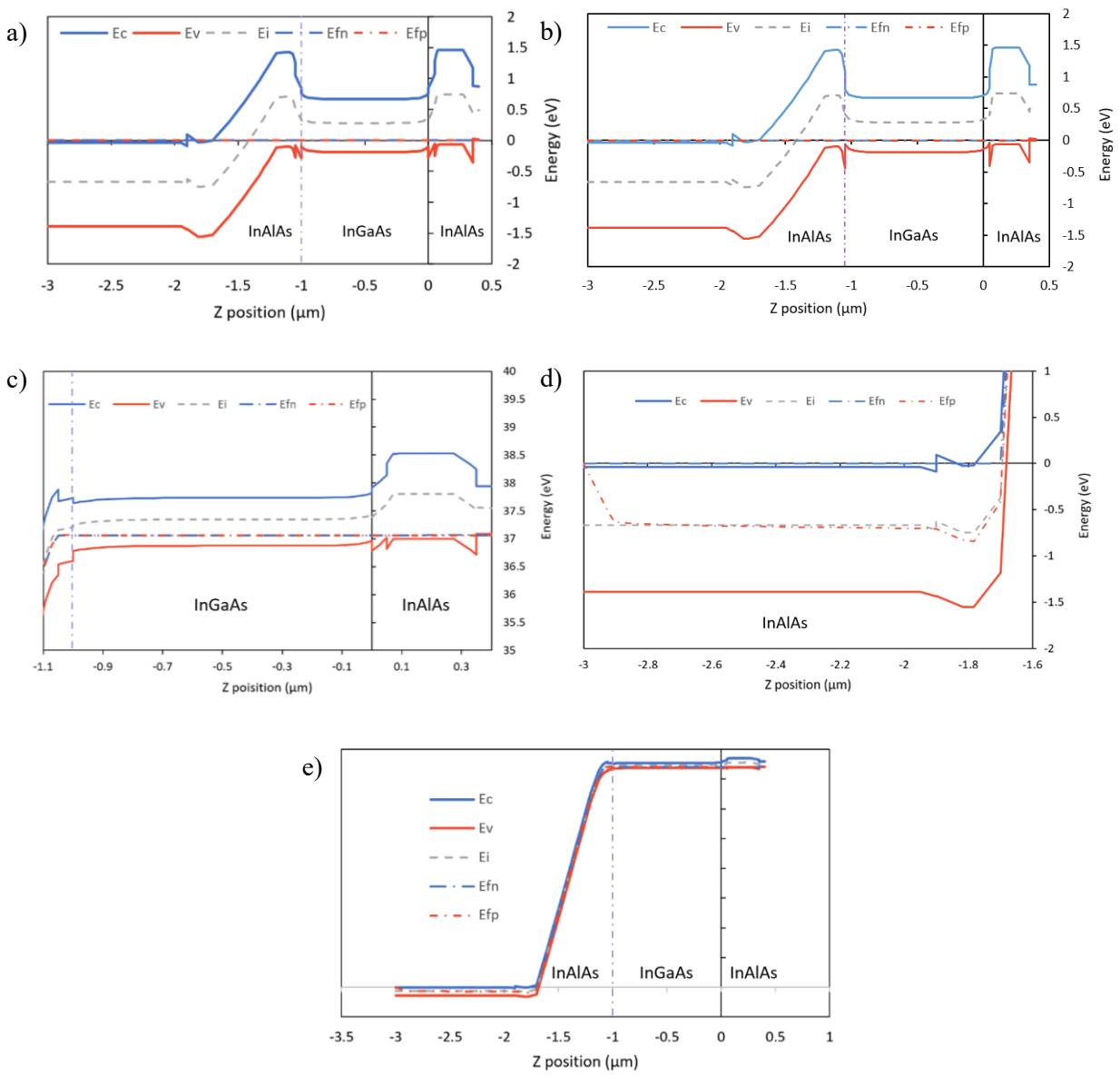

Figure 7-4: Modelled InGaAs/InAlAs nanowire (NW) single-photon avalanche diode (SPAD) energy band diagrams. a) Modelled NW energy band diagram at x = 0 μm and 0 V reverse bias. **b)** Same as **a)** except with InAlGaAs layers substituted for InGaAs in the material stack. **c)** -37 V NW energy band diagram at x = 0 μm and with the z-axis range reduced to the NW tip. **d)** -37 V energy band diagram at x = 0 μm and with the z-axis range reduced to the metamaterial substrate surface. **e)** Modelled NW energy band diagram at x = 0 μm and -37 V reverse bias.

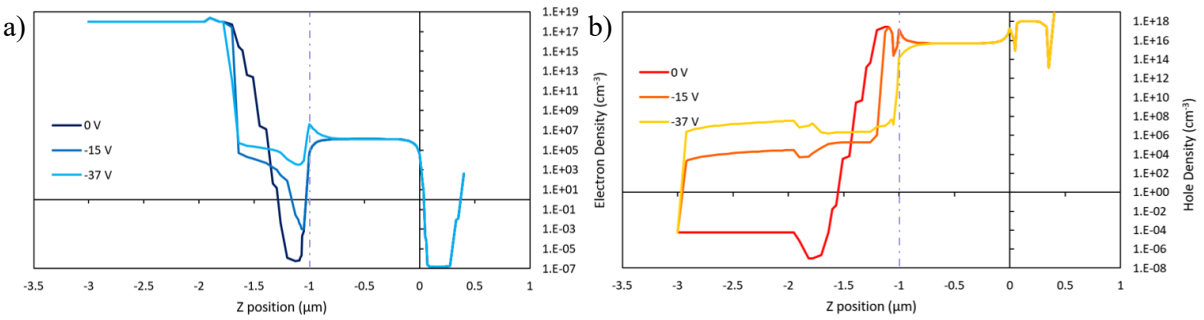

Figure 7-5: Modelled InGaAs/InAlAs nanowire single-photon avalanche diode carrier density profiles. a) Electron density profile at $x = 0$ µm and increasing reverse bias. **b)** Hole density profile at $x = 0$ µm and increasing reverse bias.

The Lumerical modelled NW electron density surface plots obtained at 0 V and -37 V reverse are included in Figure 7-6a and Figure 7-6b, respectively. Similarly, the hole density surface plots at 0 V and -37 V reverse bias are included in Figure 7-6c and Figure 7-6d, respectively. These figures compliment the electric field surface plots, which show relative uniformity. However, at higher reverse biasing it appears that electron buildup is occurring in a ring-like shape in the planar region around the base of the NW. Similarly, an absence of holes is present in the same areas; complimented by a buildup of holes at the inner base of the NW.

7.2.6 Current-Voltage Relationships

Other design factors which can offer critical insight for determining the quality of a SPAD design are photo and dark I-Vs. Several examples of target I-Vs can be found from literature, including modelled and measured InGaAs/InAlAs SPAD I-Vs[2–4,9]. A diagram illustrating a SPAD's desirable avalanche breakdown dark and photo I-V for the modelled device is included in Figure 7-7 with approximate trends and current values. The desired dark I-V profile resembling SPADs with typical active areas (diameter ≈ 25 µm) have a slowly increasing and low dark current (under ~10 nA) until avalanche, where the current increases exponentially into the microamp range. Furthermore, steps in the I-V (if any) which resemble a change in the predominant dark current contributor should be small, as to not cause destructive currents before reaching avalanche breakdown. In the photo I-V, the avalanche breakdown should present itself at a similar voltage and may exaggerate the step observed in the dark current due to punch-through i.e., the depletion of the charge layer to the edge of the absorbing layer[10].

Though photocurrent figures can be generated in the Lumerical software, they require additional optical modelling setup and have not yet been studied here. As a result, the discussion focus is shifted solely to dark current analysis and only the modelled NW dark I-V is presented (Figure 7-8). In the numerically modelled SPAD I-V example from literature, the lower bound on the dark I-V makes it difficult to discern common features with the numerically modelled SPAD here; however, a clear quality of the reference example I-V is the unmatched current rise observed at the breakdown[2]. The modelled NW I-V here has small steps in the current which resemble the onset of different predominant dark current contributors at ~11 V and ~26 V. While these steps in the I-V indicate that some SPAD qualities are being modelled, the result lacks the unmistakable current rise of an avalanche breakdown. This supports the analysis of past sections which found that the max voltage achievable in this Lumerical NW model is currently unable to capture the device breakdown trends in their entirety. Another unusual quality in the modelled NW SPAD I-V is the drop in current that occurs despite the increasing reverse bias in the higher reverse bias range. The sharp rise in current that follows this drop might be the result of the desirable avalanche breakdown, but it is not substantiable. The effects responsible for the modelled NW I-V behaviours are not yet fully understood and should be analyzed further. For instance, analysis of the effect of heat on the I-V should be run to determine thermal and electric field dominant contributions, critical aspects studied in literature. These contributions are necessary for further understanding and gaining confidence in the accuracy of the modelled NW results[11]. Additionally, the inclusion of incident light into the model is expected to aid in distinguishing the punch-through voltage. To better understand the cause and affirm breakdown, further attempts should also be made towards modelling higher VAs (and currents towards 1 nA) through modified physical models, model parameters, and boundary conditions. Also, since the example target I-Vs are the result of bulk structure SPADs, single NW I-Vs should also be investigated for the insightful comparison of current magnitudes.

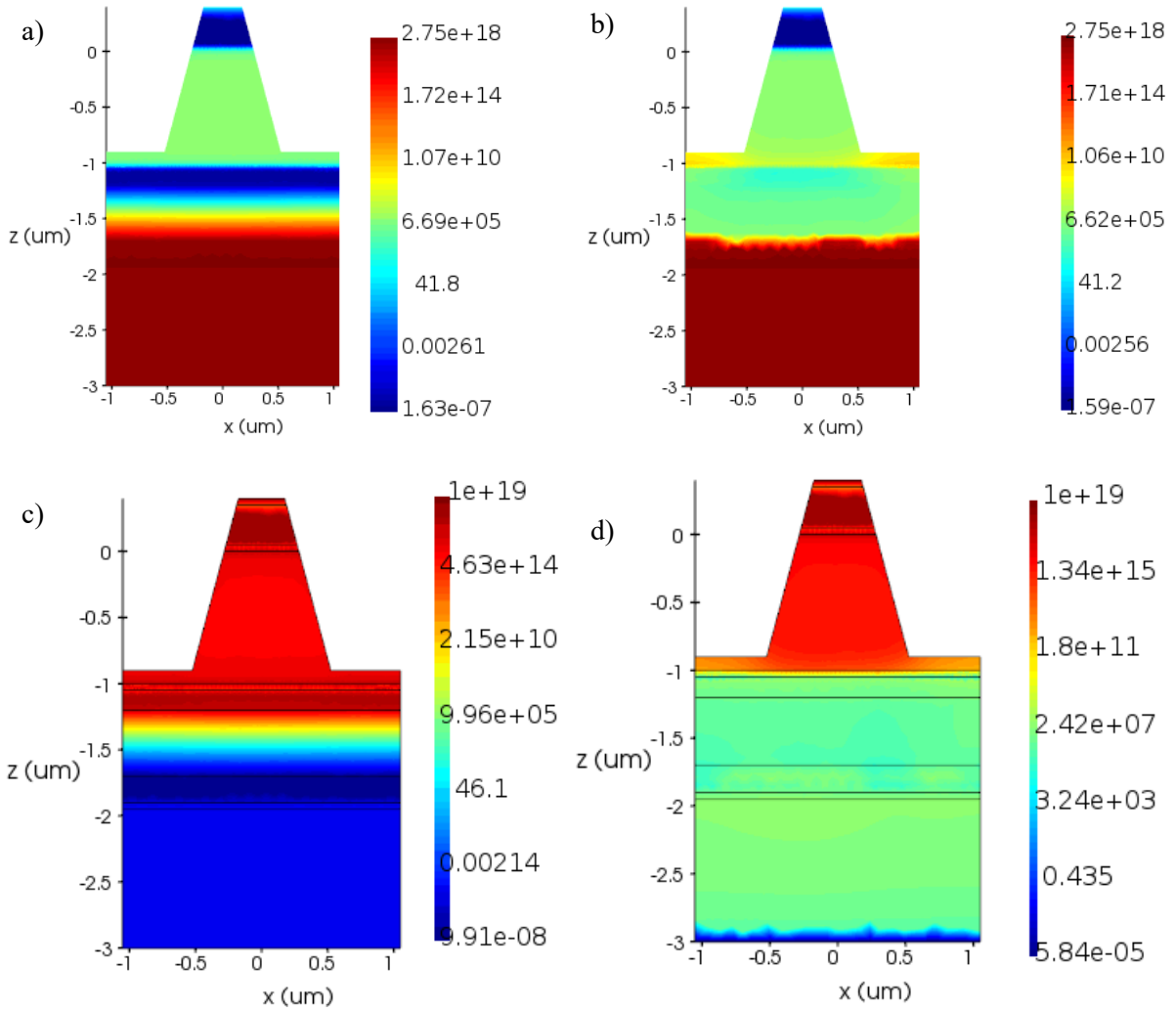

Figure 7-6: Modelled InGaAs/InAlAs nanowire single-photon avalanche diode *xz*-plane cross-section carrier density surface profiles. a) Electron density surface profile at 0 V reverse bias. **b)** Electron density surface profile at -37 V reverse bias. **c)** Hole density surface profile at 0 V reverse bias. **d)** Hole density surface profile at -37 V reverse bias. The colour bar in all of the plots indicates the carrier concentration, per cubic centimeter, of the respective figure.

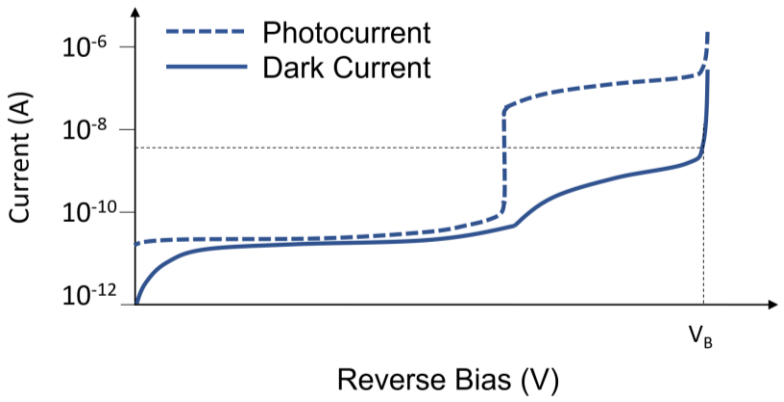

Figure 7-7: Profiles of desirable InGaAs/InAlAs nanowire single-photon avalanche-diode dark (solid) and photo- (dashed) current-voltage (I-V) relationships. The desired dark I-V profile has a slowly increasing and low dark current until avalanche, which then increases exponentially. If there are steps in the current they may indicate a change in the predominant dark current contributor and should be small. Regarding the photo I-V, the avalanche breakdown is expected to be present at a similar voltage and the step in the current at punch-through is expected to be exaggerated.

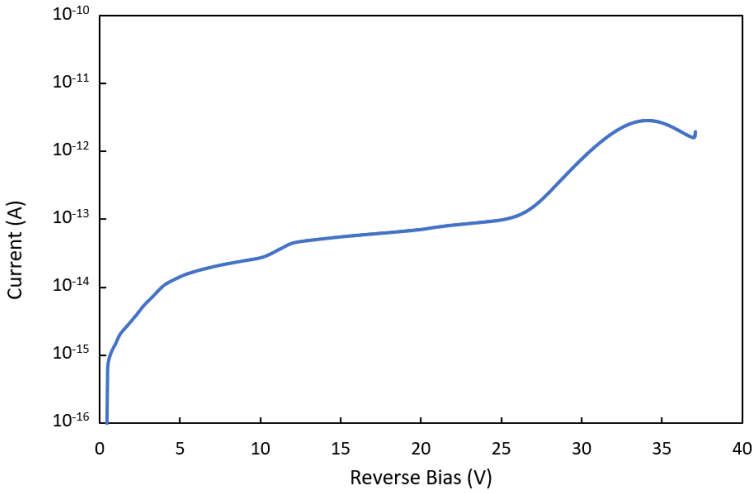

Figure 7-8: Modelled InGaAs/InAlAs nanowire single-photon avalanche diode (SPAD) dark current-voltage (I-V) relationship. The small steps in the current at ~11 V and ~26 V resemble the onset of different predominant dark current contributors and punch-through. These features indicate that some SPAD qualities are being modelled, but the I-V lacks the unmistakable current rise of an avalanche breakdown. The exact cause of the steps in the current and lack of avalanche breakdown behaviour in the numerical model are not yet fully understood and require further study.

7.2.7 Conclusion

In conclusion, Lumerical's electrical modelling software offers many beneficial and unique tools for the design and analysis of potential SPAD designs. Though the modelled NW based SPAD is unique in its design, useful insights were still gained through its analysis with Lumerical. Many similarities were found between the modelled NW SPAD and bulk examples from literature. No observations throughout the study indicated that the fabrication and operation of the NW array-based InGaAs/InAlAs SAGCM as a SPAD is infeasible, supporting the continued potential of the design. Further work, however, is still required to achieve the confidence in the modelling and analysis required to influence device design and fabrication decisions. Such work includes achieving higher modelled operating voltages, more rigorously analyzing and understanding the SPAD I-V behaviour and breakdown variation between NWs, and optimizing various design elements, such as the doping concentration and layer thicknesses design around the fabrication etch depth. The completion of these extended objectives will provide additional necessary understanding for the incorporation of a NW metamaterial with an InGaAs/InAlAs SAGCM SPAD.

7.3 Signal Processing

The high-performance properties of the tapered NW p-n junction array was first demonstrated in its operation as a photodetector; however, additional electronics and quenching circuitry are required to characterize the detector in Geiger-mode operation and understand the potential of this detector as a SPAD against current leaders like SNSPDs. An integral part of the SPAD detection comes from the quenching circuit which, fundamentally, resets and prepares the SPAD after a trigger event. The assembly of an optimized quenching circuit is as important to the SPAD design as the detector itself, as critical metrics can be optimized through proper quenching circuit design including the count rate and timing jitter[6]. Additionally, a SPAD's quenching circuitry must be tailored according to the detector's application. For instance, the total device for imaging is composed of a photodetector array, and each detector in the array requires its own quenching circuitry. To maximize the resolution in such devices, the quenching circuitry may be simplified at the expense of its maximum count rate to make it more compact for a reduced footprint size. Imaging devices are just one of many applications where SPADs act as a critical component of a larger system, and SPAD advancement could further enable the capabilities of these larger systems. The quenching circuit governs SPAD operation, and it is a crucial element in SPAD signal processing developments. Quenching circuits generally fall within one of the

three classes: passive, active, and mixed. The general operations of these different quenching circuit schemes are introduced and modelled through LTspice in the following section, along with gating and a comparison of modern prospective circuits considered for the metamaterial SPAD. Further design details and governing formulas of quenching circuits have been well-studied in published literature[12].

7.3.1 Passive Quenching Circuit

A passive quenching circuit (PQC) design relies on passive components to execute the quenching process, as the name suggests. These circuits have the advantage of being composed of few components, but they generally operate slower than active quenching circuit (AQC) designs. However, with stray capacitance reduced through integrated circuit designs and miniature PCB components, the speed and thereby count rate can be improved, achieving less than 1 μs reset times with modern integration techniques[6]. Despite the lower count rate performance capability, the relative simplicity of the passive quenching circuit is valuable for applications such as high-resolution imaging systems and novel SPADs, where count rate is traded for a smaller pixel footprint and the relative ease of its integration. Figure 7-9a illustrates a PQC in current mode, which was modelled for incorporation into the SN-SPADs.

The SN-SPAD equivalent circuit used and modelled in LTspice is included in Figure 7-9b, and the expected triggered and passively quenched signal output of the SN-SPAD is presented in subsequent circuit modelling[12]. In contrast to an actual SPAD, which has a continuous I-V dependence with diode and complex breakdown behaviours, its equivalent circuit model is reduced to two states. The equivalent circuit SN-SPAD is biased above breakdown and either *on* (triggered) with the switch closed or *off* (not triggered) with the switch open. In the *on* state, the equivalent circuit is equipped with a built-in voltage drop and resistance in parallel to a built-in capacitance to model an SN-SPAD that is undergoing avalanche. In the *off* state, the equivalent circuit is equipped with an open circuit in parallel with a built-in capacitance to model an SN-SPAD that is not undergoing avalanche.

The quenching and reset processes in the PQC are attributed to the ballast resistor (*RL*) in series with the SN-SPAD. When a photon is absorbed by the quiescent SN-SPAD, it triggers an avalanche, which subsequently produces a voltage drop across the ballast resistor. This voltage drop across *RL* reduces the SN-SPAD bias close to VB. This reduced bias sets the SN-SPAD into a state where the current is low enough to statistically cause the continued avalanche to eventually fail. The sensing resistor (*RS*) is probed by the comparator to output a *low* or *high* state to indicate the state of the circuit. The

comparator indicates the triggered state from SN-SPAD photon absorption with a *high* output and return to quiescent state with a *low* output. The circuit schematic shown in Figure 7-10 is used in LTspice to model the passive quenching operation for the SN-SPAD.

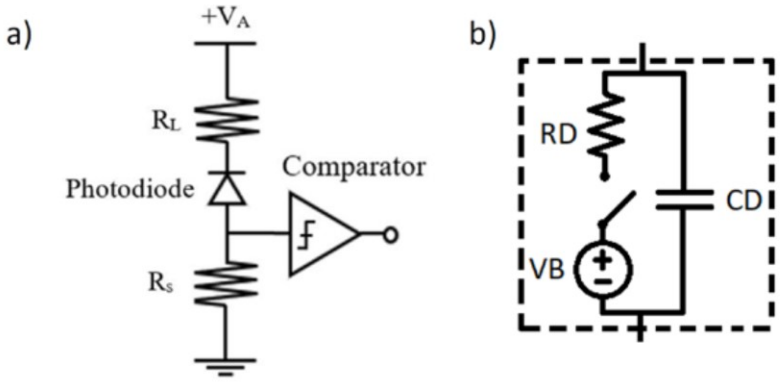

Figure 7-9: Passive quenching circuit scheme. a) Passive quenching circuit configuration modelled for implementation in semiconductor nanowire single-photon avalanche diode (SN-SPAD) development. **b)** An equivalent single-photon avalanche diode circuit model used to model the avalanche behaviour in an SN-SPAD biased above breakdown with two-state (*on* and *off*) operation. Figure 7-9a and Figure 7-9b adapted from ref. 12, Optica.

The LTspice transient modelling is performed with a pulse (*Vsw1*) voltage-controlled switch (*SW1*) and equivalent SN-SPAD circuit to emulate an SN-SPAD trigger event following photon absorption. The components making up the equivalent circuit include a VB, diode resistance (*RD*), and junction capacitance (*CD*). The LTspice model also includes the stray capacitance (*Cs*), the capacitance to ground from the SN-SPAD. The values selected for the modelled circuit are comparable to those measured from the SN-SPADs and used in literature[12]. The diode is reversed biased in excess of its breakdown (VA = 14 V) and the ballast resistor is selected to be sufficiently high as to limit current through the SN-SPAD (*ID*), a good practice for protecting the SN-SPAD from high (destructive) currents. Also, a Schmitt trigger is used as the comparator. A voltage spike received at the positive terminal (SN-SPAD photon absorption) of the Schmitt trigger surpasses its threshold voltage (V_T = 1 mV) point, transitioning the comparator from a *low* (0 V) to *high* (1 V) output state for photon counting. After some time, post trigger, the subsequent quenching from the ballast resistor transitions the comparator back to its *low* state.

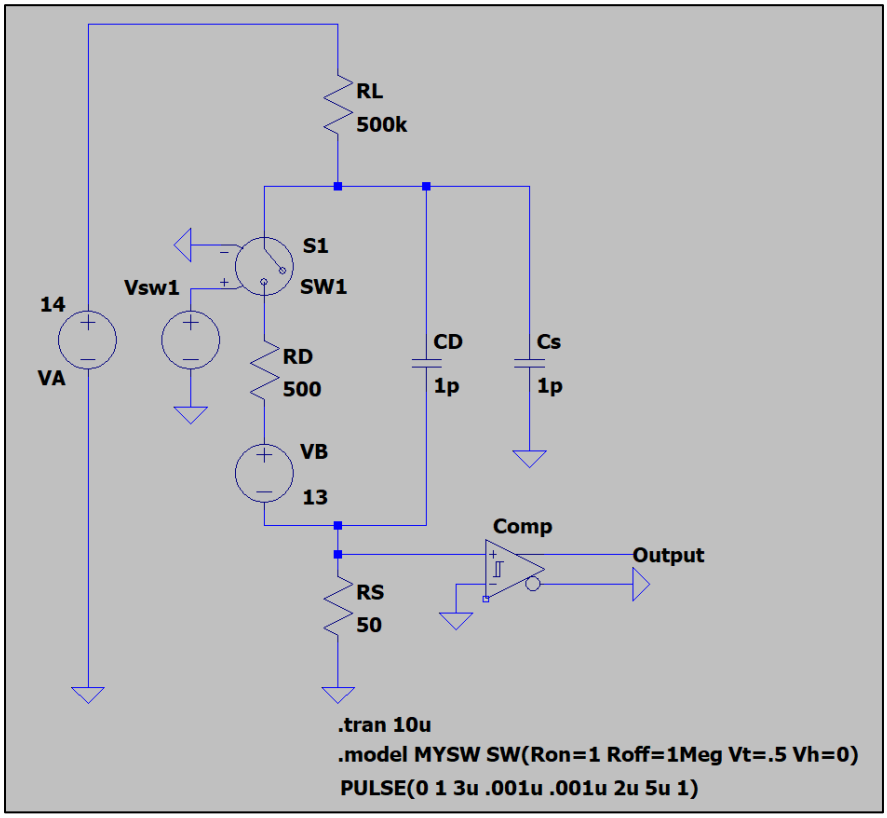

Figure 7-10: Passive quenching circuit scheme modelled in LTspice.

To demonstrate the circuit performance with a high frequency response (10 ns pulse) from the SN-SPAD, the switch with the trigger-event input pulse in Figure 7-11 is modelled. When the SN-SPAD trigger event occurs (1 V to the switch), the switch closes, emulating photon absorption by the avalanching SN-SPAD. The closed switch enables current to flow and voltage to drop across the ballast resistor, quenching the triggered SN-SPAD. Figure 7-12a and Figure 7-12b depict the voltage drop and current response through *RL* coinciding with the SN-SPAD trigger event, respectively. The result observed in the voltage after *RL* indicates the diode bias drops to VB following photon absorption. This behaviour indicates the diode is no longer in an avalanche capable regime, demonstrating the quenching functionality and a successful (approximate) model of a functioning passive quenching scheme.

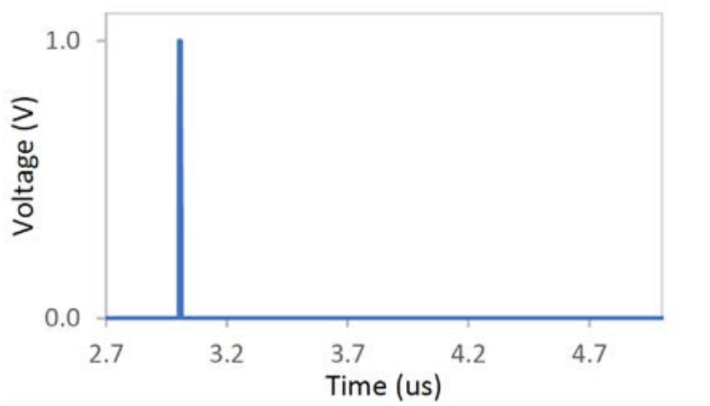

Figure 7-11: Single-photon avalanche diode trigger-event pulse sent to the voltage-controlled switch in the semiconductor nanowire single-photon avalanche diode equivalent circuit. The switch is open at 0 V and closed at 1 V.

The modelling results in Figure 7-12 reflect the expected cathode measurement trends, further indicating the successful modelling of the PQC[12]. Namely, similar maximums and quenching trends towards the asymptotic steady-state diode voltage (V_f) and current (I_f) are observed. Note that the minimum current through *RL* in the model is non-zero. The non-zero open switch current is due to a non-ideal open switch resistance of 1 MΩ in the model and will be rectified in the implementation.

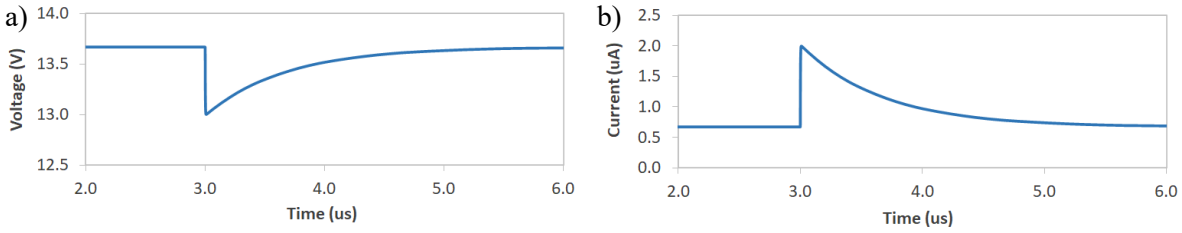

Figure 7-12: Passive quenching circuit response curves. The modelled passive quenching circuit operating **a)** voltage measured at the cathode and **b)** current measured through RL.

Figure 7-13 illustrates the faster PQC sensing voltage output at the anode which results from the reduced (50 ps) decay time constant. This reduced time constant arises because only the discharging current from *Cs* flows in the loop with *RS*[12]. The modelled SN-SPAD signal for sensing is illustrated in Figure 7-13a. The comparator output from sensing the SN-SPAD trigger event (*high* = 1 V) and its quiescent state (*low* = 0 V) utilized in photon counting and analysis through correlation software is included in Figure 7-13b.

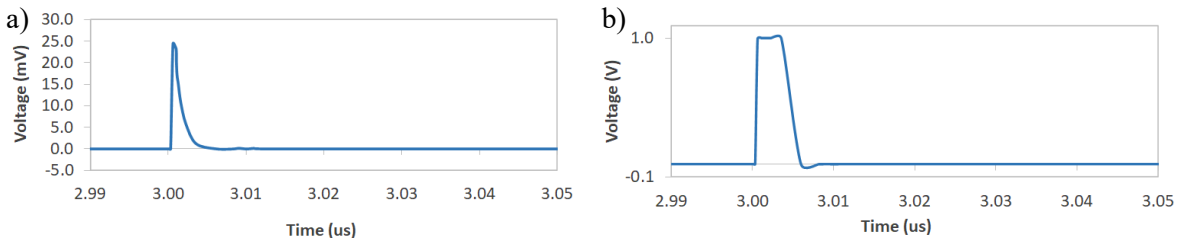

Figure 7-13: Passive quenching sensing outputs. a) The rapid voltage drop across the sensing resistor, *RS*, utilized for discerning photon absorption due to the reduced decay time constant of 50 ps and **b)** the respective comparator voltage output.

7.3.2 Active Quenching Circuit

An example design for the AQC is shown in Figure 7-14[12]. Several expected circuit nodal voltages are presented in literature, providing a target for the AQC modelling results[12]. The quenching and reset processes in the AQC rely on sensing the SPAD trigger signal and responding with quenching and reset mechanisms, and designs are capable of over 10 MHz count rates[13,14]. In the diagram provided, this quenching and reset process is executed by the voltage driver (*D*) acting on the diode in response to the comparator's output. When the comparator is output *low*, the driver is *on*, applying a relatively high voltage to keep the diode in a prepared quiescent state. When a photon is absorbed, current flows through the diode and changes the voltage between nodes *b* and *c*, which is registered by the comparator. This change in voltage sets the comparator output to *high*, swapping the driver to a *low* state where it supplies a negative voltage for a set hold-off time to quench the avalanching photodiode before resetting its output to *high*, as observed by the voltage drop and rise at nodes *a*, *b*, and *c*. The voltage drop and hold-off quenches the SN-SPAD by actively holding the diode bias in a non-avalanching state, stopping the first avalanche current and preventing the onset of subsequent avalanche currents caused by the release of trapped carriers (afterpulsing). The hold-off mechanism can be employed for longer times to reduce SPAD afterpulsing at the expense of count rate. With the driver output reset to *high*, the SN-SPAD is in the operational state once again, prepared for subsequent photon detection. During operation, a short pause in the node *b* voltage is not observed in nodes *a* and *c*, and it is the result of the timing delay (speed) of the quenching and reset electronics responding to the SN-SPAD trigger event.

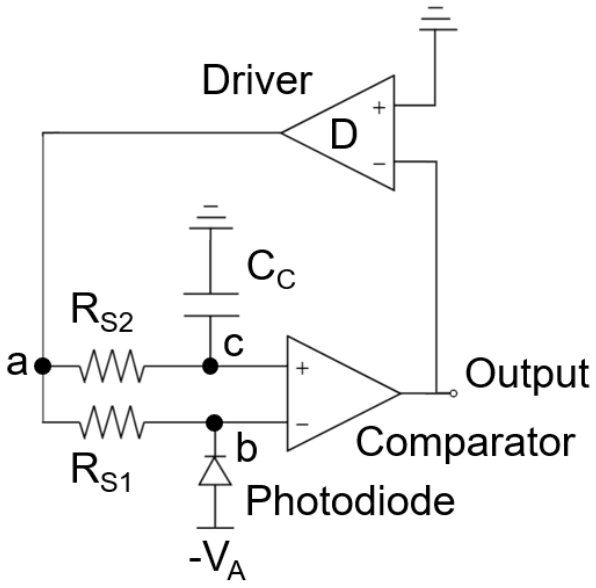

Figure 7-14: Coincident terminal configured active quenching circuit diagram modelled for potential implementation in semiconductor nanowire single-photon avalanche diode development. Figure 7-14 adapted from ref. 12, Optica.

Further control over the SN-SPAD-circuit interface can done by tuning the resistors, *RS1* and *RS2,* and capacitor, *Cc*. *RS1* can be altered to tune the voltage drop between the different nodes and the comparator. *RS2* and *Cc* are implemented to prevent the circuit from being locked in the triggered state, and to avoid quenching pulse induced circuit oscillations from overshoots and ringing. Similar to the PQC, the comparator probes the sensing resistors to output *high* and *low* states corresponding to the SN-SPAD trigger and operational states, respectively.

The LTspice transient modelling of the AQC followed similar methods and use of components as in the PQC modelling, along with the same switch properties for *SW1- SW4*. The circuit schematic created in LTspice to model the AQC operation is illustrated in Figure 7-15 and the SPAD trigger-event pulse sent to the voltage controlled switch is shown in Figure 7-16. This AQC modelling was performed to study the circuit logic and implements idealized switches to execute operations. While switches are useful for simplifying the numerical model setup, it inhibits the prediction of practical circuit signals. As a result, the more idealistic behaviour is reflected in the subsequent signal analysis. A model for more realistic circuit operations would benefit from the substitution of the idealistic switches for transistors with practical operating speeds and impedance characteristics.

The AQC model substituted the equivalent circuit in place of the SN-SPAD, which is controlled using a (100 ns) pulsed voltage-controlled switch, and the diode is reverse biased at VA = -14 V. Values for *RS1*, *RS2*, and *Cc* were matched with *CD* and *RS2* with *RD* for circuit symmetry to avoid oscillations, and *RS1* = 50 Ω is selected anticipating its role as a sensing resistor mirroring *RS* in the PQC. A Schmitt trigger is used as the comparator, where the voltage drop at its negative terminal following SN-SPAD photon absorption causes the V_T to be surpassed, transitioning the comparator from a *low* (0 V) to *high* (1 V) output state for photon counting and activating the voltage driver.

In the operational SPAD state (Vb > Vc), the comparator outputs *low*, switch *SW2* is kept open, and the driver comparator sends *low* through the main channel and *high* through the inverted channel. This state has the quench voltage source (*VQ*) switch (*SW3*) open and the operating level switch (*SW4*) closed. When the SN-SPAD is in the triggered state (Vc – Vb > V_T), the comparator outputs *high*, switch *SW2* closes, and the driver comparator sends *high* through the main channel and *low* through the inverted channel. This state closes *SW3* and opens *SW4* to drop the voltage at node *a* to *VQ*, quenching the avalanche. The resulting voltage drop at node *c* resets the comparator, swapping its output back to *low* and opening *SW2*. Once the RC delay circuit (parallel *RR* and *CR*) discharges to the driver comparator's V_T, the driver comparator will reset node *a* to the operating voltage. The RC delay and driver comparator V_T can be designed to tune the AQC hold-off time, a critical parameter for controlling after pulsing and SPAD performance. Without the RC delay, the quenching process duration would be governed by the speed of the comparator and voltage driver.

Figure 7-17 illustrates the voltage outputs which may be used for single-photon counting by correlation software. First, Figure 7-17a illustrates the VE across the SN-SPAD. When VE < 0, the SN-SPAD is biased in an active state, prepared to receive a photon and avalanche. Post avalanche, the SN-SPAD is quenched by driving VE > 0. For the short time the SN-SPAD is triggered and the reset electronics have not responded with a quench, the AQC comparator in Figure 7-17b outputs the *on* (*high*) state which can be used for photon counting. After the quenching pulse occurs, the conditions on V_T for the SN-SPAD comparator are no longer satisfied and the output returns to *low*.

7.3.3 Mixed Quenching Circuit

A variety circuits employ both active and passive elements to leverage the advantages from both. Such circuits are referred to as mixed quenching circuits (MQCs). MQCs take on numerous designs and

behaviours[12]. In general, they pick and choose fundamental mechanisms introduced in the PQC and AQC operation to execute.

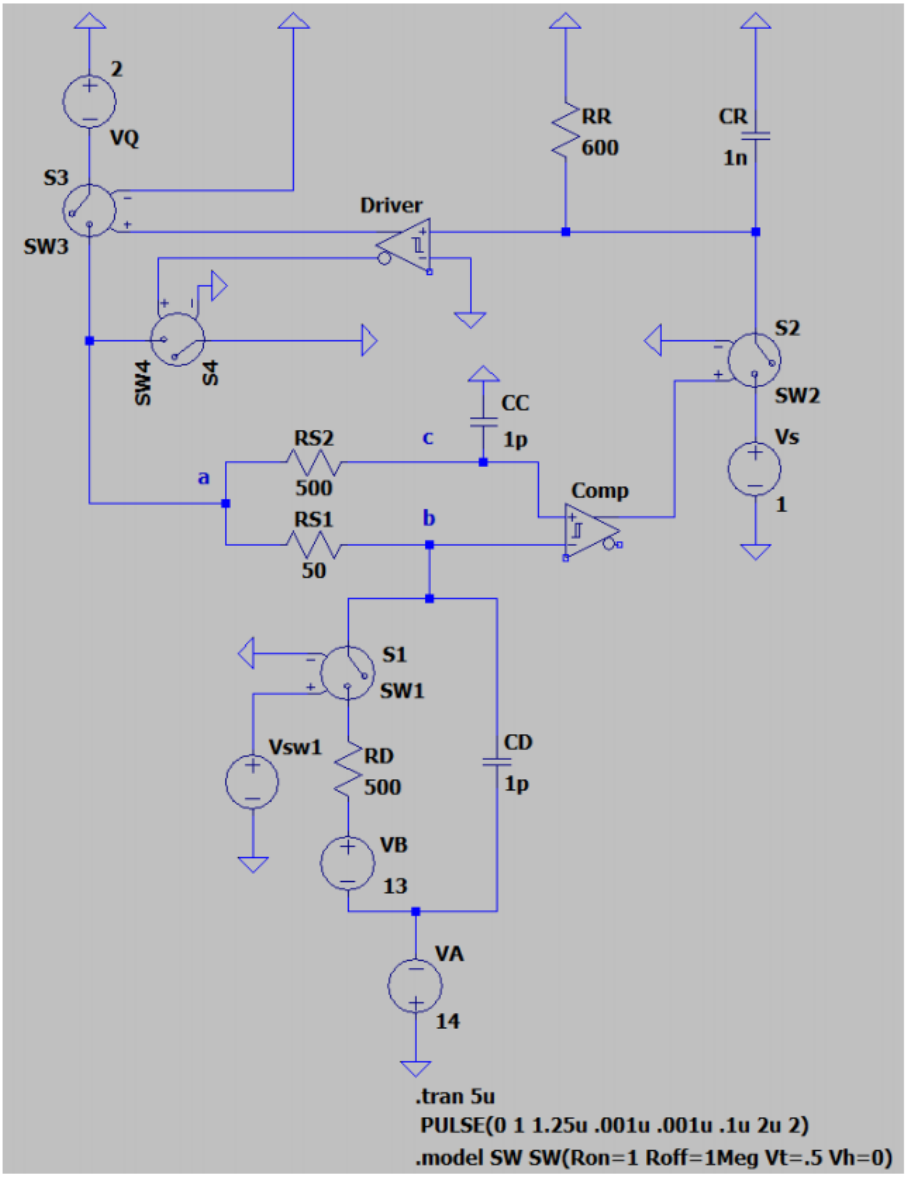

Figure 7-15: Active quenching circuit scheme modelled in LTspice.

7.3.4 Free-Running and Gating

Another notable trait of quenching circuitry is its operation in free-running mode or with gating. When a circuit is designed to be prepared to receive a photon at any time (outside of deadtime), it is considered

free-running mode operation. In this way, a free-running SPAD can sense and respond to photons from unpredictable sources. Quenching circuits may, however, employ a mechanism that actively prepares and quenches the SPAD for set intervals. This circuit operation method is referred to as gating. Gating is particularly useful for predictable sources because the gate timings can be set according to expected photon arrival times, and critical SPAD performance metrics, such as DCR and afterpulsing, can be improved due to the active dead time[11].

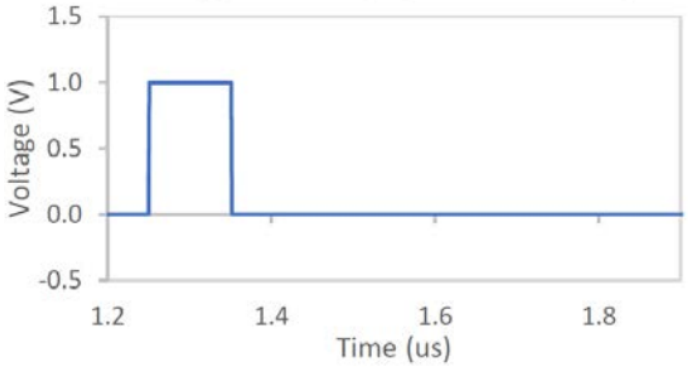

Figure 7-16: Single-photon avalanche diode trigger-event pulse sent to the voltage-controlled switch in the semiconductor nanowire single-photon avalanche diode equivalent circuit. The switch is open at 0 V and closed at 1 V.

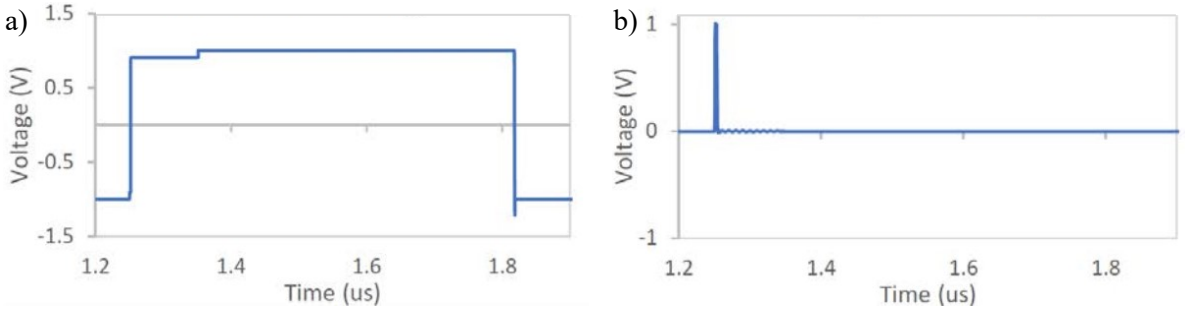

Figure 7-17: Semiconductor nanowire single-photon avalanche diode (SN-SPAD) sensing signals. a) The excess voltage across the SN-SPAD, indicating the successful operation of the quenching pulse to change the state out of the reverse breakdown regime. b) The AQC's comparator output from the triggering of the SN-SPAD.

7.3.5 Active Quenching Circuit Design Considerations

Three promising AQC designs were selected from a literature search to consider for SN-SPAD application based on their feasibility, component availability, performance, and resemblance of their device under test. A fast active quenching circuit (FAQC) design by Junliang Liu et al.[15], AQC by Stipčević[14], and MQC by M. Ghioni et al.[13] were the promising quenching circuit schemes studied. The operations of these circuits were modelled using LTspice for further analysis following similar methods to those employed in Section 7.3.1 and Section 7.3.2. The modelling was performed with comparable components and signals that emulated the SPAD. In this way, key operation details were obtained to compare the AQC designs and determine the expected signals to reproduce during implementation.

After the review and modelling of these potential quenching circuits, the Junliang Liu et al. FAQC was found to be the preferred circuit for immediate and early implementation with the SN-SPADs, from which adaptations can be implemented. This choice was made based on its relatively simple design and use of state-of-the-art heterojunction bipolar transistor (HBT) components for their rapid operating speeds. This circuit implementation prioritizes rapid avalanche quenching (1.6 ns avalanche duration) and current limiting ability, crucial qualities to InGaAs/InP SPAD performance and failure prevention. This circuit is the most modern of those reviewed (2016) and many of the components are still commercially available. The FAQC also operates in free-running mode, a quality desired for early experimental testing and necessary for many applications. The FAQC design also incorporates an easily controllable hold-off time. Gated mode operation of the circuit is not discussed or suggested to be possible with the current circuit design. However, future adaptations of this FAQC can be investigated to include gating, or another quenching circuit design can be pursued when the need for gating the SN-SPADs arises. Another shortcoming of this FAQC is its dependence on a field-programmable gate array (FPGA) i.e., user-configurable integrated-circuit logic hardware, to control it. The FPGA plays a critical role in the quenching process, which requires precise timings for the correct operation of the circuit. Though the need for an FPGA has its drawbacks, it could also be advantageous by providing additional avenues for control of the SPAD electronics. This capability might be necessary for later experiments and future iterations of the quenching circuit design, including gating.

The Stipčević AQC design makes for an admirable low-cost alternative to the FAQC. With this circuit, a deadtime of less than 40 ns and avalanche duration of ~10 ns was demonstrated with their SPAD. This AQC also minimizes the use external components to control the circuit, such as an FPGA, and claims to work with virtually any biasing voltage. The quenching circuit is relatively easy to build with

off the shelf components, but it is not without its shortcomings. It is not clear if this AQC design incorporates hold-off functionality, as there is no discussion of hold-off related performance included. The lack of a clear hold-off mechanism without immediate adaptations to the circuit design makes this circuit undesirable for early adoption with the SN-SPADs. Another notable drawback of this AQC is its limit of VE < 5 V. Though this design is less desirable for the preliminary quenching circuit implementation, its strengths and design attributes can be considered for adapting into later circuit design iterations. Also, while the reported deadtime is a critical metric for SPAD performance, the value itself is less significant in the circuit comparison here because the operating deadtime is generally limited by the hold-off required of the SPAD. The circuit operating speed is still important to SPAD deadtime, however, through the avalanche pulse quenching speed. A more rapidly quenched SPAD has fewer charges flowing through it and a reduced afterpulse probability. As a result, faster quenching circuitry can find reduced deadtime through a lessened demand on the hold-off[15].

The M. Ghioni et al. MQC design provides many unique qualities and minimizes the use of external control components. The circuit demonstrated good deadtimes (36 ns), but the passive quenching phase of the avalanche pulse alone exceeded 10 ns. Other good qualities include controlled hold-off, high quench voltages, passive and active quenching, gating functionality, power dissipation consideration, and transistor level design details. The qualities of this MQC that make it unique and desirable from a functional perspective also make it difficult to implement, especially due to the date of its implementation. Many of the components used in this MQC are commercially unavailable, so adopting it for the SN-SPADs will require a relatively extensive component selection process. The circuit's performance with modern components is suspected to be much better but whether or not it can outperform the alternatives with modern component substitutions is unknown. Other considerable drawbacks of the MQC design includes those attributed to the bootstrapping voltage driver configuration detailed in the literature reference. Swapping a bootstrap configuration for complimentary n- and p-channel transistors in the modern application of this MQC may improve the design, but the performance impacts of this change are also unknown. Because of this circuit's relative complexity and the unknowns of the modernized MQC's achievable performance, it takes a lower precedence for early adoption over the FAQC design. Like the Stipčević AQC, however, the MQC's uniqueness offers insight into possible components and mechanisms to be adapted into later circuit iterations.

7.4 Nanowire Metamaterial Single-Photon Avalanche Diode Operation

The SPAD operation of the tapered p-n junction NW arrays that were developed and tested required the application of quenching circuitry, cooling systems, and additional external electronic and optical equipment in an experimental measurement setup. The following section elaborates on the design of these necessary SPAD operating elements, which are employed on the InP NW metamaterial devices of Chapter 3 and the InGaAs/InAlAs metamaterial devices of Section 7.2.

Previous APD performance measurements of the InP tapered NW p-n junction arrays demonstrated its potential for high single-photon detection performance[16]. The measured devices achieved high-efficiency, broadband, and high speed photodetection, capable of single photon per pulse resolution. The EQE exceeded 85% over a broad bandwidth of ~500 nm with pulse rise times and timing jitter of < 1 ns and < 20 ps, respectively. This performance paired with high gain of 10^5 and low dark current at room temperature made it unrivaled among commercial detectors at the time. These combined qualities also indicated promise in extending its application to single-photon detection through its development into an SN-SPAD in Geiger-mode operation.

Sections 7.5 (InP SN-SPAD) and 7.6 (InGaAs/InAlAs SN-SPAD) report details of the approach to transform the NW p-n junction array technology into an SN-SPAD for single-photon detection applications. The aim is to present the critical facets to the SN-SPAD design, including the detector material and performance, quenching circuitry, and thermoelectric cooling system. Each section details relevant design options, trade-offs, and choices. Conclusions are made with future work and an outlook, which elaborates on the SN-SPAD design decisions in a long-term perspective with future directions.

7.5 InP P-N Junction Metamaterial Single-Photon Avalanche Diode Measurement

In this section, the performance of an SN-SPAD detector module prototype operated in Geiger mode is presented. The module is composed of the InP tapered NW p-n junction array SPD chip mounted on a carrier and a quenching circuit PCB. The control electronics were successfully built around the semiconductor NW p-n junction array to operate the detector in Geiger mode for single-photon operation. However, due to the dark noise of the InP SN-SPAD, single-photon detection events could not be distinguished in Geiger mode. As such, the excessive measured InP SN-SPAD dark noise characterization results and signal analysis are included here along with the discussion of proposed contributors, solutions, and future work. Although single-photon detection is not demonstrated with the

InP SN-SPAD samples measured, there are no foreseen fundamental physical limits prohibiting the excessive DCR from being overcome.

7.5.1 Quenching Circuit

PQCs were selected as the first designs to be implemented with the SN-SPADs. The count rate of the PQC relies on the recovery time, which is governed by the ballast resistor, stray capacitance, and capacitance of the SPAD[12]. Since the InP SN-SPADs exhibited low capacitance, as determined by its temporal response measurements, the PQC could leverage this quality for higher performance. Furthermore, passive quenching offers free-running mode and is of the simplest designs to implement for proof of principle.

The PQC implemented for operating the InP SN-SPADs for single-photon detection consists of a two-part PCB design: a PCB base board to mount the 24-pin dual in-line package (DIP) housing the bonded InP SN-SPAD sample chip and a modular passive quenching PCB that connects to the PCB base board. The two PCB schematics are shown in Figure 7-18, while the PCB layouts are presented in Figure 7-19. The PCB base board design (Figure 7-18a and Figure 7-19a) is centered around 24 connections, which accepts the 24-pin DIP of the InP SN-SPAD sample chip carrier. The PCB base board also has radio frequency (RF) snap-fit adapters for connection to the modular passive quenching board for single-photon operation, and lines to ground for unused devices. The modular passive quenching board (Figure 7-18b and Figure 7-19b) includes the quenching circuitry and it snap-fits to the device under test's RF connector. The PQC PCBs included 50 Ω RF transmission lines and probe line connections for more robust measurement at the anode or cathode of the device under test, overcoming limitations from oscilloscope probes for parameter characterization. The fully assembled PQC for the InP SN-SPADs is presented in Figure 7-20.

7.5.2 Measurement Setup

The measurement setup implemented to test the SN-SPADs is outlined in Table 7-1 and the respective equipment and connections are presented Figure 7-21a. Statistically illuminated single photon per pulse measurements were performed with this experimental setup by attenuating the laser beam (after the fiber splitter and before incidence on the device).

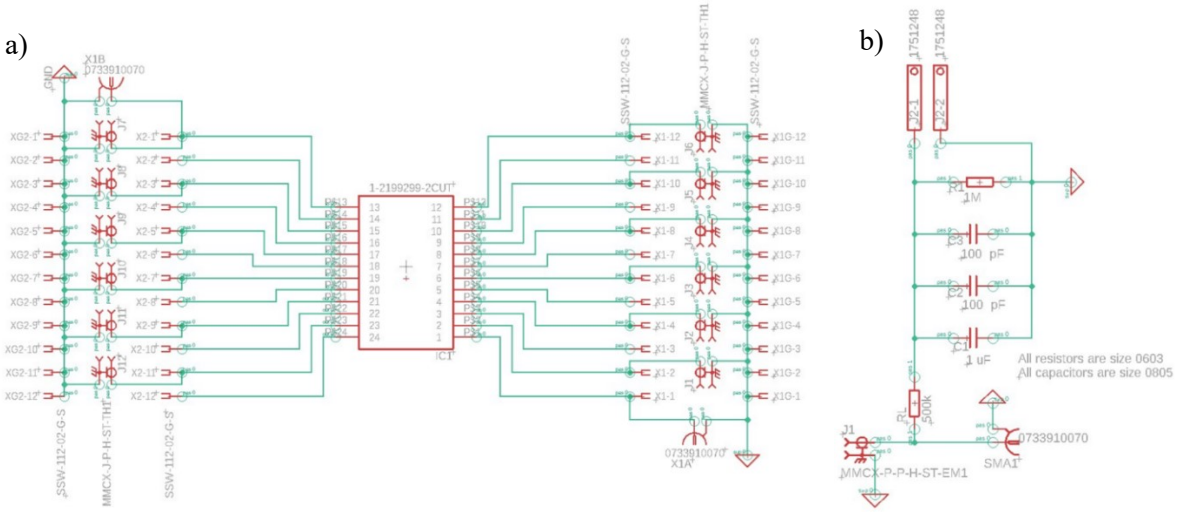

Figure 7-18: Schematics of the printed circuit board designs for the InP semiconductor nanowire single-photon avalanche diodes (SN-SPADs). a) Modular printed circuit board (PCB) base board which accepts the 24-pin package of the InP SN-SPAD sample chip carrier. **b)** Passive quenching PCB for operating the InP SN-SPADs for single-photon detection.

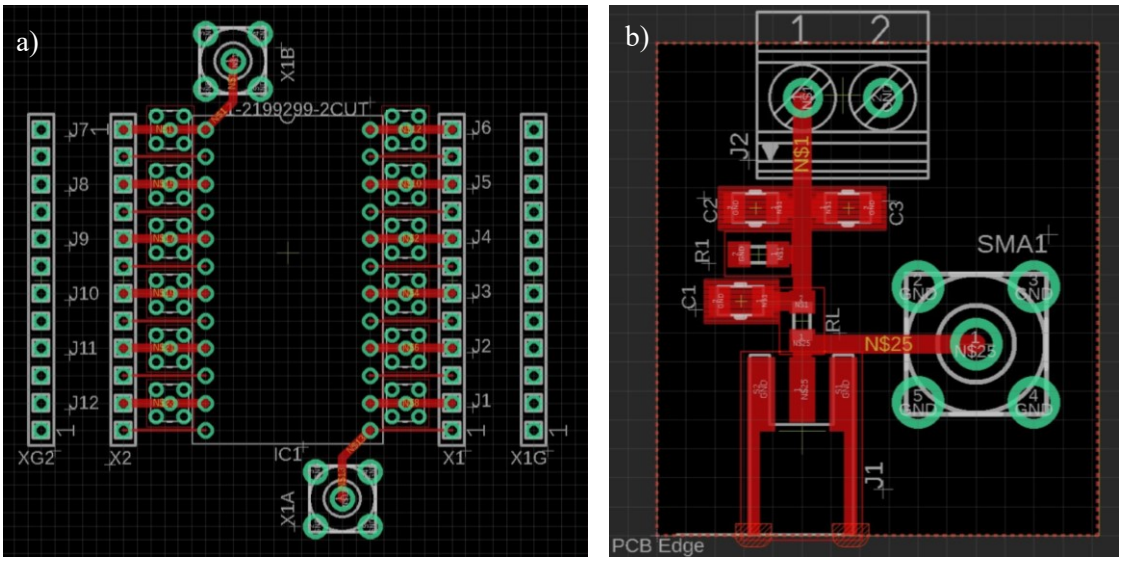

Figure 7-19: Printed circuit board layout designs for the InP semiconductor nanowire single-photon avalanche diodes (SN-SPADs). a) Modular printed circuit board (PCB) base board which accepts the 24-pin package of the InP SN-SPAD sample chip carrier. **b)** Passive quenching PCB for operating the InP SN-SPAD for single-photon detection.

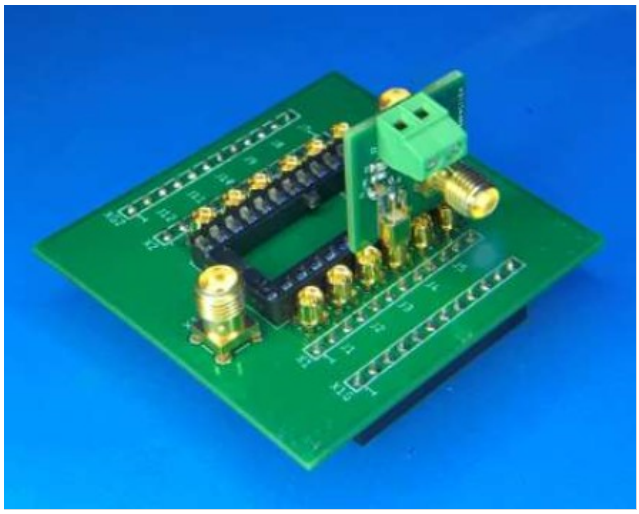

Figure 7-20: Fully assembled modular passive quenching circuit for operating the InP semiconductor nanowire single-photon avalanche diode samples on the 24-pin package chip carrier for single-photon detection.

The number of photons per pulse incident on the device is deduced using the energy per photon in each light source pulse according to $E = nhc/\lambda$, where n is the number of photons per pulse, h is Plank's constant, c is the speed of light, and λ is the photon wavelength. The power incident on the device follows $P_D = Ef_p$, where f_p is the pulse rate of the laser. The measured power (power meter readout) from the 90% line informs the correct signal is being sent to the device. Since the power at the device is attenuated on the 10% path, the measured power on the 90% path informs the power to the device according to $P_{90} = 9P_D/A$, where A is the optical attenuation in the 10% beam path. Thus, when statistically sending a single photon per pulse at the device with an 80 MHz laser at 750 nm and $1x10^{-6}$ attenuation, the measured power at the power meter readout is 0.191 mW. The Geiger-mode operation of the SN-SPAD is performed by the quenching circuit PCB on which it is mounted, interfacing with necessary equipment in the experimental setup as observed in Figure 7-21b. An image of the experimental setup implemented for the dark and single-photon measurements is included in Figure 7-21c. The complete SN-SPAD detector module prototype is shown in Figure 7-22. The module is composed of the InP SN-SPAD chip mounted on a carrier and a quenching circuit PCB. The two-part PCB design maintains a small footprint and allows for testing the currently wire-bonded InP SN-SPAD devices of Chapter 3 for single-photon detection as well as future devices on a matching carrier and currently unconnected devices, which may be wire-bonded to other package output pads.

Table 7-1: Experimental setup items with corresponding operation detail notes.

Number	Item	Notes
1	Laser	• λ = ~750 nm
2	90:10 fiber splitter	• 10% of the optical signal is sent into the enclosure and to the device • 90% of the optical signal is sent to the power meter (4)
3	Dark Faraday cage enclosure	• The optical fiber feedthrough is sent to a launcher, collimator, attenuators, then focusing lenses to illuminate the device (gold) at the single-photon level • Quenching circuit printed circuit board (PCB) (green) with a mounted semiconductor nanowire single-photon avalanche diode (SN-SPAD) (gold) • PCB and device are mounted on an x, y, z translation stage to focus the spot size onto the connected device's active area • Twisted pair (red and black) connections to the direct current (DC) supply (7) • Coax (brown) connections from the SN-SPAD signal output to the amplifier (5)
4	Optical power meter	• Receiving the 90% fiber path from the laser for tuning the incident power on the detector (10% path)
5	Current pre-amp	• Receiving and amplifying the SN-SPAD trigger-event signal, which is sent to the oscilloscope (6) • Omitted in cathode-based SN-SPAD measurements
6	Oscilloscope	• SN-SPAD signal acquisition
7	B&K 1761 DC power supply	• Applied voltage to the SN-SPAD
8	Power bar	• Shared power for equipment with a common (lab) ground to the Faraday cage (3) and copper strapping (orange)
9	B&K 1761 DC power supply	• Amplifier power supply

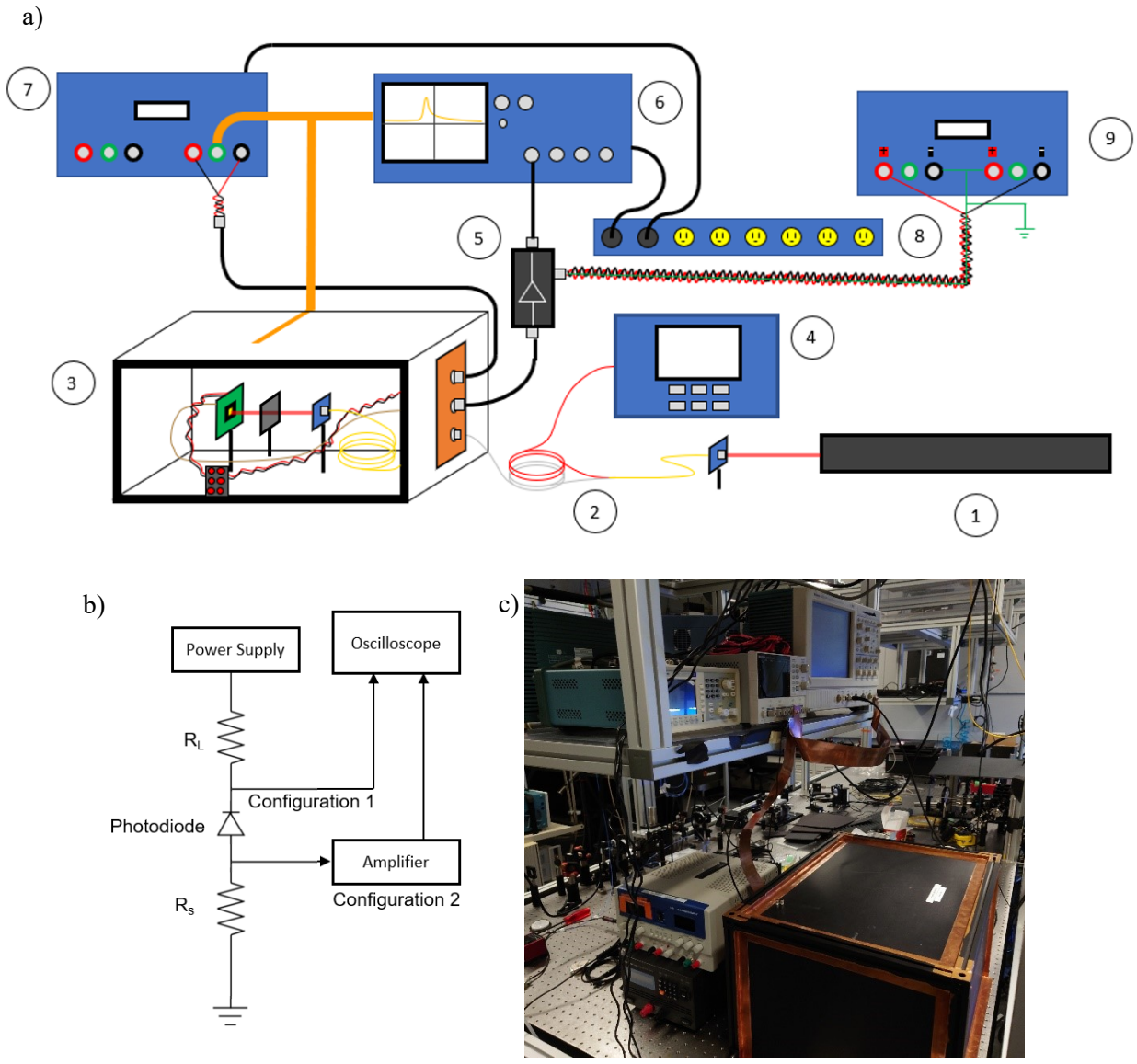

Figure 7-21: InP semiconductor nanowire single-photon avalanche diode (SN-SPAD) characterization equipment and setup. a) Diagram of experimental setup with connections made to the equipment noted in Table 7-1. **b)** Simplified block diagram of the equipment connections made with respect to a simplified passive quenching circuit schematic. **c)** Image of the experimental setup used in the characterization of the InP SN-SPAD.

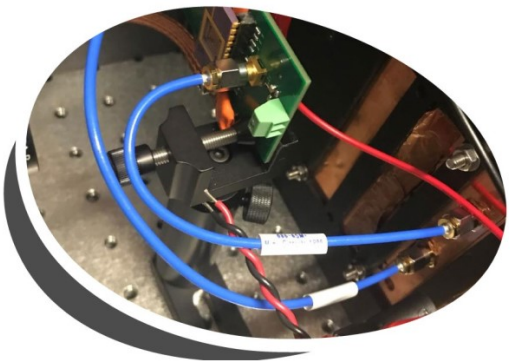

Figure 7-22: The complete and connected semiconductor nanowire single-photon avalanche diode detector module composed of an InP tapered nanowire p-n junction array single-photon detector chip mounted on a carrier and a passive quenching circuit printed circuit board.

7.5.3 InP Metamaterial Single-Photon Avalanche Diode Characterization Results

Preliminary PQC measurements were run on a mock SPAD setup, which included an equivalent SPAD circuit (capacitor, resistor, switch) and signal generator to emulate a trigger event. The emulated response showed the modelled PQC characteristics, so the PQC measurements on the InP samples were run. The device characterization was first performed in the dark, absent signal from the laser, to characterize the performance of the SN-SPAD detector module. Figure 7-23 shows the experimental results of the SN-SPAD detector module on an oscilloscope without incident light and a ballast resistor of 50 kΩ. At a reverse bias voltage below the NW diode VB, no trigger voltage signal on the cathode or change in the measured output is observed at the measured scale (yellow trace in Figure 7-23a). Only as the bias is increased above the NW diode VB does the oscilloscope trigger on the small voltage pulses (-1.32 mV), as shown in Figure 7-23b. Owing to the shape of these voltage pulses on the cathode, they are likely the result of a high DCR in the SPAD as they resemble rapid avalanche events and quenching in Geiger-mode operation. Raising the bias voltage further above VB expectedly increases the voltage pulse height (see Figure 7-23c and Figure 7-23d). However, the heights of these peaks are much smaller than expected. The voltage pulses were expected to increase to the order of hundreds of millivolts (from LTspice modelling), but the measured voltage pulses were under 5 mV. The smaller peak amplitude than expected is further indicative of retrigger avalanche events that occur during the recovery period of the SN-SPAD in a PQC. As a result, the current generation of the InP-based SN-SPAD devices is suspected to have too high of a DCR to distinguish for single-photon detection in Geiger-mode operation.

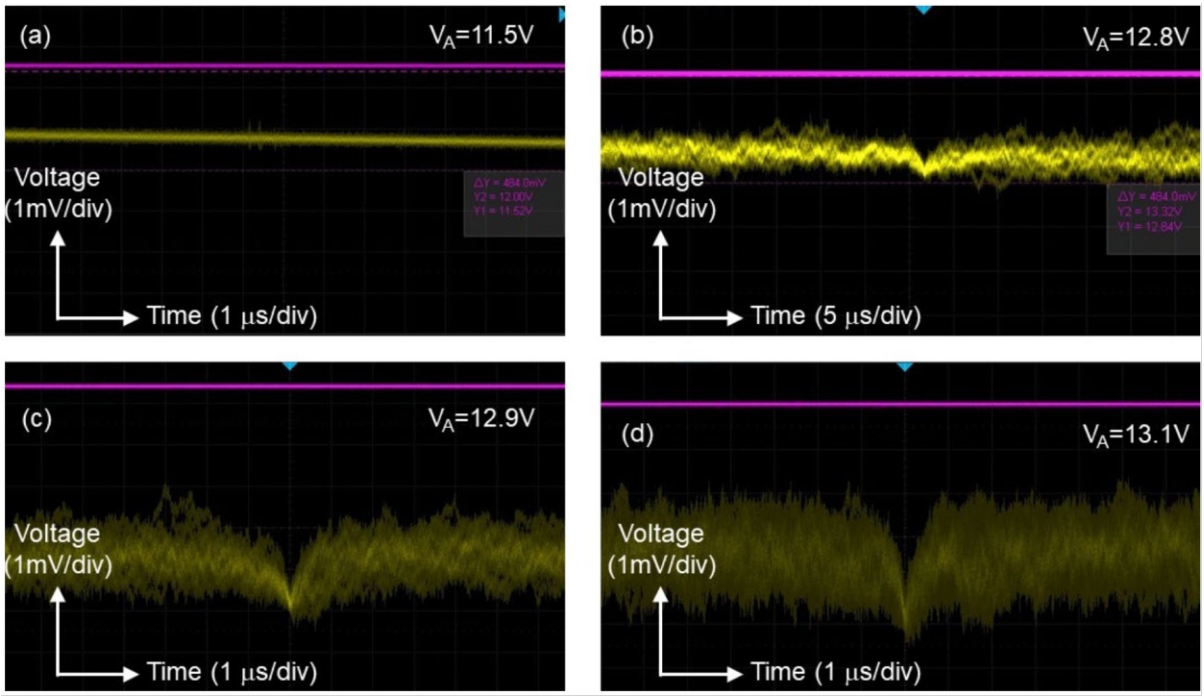

Figure 7-23: Semiconductor nanowire single-photon avalanche diode (SN-SPAD) dark voltage pulse response in a passive quenching circuit as a function of applied reverse bias, VA. Purple trace: applied reverse bias. Yellow trace: SN-SPAD response at the cathode due to dark current avalanche triggering events. The amplitude of the voltage pulses rises with increasing reverse bias above the nanowire diode's reverse breakdown voltage (VB ≈ 12.8 V). **a)** Cathode trace at VA = 11.5 V (below VB). No voltage response is observed due to avalanche trigger events. **b)** Cathode trace with VA exceeding VB with **b)** VA = 12.8 V; **c)** VA = 12.9 V; and **d)** VA = 13.1 V. Triggered peaks are observed which reach an amplitude of -3.64 mV at VA = 13.1 V. The resolution of the oscilloscope is 1 mV/division and 1 μs/division. The only exception is for **b)** where the timing resolution is 5 μs/division. Each cathode trace consists of many suspected avalanche trigger events.

To characterize the measured DCR and determine the upper bound of the DCR with a distinguishable trigger-event signal, a DC offset is applied with an alternating current (AC) signal through a bias tee to bias the InP SN-SPAD above and below VB. The VA is set with a DC offset of 12 V reverse bias and an AC signal of 1 kHz and 4 V peak-to-peak. The result of this measurement is shown in Figure 7-24a. The SN-SPAD cathode voltage (yellow trace) shows a peak that flattens close to the reverse bias VB, while the anode voltage (magenta trace) is shown to have acquired some voltage. In contrast, when setting the DC offset to 9.5 V, the AC supply does not surpass the SN-SPAD VB and an untruncated

sine wave is observed for the voltage at the cathode (see Figure 7-24b). Since there are no trigger events with VA < VB, the lower DC offset result presents the expected waveform with low DCR where no trigger events occur during an *on*-state period.

Next, LTspice modelling of the SN-SPAD in the PQC with the sinusoidal VA is run with different levels of DCR. The results of the modelling are shown in Figure 7-25. With low DCR, there are few trigger-event signals in the cathode voltage, and they are distinguishable from the sine wave (above VB), as observed in the 10 kHz DCR (light blue) curve in Figure 7-25. These trigger-event signals are distinguishable because they have sufficient time between them to recover i.e., for the return of the cathode voltage to ~VA. However, when the DCR is too high and the electronics response time is slow, there is not enough time for the trigger-event signals to recover and present distinguishable trigger events from the sine wave, as observed in the 10 MHz DCR (green) curve in Figure 7-25. Thus, high DCR results in the appearance of a flattened waveform top, which is consistent with the observed behaviour in the measurement of Figure 7-24a. The minimum DCR found in the modelling to cause this flattened sine waveform effect in the cathode voltage is ~10 MHz.

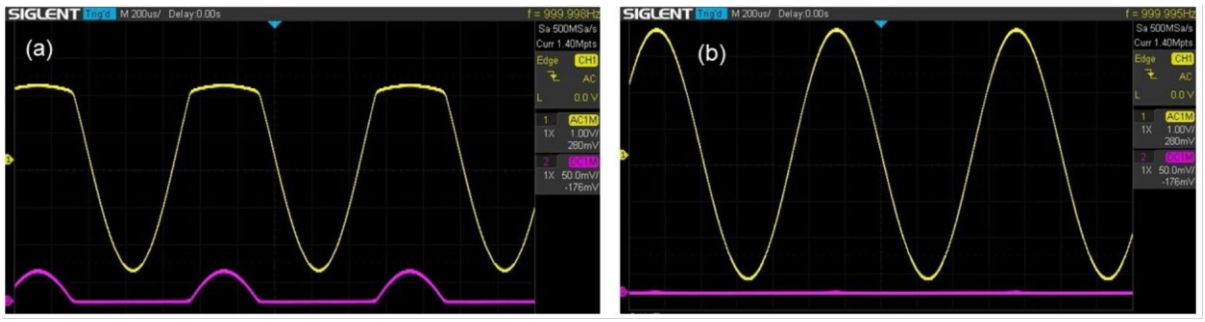

Figure 7-24: Measured semiconductor nanowire single-photon avalanche diode (SN-SPAD) operation in a passive quenching circuit while operated under a sinusoidal applied voltage (VA) and direct current (DC) offset. a) A DC offset reverse bias voltage of 12 V and alternating current (AC) bias of 1 kHz and 4 V peak-to-peak is used to bias the SN-SPAD above and below the breakdown to determine the dark count rate (DCR). **b)** A DC offset reverse bias voltage of 9.5 V and AC bias of 1 kHz and 4 V peak-to-peak is used, maintaining VA below the SN-SPAD breakdown voltage (VB). The response in **a)** is indicative of a high DCR in the InP SN-SPAD devices, and the response in **b)** presents the signal expected from a low DCR, since the SN-SPAD is biased below VB. That is, the voltage in **b)** is kept below the VB of the SN-SPAD so that there are no avalanche trigger events. Here, the yellow trace is the cathode voltage and magenta trace is the anode voltage of the SN-SPAD.

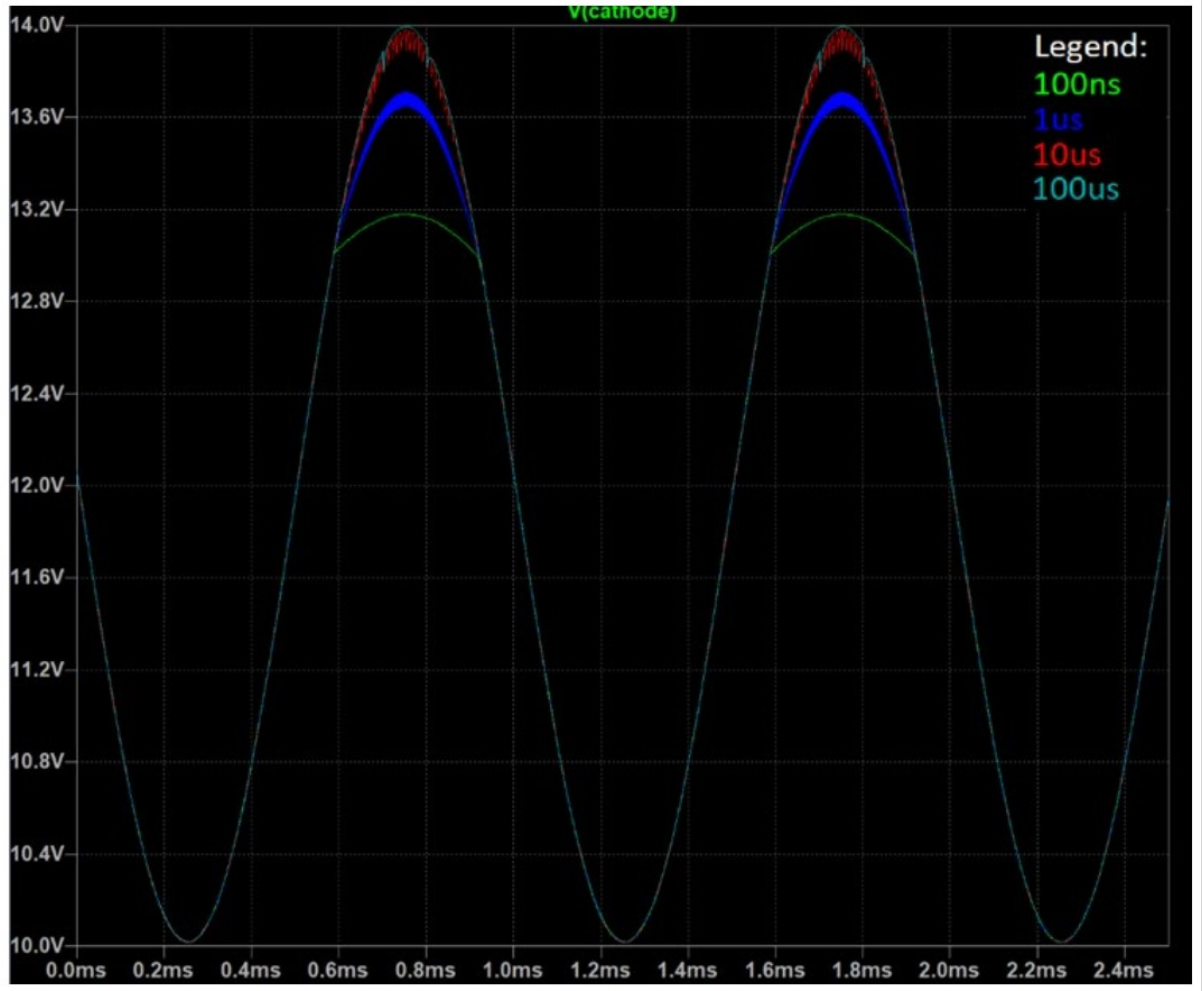

Figure 7-25: Modelled dark count rate (DCR) dependent cathode voltage of a semiconductor nanowire single-photon avalanche diode operating in a passive quenching circuit under a sinusoidal applied voltage (VA) (1 kHz and 4 V peak-to-peak) with a direct current offset (12 V). The legend denotes the modelled DCR: 100 ns = 10 MHz; 1 µs = 1 MHz; 10 µs = 100 kHz; and 100 µs = 10 kHz. As the DCR increases the cathode voltage waveform truncates at the top of the sinusoidal voltage peak to a level close to the SN-SPAD breakdown voltage (VB) instead of returning to VA. This truncated peak occurs because there are too many dark-count avalanche trigger-event signals, which do not have sufficient time between them to recover.

This high DCR combined with a high time constant of the PQC prevents the measurement of the SN-SPAD in Geiger mode for single-photon counting operation. The high observed DCR in the current generation of InP SN-SPAD devices is expected to be partly attributed to the large active area of the

NW array (300 μm x 300 μm)[17]. In InGaAs/InP SPAD modelling from literature, the trap-assisted tunnelling was found to be the predominant mechanism for DCR in the InP multiplication region[11]. As a result, the larger active area of the InP SN-SPADs may be susceptible to a greater number of trap sites and thus higher DCR from trap-assisted contributors. In future device generations, the active area should be reduced by more than two orders of magnitude to reduce the DCR towards acceptable values for single-photon counting operation. Figure 7-26 demonstrates the trend for lowering the DCR by reducing the active area size in a gated InGaAs/InP SPAD from literature, which demonstrates significant improvement in the DCR when the device active area is reduced by two orders of magnitude[17]. In this example, a change in the active area from 7,854 μm^2 (100 μm diameter circular active area) down to 79 μm^2 (10 μm diameter circular active area) corresponds to a reduced DCR of ~300 kHz down to ~3 kHz. For comparison, the InP SN-SPAD device area (300 μm x 300 μm = 90,000 μm^2) is significantly larger than the largest InGaAs/InP SPAD (100 μm active area diameter) in the literature reference for the DCR dependence on active area. Also, while the whole active area of the SN-SPAD is sensitive to incident light, the material fill factor contributing to trap sites is approximately 0.187 or 18.7% of the device active area. This fill factor was derived using a NW radius of 125 nm, the average of the fabricated NW top and bottom radii, and it means the depleted NW material area (and volume) may be more comparable to a ~150 um diameter planar device. Despite this conservative estimate, however, the diameter of the equivalent planar device is still large. Thus, it is expected that decreasing the SN-SPAD active area diameter to ~25 μm will significantly reduce the DCR, and have a notable impact towards realizing its successful Geiger-mode operation for single-photon detection[17]. Note also that it is this same difference in active area between the SN-SPAD and equivalent planar SPAD that is suspected to be a notable contributor to the reduced capacitance and improved response time observed in the InP SN-SPAD devices.

In room temperature operating InGaAs/InP SPADs, the DCR contributions from thermal generation is found to be the predominant mechanism[11]. Though the predominance of thermal DCR contributions in the InGaAs/InP SPADs were found to be dominant in the InGaAs absorbing region, the operating temperature plays a critical role in III-V SPAD noise performance through its impact on the thermal DCR contributors. As such, operating temperature of the SN-SPADs can also be reduced to aid in alleviating the excessive DCR. Other methods for reducing DCR, outside of rigorous device design and material considerations, include circuit-based solutions such as hold-off by active quenching circuitry and gating. The aim of subsequent InP-based SN-SPAD development includes the implementation of

thermoelectric cooling on the samples and altered device design developments, which included different materials and a smaller (circular) device active area from 10 µm to 50 µm in diameter.

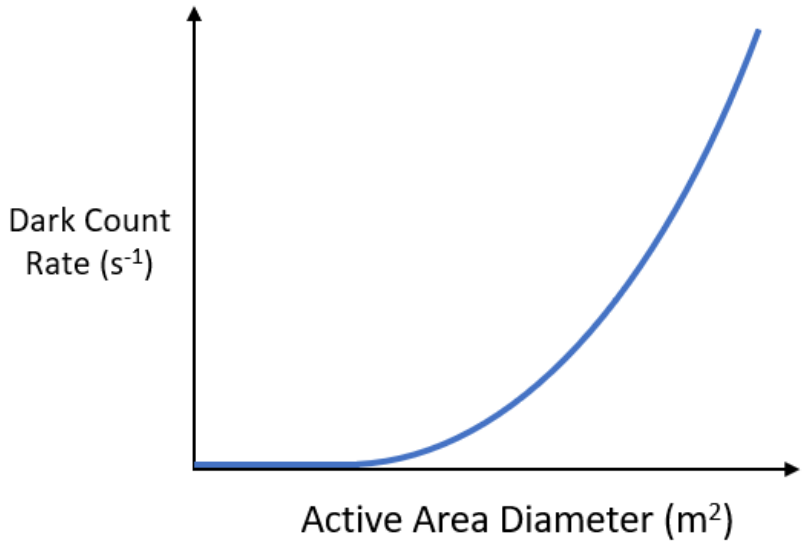

Figure 7-26: Diagram illustrating the conventional single-photon avalanche diode tradeoff behaviour between dark count rate and active area size. Figure 7-26 adapted from ref. 17, Proceedings of the International Society for Optics and Photonics.

7.5.4 Prototyping Thermoelectric Cooling System

The goal of the Geiger-mode operation of the InP SN-SPAD was to measure its performance in critical SPD metrics, such as DCR, afterpulsing, DE, etc. but the DCR was found to inhibit single trigger-event signal acquisition. Planar III-V SPADs are known to have a notable performance dependance on temperature, including DCR and afterpulsing performance. To an extent, DCR scales with temperature and has a tradeoff in performance with afterpulsing, which inversely scales with temperature[9]. The ideal operating temperature for SPADs varies between devices and application, but can often be achieved in a range achievable by TECs[18]. As such, TEC operation of the InP SN-SPADs was considered. Early testing of the InP SN-SPAD inside of a cryostat was also considered, but the sample carrier size implemented for the InP samples limited this option. Quenching circuit PCBs were designed for transferring the InP sample to, from the 24-pin DIP chip carrier, but a less invasive method implementing a thermoelectric cooling system is designed and integrated with the InP SN-SPADs

instead, along with quenching circuitry and appropriate commercial packaging to improve the InP SN-SPAD performance.

A simple thermoelectric cooling system is developed for the InP SN-SPADs to be flexible for rapid prototyping around the 24-pin DIP InP sample carrier. The PCB is design to socket the DIP into it for a swappable connection to external electronics. The flexible TEC solution utilizes a small single-stage cooling unit placed on the underside of the ceramic carrier with thermal putty, as shown in Figure 7-27. Additional hardware including bolts, O-ring raisers, and a DIP socket are incorporated to mount the TEC and package to the PCB. This solution provided the structural integrity to hold all components together without a permanent mounting solution, such as epoxy. Absent a permanent mounting solution, the package can be easily disassembled and implemented with other samples. As such, the flexible design enables the essential flexibility for prototyping. A thermistor is mounted near the TEC to measure the ceramic carrier and approximate device temperature. A simple heat sink is implemented through the thermal coupling of the hot TEC side with the optics table through a copper braid, relying on natural convection to cool.

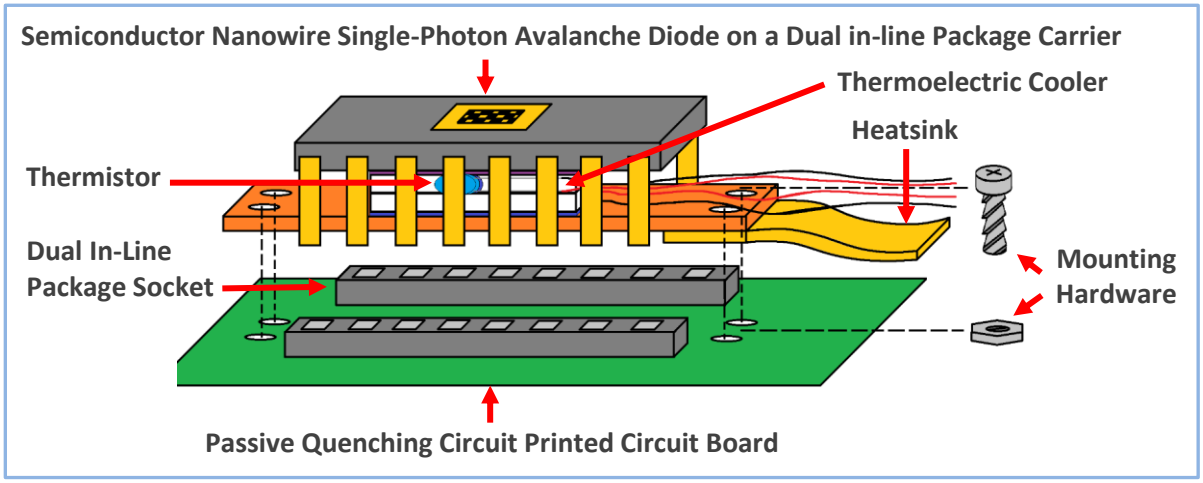

Figure 7-27: Flexible thermoelectric cooling system implementation concept. The InP semiconductor nanowire single-photon avalanche diodes are mounted on a dual in-line package (DIP) chip carrier. Thermal putty holds the thermoelectric cooler (TEC) to the carrier and heatsink, which are held together on the passive quenching circuit printed circuit board in the DIP socket by mounting hardware. Also, a thermistor is mounted near the TEC cold side for temperature readout. The components of the flexible cooling system are labelled accordingly.

A power supply or source meter can be used to control the TEC, but they are less compact. As such, William Losin developed an Arduino-based control module which measures and displays a user defined temperature. Several cooling units (TEC, thermistor, and connections) were produced to be swapped between and operated with one control module.

Some of the most critical performance requirements for the TEC design include the maximum operating temperature difference (dT_{max}) and cooling power. The ideal operating temperatures of the SN-SPADs are unknown. However, inspection of other SPAD photodetectors designs indicate that -70 °C is a good benchmark for selecting the commercial TEC (~90°C dT_{max}). Cooling below this is also advantageous, as it can be critical in finding the highest performance SN-SPAD operation achievable by TECs[6]. TEC Microsystems commercial cooler solutions were considered as they are capable of achieving temperatures well below this benchmark (https://www.tec-microsystems.com/). For instance, one of their four stage thermoelectric mini-cooler systems can provide a dT_{max} of ~126°C. In comparison, low cost off the shelf TECs are quite capable and could be made into a general-purpose cooling system with relative ease (https://www.digikey.ca/). Due to the initial complexity that the implementation of the TEC Microsystems solutions would entail, the CM35-1.9-08AN TEC was selected as the immediate cooler implementation in the general-purpose TEC design.

The InP SN-SPAD devices are small and have a limited capacity for heat production. As such, the cooling power demand of the SN-SPADs was relatively low. This was confirmed through a consultation with a TEC Microsystems engineer who indicated that the cooling power demand of the SN-SPAD samples can be easily accommodated to achieve the dT_{max} of their TECs. A more significant factor for the dT_{max} performance was initially thought to be the enclosure environment (nitrogen or Vacuum). The TEC Microsystems mini cooler with dT_{max} ~126 °C achieves this cooling performance at 27°C in vacuum and at 50°C in nitrogen. At these external temperatures, their mini-cooler can achieve ~-99°C in vacuum and ~-76°C in nitrogen. Though TEC units listed higher performance in a vacuum environment, preliminary testing is performed at room (external) temperature in the nitrogen-purged dark Faraday cage enclosure. The Faraday cage included a feedthrough where a lab nitrogen supply line is used to purge the enclosure after partially sealing it to limit Nitrogen outflow. The CM35-1.9-08AN achieves dT_{max} of 71°C at 27°C with a cooling power of 5.2W at 27°C. In comparison, a similar TEC from TEC Microsystems achieves 3.6W to 9.8W at 27°C, suggesting there is not a drastic compromise in cooling power with the CM35-1.9-08AN. Though, the dT_{max} of the CM35-1.9-08AN means it can only cool to -44°C, which does not meet the desired benchmark temperature of -70°C.

The TEC Microsystems option provides substantial performance benefits over the off the shelf option. However, the TEC Microsystems option requires elaborate design and engineering to implement. Also, even with extensive design, it would be difficult to swap between devices during the prototyping phase. The capabilities and demands of a TEC Microsystems solution makes such a system desirable for later adoption rather than implementation in early prototyping stages. Comparably, the opted for CM35-1.9-08AN is more flexible, thus capable for incorporating into the general-purpose TEC design for early prototyping stages, where a modular TEC design is essential for the SN-SPAD development process. Images of the flexible and high-performance cooling unit options are included in Figure 7-28a and Figure 7-28b, respectively.

a) b)

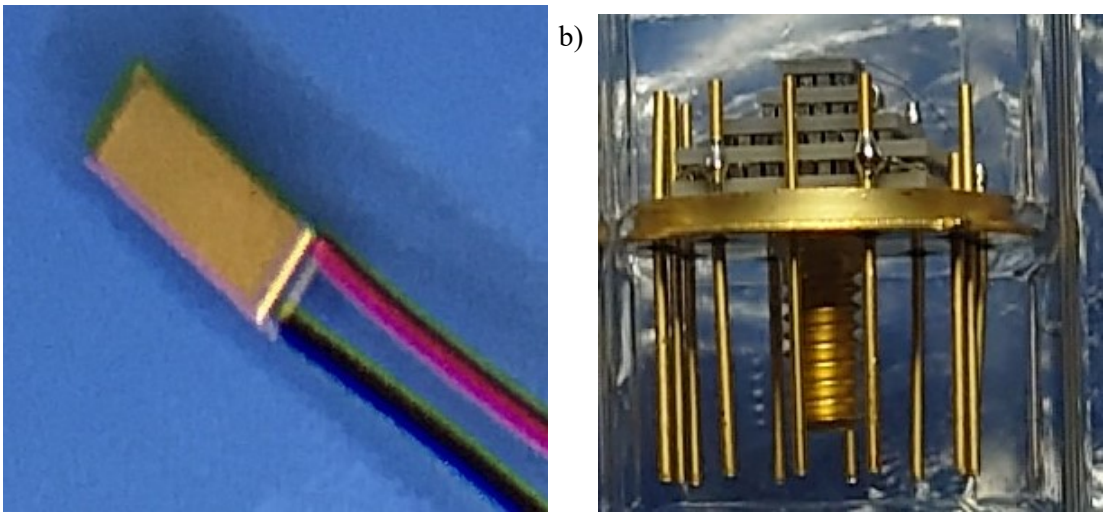

Figure 7-28: Thermoelectric cooling unit options. a) Flexible off the shelf thermoelectric cooler CM35-1.9-08AN. **b)** A 4-stage high-performance thermoelectric cooling system from TEC Microsystems.

The general-purpose TEC unit is controlled by a TEC control module i.e., a custom control unit designed to supply the required current to the CM35-1.9-08AN and display the measured temperature on a screen. The TEC control module enclosure houses an Arduino controller, potentiometers, and a PCB with the required ports and circuitry. The cooling element is composed of the CM35-1.9-08AN TEC, a thermistor, and connecting cable. The assembled TEC control module and cooler unit is included in Figure 7-29. The primary functions of the controller are to supply current to the TEC, read the temperature via the thermistor, and display the temperature on the liquid crystal display (LCD). The user is able to control the temperature by tuning the potentiometer resistance, which modifies the

current injected into the TEC. The control module's hardware, programmed by William Losin, also performs the necessary computations involved. The Arduino reads the thermistor current and calculates the respective temperature from a known dataset. The control module then displays the calculated temperature on the LCD. A PCB acts as an interface for all the cooling system components. William performed the required circuit modelling to ensure the controller outputs an accurate current supply to the TEC and receives the necessary power supply to the Arduino.

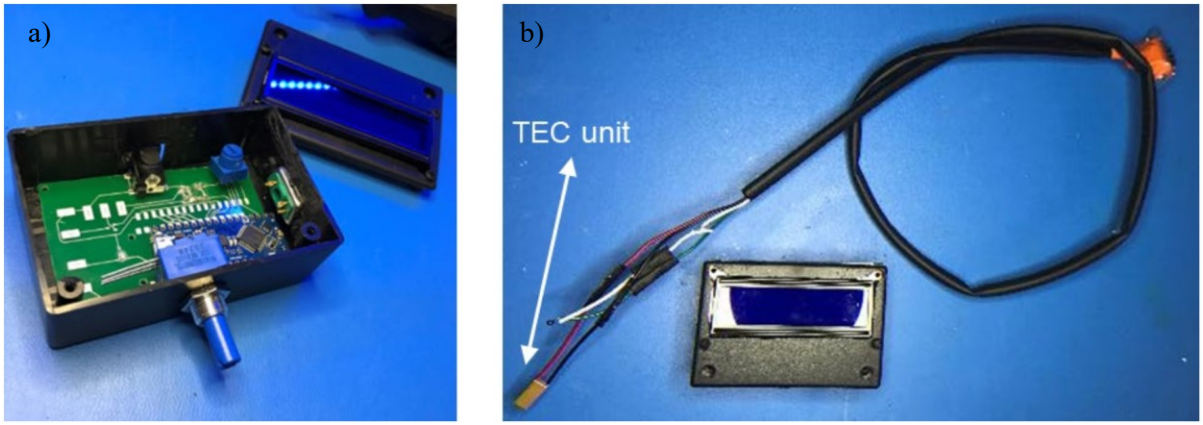

Figure 7-29: Custom thermoelectric cooler controller developed with off the shelf components. a) Cooling controller composed of a printed circuit board with control hardware, liquid crystal display to observe the measured temperature, and potentiometer for user temperature control **b)** Cooling element composed of a thermoelectric cooler unit, thermistor for temperature reading, and D-subminiature adapter for connecting it the assembled controller.

After the complete assembly and application of the general-purpose TEC to the InP SN-SPAD package, as shown in Figure 7-27, the desired operation of the TEC was found to be unattainable with the proposed design. The controller module behaved as intended, but the TEC is unable to properly cool. During operation, the TEC begins to cool but subsequently increases in temperature well above the room temperature environment, melting the solder of the TEC leads. The suspected cause of failure is insufficient heat sink performance. The heat production from the devices themselves are still expected to be low, but the heat sink demands to cool the entire system (device, carrier, etc.) were underestimated. As such, the rapid prototyping approach to thermoelectric cooling system design is substituted for a more sophisticated cooling system and packaging design in subsequently developed (InGaAs/InAlAs) SN-SPAD samples.

7.5.5 Future Work

While the InP SN-SPAD demonstrates high performance, initial implementations for Geiger-mode operation and single-photon detection are less successful. A passive quenching design with the device operated with some expected behaviour, but the SN-SPAD operation shows signs of the signal response being inhibited by a high DCR. Though the preliminary tests show a high DCR, there are methods which can be employed to reduce it. First, the measured InP SN-SPAD has a large active area size, which is known to increase DCR. Implementing such a change can improve the DCR in the InP SN-SPAD, but it can only be addressed during device fabrication. While this analysis was deduced through reference to literature, the direct cause of the high DCR can be further analyzed by measuring for trap activation energy in the devices and observing trends with temperature, as noted in Section 2.2.7. This analysis may further educate fabrication direction to address the major contributors through other fabrication level modifications on a device design and material quality level. SPAD developments in these areas were a focus of Burak Tekcan's thesis work and were applied in the InGaAs/InAlAs SN-SPAD devices. The active area changes in the InGaAs/InAlAs SN-SPADs included a smaller circular device area size of ~50 μm in diameter instead of the 300 μm x 300 μm square area of the InP devices. Also, since passive quenching demonstrated some desirable qualities, it is determined to still be valuable for implementation with subsequent samples prior to implementing a more intricate AQC design. Nonetheless, the success of the AQC modelling shows its promise for future implementations, which will involve selecting commercially available components for an updated FAQC design tailored for the SN-SPADs. Several components used by Junliang et al. in their FAQC implementation are still available and can be immediately considered in the quenching circuit design[15]. The identified components in the FAQC reference article include the comparator, amplifier, and DFF i.e., D-type flip flop, but the amplifier is discontinued. Minimal information on the FPGA and DAC i.e., digital-to-analogue converter, is provided, so substitutes should be found according to their expected functional requirements. The simulations should be updated to accurately model the FAQC design, which will also aid in refining the preliminary FAQC design for development. After refining the FAQC design it can be developed, measured, and compared to the targeted results from the updated modelling.

The FAQC's expected behaviour can be tested experimentally first with a simple PCB, equivalent circuit SPAD, and signal generator. This demonstration will produce results which best reflect the modelling, and it offers a controlled process for validating the measurement methods, circuit, and theory. Preliminary controlled testing with an equivalent circuit SPAD first is also precautionary to

limit the chances of damaging the sensitive nanofabricated SN-SPAD devices. The circuit voltages and currents can be studied and engineered in these initial measurements, tuning the FAQC prior to use with the SN-SPADs and revealing any required component substitutions or adaptations in the process.

Further development focus was also to be made on the TEC, as the early-stage testing established that the CM35-1.9-08AN flexible prototyping design detailed here is not capable of providing the required cooling performance. While the rapid prototyping design had the potential to provide cooling with ease of disassembly, a more sophisticated TEC and packaging design is required to improve the thermal performance. Additional refinement of the controller solution should also be considered in future SN-SPAD implementations. A more elegant design may include improved control accuracy by substitution of the variable resistor for a digital controller and improved packaging for a more compact handheld high-performance solution.

7.6 InGaAs/InAlAs Nanowire Metamaterial Single-Photon Avalanche Diode Measurement

The SN-SPAD prototyping on the InP-based devices is followed by implementation on the InGaAs/InAlAs SAGCM devices developed by Burak Tekcan. These devices incorporated an InGaAs tapered NW array metamaterial as the absorbing material to broaden the spectral detection range from the NIR region to 1.7 μm and InAlAs for lower noise carrier multiplication. The results from the InP SN-SPAD characterization found that the thermoelectric cooling system was inadequate, so an improved thermal electric cooling system and packaging are incorporated with modified quenching PCBs into an updated SN-SPAD detector-assembly prototype. These updates included a higher performance TEC inside of a hermetically sealed conventional SPAD transistor outline package (TO-8). The InGaAs/InAlAs SAGCM SN-SPAD was again operated with a PQC, which is designed to accommodate the packaging change of the device carriers. The PQC is employed because of its relative simplicity and familiarity from its use in the InP SN-SPAD developments. Re-use of the PQC design allows for a continuity in the study from the InP SN-SPADs, lessening device unknowns at the expense of some known performance disadvantages compared to more complex active quenching schemes. After successfully demonstrating an SN-SPAD detector-assembly prototype with PQC operation, subsequent developments of the SN-SPAD with active quenching schemes can be executed to further improve its operating performance.

7.6.1 Thermoelectric Cooler and Packaging

A more sophisticated thermoelectric cooling system and packaging design is implemented on the InGaAs/InAlAs SAGCM SN-SPADs due to the limitations of the InP SN-SPAD flexible thermoelectric cooling system design. A higher performance design was developed at the expense of some practicality. The revised design accommodated a more powerful TEC operated inside of a hermetically sealed package and implemented a forced convection heatsink. The TEC and packaging for the device was designed with industry standard SPAD options to provide the benchmark cooling, good electrical performance, and portability.

The selected cooler unit was the 4MD04-160-05AN TEC from TEC Microsystems, and its means of operation allowed the InP SN-SPAD cooler control module to be used. William Losin made the required changes to the control module design to accommodate the required operating conditions for the new TEC, which was mounted on a TO-8 Kovar header from Advanced Technology Group. The TO-8 header was equipped with a metal stud for thermal coupling to a heatsink through a custom metal adapter. A windowed TO-8 can was obtained through Advance ADY/Santek to fit the header and enclose the TEC and SN-SPAD inside of an inert low moisture environment. The can is made from Alloy 46, complementing the Kovar header, and has an anti-reflection coated sapphire window for optimal performance with the InGaAs/InAlAs SN-SPAD between 400 nm – 1600 nm (peak 1500 nm). The header and can were hermetically sealed with low-temperature reflow solder inside of a low moisture content Nitrogen glovebox to isolate the enclosed TEC and mounted device from the outside (room temperature) environment. The low temperature reflow solder ensured that the solder mounting the TEC to the header remained intact and the low-moisture hermetic environment is provided for the TEC with the required operating conditions for proper function and minimal risk of damage. The TEC included a metallized top plane which was wire-bonded to a TO-8 header pin during assembly by TEC Microsystems. TEC Microsystems also mounted a thermistor on the TEC cold side to monitor the cold-side TEC temperature after hermetic sealing. The thermistor and TEC lead connections were soldered to the TO-8 header pins by TEC Microsystems. The TEC mounted on the TO-8 header, the joined TO-8 header and cap, and a close-up of the hermetically sealed package are included in Figure 7-30.

The TEC, relative humidity inside of the enclosure, and heatsink performance is engineered to cool the mounted SN-SPAD devices to the benchmark temperature, -70°C. TEC Microsystems provided scenario performance references that indicate a required heat sink thermal resistance of < 2K/W. Benchmarks of commercial personal-computer processor heatsinks exceed this performance, so a well-

reviewed stock option that surpassed the thermal resistance requirements (Cooler Master i71C) is selected for the prototyping implementations. A high conductive copper adapter is designed, machined, and tapped to fasten to the TO-8 header stud to thermally couple to the heat sink's copper core (with thermal puddy). A CAD i.e., computer aided design, model of the copper adapter is presented in Figure 7-31. Though the cooler and packaging are designed for -70°C (temperature difference, dT = 95K) operation, the TEC itself is capable of a 123 K temperature difference, but improved thermal management is required of the design to approach this operating temperature difference limit.

The SN-SPADs are mounted via a conductive silver paste to the metallized TEC top contact, where the bottom of the sample wafer acts as a common electrode accessible through the top metallized plane wire-bond pin. The sample pads on the top of the chip to the SN-SPAD electrodes are wire-bonded to the header outputs for their transmission line connection to and Geiger-mode operation by an external PQC. An image of the mounted tapered NW array InGaAs/InAlAs metamaterial samples (SN-SPADs) on the TEC prior to hermetic sealing with individual wire-bonded devices is presented Figure 7-32a. Images of the unfinished packaging before and finished packaging after hermetic sealing with the mounted SN-SPAD sample chip are included in Figure 7-32b and Figure 7-32c, respectively.

a) b) c)

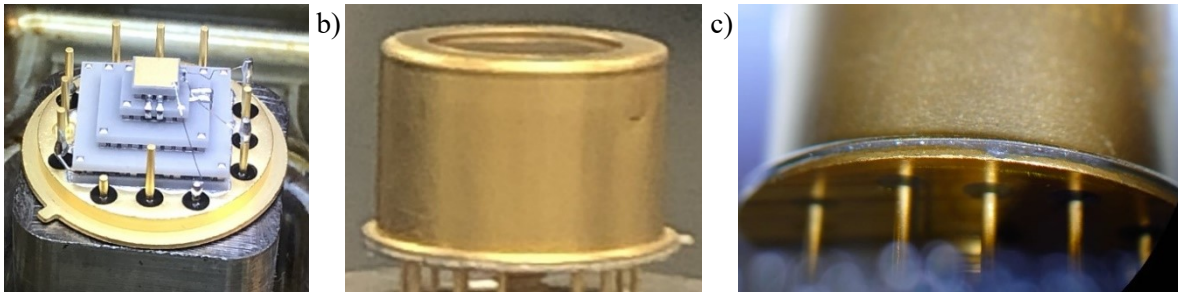

Figure 7-30: Semiconductor nanowire single-photon avalanche diode header, can, and thermoelectric cooler (TEC) packaging. a) Thermoelectric cooler and transistor outline package (TO-8) header assembly including the wire-bonded top metallized plate, TEC supply, and thermistor wire connections to header output pins. **b)** Advance ADY/Santek Sapphire windowed can on the TO-8 header. **c)** Cap-header interface hermetically sealed in a nitrogen glovebox enclosure by reflow soldering.

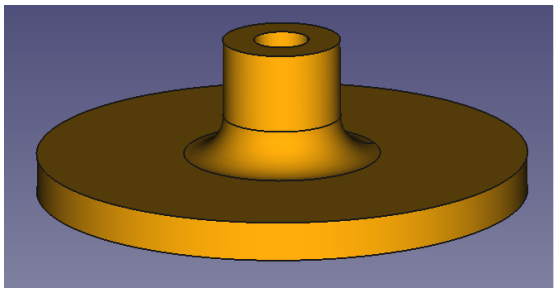

Figure 7-31: Machined copper adapter part model which thermally couples the transistor outline package (TO-8) header stud to the copper core of the forced convection heat sink.

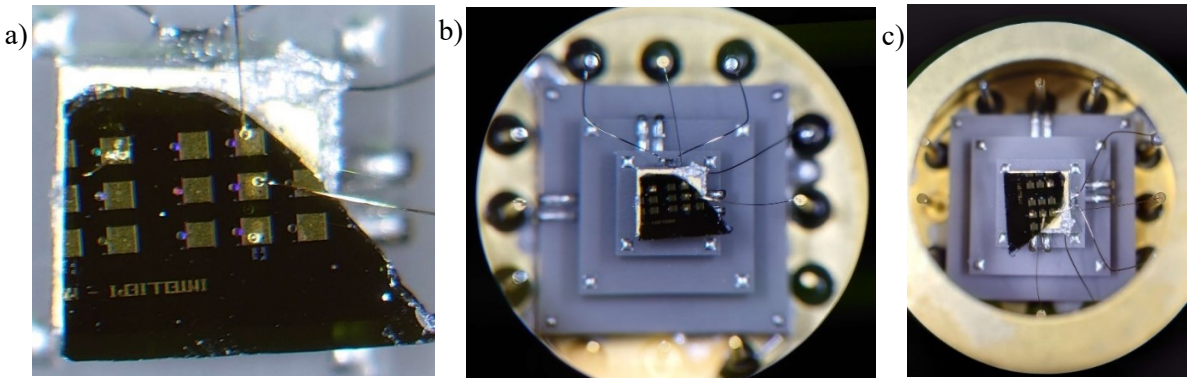

Figure 7-32: Mounted InGaAs/InAlAs semiconductor nanowire single-photon avalanche diodes (SN-SPADs) on the revised thermoelectric cooler (TEC) and inside of the hermetically sealed transistor outline package (TO-8). a) A sample chip of tapered NW array InGaAs/InAlAs metamaterial devices (SN-SPADs) mounted to a high-performance TEC by silver paste with individual wire-bonded devices before hermetic sealing. **b)** reduced magnification image of **a)**. **c)** The finished hermetically sealed TO-8 package with the enclosed, mounted, and connected InGaAs/InAlAs SN-SPAD samples.

7.6.2 Quenching Circuit

The PQC PCBs are revised to accommodate the updated (TO-8) package and thermal systems employed with the InGaAs/InAlAs metamaterial samples. Revising the PQC layout required modifications to accommodate the following elements: 50 Ω impedance matched transmission lines, TO-8 header footprint with a through hole for the TO-8 stud fitting copper adapter, heat sink mounting holes (four corners), miniaturized PQC components including the common ballast resistor and RF filter (Capacitors: one 4.7 µF, two 100 pF), 1 kΩ (anode) and 1 MΩ (cathode) electrostatic discharge (ESD)

protection resistors, thermistor and TEC connection terminals, heat sink fan pin connections, and RF probe and VA supply line connections to the SN-SPAD cathode and anode pins. The holes on the board are for mounting the heatsink and are sized and dimensioned for clearance of the integrated heatsink bolts. These bolts are used with proper hardware and spacers to secure the heatsink and mount it to the copper adapter. Ballast resistors ranging from 50 kΩ to 1 MΩ are considered to passively quench and reset the triggered SN-SPAD. The ESD protection resistors protect the device from potential mishandling, and the RF filters are included to reduce noise in the power supply line to the connected device samples. The EAGLE PCB schematic and layout of the PQC is presented in Figure 7-33.

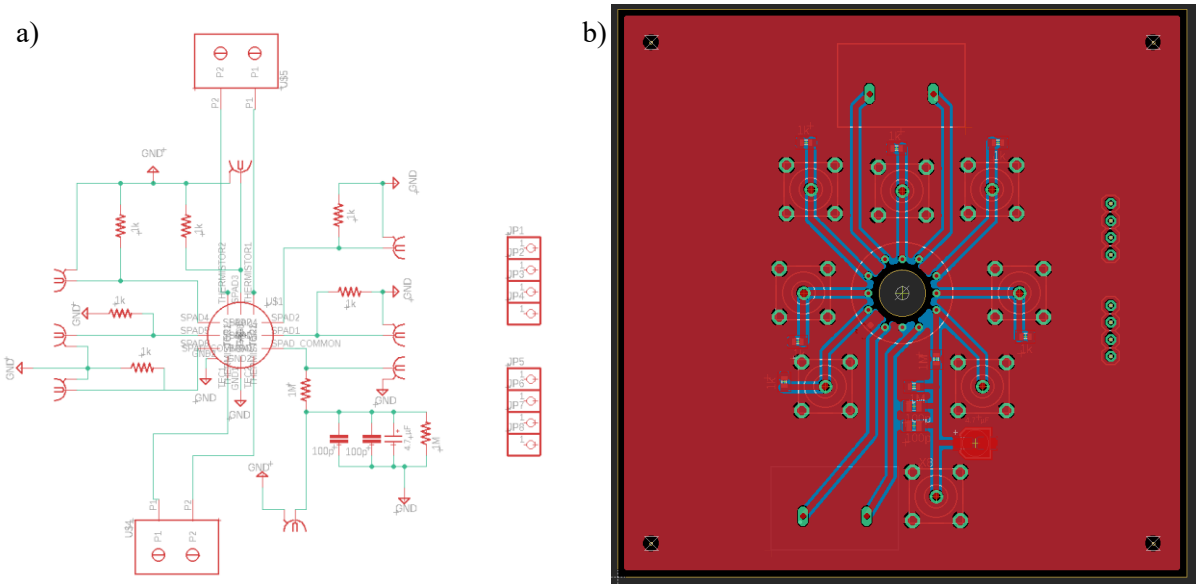

Figure 7-33: Passive quenching circuit for the revised InGaAs/InAlAs semiconductor nanowire single-photon avalanche diode sample cooling and packaging design. a) Revised passive quenching circuit schematic and **b)** board layout.

7.6.3 Measurement Setup

A similar measurement setup as that of the InP SN-SPAD devices of Section 7.5.2 is employed to measure the InGaAs/InAlAs SN-SPADs since the circuits are designed for similar operation and characterization. The InGaAs/InAlAs SN-SPAD characterization is run in the dark and on the cathode probe line. Several additional connections are required in this measurement setup, however, for power and readout of the thermal systems. These connections include power to the TEC and temperature readout (the thermistor) from the TEC control module and the heatsink fan connection to the power

supply. The fully assembled and connected InGaAs/InAlAs SN-SPAD detector-assembly prototype is included in Figure 7-34.

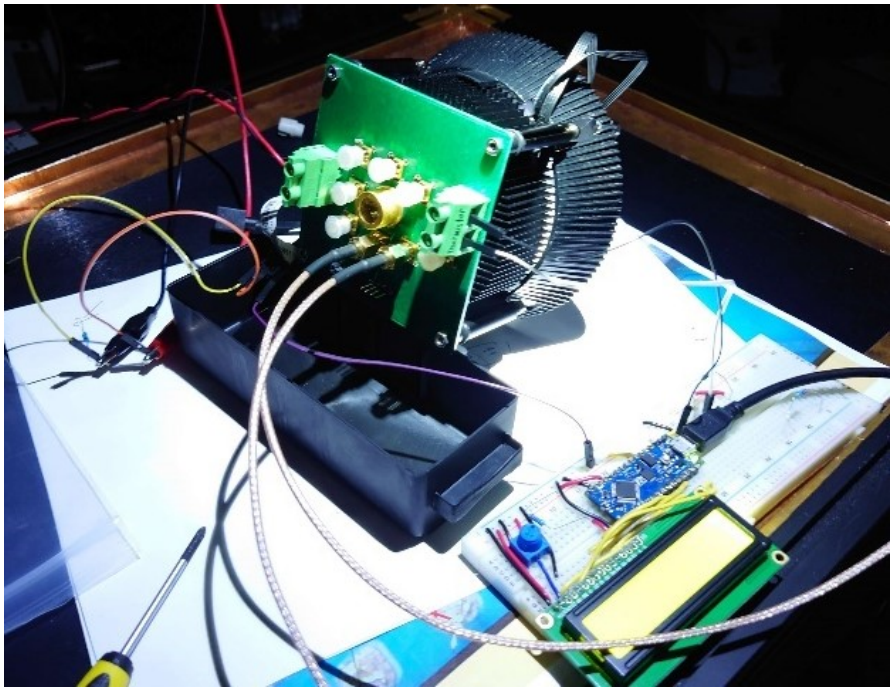

Figure 7-34: The complete semiconductor nanowire single-photon avalanche diode (SN-SPAD) detector module comprising of the packaged InGaAs/InAlAs nanowire p-n junction array single-photon detector chip mounted on a passive quenching circuit printed circuit board. The imaged SN-SPAD detector-assembly prototype also includes the heatsink and the necessary SN-SPAD characterization and cooler connections.

7.6.4 InGaAs/InAlAs Metamaterial Single-Photon Avalanche Diode Characterization

The thermistor mounted on the TEC by TEC Microsystems was not provided with calibration data down to the -70°C, the target operating temperature. Thus, temperature-resistance calibration data on the thermistor is required for the TEC control module to calculate the TEC operating temperature. To acquire this extended data, resistor-temperature calibration measurements are run on a group of matching thermistors by Cole Fehr in one of Dr. Reimer group's cryostats with the help fellow group members. The extended calibration curve data is included in Figure 7-35. The Steinhart–Hart model is used to fit the extended data which is then used in the control module calculations for TEC temperature readout. After calibrating the thermistor, the TEC performance is characterized. Cole Fehr assembled

a complete SN-SPAD package (absent the sample) and connected it to the heatsink to run the TEC performance measurements. The TEC is cooled with increasing supplied current, so the thermistor resistance is measured against TEC input current, as shown in Figure 7-36. The cooling of the TEC clearly increases, up until a critical current is reached where the heat begins to accumulate and temperature increases. By cross-referencing the resistance of the TEC performance results with the thermistor data, the cold side temperature of the TEC during the measurement is determined. Furthermore, to ensure the measured temperature can be applied by the TEC to the SN-SPADs for prolonged periods of stable operation, TEC temperature performance measurements are taken against time with increasing levels of supplied current to produce the temperature transient results of Figure 7-37. From the temperature transients, it is clear to see that stable TEC operation is achieved and there are no runaway affects which cause its temperature to increase to above environmental temperature values, as was the case in the previous TEC design of Section 7.5.4. Even after the supplied current surpasses the threshold where temperature begins to increase with increasing current, the TEC cold side temperature is shown to stabilize to a predictable level. From these results, it can be observed that a minimum (stable) TEC operating temperature of approximately -70°C, the targeted benchmark, is achievable for the SN-SPADs with the cooling system design at a supplied TEC current of 0.75 A.

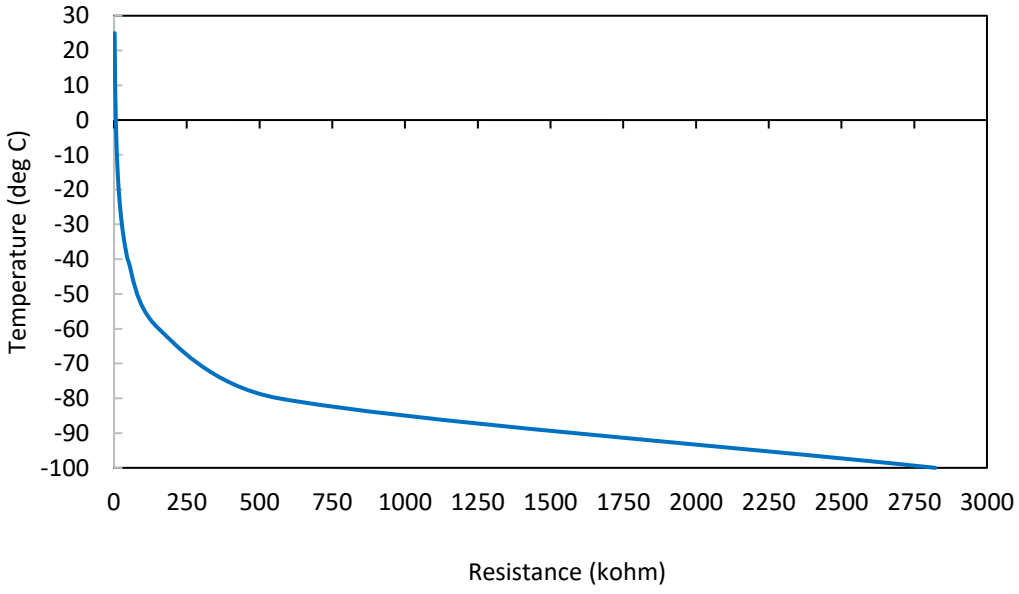

Figure 7-35: Extended resistor-temperature calibration data for the thermoelectric cooler mounted thermistor.

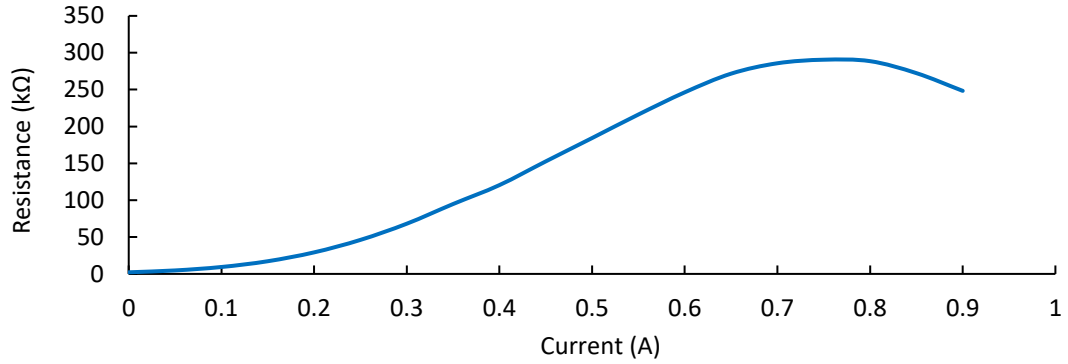

Figure 7-36: Measured thermoelectric cooler thermistor resistance readout inside of the transistor outline package (TO-8) during the semiconductor nanowire single-photon avalanche diode detector module operation in a room temperature envinronment (~25°C).

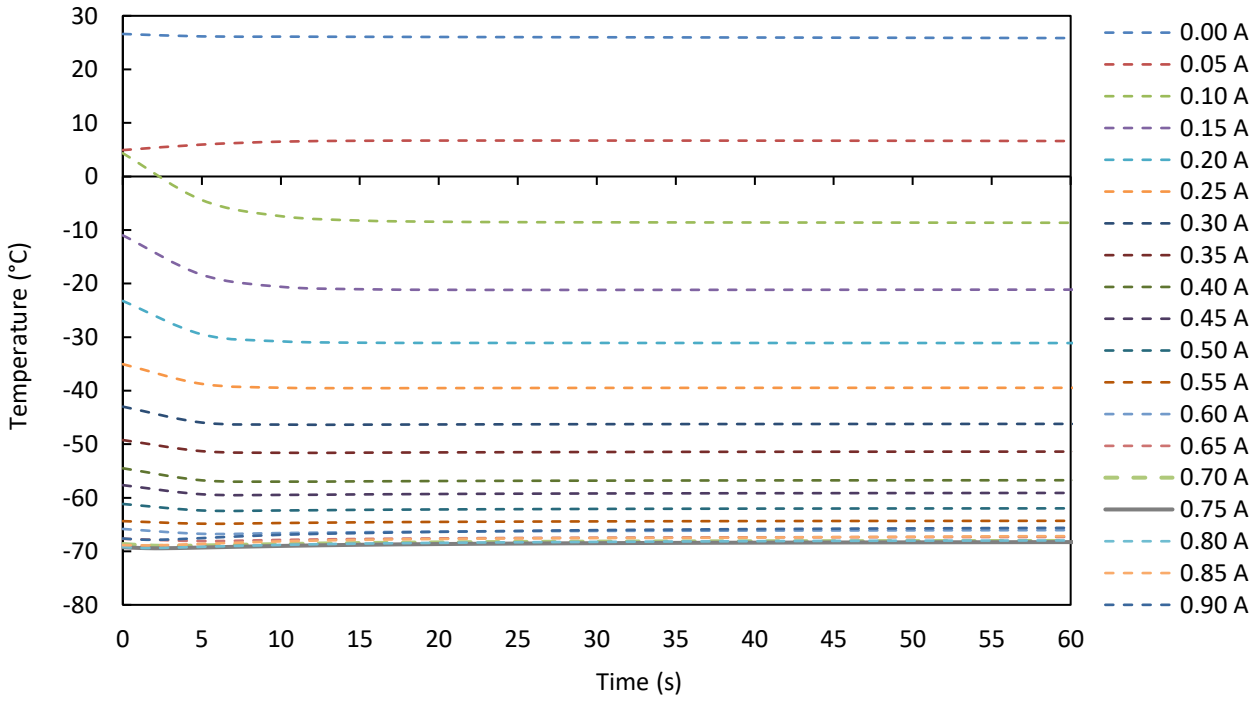

Figure 7-37: Measured temperature transients of the operating thermoelectric cooler (TEC) thermistor readout converted to degrees Celsius. The thermistor measurements were taken for 60 seconds at increasing TEC operating currents during semiconductor nanowire single-photon avalanche diode detector module operation in a room temperature environment (~25°C). The solid dark gray line at 0.75 A shows the best operating performance of the TEC where the benchmark (approximately -70°C) is achieved.

With the benchmark thermoelectric cooling performance achieved, a fully packaged InGaAs/InAlAs SN-SPAD sample detector-assembly prototype is constructed (absent the PQC) to measure its DC characteristics at approximately -70°C operation. The InGaAs/InAlAs sample chip had several wire-bonded devices to be measured, but none had a desirable characteristic SPAD I-V. One of the better performing I-Vs from the batch of InGaAs/InAlAs SN-SPADs is presented in Figure 7-38a alongside a characteristic (desirable) SPAD I-V profile (Figure 7-38b). For a SPAD of comparable active area, a more desirable I-V profile has a slowly increasing and low dark current (under ~10 nA) until avalanche, where the current increases exponentially into the microamp range. Comparatively, the measured I-V of Figure 7-38a shows a rapidly increasing current to above desirable values and a catastrophic failure prior to any indication of avalanche breakdown. Characterization of any avalanche breakdown behaviour was determined in the measured InGaAs/InAlAs devices by their temperature dependent I-V, as discussed in the supplementary information of the published article of Chapter 3[16].

Several InGaAs/InAlAs devices were found with I-Vs more closely resembling the desired I-V for SPAD operation. These samples were placed on a different sample carrier equipped for measuring in the Dr. Reimer group optical cryostat as part of fabrication studies by Burak Tekcan. One of the more promising InGaAs/InAlAs SAGCM metamaterial devices for SPAD operation measured at 100 K is included in Figure 7-39. This sample exhibited promising trends including low dark current (< 1 nA) until breakdown (~45 V), qualities of punch through (~20 V), and avalanche behaviour with a gain of 20 at ~40 V[2–4,9]. These prospective samples often exhibited excessively high (undesirable) dark currents for single-photon operation, however, which resulted from leakage current. The surface recombination and etch depth of the tapered NW structures are suspected to be responsible for the leakage current, having a NW base positioned just above the multiplication layer.

A prominence of surface states may also be a notable contributor to DCR because of the metamaterial's large surface area to volume ratio. As such, the reduction of surface state DCR contributions may be critical for mitigating excessive noise in future SN-SPAD devices for Geiger-mode operation. To alleviate the impact of the larger sidewall area on the dark current, surface passivation techniques can be implemented in fabrication alongside the optimized NW base etch depth with respect to the SAGCM material stack. Burak Tekcan covers the sample devices that showed promise, like that of Figure 7-39, in detail and provides future direction for improvement in his thesis. The prospective samples were unavailable, however, for their characterization in a complete InGaAs/InAlAs SN-SPAD detector-assembly prototype and measuring their performance in Geiger-mode operation, as part of this thesis.

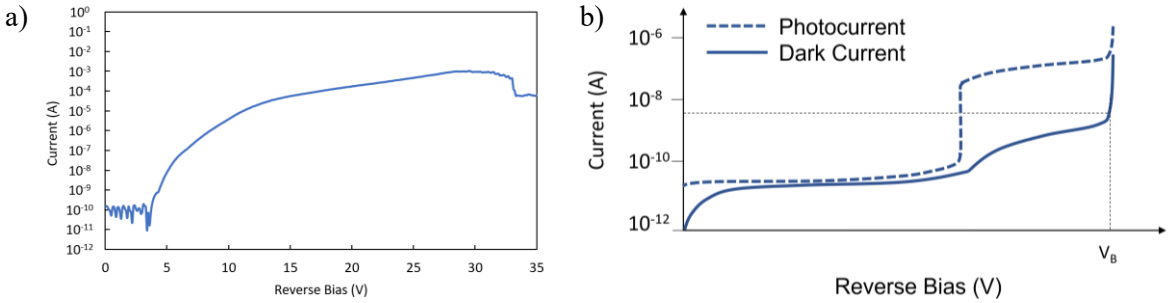

Figure 7-38: InGaAs/InAlAs semiconductor nanowire single-photon avalanche diode (SN-SPAD) current-voltage (I-V) relationships. a) Thermoelectrically cooled (-70°C) SN-SPAD detector module measured dark I-V. **b)** Concept diagram of the desirable dark (solid) and photo- (dashed) I-Vs. The desirable SN-SPAD (active area diameter ≈ 25 µm) dark I-V profile has a slowly increasing and low dark current (under ~10 nA) until avalanche, where the current increases exponentially into the microamp range.

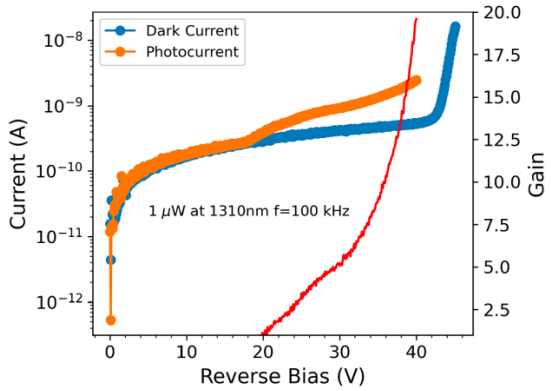

Figure 7-39: Prospective InGaAs/InAlAs semiconductor nanowire single-photon avalanche diode (SN-SPAD) sample current-voltage (I-V) relationship measurements. This presented result is also part of the thesis fabrication studies of fellow Dr. Reimer group member, Burak Tekcan. The measured dark current (blue) and photocurrent (orange) I-Vs demonstrating avalanche qualities were measured in an optical cryostat at 100 K. The SN-SPAD photocurrent I-V was measured under pulsed illumination of 1310 nm wavelength, 100 kHz pulse rate, 1µW power. The corresponding gain with increasing voltage is included in red.

7.6.5 Outlook

InGaAs/InAlAs SAGCM tapered NW arrays have demonstrated some promise for semiconductor metamaterial optoelectronic devices; however, further work is required for their application as SPDs. The thermoelectric cooling system design and packaging have demonstrated promise, achieving the benchmark -70°C operating temperature in a hermetically sealed RF package. Though flexibility is not emphasized in this design, the solder paste seal still allows the assembly to be disassembled to substitute SN-SPAD samples and modify wire-bonds. Also, a large temperature difference cooling capability is provided by the TEC Microsystems cooler to push the limit of TEC-based SN-SPAD operating temperature for characterization, but realizing further cooling requires improved thermal management such as a higher thermal resistance from the heatsink. The large thermal resistance requirement of the InGaAs/InAlAs SN-SPAD detector-assembly prototype motivated the selection of a forced convection heatsink. In future designs, however, it is suspected that the cooling demands will be lessened for optimal SN-SPAD cooling. In a more sophisticated final SN-SPAD detector-assembly design with improved thermal management, a cooler system employing a less bulky heatsink solution can be pursued, including a natural convection heatsink to prepare an ideal SN-SPAD operating temperature without the need of a fan and moving parts.

Regarding the RF packaging designs, commercial components were purchased based on similar applications and input from the manufacturers. Though the revised packaging design of the InGaAs/InAlAs SN-SPAD developments provided necessary qualities such as accommodating the relatively large TEC, a window for the proper wavelength range, and hermetic sealing, the potential for improvement remains. For instance, a change in the TEC design may also have a reduced footprint size and not require the large TO-8 packaging, so slimmer packaging options could be explored. The RF capabilities of the current header were not fully characterized, and its impact on the signal analysis of the SN-SPADs remains unknown. Though RF performance was considered in the packaging design, subsequent packaging implementations can potentially utilize a slimmer profile package with surface mount capability and better transmission line profiles for tuned RF performance to accommodate the SN-SPAD signal output. Such a solution would be more practical after the prototyping stage, when the requirements of the contained components from the packaging are better defined, and a more permanent hermetic sealing solution can be employed. Given the successful performance and (some) flexibility of the current thermoelectric cooling system and packaging design, it is found to be sufficient for further SN-SPAD implementations and characterization with future SN-SPAD samples.

The InGaAs/InAlAs metamaterial SAGCM samples showed some prospect for testing in an SN-SPAD detector-assembly prototype, having demonstrated avalanche breakdown. However, the dark current of these devices were typically too high for Geiger-mode operation, as a result of an excessive leakage current. The surface recombination should be addressed by surface passivation and the NW etch depth optimized with respect to the SAGCM stack to reduce the leakage current to acceptable levels for Geiger-mode operation. A study can also be performed on the passivation efficacy on reducing dark current to gain further insight into the impact of the NW's high surface area to volume ratio. After Geiger-mode operation is achieved with these SN-SPADs, the passivation study can extend to the DCR dependence on the NW surface area to volume ratio. Furthermore, trap activation energies along with temperature dependence measurements can be performed to study potentially prominent DCR mechanisms. These measurements can be run along with emission intensity characterization of breakdown uniformity to inform subsequent SN-SPAD design and development decisions.

The prospective InGaAs/InAlAs SN-SPAD samples exhibiting the desirable avalanche breakdown I-Vs were unavailable and they could not be studied in the complete SN-SPAD detector-assembly prototype and PQC for Geiger-mode operation. However, given the relative simplicity of the PQC, its successful construction into the complete InGaAs/InAlAs SN-SPAD detector-assembly prototype, and the characterization potential it demonstrated in the InP SN-SPAD measurements, it remains a valid option for immediate free-running mode characterization of future SN-SPAD device samples. Though the current detector-assembly PQC is useful for the SN-SPAD prototyping phase, other quenching circuit options should be explored, as different designs can aid in maximizing the targeted performance of critical SPAD metrics. From the quenching circuit comparison, for instance, an FAQC showed promise as a higher performance solution for III-V SPADs. The relatively simplicity, free-running mode operation, hold-off capability, and rapid quench times of the FAQC makes it an excellent option for future quenching circuit implementations. Not all of the components used in the FAQC of the reference article[15] are introduced and some of the described components are not commercially available, so the potential implementation of the FAQC on the SN-SPADs will rely on finding substitute components. Given the rapid pace of integrated circuit technology development, new components may be faster and benefit the FAQC design with higher speed operation for higher performance with the SN-SPADs. Such FAQC developments can be pursued in parallel with the SN-SPAD device development by adapting the circuit being studied to operate a commercial or mock (equivalent circuit model) SPAD. As such, the components and practical implementation of the circuit can be studied

without the metamaterial devices under development. Performance analysis of the FAQC can also be further studied in LTspice modelling after including more realistic components in the model. Components like transistors with accurate response and impedance characteristics can be added to model more practical FAQC response times and expected signal outputs when paired with SN-SPADs.

Alternative metamaterial designs utilizing different materials, device (material stack), and geometry can also be explored. For instance, InGaAs/InP-based devices are popular among planar SPADs, and this material option in smaller active area SN-SPADs which incorporate qualities of the InP metamaterial of Chapter 3 remains a viable approach for device level redesign[6,11,16,19]. Additionally, SPAD developments from different metamaterial platforms, such as those of Chapter 4 and Chapter 5, can be investigated and tuned to target applications for alternative selective and broadband devices. The metamaterials discussed in this thesis have shown high optoelectronic performance and advantageous behaviour. As such, further studies should be performed on the NW-metamaterial electronic attributes to further the fundamental understanding of their operation. Examples of such studies include the role of NW dimensional effects on the avalanche process, carrier transport dependence on electric field, breakdown variation between NWs, and surface depletion qualities in SN-SPAD devices[20]. An understanding of such operating principles will aid in the design of metamaterial optoelectronics, and the numerical modelling methods implemented in this thesis have already demonstrated a capability for insight into these effects.

Prospective metamaterial alternatives and future fabricated NW-based metamaterial devices should have their optoelectronic properties characterized for their SPD potential. Such properties include reflectivity, absorptance, EQE, IQE, responsivity, temporal response, and temperature dependence. After successfully demonstrating Geiger-mode operation in the designs, the metamaterial-based SPADs can be characterized and advanced for their performance in critical SPD metrics including DCR, DE, timing jitter, afterpulsing, etc. Alternative approaches and remodeling at the device level will be crucial for the successful Geiger-mode operation of the SN-SPAD and other metamaterial-based SPADs to realize the prospect of utilizing the enhanced metamaterial qualities for the next generation of high-performance SPDs.

7.7 References

1. Itzler, M. A. *et al.* Advances in InGaAsP-based avalanche diode single photon detectors. *Journal of Modern Optics* **58**, 174–200 (2011).
2. Cao, S. *et al.* Theoretical Analysis of InGaAs/InAlAs Single-Photon Avalanche Photodiodes. *Nanoscale Research Letters* **14**, 3 (2019).
3. Karve, G. *et al.* Geiger mode operation of an In0.53Ga0.47As-In0.52Al0.48As avalanche photodiode. *IEEE J. Quantum Electron.* **39**, 1281–1286 (2003).
4. Meng, X. *et al.* InGaAs/InAlAs single photon avalanche diode for 1550 nm photons. *R. Soc. open sci.* **3**, 150584 (2016).
5. Tekcan, B. *et al.* Semiconductor nanowire metamaterial for broadband near-unity absorption. *Sci Rep* **12**, 9663 (2022).
6. *Single-photon generation and detection: experimental methods in the physical sciences*. (Elsevier/AP, Academic Press is an imprint of Elsevier, 2013).
7. Susa, N., Nakagome, H., Mikami, O., Ando, H. & Kanbe, H. New InGaAs/InP avalanche photodiode structure for the 1-1.6 um wavelength region. *IEEE J. Quantum Electron.* **16**, 864–870 (1980).
8. Tosi, A., Acerbi, F., Dalla Mora, A., Itzler, M. A. & Jiang, X. Active Area Uniformity of InGaAs/InP Single-Photon Avalanche Diodes. *IEEE Photonics J.* **3**, 31–41 (2011).
9. Tosi, A., Calandri, N., Sanzaro, M. & Acerbi, F. Low-Noise, Low-Jitter, High Detection Efficiency InGaAs/InP Single-Photon Avalanche Diode. *IEEE J. Select. Topics Quantum Electron.* **20**, 192–197 (2014).
10. Hiskett, P. A. *et al.* Performance and design of InGaAs/InP photodiodes for single-photon counting at 155 μm. *Appl. Opt.* **39**, 6818 (2000).
11. Acerbi, F., Anti, M., Tosi, A. & Zappa, F. Design Criteria for InGaAs/InP Single-Photon Avalanche Diode. *IEEE Photonics J.* **5**, 6800209–6800209 (2013).
12. Cova, S., Ghioni, M., Lacaita, A., Samori, C. & Zappa, F. Avalanche photodiodes and quenching circuits for single-photon detection. *Appl. Opt.* **35**, 1956 (1996).
13. Ghioni, M., Cova, S., Zappa, F. & Samori, C. Compact active quenching circuit for fast photon counting with avalanche photodiodes. *Review of Scientific Instruments* **67**, 3440–3448 (1996).
14. Stipčević, M. Active quenching circuit for single-photon detection with Geiger mode avalanche photodiodes. *Appl. Opt.* **48**, 1705 (2009).

15. Liu, J. *et al.* Fast Active-Quenching Circuit for Free-Running InGaAs(P)/InP Single-Photon Avalanche Diodes. *IEEE J. Quantum Electron.* **52**, 1–6 (2016).
16. Gibson, S. J. *et al.* Tapered InP nanowire arrays for efficient broadband high-speed single-photon detection. *Nat. Nanotechnol.* **14**, 473–479 (2019).
17. Sanzaro, M. *et al.* InGaAs/InP single-photon detector with low noise, low timing jitter and high count rate. in (eds. Razeghi, M., Tournié, E. & Brown, G. J.) 93701T (2015). doi:10.1117/12.2079778.
18. Hadfield, R. H. Single-photon detectors for optical quantum information applications. *Nature Photon* **3**, 696–705 (2009).
19. Donnelly, J. P. *et al.* Design Considerations for 1.06-um InGaAsP–InP Geiger-Mode Avalanche Photodiodes. *IEEE J. Quantum Electron.* **42**, 797–809 (2006).
20. Spinelli, A. & Lacaita, A. L. Physics and numerical simulation of single photon avalanche diodes. *IEEE Trans. Electron Devices* **44**, 1931–1943 (1997).